Investigations of Structures and Dynamics of Transmembrane Proteins and Implications in the Action of Inhalational Anesthetics

by

Tanxing Cui

Bachelor of Science, Nankai University, China, 2001
Master of Science, Nankai University, China, 2004

SUBMITTED TO THE GRADUATE FACULTY OF SCHOOL OF MEDICINE IN PARTIAL FULFILMENT OF THE REQUIREMENTS FOR THE DEGREE OF

DOCTOR OF PHILOSOPHY
AT THE
UNIVERSITY OF PITTSBURGH

University of Pittsburgh
2010

This dissertation was presented by Tanxing Cui.

It was defended on July 30th, 2010
and approved by

Professor Yan Xu
(Dept. of Anesthesiology) _____ Thesis Advisor

Professor Gregg Homanics
(Dept. of Anesthesiology) _____ Chairperson

Professor Rieko Ishima
(Dept. of Structural Biology) _____

Professor Hagai Meirovitch
(Dept. of Computational Biology) _____

Professor Peijun Zhang
(Dept. of Structural Biology) _____

Investigations of Structures and Dynamics of Transmembrane Proteins and Implications in the Action of Inhalational Anesthetics

Tanxing Cui, M.S.
University of Pittsburgh, 2010

The nicotinic acetylcholine receptor (nAChR) mediates fast signal transduction in peripheral and central nervous systems. It is a pentameric ion channel that belongs to the Cys-loop receptor superfamily. nAChR is one of the plausible targets for general anesthetics. The current concern about nAChR is ambivalent structures of the transmembrane (TM) domain, missing information for the intracellular (IC) domain and elusive mechanisms of the action of general anesthetics. Therefore, this thesis focuses on the following two important aspects: first, the structure and dynamics of the nAChR TM and IC domains; and second, general anesthetic effects on various proteins.

Part I. The secondary structure of human nAChR α7 TM domain and the monomeric tertiary structure of the water-soluble mutant of nAChR α1 TM domain from the Torpedo electrical ray were determined by NMR. The structures among WSA, nAChR α7, and a bacterial analogue of the pentameric channels (GLIC) are similar, but different from the cryo-EM structure of the nAChR. The backbone dynamics analyses of human nAChR α7 with and without the IC domain suggest that the presence of IC domains dramatically affected the intrinsic dynamics of the TM domains.

Part II. The general anesthetic effects on the structure and dynamics of the proteins including two analogues and a real anesthetic target in non-channel and channel-like oligomers were studied. It revealed that general anesthetics prefer amphipathic environments. Compared

to the effect on the structures of proteins, general anesthetics show stronger effect on the dynamics. The effect on the dynamics of proteins can manifest directly or allosterically.

Part III. The anesthetic effects on the Na^+ flux through the reconstituted channels of nAChR TM domains were investigated by fluorescence microscopy. The anesthetic effects on them are the same as on the full-length nAChR. This indicates that the studies of anesthetic effects on the TM domains of nAChR are functional relevant.

In summary, this dissertation clarifies the current structural ambiguities, provides additional invaluable dynamic information for the TM and IC domain and reveals the possible mechanism of action of general anesthetics.

TABLE OF CONTENTS

LIST OF TABLES

LIST OF FIGURES

LIST OF ABBREVIATIONS

14-O-PC	1,2-O-ditetradecyl-sn-glycero-3-phosphocoline
6-O-PC	1,2-O-dihexyl-sn-glycero-3-phosphocholine
CD	circular dichroism
CPMG	Carr−Purcell−Meiboom−Gill
Cryo-EM	cryo-electron microscopy
CSI	chemical shift index
DHPC	1,2-dihexyl-sn-glycero-3-phosphocholine
DMPC	1,2-dimyristoyl-sn-glycero-3-phosphocoline
DPC	decyl phosphocholine
DTT	dithiotreitol
EC	extracellular
ECD	extracellular domain
ELIC	prokaryotic pentameric ligand-gated ion channel from the bacterium *Erwinia chrysanthemi*
GLIC	prokaryotic pentameric ligand-gated ion channel from the bacterial *Gloeobacter violaceus*
GlyR	glycine receptor
HSQC	heteronuclear single quantum coherence
IC	intracellular
IMP	integral membrane protein
IPTG	isopropyl β-d-1-thiogalactopyranoside
LDAO	lauryl dimethylamine oxide
LPPG	1-Palmitoyl-2-Hydroxy-*sn*-Glycero-3-[Phospho-*rac*-(1-glycerol)]
LUV	large lamellar vesicles
MIT	magnetization inversion transfer
MTSL	(*S*-(2,2,5,5-tetramethyl-2,5-dihydro-1H-pyrrol-3-yl)methyl methanesulfonothioate)
nAChR	nicotinic acetylcholine receptor
NMR	nuclear magnetic resonance
NOE	nuclear overhauser effect
NOESY	nuclear overhauser effect spectroscopy
PCR	polymerase chain reaction
PC	L-α phosphatidylcholine
PG	L-α phosphatidylglycerol
PISA	Polar Index Slant Angle
pLGIC	prokaryotic pentameric ligand-gated ion channel
PMP	peripheral membrane proteins
PRE	paramagnetic relaxation enhancement

PTX	picrotoxin
PISEMA	polarization inversion spin exchange at the magic angle
RDC	residual dipolar coupling
RMSD	root mean square deviation
SR	chemical shift reagent
STD	saturation transfer difference
TFA	trifluoroacetic acid
TFE	2,2,2-trifluoroethanol
TM	transmembrane

PREFACE

Part of this thesis has been published.

Cui, T., Bondarenko, V., Ma, D., Canlas, C., Brandon, N. R., Johansson, J. S., Xu, Y. & Tang, P. Four-alpha-helix bundle with designed anesthetic binding pockets. Part II: halothane effects on structure and dynamics. *Biophys J* **94**, 4464-4472, (2008).

Cui, T., Canlas, C. G., Xu, Y. & Tang, P. Anesthetic effects on the structure and dynamics of the second transmembrane domains of nAChR alpha4beta2. *Biochim Biophys Acta* **1798**, 161-166, (2010).

Canlas, C. G., **Cui, T.**, Li, L., Xu, Y. & Tang, P. Anesthetic modulation of protein dynamics: insight from an NMR study. *J Phys Chem B* **112**, 14312-14318, (2008).

Ma, D., Brandon, N. R., **Cui, T.**, Bondarenko, V., Canlas, C., Johansson, J. S., Tang, P. & Xu, Y. Four-alpha-helix bundle with designed anesthetic binding pockets. Part I: structural and dynamical analyses. *Biophys J* **94**, 4454-4463, (2008).

Part of this thesis has been submitted for review.

Cui, T., Jia, Y., Ma, D., Mowrey, D., Makhov, A. M., Zhang, P., Tang, P. & Xu, Y. NMR structure of full-length transmembrane domain of human glycine receptor α1 subunit.

Xiong, W., Chen, K., **Cui, T.**, Godlewski, G., Rice, K., Xu.,Y. & Zhang, L. The site of action of cannabinoid potentiation in glycine receptors

Part of this thesis is in manuscript preparation.

Cui, T. et al. NMR Structure of Water-Solubilized Transmembrane Domain of Nicotinic Acetylcholine Receptor

ACKNOWLEDGMENTS

Hereby, I would like to have the honor to express heartily thanks to my mentor and research advisor, Professor Yan Xu, for his excellent and professional guidance, consistent support, and tireless encouragement. I would also like to thank Professor Pei Tang for her constant guidance, invaluable suggestions, great perseverance, and patience. I am truly lucky to be able work with both of them and to be trained in their laboratories. Without their help, this thesis would not have been possible.

I especially would like to acknowledge the members of my dissertation committee, Professor Gregg Homanics (chairman), Professor Rieko Ishima, Professor Hagai Meirovitch, and Professor Peijun Zhang for agreeing to serve on the committee and for their patience and support throughout this process.

I would like to extend my warmest thanks to colleagues, Dr. Dejian Ma, Dr. Vasyl Bondarenko, Dr. Chris Canlas, and Ms. Nicole R. Brandon for their great help with NMR techniques; Dr. Tommy Tillman, Mrs. Ling Li, and Dr. Yuanyuan Jia with protein expression and purification; Dr. Aaron C. Hirko, Mr. Andy Samuelsson, Dr. Xuehui Geng, and Dr. Peter Drain with fluorescence experiments; Dr. Jun Li, Dr. Qiang Chen, and Dr. Patrick van der Wel with solid state NMR; and Dr. Lu Liu, Dr. Esmael J. Haddadian, and Mr. David Mowrey with the computational works. I would also like to thank Mrs. Sandy Hirsch for proofreading all chapters of this dissertation.

I would also like to thank other lab members, Dr. Mary Hongying Cheng, Dr. Jianjun Pan, Dr. Dan Willenbring, Mr. Adam Goldring, and Professor Tetsuro Sakai.

Also, I would like to thank Dr. Angela Gronenborn and the Molecular Biophysics and Structural Biology graduate program to give me the opportunity to pursue my PhD studies; Ms. Jennifer Walker, Ms. Janet Zambotti, and Mr. Dean Duncan for their administrative support; and Mr. Mike Delk for support on using the NMR machines.

I am grateful to all my friends from Pittsburgh for being my surrogate family for many years.

Finally, I would like to extend my immense gratitude to my parents. I am forever indebted to my parents for their understanding, endless patience and encouragement.

CHAPTER 1

INTRODUCTION AND BACKGROUND

1.1 FIELDS OF STUDIES

1.1.1 Membrane proteins

Membrane proteins are proteins located in the biological membranes and interact or associate with membrane lipids. It is estimated that more than 30% of the proteins in cells are membrane proteins, which play a vital role in the biological functions [1]. Membrane proteins can be simply divided into two classes, integral membrane proteins (IMPs) and peripheral membrane proteins (PMPs). IMPs are usually deeply buried in the phospholipids of the membranes with their one or more membrane-spanning domains (TM domains). On the contrary, PMPs do not enter the hydrophobic cores formed by the phospholipids and they usually interact with the IMPs or the polar head groups of the membrane lipids. Until now, the membrane-spanning domains of the IMPs were found to be α helices or multiple β strands. These TM domains contain the hydrophobic residues, which interact with the hydrophobic core of the membrane lipids. Above 50% of the membrane proteins in the cells are predicted to be pharmaceutical targets [2]. Knowing their structures and dynamics can help us to understand their important intrinsic functions. However, less than 1% of the deposited protein structures in the Protein Data

Bank (PDB) are membrane proteins. The low percentage of resolved structures reflects the difficulties of the structure determination for membrane proteins. Membrane proteins are usually very hard to be expressed and purified. After they are solubilized in the detergent micelles from the membrane lipid, membrane proteins are often misfolded and lose their native function. Therefore, how to perform structural studies on membrane proteins is a very challenging task.

1.1.2 Nicotinic acetylcholine receptors

Acetylcholine receptors are IMPs, which respond to the binding of the neurotransmitter acetylcholine. Based on their different responses to nicotine and muscarine in addition to the acetylcholine, acetylcholine receptors are classified into two receptor types, nicotinic acetylcholine receptors (nAChRs) and muscarinic acetylcholine receptors (mAChRs). nAChRs belong to ligand-gated ion channels and are members of a superfamily of Cys-loop receptors that contain a characteristic loop formed by a disulfide bond between two cysteines. mAChRs are G protein-coupled acetylcholine receptors. In addition to acetylcholine receptors, the cys-loop receptor superfamily also includes glycine (Gly), γ-aminobutyric acid ($GABA_A$ and $GABA_C$) and serotonin ($5\text{-}HT_3$) receptors. Based on their different expression sites at neuromuscular junction or nerve synapse, nAChRs can be generally divided into two subtypes: muscle type and neuronal type.

Neurotransmitters, such as acetylcholine, are packaged in vesicles inside a presynaptic neuron. When the neuron is activated, these IC vesicles fuse with the neuron membrane and release the neurotransmitters into the synaptic cleft. Once the neurotransmitter is released in the synapse, it may diffuse across the synapse and bind to its receptor, such as nAChR on the postsynaptic membrane. However, the acetylcholine may also diffuse back to the presynaptic neuron and bind to a presynaptic

receptor to further modulate the release of neurotransmitters. Other events can also happen. For example, the neurotransmitters may be chemically altered by an enzyme in the synapse, or may be transported into a nearby cell. The binding of an acetylcholine to its receptor plays a very important role for the nAChR to mediate the fast synaptic transmission of electrical signals. It is also a key event in the action of many other neurotransmitters. The response of nAChR to acetylcholine is referred to as 'fast-acting' because the cellular effect occurs in the millisecond timescale after the acetylcholine binds to the nAChR. It has been proposed that the binding of acetylcholine to the nAChR could induce a conformational change of the receptor and thus allow sodium ions to flow inside the neuron through modulating the channel state. It also causes the depolarization of the cell, which could further result in the continuous nerve impulse.

The atomic structure of nAChR has been a hot topic in structural biology for a long time and several key breakthroughs have emerged recently. X-ray structures of homologues of the extracellular domain (ECD) of nAChRs from acetylcholine binding proteins (AChBPs) and the ECD of α1-nAChR have been solved. These crystal structures give us atomic structural information for the ECD [3-6]. The *Torpedo marmorata* nAChR, solved by electron microscopy at 4 Å resolution, provides additional structure information about the TM and partial IC domains [7,8]. Until very recently, the prokaryotic pentameric ligand-gated ion channel (pLGIC) from the bacterium *Erwinia chrysanthemi* (ELIC) and the bacterial *Gloeobacter violaceus* pLGIC homologue (GLIC) have been solved by X-ray at atomic resolution [9-11]. nAChRs are typically homo-pentameric or hetero-pentameric ion channels with a molecular mass of ~290 kDa [12]. Each subunit includes a large N-terminal ECD, a TM domain and a large IC domain. The ECD is mainly composed of β sheets [5]. They are divided into two groups, outer sheets and inner sheets, based on their relative position to the central pore. Two sheets are connected by

the characteristic loop formed by a disulfide bond between two cysteines in each sheet. The ECD is the main target of various ligands [13]. On the contrary, α-helix is the main component of the TM domain [7]. Each TM domain is formed by four TM α helices. Along these helices, TM2s from each subunit join together to form the central pore, while TM1, TM3 and TM4 form another two concentric circles. The conserved pore lining residues are located in the TM2 domain; these residues are responsible for the ion selectivity and conductivity [7]. Until now, the understanding of the structure of the IC domain has been limited due to the lack of any atomic structure information of the IC domain. Previous studies on the IC domain suggest that this domain plays an important role in interaction with IC proteins, receptor targeting and ion channel properties [14-20].

1.1.3 General anesthetics and mechanisms of general anesthesia

Anesthetics are drugs that can cause anesthesia, temporary loss of consciousness or sensation, thereby allowing a patient to undergo surgery without suffering. Anesthetics can be categorized into two classes based on their effects: general anesthetics and local anesthetics. General anesthetics cause a reversible loss of consciousness (general anesthesia), while local anesthetics result in a reversible loss of sensation in a local region without loss of consciousness. General anesthetics are a diverse range of molecules, from structurally featureless gases to complex steroids. They are further classified roughly into two types, inhalational anesthetics and intravenous anesthetics, based on the anesthetics' mode of administration. Inhalational anesthetics are volatile liquids or gases such as halothane and isoflurane and are usually delivered by an anesthesia machine. Intravenous anesthetics, such as etomidate, are administrated by injection.

General anesthetics render people into a state of unconsciousness known as general anesthesia and have been widely used in modern medicine; however, the molecular processes underlying general anesthesia remain largely unclear [21-27]. Two distinct hypotheses, the lipid hypothesis and the membrane protein hypothesis, have been proposed. In the lipid hypothesis, nonspecific anesthetic-lipid interaction in the central nervous system may alter the property of membrane lipids. This change in the membrane could impact the response of neuronal membrane proteins. Although modulation of neuronal protein functions through nonspecific anesthetic perturbation to the lipids remains a distinct possibility, the current consensus is the protein hypothesis that anesthetic molecules interact specifically with proteins. It was first evidenced by observation of anesthetic effects on several water-soluble proteins that anesthetics can directly modulate their native function. For example, luciferase is in the class of oxidative enzymes, which are used by bioluminescent animals and bacteria to produce light. It was found that general anesthetics could inhibit these proteins through directly interacting with specific hydrophobic residues of luciferase [28]. General anesthetics' ability to inhibit proteins was directly correlated with their anesthetic potencies [29]. From these studies on the water-soluble proteins, it was found that general anesthetics bind to preexisting pockets with amphiphilic environments that exist within protein monomers or the interface between subunits [29,30]. The binding of anesthetics does not induce major changes in protein structure [31-34]. Although general anesthetics can directly interact with water-soluble proteins, providing detailed information about the molecular interaction characters and protein motifs, these proteins are often not physiologically relevant. It has been demonstrated that neurotransmitter-gated ion channels, particularly Cys-loop receptors, are plausible targets for general anesthetics in the central nerve system [21,30]. nAChRs are one of the potential targets, along with receptors for $GABA_A$, glycine, and

$5HT_3$. A wealth of electrophysiology experiments showed that the nAChR could be inhibited by general anesthetics [35-37]. By anesthetic direct photoaffinity labeling of the nAChR, the TM domains (TM1, TM2, and TM3) were identified to be the targets of inhalational anesthetics [38]. Due to a fundamental resolution limit on the photoaffinity labeling method, the anesthetic binding sites were not determined. Most important, how anesthetics specifically interact with proteins, and thus alter the protein's native function remain unclear. The specific interaction sites between general anesthetics and nAChR are critical for anesthetic actions [39]. NMR is a very powerful tool to study the mechanism of anesthetic effects on nAChR. It can offer not only the high-resolution picture with regard to the anesthetic binding sites, but also the unique dynamic information that corresponds to the protein critical function. In our group, advanced NMR techniques have been applied to the study of the anesthetic effects on various proteins including nAChRs [25,26,40-46]. Based on our studies, we have hypothesized that the anesthetics alter the target protein's biological function through specifically interacting with their targets and modulating the targets' global dynamics.

1.2 GOALS AND ACCOMPLISHMENTS

1.2.1 Open questions and significance

Several questions warrant further investigation. First, emerging structural studies [7-11] on the nAChR provide certain structural details. However, their limited resolutions in the case of the cryo-electron microscopy (cryo-EM) structure model from Torpedo electric ray or low sequence identities between the nAChR and recently published ELIC and GLIC structures from X-ray are inadequate to provide the structural basis for nAChR.

Second, by closely comparing the structures in the TM domains (TMs) along these proteins, the TM domain structures obtained from ELIC and GLIC are not consistent with the cryo-EM model structure form the torpedo nAChR. The differences exist particularly in the TM2 domain and its related loops. Third, both the cryo-EM model structure and X-ray structures have failed to provide complete information about the IC domain. The present structural studies on the nAChRs not only clarify the current ambiguities and provide more structural details including the TM domains and the IC domain, but also offer additional invaluable dynamic information of the nAChR. The high-resolution structures, plus detailed backbone dynamic information, will finally allow us to understand the important channel function of nAChR.

Much evidence suggests that the nAChR is one of the potential molecular targets for the general anesthetics [35-37]. However, there is no comprehensive understanding of how general anesthetics modulate the structure and the dynamics of the nAChR at the molecular level, and ultimately modulate the protein function. In my current studies, general anesthetic effects on various proteins were intensively studied by multiple biophysical methods. These proteins ranged from a water-soluble protein to a membrane protein, from an analogue to a real anesthetic target, from a 'non-channel' monomer to a 'channel-active' oligomer. The results from these studies further enrich our understanding of the mechanism of general anesthetic effects.

1.2.2 Strategies

Two specific constructs, the nAChR α1 subunit from torpedo and the α7 subunit from human, were reconstituted for structural studies.

The previous cryo-EM study [7,8] on the nAChR showed different results from the new published X-ray structures of GLIC and ELIC [9-11]. Three possible reasons could be

responsible for this difference. First, the sequence similarity between nAChR and GLIC/ELIC is low, even though GLIC/ELIC are considered to be analogues of the ligand-gated ion channels. The poor sequence identity may give rise to the structural difference. Second, the full-length nAChR structure of torpedo includes an IC domain, while GLIC and ELIC do not contain an IC domain. The presence of an IC domain in the torpedo nAChR could cause the structural difference between nAChR and GLIC/ELIC. However, the most distinct structural difference among them is at the TM23 loop, which is far away from the IC domain. Therefore, it is unlikely that the absence of the IC domain can cause the structural difference. Last, the structure of torpedo nAChR represents a closed state, which is different from GLIC. GLIC is in the open state. The different states may cause the structural difference between GLIC and torpedo nAChR. ELIC is also considered in a closed state. However, the artifacts from crystallization may contribute to the difference between ELIC and nAChR. In consideration of the size limitation of protein NMR, we only focused on the TM domain of nAChR from torpedo in the present study. The EC domain and IC domain were truncated and a five-glycine link was used to replace the entire IC domain. Since the resulting protein has the same sequence and no IC domain, the structure determination of this resulting protein can address the structural difference between nAChR and GLIC/ELIC. In practice, however, structure determination of mammalian membrane proteins is challenging due to a low expression level, unpredictable folding, and poor protein stability. In order to overcome these critical issues, a novel water solubilization approach was applied. In such a way, the membrane protein was transformed into a completely or partially water-soluble protein, while retaining its original structure and important function. The new redesigned nAChR is suitable for structure determination by solution-state NMR.

The structure study of the IC loop domain was performed on the human nAChR α7. Two protein constructs, the TM domain only and the TM domain plus the full-length

IC domain, were prepared. The water solubilization approach was only applied to the TM domain and the IC loop domain remained unchanged. Through studying the human nAChR α7 in the presence and absence of the IC domain, we not only can obtain structural information about the IC domain, but also confirm the structures of the TM domains for nAChR α1 subunit, GLIC and ELIC. Further, the IC domain effects on the TM domain can also be addressed.

For the study of the mechanism of general anesthesia, we focused on three distinct proteins.

nAChR is a potential anesthetic target, however, as a membrane protein, nAChR is usually difficult to study directly. The water-soluble dimeric protein $(A\alpha_2\text{-}L1M/L38M)_2$ was engineered to simplify this study by de novo design, which mimics the nAChR with a long hydrophobic core within a ubiquitous four-*α*-helix bundle scaffold. More importantly, this four-*α*-helix bundle also has an anesthetic binding affinity in the range of clinical volatile anesthetic concentration. Therefore, $(A\alpha_2\text{-}L1M/L38M)_2$ is regarded as a suitable model for the study of general anesthetic effect.

It has been shown that general anesthetics are presumed to binding to the TM domain of nAChR [38]. A membrane model protein (membrane integrating sequence for translation of integral membrane protein constructs, or Mistic) shares a four-α-helix bundle structural motif with the TM domain of nAChR. Mistic was chosen as a model of the target of general anesthetics not only because it naturally folds into a four-α-helix bundle motif in micelles, but also the structure of Mistic has been previously determined by NMR spectroscopy in lauryl dimethylamine oxide (LDAO) micelles, which will simplify our research [47].

Neuronal α4β2 nAChR is one of the receptor subtypes that are hypersensitive to general anesthetics. It is also one of the most abundant nAChR subtypes in the brain.

Despite ample evidence showing that general anesthetics could alter α4β2 nAChR functions, it remains largely unclear at a molecular level how anesthetics perturb the protein structures and dynamics that ultimately affect the protein functions. It has been reported that the TM2 domains of nAChR themselves can form an authentic channel [48]. Due to the size limitation of protein NMR, we focused on the most relevant TM2 domains of neuronal α4β2 nAChR, instead of the full-length protein.

TM domains are the presumed anesthetic binding sites [38]. In electro-physiological experiments, the functional studies indicate that the full-length neuronal α7 nAChR is insensitive to general anesthetics, while the neuronal α4β2 is sensitive to general anesthetics [35]. Therefore, we hypothesize that the general anesthetics may directly interact with the TM domains and be capable of modulating the channel function of the TM domains even without the EC and IC domains. The TM domains of neuronal α4β2 and α7 were separately reconstituted into lipid vesicles. The channel activity was monitored using fluorescence microscopy.

1.2.3 Summary of achievements

Structure Determination

Monomeric structures of water-solubilized nAChR TM domains, WSA, were solved to a backbone RMSD of ~1.1 Å. The overall structure of WSA is similar to the GLIC rather than the cryo-EM model of torpedo nAChR. The very short TM2-TM3 loop (VPLI) in the cryo-EM structure was replaced by a significantly longer loop (LIPSTSSA) and shifted by five residues towards the TM2 domain in both WSA and GLIC. More interestingly, the structure and dynamics obtained from the solution sample provide additional details. For example, STSSA in loop23 exists in two conformations: a rigid distorted helix and a flexible coil, and these two conformations are in slow exchange on

the NMR timescale. Given that the interaction between the TM23 loop and the EC domain likely mediates channel gating, the two conformations in this important loop might represent the critical transitions required for the channel to open.

Human nAChR α7 TM domains with (nAChRα7TM-IC) and without the IC domain (nAChRα7TM-5G) were successfully heterologously over-expressed in *E. coli*. The expression yield for these proteins were 5 mg/l and 10 mg/l, respectively, in M9 media. The secondary structures of our recombinant proteins have been investigated by circular dichroism (CD). Both nAChRα7TM-IC and nAChRα7TM-5G folded into stable structures in ~1% empigen with helical content of 41% and 50%, respectively. Highly resolved NMR HSQC spectra for the two proteins have been obtained. Both CD and NMR spectra suggest that the expressed proteins are well folded. Furthermore, backbone dynamics R_1, R_2, and heteronuclear NOE were performed and qualitatively analyzed using the histogram method. The comparison of the backbone dynamics of these two proteins indicates that the IC domain dramatically affects the intrinsic dynamics of the TM domain and makes the TM domain much more flexible.

In summary, the NMR studies on both monomeric WSA and nAChRTM-5G/IC are consistent with the X-ray results of GLIC [9,11]. All of them differ from the cryo-EM model structure of nAChR from torpedo with regard to the length of the helix and the loop positions [7,8]. The new findings from our studies not only clarify the discrepancies among several structures and offer more structural details, but also provide invaluable dynamic information for both the TM domain and the IC loop domain, which is missing from both the cryo-EM and X-ray structures.

Anesthetic-protein interaction

The high-resolution structure of $(A\alpha_2\text{-L1M/L38M})_2$ in the presence of halothane, a clinically used volatile anesthetic, was determined by NMR. The 1.8 Å resolution

structure (2JST) confirmed that the primary halothane binding site is located between two side-chains of W15 from each monomer. While halothane produces minor changes in the monomer structure, the quaternary arrangement of the dimer is shifted by about half a helical turn and twists relative to each other, leading to the closure of the lateral access pathway to the binding site. Dynamics studies confirm that the anesthetics make the helix regions more ordered and at the same time suppress the conformational exchange term (R_{ex}) at several residues. Our results revealed a novel mechanism of an induced fit between the anesthetic molecule and its protein target, with the direct consequence being the change in protein dynamics on a global rather than a local scale. This mechanism may be universal for anesthetic action on neuronal proteins.

NMR studies of anesthetic halothane interaction with the membrane protein Mistic in DPC micelles provide an experimental basis for understanding molecular mechanisms of general anesthesia. Although the presence of halothane had little effect on Mistic structure, ^{15}N NMR relaxation dispersion measurements revealed that halothane affected Mistic's motion on the microsecond−millisecond time scale. The motion on the microsecond−millisecond time scale in several residues disappeared in response to the addition of halothane. Most of the residues experiencing halothane-induced dynamics changes also exhibited profound halothane-induced changes in chemical shift, suggesting that dynamics modification of these residues might result from their direct interaction with halothane molecules. Allosteric modulation by halothane was also found to contribute to the dynamics changes, as reflected in residues I52 and Y82 where halothane introduction brought about dynamics changes but not chemical shift changes. The study suggests that inhaled general anesthetics could act on proteins via altering protein motion on the microsecond−millisecond time scale, especially motion in the flexible loops that link different alpha helices. The validation of anesthetic effect on

protein dynamics that are potentially correlated with protein functions is a critical step in unraveling the mechanisms of anesthetic action on proteins.

The structure, topology, and dynamics of the α4 TM2 and $(\alpha4)_2(\beta2)_3$ TM2 in magnetically aligned phospholipid bicelles were investigated using solid-state NMR spectroscopy in the absence and presence of halothane and isoflurane, two clinically used volatile anesthetics. ^{2}H NMR demonstrated that anesthetics increased lipid conformational heterogeneity. Such anesthetic effects on lipids became more profound in the presence of TM proteins. PISEMA experiments on the selectively ^{15}N-labeled α4 TM2 showed that the TM2 formed TM helices with tilt angles of 12° and 16° relative to the bicelle normal for the α4 and $(\alpha4)_2(\beta2)_3$ samples, respectively. Anesthetics changed the tilt angle of the α4 TM2 from 12° to 14°, but had only a subtle effect on the tilt angle of the $(\alpha4)_2(\beta2)_3$ TM2. A small degree of wobbling motion of the helix axis occurred in the $(\alpha4)_2(\beta2)_3$ TM2. In addition, a subset of the $(\alpha4)_2(\beta2)_3$ TM2 exhibited counterclockwise rotational motion around the helix axis on a time scale slower than 10^{-4} s in the presence of anesthetics. Both helical tilting and rotational motions have been identified computationally as critical elements for ion channel functions [49]. This study suggested that anesthetics could alter these motions in order to modulate channel functions.

The anesthetic effects on the Na^+ flux through the reconstituted channels of nAChRs were investigated by fluorescence microscopy. Two sub-types of human nAChRs, α4β2 and α7, were studied. For the TM domains of nAChR α4β2, the apparent flux rates were distributed between 0.5 s^{-1} and 3.5 s^{-1} in the absence of isoflurane. The flux rates were obviously decreased by the addition of the isoflurane. This suggests that the general anesthetics did inhibit the channel function. However, for the TM domains of nAChR α7, there was no difference with or without the addition of the isoflurane. The TM domains of α7 were therefore determined to be insensitive to isoflurane. The anesthetic

effects on the truncated nAChR with TM domains only are the same as on the full-length nAChRs. This indirectly proves that the TM domains are probably the main targets of general anesthetics.

In conclusion, anesthetic effects on various proteins were examined through multiple biophysical methods. The structural and dynamical analysis of these proteins indicate that anesthetics not only directly interact with the proteins and alter the dynamics of the specific residues within the binding sites, but also allosterically regulate the dynamics of the residues in other regions. Anesthetics have more obvious effects on the dynamics rather than the structures of the target proteins. The allosteric effects and dynamic changes caused by general anesthetics may be critical to the anesthetic effect.

CHAPTER 2

GENERAL OVERVIEW OF METHODS

2.1 PROTEIN EXPRESSION AND PURIFICATION

2.1.1 Introduction

Protein expression is a process that specifically produces a protein of interest in a cell line. It is a part of gene expression. In gene expression, a gene of interest is translated into functional gene products such as proteins (protein expression) or RNAs. Protein expression exists everywhere in all known life, eukaryotes, prokaryotes and viruses. The basis of protein expression involves transcription and translation. Two expression systems are used: cell-based systems and cell-free systems. The cell-based expression system is the most widely used expression system. The cell-based expression system requires a cloned foreign DNA segment that will be translated into the protein of interest, an expression vector that will be ligated with a DNA segment, and a host cell that will be transformed with the plasmid. The common expression host cells, which the expression systems are usually referred to, are bacteria, yeast, insect, and mammalian cells.

Each expression system has its own advantages and disadvantages. Therefore, a specific expression system is usually selected to express the particular protein. For

instance, if one protein requires posttranslational modification (PTM) such as acylation to be functional, the yeast expression system will be preferred over the bacterial one. Nevertheless, the bacteria expression system is the most simple, rapid, and highly efficient expression system, which can yield enough proteins for the structural studies. In some cases, the function of the expressed protein is either toxic to the bacterial host cells or the protein is heterologous and does not originate from bacteria; therefore, these proteins are very difficult to overexpress in the bacteria. In order to overcome these problems, many series of *E. coli* bacteria host strains have been developed including BL21, Rosetta, C41, C43, etc. BL21 is one of the most widely used *E. coli* host strains. In the BL21, there is a sub-strain known as BL21 (DE3) CodonPlus-RP, which is specifically modified to express heterologous protein in *E. coli*. The resulting BL21 (DE3) CodonPlus-RP host strain allows the expression of genes encoding tRNAs for rare amino acids codons for the heterologous protein such as arginine codons AGA and AGG and proline codon CCC.

Besides the host cells, expression vectors are also important to protein expression. An expression vector is a plasmid that will introduce a foreign DNA into a host cell. When the expression vector is inside the host cell, the foreign DNA will be transcribed and translated by the host cell. Different types of host cells require different expression vectors. More importantly, to facilitate the subsequent purification of the overexpressed protein, a tag is usually engineered into the expression vector with the cloned gene.

In order to isolate the specific protein to further study its function or structure, protein purification is conducted. Although various proteins are usually purified in different ways, in general, the procedure is similar. The overexpressed protein of interest coexists with all the endogenous bacterial proteins after the culture is harvested and the cells are lysated. Therefore, the aim of the first step is to achieve a large quantity of pure

protein for subsequent study. In the purification process, we first remove non-protein components from the proteins, such as DNA, and then separate the protein of interest from other proteins based on its own properties, such as binding affinity and protein size. Based on the protein's solubility, the protein of interest can be expressed in the membrane part, inclusion body, or the water-soluble part. Because they are expressed in different places in the host cell, we usually selectively collect the part where the protein is located. In this way, the protein undergoes the first primary purification process. In the second step, more accurate procedures are performed. For example, a protein engineered with a His tag can be purified by nickel affinity column. We can also purify them using ion exchange chromatograph based on their charge. Different proteins are of different size thereby allowing us to separate them based on their size.

2.1.2 Expression vector design and plasmid construction

Usually the expression system and expression method will determine what kind of expression vector should be chosen. For example, if the study focuses on the structure determination using NMR spectroscopy or X-ray tomography, the protein yield will be one of the important factors. In this case, bacteria expression systems such as *E.coli* may be a reasonable candidate.

Although *E.coli* is a convenient host for the heterologous protein expression, sometimes, the protein yield of interest is low or the gene expression may lead to insoluble or nonfunctional products. This is often due to the toxicity of the target proteins. For example, the overexpressed channel proteins may form pores on the cell membrane thereby causing cell death. Or the absence of co-factors, such as chaperons, leads to protein misfolding. A recombinant fusion protein, in many cases, may solve these problems. Here the recombinant fusion protein is the combination of two proteins, a

fusion protein and the protein of interest. The fusion protein is usually an independent domain from a homologous bacteria protein or a functional peptide such as a hexahistidine. The recombinant fusion protein is created through a genetic engineering approach. The gene for the fusion protein is ligated with the target gene by polymerase chain reaction (PCR) or ligation methods. The fusion protein does not only facilitate the protein yield but also helps with the protein purification. Hexahistidine can bind to the nickel affinity column, while glutathione S-transferase (GST) or maltose-binding protein (MBP) can bind to their respective affinity columns. After the protein is expressed and purified, the fusion proteins are usually cleaved off to prevent potential distortion caused by the extra fusion protein. A specific protease cleavage site is created between the fusion protein and the target protein, which is recognized and cleaved by its corresponding enzyme.

2.1.3 Purification methods and strategies

Protein purification is essential for the structural and functional studies of the target proteins. The development of a general successful and efficient protein purification protocol is challenging due to the diversity of biological samples. In general, three phases of purification strategies are considered, which are capture, intermediate purification and polishing (Protein Purification Handbook. Amersham Biosciences. 18-1132-29, Edition AC). In the capture phase, the protein is solubilized, isolated, concentrated and stabilized. The majority of impurities of non-protein parts and other proteins are removed in the intermediate purification phase. In the polishing phase, the purity of the protein is further improved by removing traces of impurity. Before we choose the appropriate purification methods for each phase, the objective of the purification should be defined first. What the recombinant protein is applied for will

determine the purity of the protein. High purity will require more purification steps. For example, if the protein of interest is for therapeutic use, the purity should be extremely high >99%. However, the protein purified for the NMR experiments usually has a purity less than 90% because impurities are usually below the NMR detection limit for most of the practical purposes. In such a case, three phase purification steps are not necessary. Intermediate purification will be enough to achieve the appropriate purity for an NMR study. For the studies covered in this thesis, all of the proteins I worked with are purified using His affinity column. Whenever necessary, additional steps with size exclusion chromatography were used.

2.2 SPECTROSCOPIC TECHNIQUES

2.2.1 Nuclear magnetic resonance

Nuclear magnetic resonance (NMR) is a phenomenon in which a physical property of an atom's nucleus called "nuclear spins" absorbs the energy in a magnetic field from an electromagnetic pulse, which causes a transition of the spins from the ground state to one of the excited state. A mathematical description is presented as $\vec{\mu} = \gamma \hbar \vec{I}$, where the magnetic moment of a nuclear spin $\vec{u}$ is proportional to its spin angular momentum $\hbar\vec{I}$; γ is the gyromagnetic ratio and $\hbar$ is the reduced plank constant. The energy of a nuclear magnetic moment $\vec{u}$ in the presence of an externally applied magnetic field $\vec{B}_0$ is given by $E = -\vec{u} \cdot \vec{B}_0$. For a spin one-half nucleus such as ^{1}H, ^{15}N and ^{13}C, there are two possible spin angular momentums: $-\frac{1}{2}\hbar$ and $+\frac{1}{2}\hbar$. Therefore, the low energy state (the ground state, α) and the high energy (the excited state, β) correspond to $-\frac{1}{2}\hbar$ and $+\frac{1}{2}\hbar$, respectively. The energy difference between these two stare is $\Delta E = \gamma \hbar B_0$. The

Larmor frequency is given by $\omega = \frac{\Delta E}{\hbar} = \gamma B_0$, which is the emission frequency of a transition from the excited sate to the ground state in NMR spectroscopy.

Because the absorption frequency of a nuclear spin depends on the magnetic field that is actually sensed by the nucleus, the absorption frequency ω_i for a specific nuclear spin i in a protein should be $\omega_i = \gamma_i B_i = \gamma_i (1 - \sigma_i) B_0$, where B_i is the local magnetic field of the nuclear spin i and it relates to B_0 by a shielding factor, σ_i. This shielding effect is caused by the electronic environment of the nuclear spin i. Therefore, the absorption frequency can give us the local structural information from NMR spectroscopy.

2.2.2 Circular dichroism

Circular dichroism (CD) is the difference in absorption of left and right circularly polarized light when the chiral molecules are interacted with circularly polarized light. By this definition, $\Delta A = A_L - A_R$. using Beer's law: $\Delta A = (\varepsilon_L - \varepsilon_R) \cdot c \cdot l$, then, $\Delta\varepsilon = \varepsilon_L - \varepsilon_R = \frac{\Delta A}{c \cdot l}$, where ε_L and ε_R are the molar extinction coefficients for the corresponding left and right circularly polarized light; c is the molar concentration for the chiral molecules; l is the light path length. $\Delta\varepsilon$ is the molar circular dichroism, which is the intrinsic property of the chiral molecule and measured by circular dichroism. Because each type of the secondary structure, alpha helix, beta strand, and random coil, has its own distinct CD spectrum, the secondary structure can be predicted (or decomposed) based on its CD spectrum.

2.2.3 Fluorescence spectroscopy

Fluorescence is an emission of light by a substance after it absorbed a light of a different wavelength. The substance has multiple energy states and most of the times it is in the ground state, which is the most stable state. When the substance absorbs light, it is excited from the ground state to one of relative unstable excited states, followed by relaxation to a metastable excited state. As the substance transitions from the metastable state to the ground state, fluorescence light of a different wavelength is emitted. Usually, the wavelength of absorption is shorter than the wavelength of emission. Fluorescence spectroscopy measures and analyzes the fluorescence from a sample.

2.3 DATA PROCESS AND ANALYSIS

2.3.1 Spectral assignments

NMR is one of the most powerful tools that are aimed at investigating the protein structures and dynamics. Many NMR experiments are specifically designed to accomplish these aims. In these experiments, all the structural and dynamical information can be extracted from the chemical shift or intensity of each peak. In order to obtain the atomic resolution, each peak has to be assigned to a corresponding residue. This step is known as spectral assignments. Spectral assignments include, at least, two steps, backbone sequence assignment and side-chain assignment. Recently developed triple resonance heteronuclear experiments, requiring additional ^{15}N and ^{13}C labeled samples, provide much more robust methods to quickly achieve the reliable backbone assignments. For a typical membrane protein, HNCA, HN(CO)CA, and CBCA(CO)NH

are three key triple resonance experiments, which are the minimum requirements for the backbone assignments. HNCA and HN(CO)CA are a pair of experiments. HNCA spectra for residue i gives two alpha carbon resonances, C_α^i from residue i itself and C_α^{i-1} from the preceding residue. HN(CO)CA spectra for residue i only provide the alpha carbon resonance of C_α^{i-1}, helping identify the peak of the preceding residue in the two peaks in HNCA spectra. In the same way, for residue $i-1$ in HNCA and HN(CO)CA, C_α^{i-1} and C_α^{i-2} can be identified. Therefore, the connectivity between residue i and $i-1$ is defined. Similar to HN(CO)CA, CBCA(CO)NH for residue i provides additional resonance for the beta carbon, C_β^{i-1}, besides C_α^{i-1}. Based on the protein known sequence, the connectivity and the chemical shift of alpha and beta carbon, the resonances for residue i and $i-1$ can be assigned. After the backbone assignment is completed, side-chain assignment is relatively straightforward. The strategy for the side-chain assignment is similar to the backbone assignment. TOCSY type experiments provide the connectivity along the side-chain carbons and protons. Given that these resides are already known from the backbone assignment, therefore, side-chain assignment can be completed.

2.3.2 Secondary structure predictions

The secondary structure of protein can be accurately predicted by ^{13}C and ^{1}H chemical shifts without NOE information. Backbone carbon $^{13}C_\alpha$ and $^{13}C_\beta$ and backbone proton $^{1}H_\alpha$ are sensitive to the local conformation of the protein. In general, the chemical shifts for alpha helix, beta strand and random coil can be separated into three different classes. For example, $^{13}C_\alpha$ chemical shift in alpha helix conformation is higher than in random coils, while $^{13}C_\alpha$ chemical shift in beta strand conformation is lower than in

random coils. This relationship is reversed for the $^{13}C_{\beta}$ and $^{1}H_{\alpha}$ chemical shifts. By comparing the chemical shifts of backbone carbon $^{13}C_{\alpha}$ and $^{13}C_{\beta}$ and backbone proton $^{1}H_{\alpha}$ with the data base of corresponding chemical shifts in random coils, we can tell the different between the alpha helix and beta strand. A semi-empirical procedure has been incorporated in the software package TOLAS for secondary structure prediction [50].

2.3.3 Structure calculation

NMR is one of the major tools to determine high-resolution structures. Two major restraints, distance restraints and torsion angle restraints, are used in NMR structure determination. NOESY type experiments can provide the NOE restraints, which are the major distance restraints to be used for structure determination. In the NOESY type experiments, the cross-peak intensity is proportional to $1/r^6$, where r is the distance between two ^{1}H protons. They are represented as the upper bound distances, while the low bound distances are basically the sum of two van der Waals radii.

Hydrogen bonds are usually involved in defining the secondary structure. Both alpha helix and beta strand show different pattern of hydrogen bonds. By D_2O exchange experiment or temperature effect on chemical shifts, the hydrogen bonds of water-exchangeable amide proton can be determined. Applying additional hydrogen bonding constraints as distance restraints to structure calculation can further improve the quality of the resulting structures.

In NMR, it is usually challenging to detect the long-range NOESY cross peaks, which can be converted into the long distance restraints. Paramagnetic relaxation enhancement (PRE) experiment is an alternative method. For example, MTSL (*S*-(2,2,5,5-tetramethyl-2,5-dihydro-1H-pyrrol-3-yl)methyl methanesulfonothioate) is a chemical compound with an unpaired free electron, which can reduce the intensity of the

NMR signal due to nucleus-electron dipole interaction. The distance restraints generated by MTSL probes can be extended to 20~25 Å of paramagnetic centers.

Magnetic dipole-dipole interaction is the interaction between two magnetic dipoles. Each magnetic nuclear such as ^1H can generate a local magnetic field, which can interfere the magnetic field of other nuclear nearby. Therefore, the original Larmor frequency, which is determined by the external magnetic field, is modified by this additional local magnetic field. Such interaction is also called dipole coupling. The magnitude of the dipole coupling not only depends on the distance between two interacting nuclei, but also depends on the angle between the internuclear vector along two nuclei and the external magnetic field. Because the protein particles are tumbling isotropically in the solution, the dipole-dipole interaction is averaged to zero due to its angular dependence. However, in the specific alignment medium, partially restricted tumbling can be achieved. In this case, the dipole coupling is non-zero and is also called residual dipole coupling (RDC). Structural information can be obtained from RDC. In the principal axis frame of the alignment tensor, A, the RDC between two spins I and S is given by:

$$D_{IS}(\theta,\phi) = D_a[(3\cos^2\theta - 1) + \tfrac{3}{2}D_r(\sin^2\theta\cos^2\phi)] \quad (2.3.1)$$

where the polar coordinates, θ and ϕ, describe the orientation of the internuclear vector in the principal axis frame of the alignment tensor, A. D_a=1/3[D_{ZZ}-(D_{XX}+D_{YY})] and D_r=1/3(D_{XX}-D_{YY})/A_{ZZ} are the axial and rhombic components of the traceless diagonal tensor D, with D_{ZZ}>D_{YY}≥D_{XX}. D_a and D_r can be experimentally determined by measuring the magnitude of the alignment. Therefore, D_{IS} can be used to refine the calculated structures.

Dihedral angle, also called torsion angle, is defined as the angle between two planes that have a common interface. In protein geometry, two backbone torsion angles

are often used, Φ and φ. Φ is the angle along C'-N-C_α-C', while φ is the angle along N-C_α-C'-N. Therefore, dihedral angle restraints are also used to calculate the structure. Backbone chemical shifts are sensitive enough to the local conformation. It has been shown that the triplets with similar backbone chemical shifts and sequences will share the similar dihedral angles. Through searching the database, the dihedral angles can be determined.

2.3.4 Protein dynamics analysis

NMR is also uniquely suited to characterize molecular motions on the time scale from picoseconds to milliseconds. Two basic relaxation processes, spin-lattice relaxation rate (R_1) and spin-spin relaxation rate (R_2), have been applied to investigate protein dynamics. Spin-lattice relaxation rate (R_1) is the decay constant that the magnetization recovers from its excited state to its thermal equilibrium, while spin-spin relaxation rate (R_2) is the decay constant that the transverse magnetizations lose their coherence. Additionally, dynamics information can also be obtained from the nuclear Overhauser effect (NOE) experiment, which measures the perturbation of one spin through saturating its coupled spin.

Stimulated emission is considered as the major source of relaxation. It requires the presence of an oscillating electromagnetic field, which matches to the absorption frequencies of the NMR transition. The oscillating electromagnetic field is mainly generated by random tumbling of the protein or by internal molecular motion such as the reorientation of the amide bond. The spectral density function, J(ω), describes how the intensity of the oscillating electromagnetic field is distributed with the frequency. A rate W is defined as the transition rate caused by the electromagnetic fields. In principle, molecular motion can be derived in following scheme, from R_1, R_2 and NOE to W; from

W to J(ω); from J(ω) to molecular motions. However, due to limit independent information, an iterative fitting computer program, such as Modelfree [51], becomes useful.

Most biological processes occur on a slow timescale from microseconds to milliseconds or seconds. These biological processes also accompany with the conformational exchanges of proteins. Different from R_1, R_2 and NOE, which characterize the dynamics on the fast timescale (ps~ns), the conformational exchanges in the slow timescale (us~ms) can be examined by the CPMG (Carr−Purcell−Meiboom−Gill) R_2 dispersion experiment. By measuring R_2 as a function of a systematically variable CPMG field strength, v_{CPMG}, relaxation dispersion curves can be obtained, which can be further analyzed by a two-site exchange model. By fitting the curves, the detailed dynamic information of the conformational exchanges such as the exchange rate constant, the populations of each sites, and the chemical shift difference between them can be determined.

2.3.5 PISEMA and PISA Wheels

Polarization inversion spin exchange at the magic angle (PISEMA) is an experiment that correlates the chemical shift of a spin such as ^{15}N with its heteronuclear dipolar coupling to another spin ^{1}H. The theory of the PISEMA experiment has been work out previously [52]. Both the chemical shift tensors $\boldsymbol{\sigma}$ and the dipolar tensor $\mathbf{v}$ are fixed in the peptide plane. The principal axis frame for the ^{15}N chemical shift tensor is ($\boldsymbol{\sigma}_{11}$, $\boldsymbol{\sigma}_{22}$, $\boldsymbol{\sigma}_{33}$) with $\boldsymbol{\sigma}_{11}$ and $\boldsymbol{\sigma}_{33}$ in the peptide plane. The dipolar tensor is axially symmetric with unique axis along the covalent amide bond. Let (x, y, z) be the coordinates of $\mathbf{B_0}$ in the principal axis frame of the ^{15}N chemical shift tensor, then the PISEMA equations in the principal axis frame of the chemical shift tensor are

$$\sigma = \sigma_{11}x^2 + \sigma_{22}y^2 + \sigma_{33}z^2 \quad (2.3.2)$$

$$v = \frac{v_{\|}}{2}(3(\sin\beta x + \cos\beta z)^2 - 1) \quad (2.3.3)$$

where β is the angle from $\boldsymbol{\sigma_{33}}$ to the NH bond. $v_{\|}$ is the value of **v** when B_0 is the direction of dipolar interaction vector.

In Eq. 2.3.2 and 2.3.3, σ and v are measured in the PISEMA experiments. The principal values of the ^{15}N chemical shift tensors for non-glycine residues are σ11=64 ppm, σ22=77 ppm, and σ33=217 ppm [53]. Therefore, the coordinates (x, y, z) of $\mathbf{B_0}$ in the principal axis frame of the ^{15}N chemical shift tensor can be determined. If the coordinates (x, y, z) of $\mathbf{B_0}$ in the principal axis frame of the ^{15}N chemical shift tensor are known, then the orientation of the principal axis frame of the ^{15}N chemical shift tensor with respect to the magnetic field is mathematically known. In theory, all the parameters for the structure of the protein backbones can be finally resolved if the standard peptide bond geometry is assumed. In practice, to simplify it, each helical segment in the standard α-helix is defined by two parameters, which are a tilt angle τ and a rotation angle ρ. The angle τ describes the relative orientation of the helix with respect to the magnetic field. Polar Index Slant Angle (PISA) wheel defined by the two parameters (τ, ρ) is a typical fourth order curve that is used to fit the PISEMA spectrum [52]. Thus, the structure of the peptides descript by (τ, ρ) is determined.

CHAPTER 3

STRUCTURAL STUDY OF NICOTINIC ACETYLCHOLINE RECEPTORS

3.1 NMR STUDY OF THE TM DOMAIN OF THE nAChR α1 SUBUNIT

3.1.1 Significance

nAChRs are members of a superfamily of neurotransmitter-gated ion channel receptors, which also include other channel proteins such as the glycine and γ-amino-butyric acid type (GABA) receptors. These receptors are typically pentameric ion channels formed by either one or a combination of subunits. The composition of the subunits determines the receptor's subtype. Muscle AChRs have four different subunits (typically two α1, β1, γ, and δ, with the δ subunit sometimes replaced by an ε subunit). While these are the characteristic subunits for muscle AChRs, there are as many as ten kinds of α-subunits and multiple β-subunits [54]. Recent understanding is that the α-subunit is the key subunit for ligand binding and that the binding sites are located at the interface of an α-subunit and its neighboring subunit, with only one binding site per α-subunit [55]. Each subunit is comprised of a large EC domain, a four-helix TM bundle, and an IC loop domain.

Because of its nature as the key to receptor gating, the structure of the α-subunit of the AChR has drawn a significant amount of attention. However, its nature as a membrane protein makes structural studies inherently difficult. The subunit protein is too large to study by the conventional means of NMR and is not easy to crystallize. At this point, a 4-Å resolution structure of α1 nAChR from Torpedo electric ray has been solved using cryo-electron microscopy (cryo-EM). The cryo-EM structure presents the receptor in its closed form [8]. The limitation of cryo-EM's resolution and its incapability of studying the dynamics effects leave much to be desired. More recently, two bacteria analogues of pentameric ion channels, ELIC and GLIC, were solved by X-ray crystallography. The structures of ELIC and GLIC are believed to represent the closed and open form, respectively [10,11]. These structures are different from the cryo-EM structure, as a result of low sequence identity among them. High atomic resolution is still needed and will provide useful new information regarding the function of the receptors.

3.1.2 Novel water solubilization approach

This part of the designing work was done in collaboration with Professor Jeff Saven's group at the University of Pennsylvania. For completeness, the designing idea is presented in this section. My contribution is in the experimental phase of the study, covered by the rest of the chapter.

Structure determination of mammalian membrane proteins is challenging due to a low expression level, unpredictable folding, and poor protein stability. We addressed these critical issues by using a systematic approach to mutate the hydrophobic residues, which were identified in the lipid-protein interaction sites, to hydrophilic residues. In such a way, the membrane protein was transformed into a complete or partially water-soluble protein, while retaining its original structure and important function. Using a

computational approach, a designed water-soluble variant of the bacterial potassium ion channel KcsA has been developed and its solution structure has been elucidated using computer simulation and experimentally by NMR [56-58]. The resolved structure is consistent with the tertiary and quaternary structure of the wild type structure [57]. These previous findings strongly support the idea that developing water-soluble variants of membrane proteins is suitable for structural studies.

The computational redesign sequence of the nAChR α1 subunit was selected based on the cryo-EM model structure of the TM portion of the nAChR α1 subunit that was reported by Unwin et al [7,8]. This design was performed by our collaborators at the University of Pennsylvania. First, the residues with more than 40% solvent exposure, calculated by GETAREA1.1, were identified as the exposed residues [59]. Second, among the exposed residues, hydrophobic residues such as AFILMVW were considered. Third, the selected residues from above two steps were targeted for mutation, if they were expected to reside in the TM region. Residues at the interfaces between helices within the subunit were not touched and retain as in the wild type protein (I219, M243, V261, F414, I420 and V425). Eventually, 23 positions were identified, which were targeted for computational redesign (I220, L223, L224, F227, L245, I247, L251, V255, F256, L258, V259, M282, I283, I286, I290, V293, V294, L411, M415, L416, I419, V423 and F426).

The site-specific probabilities of the amino acid residues in the 23 mutation sites were calculated as described previously [58,60-64]. For each of the 23 mutation sites, 20 types of amino acids were applied while the remaining mutation sites were constrained as wild type. Side chain conformations were restricted to those from a library that includes only frequently observed conformations [65]. At most 10 rotamer states were applied to each amino acid. Two energy functions were used to characterize the ensemble of variants. The first one is to address inter-atomic interactions by using the AMBER force field [66]. The second one is to quantify hydrophobic and solvation effects.

An environmental energy was constrained to the average value of soluble proteins that have the same size as the nAChR alpha subunit [58].

In Fig. 3.1.1, a sequence representing the most probable amino acids at each of 23 mutation sites was generated by the above computational approaches (Seq. 1). An additional constraint was applied in an effort to increase the diversity of different amino acids in the protein sequence. The new sequence was generated (Seq. 2). In order to only express the TM domain of the nAChR α1 subunit as a single chain, a polyglycine loop was selected and built. To minimize the artificial linker effects on the structure and orientation of TM helices and remain the native form of TM3 and TM4 as much as possible, the flexible loop was introduced between TM4 and TM1, while truncating IC domain and leaving TM3 and TM4 open. The connectivity of the resulting protein is different compared to the wild type nAChR α1 subunit, where TM4 connects to TM3 by a large IC domain. The particular flexible loop was systematically designed through using MODELLER [67]. Different lengths of polyglycine linker (4~8 Glys) were investigated and 50 independent calculations for each length of loop were performed. The 5-glycine linker shows the lowest value of the modeling energy function. Using NAMD [68] and the CHARMM force field [69], the results were further confirmed.

```
                 220       230       240       250       260       270
WT       PLYFVVNVIIPCLLFSFLTGLVFYLPTDSGEKMTLSISVLLSLTVFLLVIVELIPSTSSAVPLI
Seq.1    PLYFVVNVIEPCKKFSELTGLVFYLPTDSGEKMTESKSVLKSLTEKLKKIVELIPSTSSAVPLI
Seq.2    PLYFVVNVIEPCKKFSELTGLVFYLPTDSGEKMTESKSVLKSLTEKLKKIVELIPSTSSAVPLI

              280       290       300          410       420       430
WT       GKYMLFTMIFVISSIIITVVVINTHHRS  AMVIDHILLCVFMLICIIGTVSVFAGRLIELSQEG
Seq.1    GKYMLFTKKFVESSIKITKEVINTHHRS  AMVIDHILKCVFEKICKIGTESVKAGRLIELSQEG
Seq.2    GKYMLFTKEFVESSIKITEEVINTHHRS  AMVIDHILKCVFDKICKIGTESVEAGRLIELSQEG


                 10        20        30        40        50        60
WSA      MAHHHHHHAMVIDHILKCVFDKICKIGTESVEAGRLIELSQEGGGGGGPLYFVVNVIEPCKKFSE
             70        80        90        100       110       120       130
         LTGLVFYLPTDSGEKMTESKSVLKSLTEKLKKIVELIPSTSSAVPLIGKYMLFTKEFVESSIKIT
                 140
         EEVINTHHRS
```

Fig. 3.1.1. Protein sequences of a wild type nAChR and its various mutants. The sequence for the wild type nAChR TM domain α1 subunit from torpedo is shown (WT). Seq. 1 represents the most probable amino acids at each of 23 mutation sites. The 23 mutation sites are bold and underlined. In Seq. 2, the 4 positions are depicted in blue due to the diversity constraint implemented. Considering protein expression and purification, Seq. 2 was further modified to the final WSA. In WSA, the IC loop domain was truncated and the TM4 was moved to precede TM1. A five-glycine linker (in Orange) was used to connect the TM4 and TM1 and a his_6-tag (in Green) was attached to the N-terminus.

3.1.3 Protein expression and purification

A his_6-tagged computationally designed nAChR α1 subunit (WSA) was expressed using a BL21 (DE3) cell line (EMD biosciences), which was obtained from our collaborators at the University of Pennsylvania. Cells were first grown at 37°C in LB media with 100 μg/ml ampicillin to an OD_{600} of approximately 0.6. Cells were then harvested and re-suspended into a quarter of the starting volume of ^{13}C and ^{15}N-rich M9 media containing 100 μg/ml ampicillin. After one hour recovery period at 30°C, cells were induced with 1 mM IPTG and continued to grow overnight.

Cells after overnight growth were collected by centrifugation at 4°C and then re-suspended into the proper volume of lysis buffer (50 mM Tris-HCl pH 7.5, 15% glycerol and 1 mM NaN_3). The suspended cells were incubated with 100ug/ml lysozyme and 25U/ml DNase for one hour at room temperature, followed by sonication. The lysate was centrifuged at 38724×g for 20 minutes. The supernatant was discarded and the inclusion bodies were solubilized in an 8 M urea, pH 8.0, 20 mM Tris-HCl buffer. After a second centrifugation at 38724×g for 20 minutes, the supernatant was incubated with 2 mL Ni-NTA resin (Sigma) for one hour at room temperature. The resin was then washed with 40 ml of wash buffer (8 M urea, 20 mM Tris-HCl, pH 8.0) and eluted with 6 ml 250 mM imidazole, 8 M urea, 20 mM Tris-HCl, at pH 8.0. A size exclusion column was optionally used to improve the sample purity. The final protein yield was approximately 7 mg/liter in M9.

WSA was then refolded into 1 mM phosphate buffer pH 8.0 by removing the 8 M urea through dialysis. The protein was only soluble in high pH and can be concentrated into at least 2 mg/ml. In order to prevent soluble aggregation and adjust pH to 5.8, which allows to generate a decent NMR spectrum, a detergent, 1-Palmitoyl-2-Hydroxy-*sn*-

Glycero-3-[Phospho-*rac*-(1-glycerol)] (Sodium Salt) (LPPG) (Avanti Lipids), was added to NMR samples to further solubilize WSA. The addition of LPPG to our WSA sample allowed WSA to fold into the expected four-α-helix bundle. The final concentration of LPPG is 2%.

3.1.4 NMR experiments and data processing

Uniformly ^{15}N- and ^{13}C-labeled WSA was prepared in 2% LPPG, 10% D_2O, and 20 mM sodium phosphate buffer at pH 5.8. NMR data were collected on Bruker Avance 600, 700, 800, and 900 MHz spectrometers with Topspin 1.3 software at 40°C. In order to complete backbone and side assignments, the following pulse sequences from the Topspin sequence library were used HNCOCA, HNCA, HNCACB, CBCACONH, HCCH-TOCSY, and 3D ^{15}N- and ^{13}C-filtered NOESY. The mixing times for the 3D NOESY spectra were 120 ms and 150 ms for ^{15}N-edited NOESY and 150 ms for ^{13}C-edited NOESY. Most of 3D experiments were acquired with complex time domain size of 1024 (direct observation dimension) × 48-80 (edit dimension) ×128-256 (indirect observation dimension).

Relaxation rate constants, R_1 and R_2 and the steady-state ^{15}N-{^1H} NOE were measured at 14.1T using 4, 2.5, and 4s recycle delays, respectively. The longitudinal rate constant, R_1, was recorded with 9 delay values: 10, 50, 150, 300, 600, 1000, 1600, 2200, 3000 ms. The transverse relaxation constant, R_2, was recorded using 7 delay values: 16, 32, 48, 64, 96, 128, and 176 ms. The steady-state ^{15}N-{^1H} NOE was measured with and without ^1H saturation in an interleaved fashion. The R2 dispersion measurements were carried out at 14.1 T and 40 °C by using the relaxation-compensated, constant-time, Carr–Purcell–Meiboom–Gill (CPMG) sequence with the following 8 CPMG field strengths: 25, 50, 75, 100, 150, 250, 400.00, and 650.00 Hz [70,71].

The reference spectrum was acquired without the CPMG period. A relaxation delay of 2.5 s was used.

NMRPipe [72] and Topspin 2.1 (Bruker NMR software) were used to process the NMR data. Sparky [73] was used to make resonance assignments. Structure calculation was performed using CYNA 2.1 [74] based on the distance restrains generated from ^{15}N- and ^{13}C- edited NOESY data and dihedral angle restrains predicted by Talos [75] based on the chemical shifts as well as the hydrogen bonding restraints derived from temperature effect on the proton chemical shifts [76]. A total of 100 structures were calculated and 20 structures with the lowest target function are presented. Structures were further analyzed using VMD [77] and Molmol [78].

The ^{15}N relaxation parameters and ^{15}N-{^{1}H} NOE were analyzed quantitatively in DYNAMICS by using the extended model-free approach [79,80]. A ^{15}N-^{1}H internuclear bond distance of 1.02 Å and a ^{15}N chemical shift anisotropy -170 ppm were used. The global tumbling correlation time (τ_m) was determined by extensive search for the τ_m value that gives the minimum reduced χ^2 value and the least number of non-fitted residues in the Modelfree data fitting.

3.1.5 Secondary structure of WSA as determined by CD and NMR

Circular Dichroism (CD) measurements were performed using a Jasco Model J-810 spectrophotometer and analyzed using the K2D algorithm on the DICHROWEB server. The results are shown in Fig. 3.1.2. The secondary structure prediction is 50% based on the K2D output, which indicated a high helical content, as would be expected for our protein. The CD result is consistent with a native acetylcholine receptor TM domain α1 subunit, given the prediction error by circular dichroism. The chemical shift index (CSI), which is a commonly accepted NMR method used for the identification of secondary

protein structures, can provide more accurate information about the secondary structure of WSA. A typical ^{1}H-^{15}N heteronuclear single quantum coherence (HSQC) spectrum is shown in Fig. 3.1.3, revealing a dramatically improved NMR spectrum for a membrane protein. With this well resolved spectrum and other high quality 3D spectra, a nearly complete backbone assignment was achieved, allowing us to predict the secondary structure using the CSI method. Fig. 3.1.4 represents the CSI for the Cα atoms. Four distinct α-helix domains with a fold similar to that of GLIC or Torpedo nAChR can be identified, indicating that the secondary structure of native acetylcholine receptor TM domains is retained in its water-solubilized counterpart. Overall, the α-helical content ~74% predicted by CSI fits well with GLIC and the Torpedo nAChR. More interestingly, there are two sets of backbone assignments with two different CSI values identified for S104-S107 in the TM23 loop region as shown in Fig. 3.1.5, suggesting that they are in two different dynamic conformations.

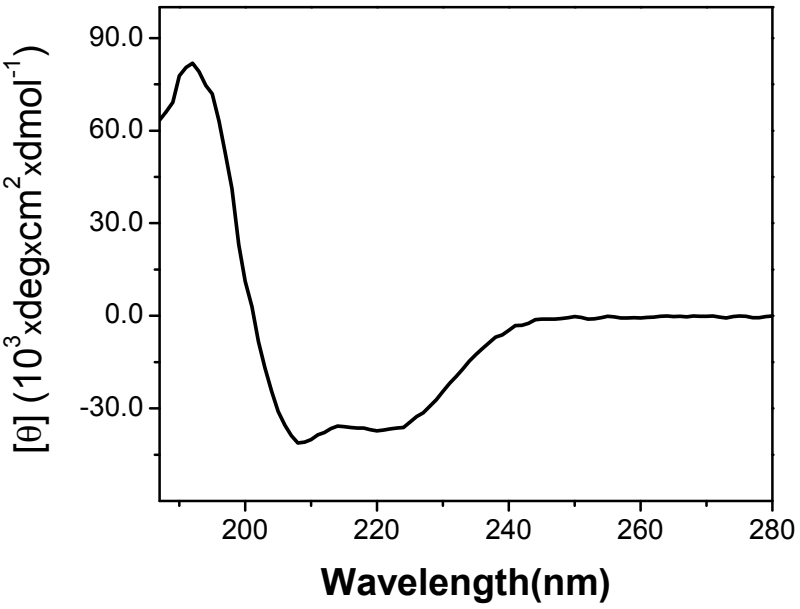

Fig. 3.1.2. Far-UV circular dichroism (CD) spectrum of WSA in LPPG micelles. It was analyzed by online server DICHROWEB K2D program, which predicted ~50% helical content. This result is in agreement with sequence-based prediction for the secondary structure of WSA.

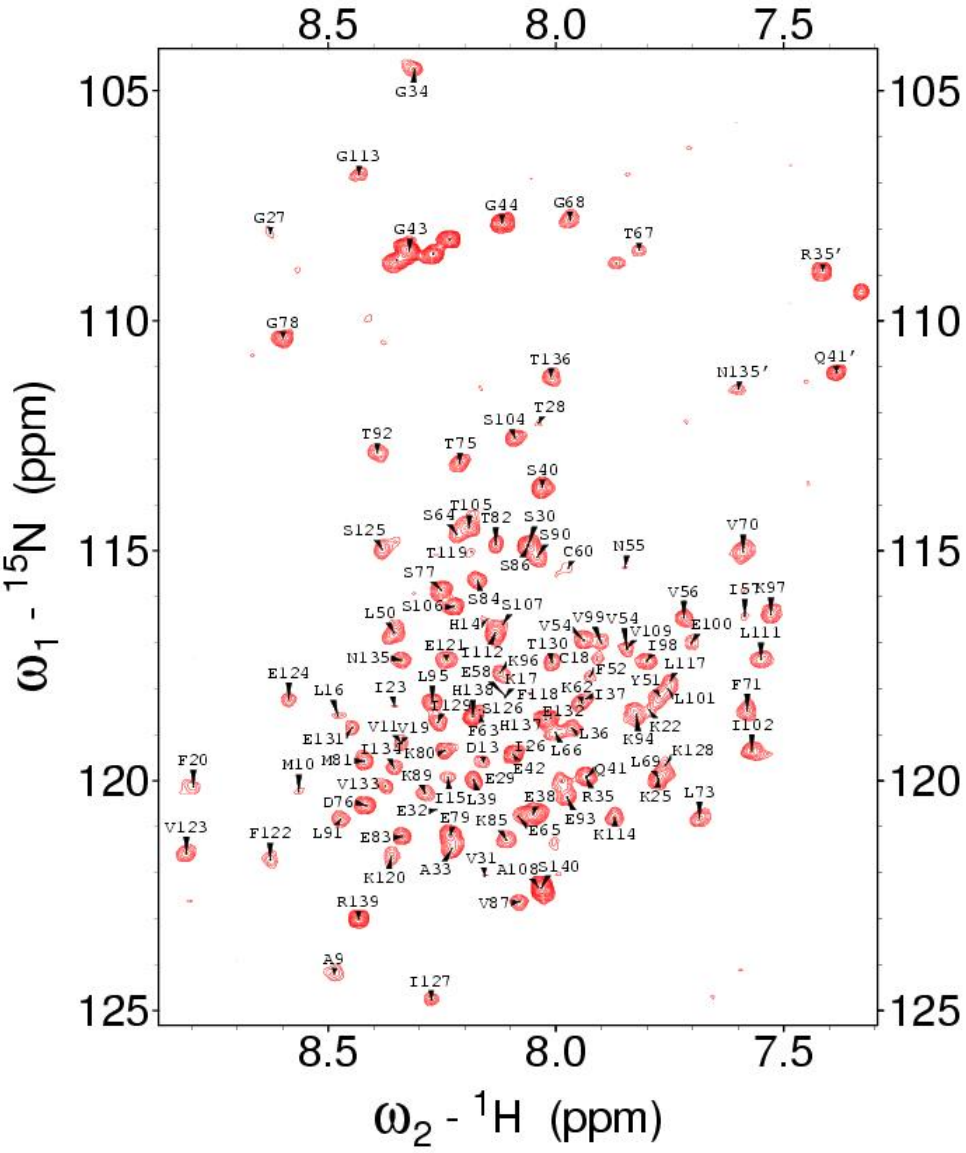

Fig. 3.1.3. Representative 800-MHz backbone amide proton ^{1}H-^{15}N HSQC spectrum of WSA in 2% LPPG micelles at 40˚C (pH 5.5). The homogeneous spectrum with a relatively large dispersion suggests WSA is monodispersed and folds correctly.

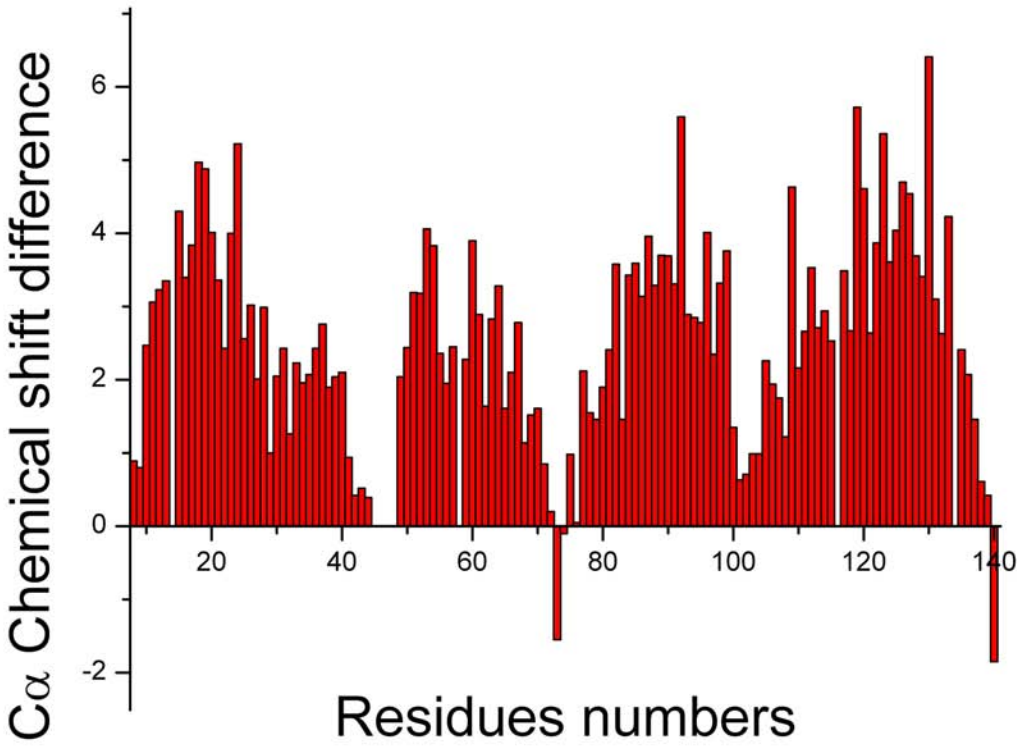

Fig. 3.1.4. $^{13}C_{\alpha}$ chemical shift index (CSI) of WSA. CSI was determined by subtracting the average $^{13}C_{\alpha}$ chemical shifts of the residues in the random coil from the corresponding residues in WSA. Higher $^{13}C_{\alpha}$ CSI indicates a higher tendency to be in the helical conformation. Obvious four helical domains were identified. The predicted secondary structure of WSA based on the $^{13}C_{\alpha}$ CSI is in agreement with two X-ray structures for GLIC and ELIC, but not with the cryo-EM model structure of nAChR. The helical contents are comparable for all three proteins.

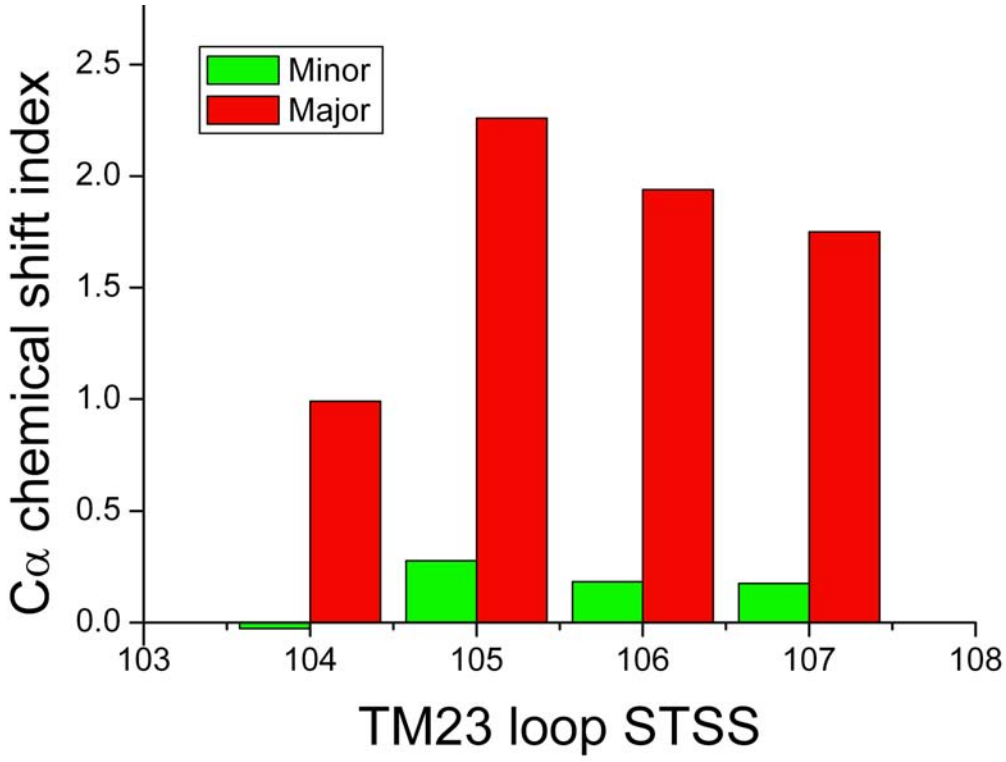

Fig. 3.1.5. $^{13}C_{\alpha}$ chemical shift index of the TM23 loop. TM23 loop residues STSS can exist in two conformations, rigid (Red) and flexible (Green) conformations, as indicated by the CSI. The intrinsic multiple conformations of TM23 loop may be caused by the absence of the EC domain in WSA. The interaction between TM23 loop and the EC domain is critical to channel gating.

3.1.6 High-resolution structure of WSA determined by NMR

The highly resolved peaks in our NMR spectrum assure the accuracy of these assignments and subsequent structure determination. For the majority of the WSA sequence, only one set of peaks was present, with only four residues in the TM2-3 loop region showing two sets of peaks, suggesting that the protein is structurally homogeneous. The solution NMR structure of WSA was determined using conventional methods. The 20 lowest-energy structures calculated from NMR constraints are shown in Fig. 3.1.6. The structure with minimal RMSD from the other structures in the bundle is highlighted in ribbon representation. In Fig. 3.1.7, the NOE connectivity of most of the residues is again suggestive of a helical structure with clear i, i+3 connectivity. A total of 1169 pairs of NOEs are assigned and summarized in Table 3.1.8. Forty-two long-range inter-helical NOEs are identified and used to define the tertiary structure of WSA. The overall backbone RMSD for the four helical regions is 1.11 ± 0.20 Å.

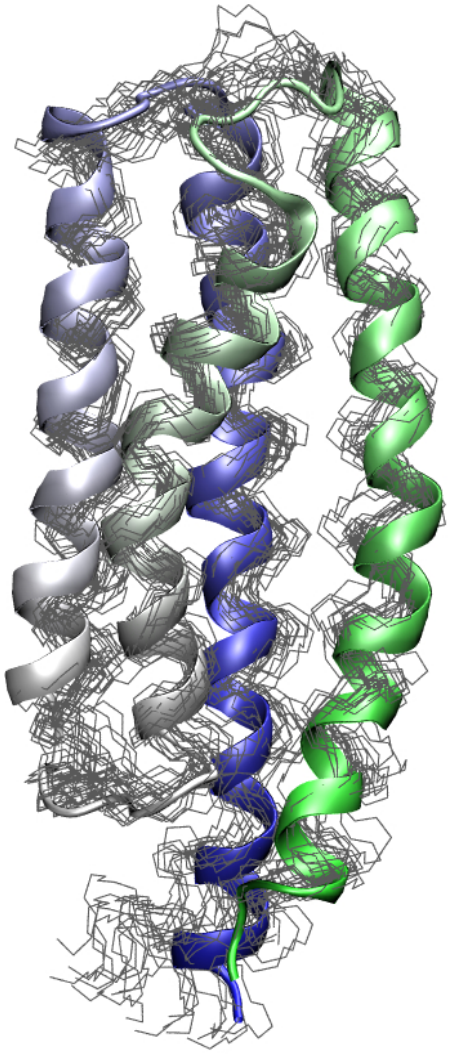

Fig. 3.1.6. Solution-NMR structure of WSA in LPPG micelles. A bundle of twenty lowest-energy structures of WSA with the ribbon diagram of the structure closest to the mean was shown. The structure was derived from NMR constraints with the backbone RMSD for the helical region being 1.11 ± 0.20 Å.

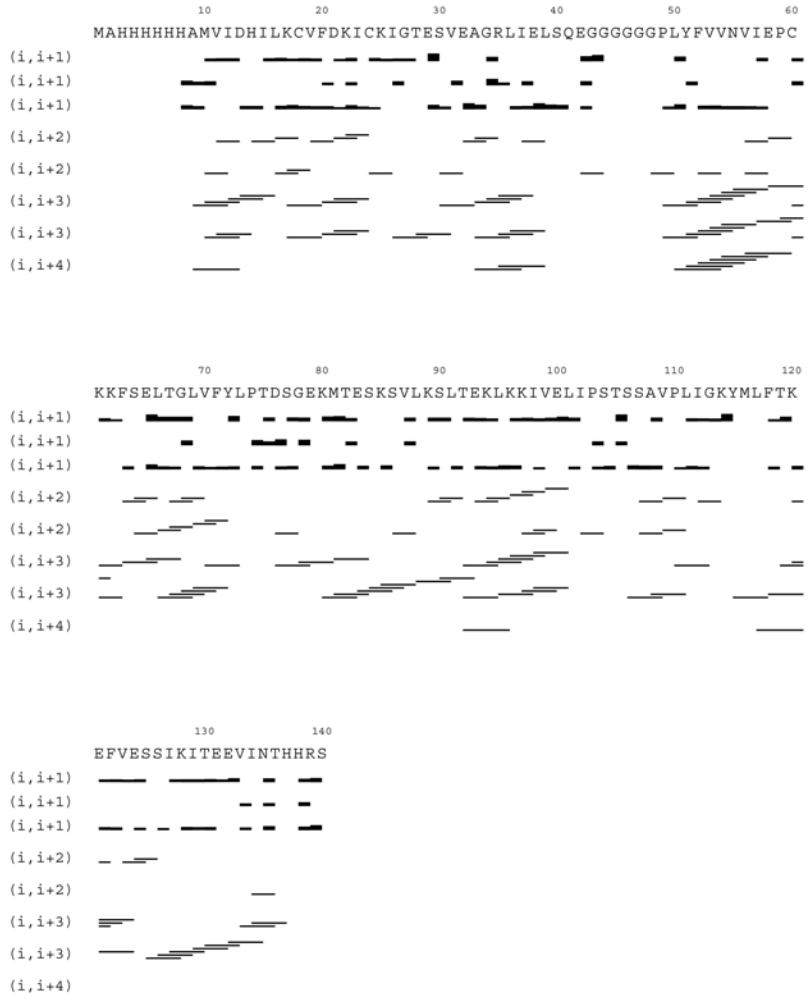

Fig. 3.1.7. Summary of the short-range NMR restraints determined for WSA. They were shown with the line thickness proportional to the intensity of the NOESY cross peaks.

Table 3.1.8. NMR structure statistics and restraints summary of WSA in LPPG micelles

Restraints	NOE distances	Intra-residue	415
		Short range (|i–j| = 1)	399
		Medium range (1<| i–j| ≤ 4)	269
		Long range (|i–j| > 4)	43
	Dihedral angles		209
	Hydrogen bonds		0
Residual upper limit constraint violations			
	> 0.5 Å		0
Residual dihedral angle constraint violations			
	> 5°		0
Backbone RMSD	Residues in helical regions only (10-40,50-70,80-100,111-136)		1.11 ± 0.20 Å
Heavy atom RMSD	Residues in helical regions only (10-40,50-70,80-100,111-136)		1.51 ± 0.21 Å
Ramachandran Plot	Residues in most favored regions		87.5%
	Residues in allowed regions		12.1%
	Residues in disallowed regions		0.4%

These structures show two long and two short TM helices, with TM3 and TM4 being of greater length, while TM1 and TM2 are shorter. In Fig. 3.1.9A and Fig. 3.1.9B, WSA was superimposed on to the GLIC X-ray structure. Given that there is less than 10% sequence identity (8.6%) between WSA and GLIC for the TM domains, the structural agreement between them is remarkable. Such an agreement cannot be reached between WSA and the cryo-EM structure of Torpedo nAChR, although there is more than 80% sequence identity. These unexpected findings indicate that WSA could represent an open state just as GLIC does, while the Torpedo nAChR cryo-EM structure is in the closed state.

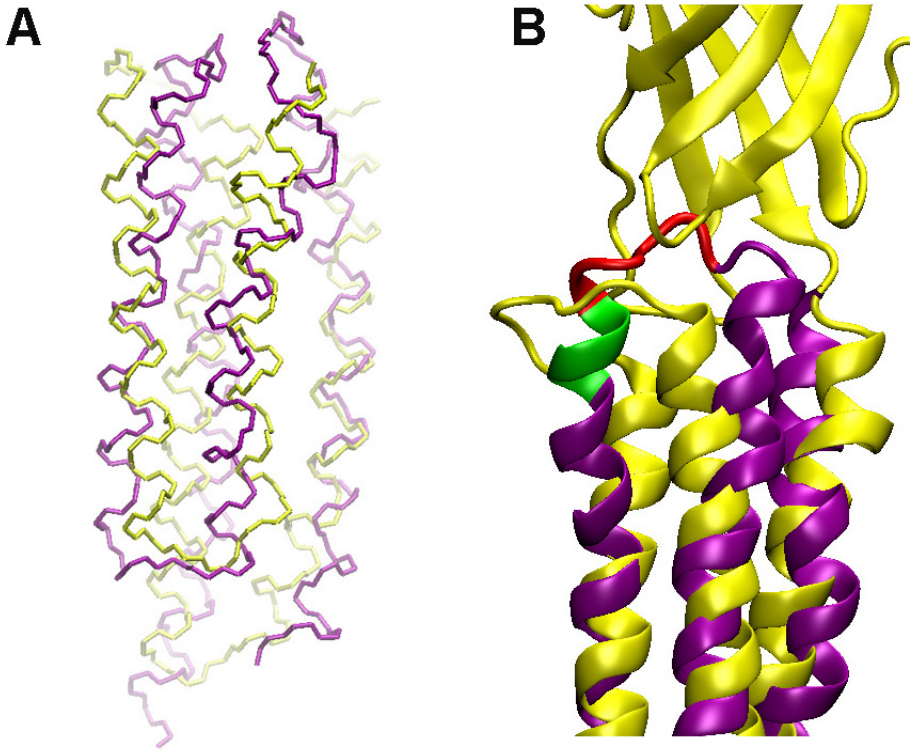

Fig. 3.1.9. Structure comparison of WSA and GLIC. (**A**) WSA structure (Purple) is aligned with GLIC TM domain (Yellow), showing that WSA has more similar structure profile to GLIC than to Torpedo nAChR α1 subunit (alignment with cryo-EM structure not shown). (**B**) WSA (Purple) superimposed onto GLIC (Yellow), with the EC domain of GLIC shown. In the absence of the EC domain, the TM23 loop region of WSA is in a different conformation from that of GLIC. In the comparison between WSA and the Torpedo nAChR, TM23 loop in WSA, LIPSTSS (Red), replaces original VPLI (Green) in the nAChR. It indicates that the TM23 loop in WSA shifts to the TM2 and the TM2 is shorter in comparison to the cryo-EM model.

A close comparison of the two structures, the WSA and the Torpedo nAChR cryo-EM structure, reveals more obvious structural differences. First, the cryo-EM structure of Torpedo nAChR shows four α helices with equal length, as shown in Fig. 3.1.10B. TM1, TM2, and TM3 span ~8 helical turns, while TM4 is tilted and spans ~10 helical turns. In contrast, both WSA and GLIC have an uneven length of helices. In Fig. 3.1.6 and 3.1.10C, TM1 and TM2 span ~6 helical turns, while TM3 and TM4 are ~8 helical turns long. In previous studies [81-85], TM1 and TM2 were truncated and isolated from nAChR or glycine receptors (GlyRs) and studied by NMR. In these studies, the helical lengths from single TM1 and TM2 are also consistent with the TM lengths in WSA. These two domains are shorter in WSA, isolated TM1 and TM2, and GLIC than in the cryo-EM structure of the Torpedo nAChR. Secondly, the loop positions are different between WSA and the Torpedo nAChR. Fig. 3.1.10A shows the sequence alignments of WSA, GLIC and the Torpedo nAChR. WSA and GLIC have very similar loop positions that are different from the cryo-EM structure of the Torpedo nAChR. Both of them shift to the N terminus resulting in longer helices in TM3 and TM4. Loop 12 in WSA is composed of residues LPTD, which are in the helical conformation in the cryo-EM structure. It is the same case for the loop 23 LIPST. The loops 12 (SGE) and 23 (VPLI) in the cryo-EM structure of the Torpedo nAChR become helices. More interestingly, residues STSS in loop 23 exist in two different conformations based on the CSI analysis. The structure we present here is the major rigid conformation. The clear differences between the NMR structure WSA and the cryo-EM structure for Torpedo nAChR suggest that WSA may represent a different state, compared to the cryo-EM structure. Interestingly, GLIC, which has been proposed to represent an open state of nAChR, has a similar loop position. Loop 12 (STS) and loop 23 (LPKTPYMT) correspond respectively to LPTD and LIPST in WSA. This suggests that WSA may represent the open channel of nAChR. The solved monomeric form of WSA was computationally assembled into a

model of the expected pentameric acetylcholine channel, using GLIC as a template. The created homopentameric WSA is shown in Fig. 3.1.11A. With the TM2 helices lining the center of the channel, the homopentameric WSA shows a clear clockwise tendency, compared to GLIC. The pore profile was calculated by using the HOLE program [86], shown in Fig. 3.1.12. E79, E83, S90, E93 and K97 were identified as the pore-lining residues. These results are consistent with the previous findings in the cryo-EM model structure of the nAChR, except for E83 [7]. Instead of E83, in WSA, T82 was supposed to be the pore-lining residue based on the cryo-EM model. However, even in the cryo-EM model, both T244 and L245, which are corresponding to T82 and E83 in WSA, are very close to pore. In WSA, L245 was mutated to E83 due to the water solubilization approach. The difference on the side chains between Glu and Leu may affect the orientation of E83, making E83 reside within the pore. The cryo-EM model structure is considered as the closed model for the Torpedo nAChR. L251, S252 and V255 are predicted to be the restriction site, which are corresponding to K89, S90 and E93. However, in the pore profile of WSA, K89, S90 and E93 are not in the narrowest region any more. In fact, they reside in a widely open region. Therefore, the pentamer arrangement of WSA is also agree with an open channel configuration. Thirdly, the WSA is more tightly packed than the Torpedo nAChR. Fig. 3.1.11A and B show the top view of WSA and the torpedo nAChR. The TM2 domain of the torpedo nAChR shows the largest displacement. More tightly coupled side chain interactions are present in the WSA structure than in the Torpedo nAChR. Last, TM1 is not straight. There is an obvious kink present in the WSA around residue P59. The same kink was also observed in previous studies for the isolated TM1 of nAChR. In GLIC, this kink also exists, although it is not obvious as in WSA.

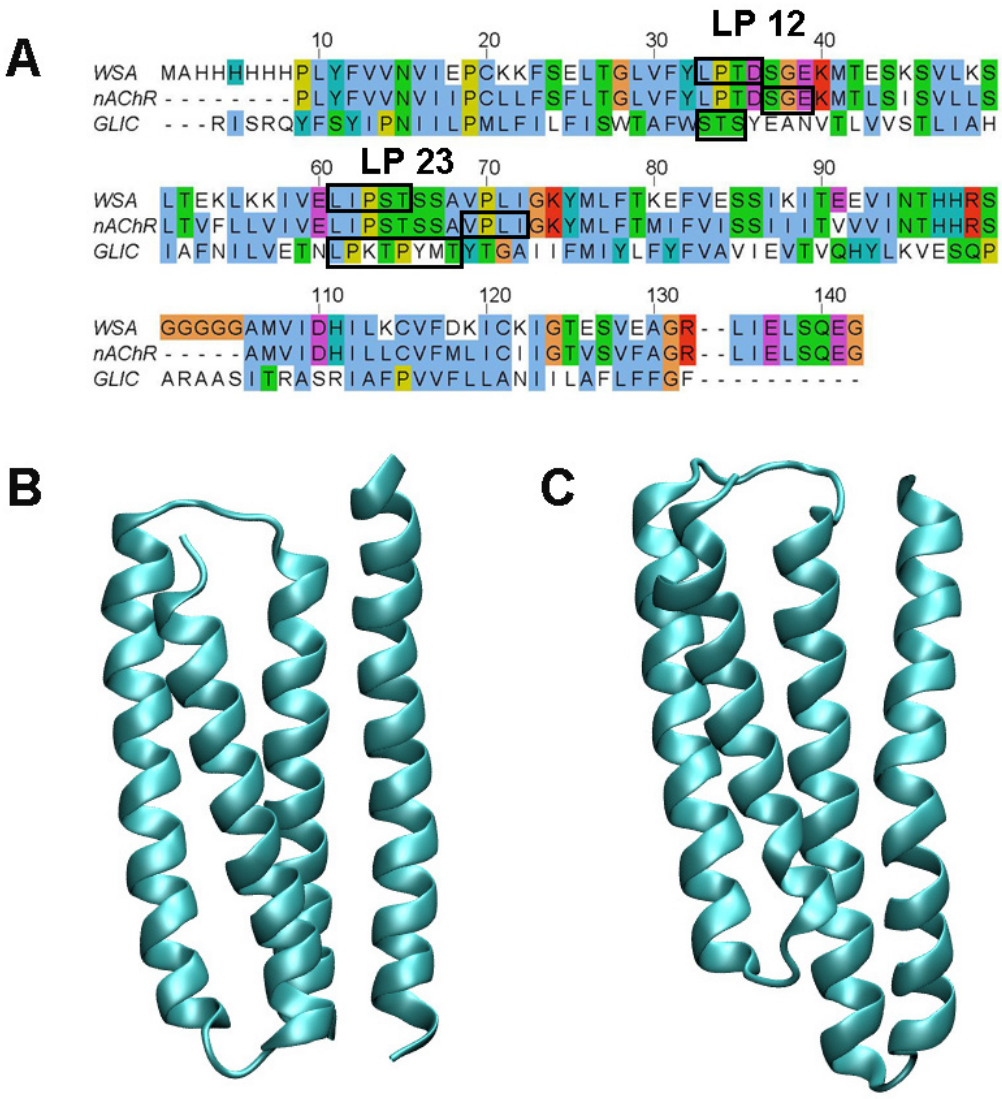

Fig. 3.1.10. Structure comparison of the cryo-EM model of Torpedo nAChR structure and the X-ray GLIC structure. (**A**) Sequence alignments of WSA, nAChR from torpedo, and GLIC. It shows 82.6% amino acid identity between WSA and nAChR and 18% between nAChR and GLIC. Two ligand-free structures have been reported: the torpedo nAChR solved by electron microscopy **(B)** and the 2.9 Å GLIC X-ray structure **(C)**. Although the two structures are similar, the difference of channel state (closed channel for nAChR and open channel for GLIC), helix length, loop position and a kink in helix is clear.

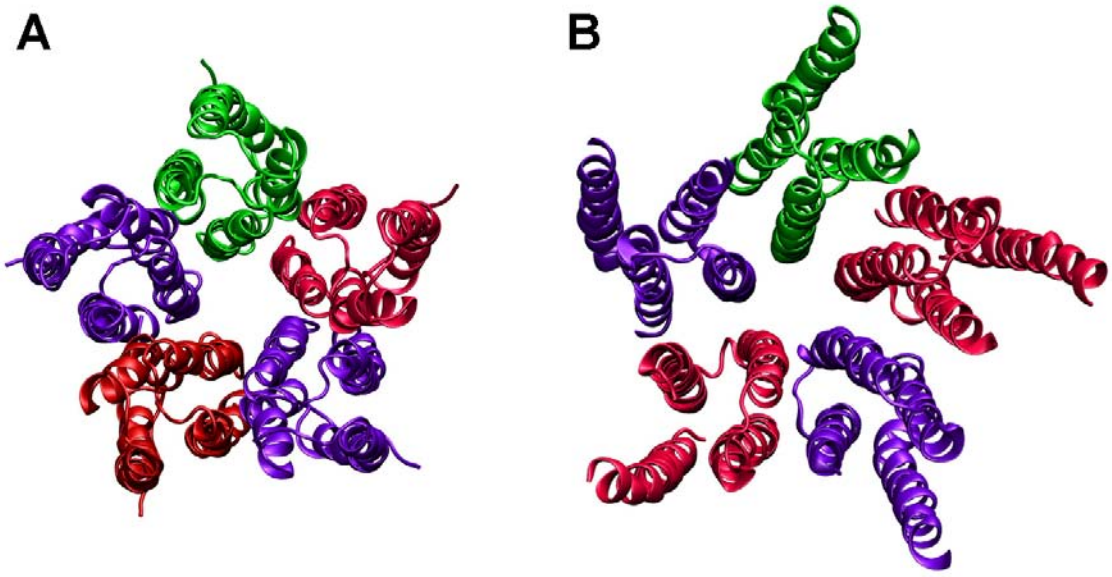

Fig. 3.1.11. Comparison of the pentameric model WSA and the GLIC TM domains. (**A**) Pentameric WSA was built by superimposing the monomeric WSA upon the pentameric ligand-gated ion channel homologue (GLIC). (**B**) The TM domain of the cryo-EM model structure of the Torpedo nAChR. WSA is more tightly packed than the torpedo nAChR.

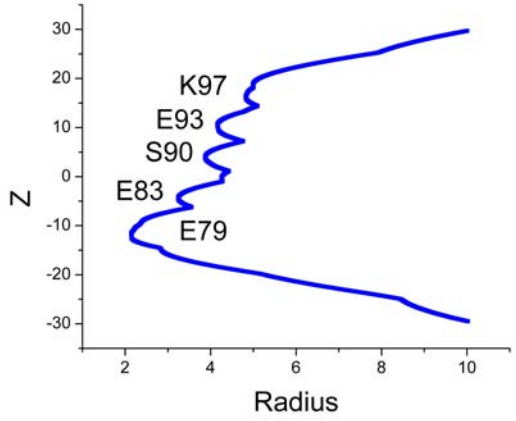

Fig. 3.1.12. Pore profile of WSA. The pore profile was calculated using the HOLE program. E79, E83, S90, E93 and K97 were identified as the pore-lining residues. The V-shape profile suggests that WSA may form an open channel.

3.1.7 Backbone dynamics of WSA

The ^{15}N relaxation parameters, R_1 and R_2, as well as the steady-state heteronuclear NOEs (hetNOE) were measured for WSA at 14.1 T, which correspond to the 600 MHz ^1H resonance. R_2/R_1 values were calculated for all residues, and all of these parameters are shown in Fig. 3.1.13. A majority of the R_1 values are between 0.8 and 1.2 s^{-1}, and the R_2 values range from 7 to 18 s^{-1}. The NOE is higher than 0.6 for most residues in the helical regions. The hetNOE values of the residues in the polyglycine linker between TM4 and TM1 are significant lower than those in the helices, suggesting that the polyglycine linker, similar to the C-terminus, is the most flexible region in WSA. Compared to the polyglycine linker, the native loop 12 and loop 23 are relatively rigid.

Given that the ratio of the average R_2 to R_1 value is approximately half the weight of the protein molecular weight, the average of R_2/R_1 for WSA is ~15, suggesting that the NMR data describes the monomeric form of the WSA in the LPPG micelles.

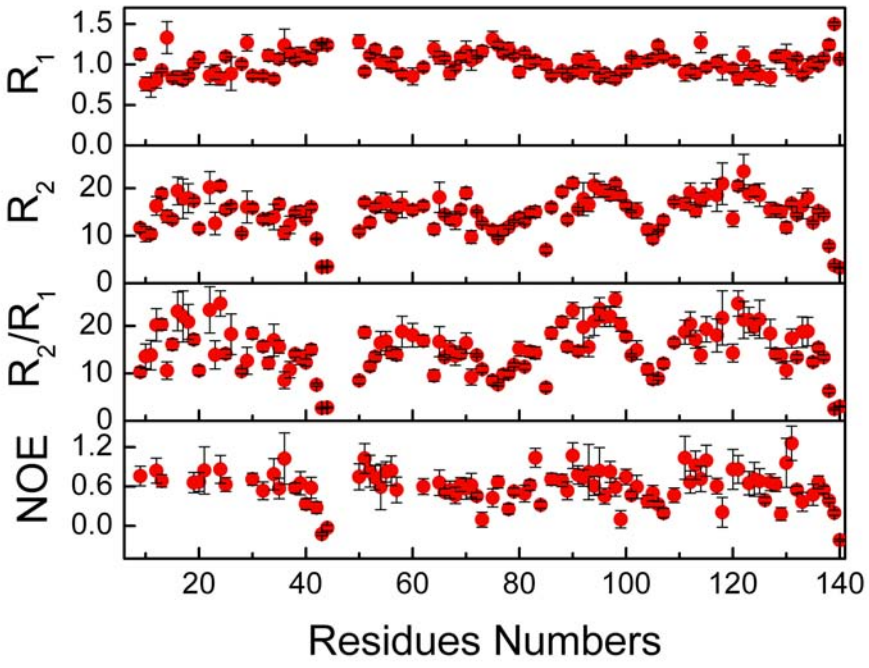

Fig. 3.1.13. Dynamics analysis of the backbone amide ^{15}N of WSA in LPPG micelles. The relaxation data were acquired at 600 MHz. Longitudinal and transverse relaxation rate constants R_1 R_2 and ^{15}N-{^1H} steady-state NOE are shown. Error bars are the standard errors of the least-squares fitting to the exponential decay function for R_1 and R_2 and the calculated uncertainties for NOE.

The quantitative analysis with the extended model-free approach was performed using DYNAMICS [79,80]. The total correlation time we used was 12 ns, which was determined by minimizing the reduced χ^2 value. Results are shown in Fig. 3.1.14. This analysis provides us with values of the generalized order parameter (S^2), the local correlation time τ_e, the exchange term (R_{ex}), the generalized order parameter for the fast effective local motion (S_f^2) and the models used to fit the data for each residue. S^2 is above 0.7 and S_f^2 is 1 in the helical regions, which is typical for globular proteins. For the loop region, most residues have τ_e ~1-3 ns and S_f^2 is smaller than 1. More interestingly, some residues have non-zero R_{ex} contributions to R_2, indicating that those residues may undergo chemical and conformation exchange. Particularly, the TM2 region shows more non-zero R_{ex} terms than other TMs. This suggests that the TM2 domain is more flexible than other TMs domains. We confirmed the presence of exchange contribution to relaxation by the CPMG R_2 dispersion measurements [87,88]. Results are shown in Fig. 3.1.15.

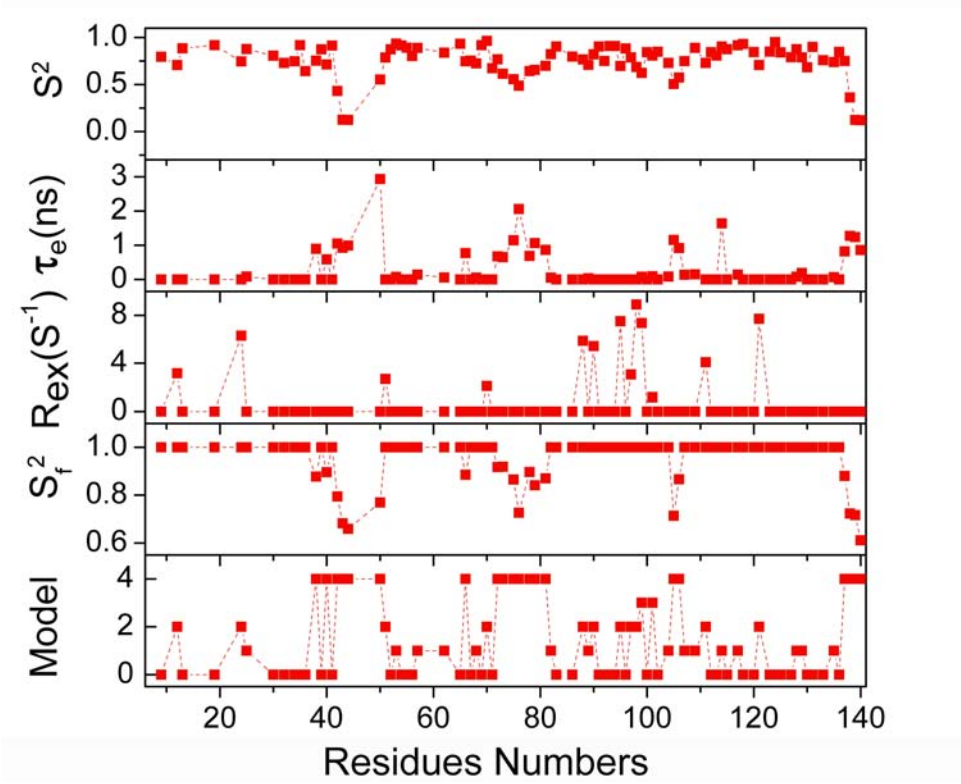

Fig. 3.1.14. Quantitative extended model free analysis of WSA by the program DYNAMICS. Total correlation time was determined as 12 ns based on minimum reduced x^2 value. The generalized order parameter (S^2), the local correlation time τ_e, the exchange term (R_{ex}), the generalized order parameter for the fast effective local motion (S_f^2) and the models used to fit the data for each residue are shown.

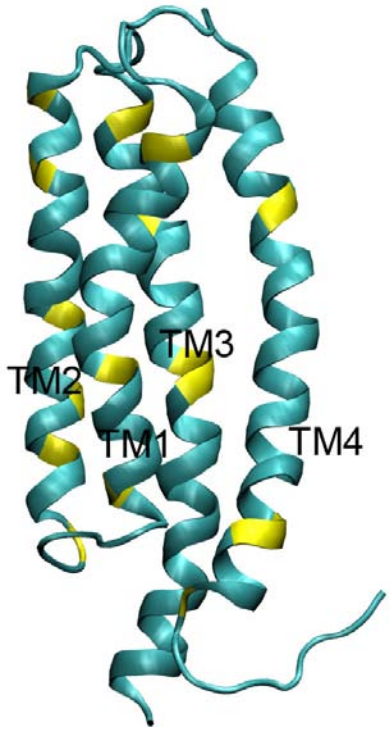

Fig. 3.1.15. Structure mapping of residues experiencing conformational exchange. CPMG R_2 dispersion measurement was performed to confirm the presence of exchange contribution to relaxation. The residues, which show the R_2 dispersion curve, are highlighted in yellow. They are TM1 51 64 70, TM2 78 82 85 89 97 100, TM3 109 114 122 123 and TM4 9 14 15 32.

Residues 79, 82, 86, 89, 93, 96, 97, and 100 in WSA are considered as the key residues lining the pore. Note that residues 89, 93, 96 and 97 have been mutated to hydrophilic residues such as E or K in order to increase the solubility of WSA. R_2 dispersion experiments show that 82, 89, 97 and 100 undergo conformation exchange on an us-ms timescale. E79 is located on the cytoplastic termini of TM2 and forms the

narrowest restriction site. In the Torpedo nAChR cryo-EM structure, E79 is located in loop 12, suggesting its large flexibility. On the contrary, the same residue is in the helical conformation in WSA, based on the CSI and structure. Interestingly, mode-free analysis of the backbone dynamics indicates that E79 does not meet the basic Lipari-Szabo assumption and can only be fitted in mode 5. It means E79 undergoes additional fast effective local motion. In fact, all the residues SGE that were originally located in the loop 12 of the torpedo nAChR and become structured in WSA now have the term S_f^2. This indicates that these residues are somewhat flexible, although they do have a helical structure in WSA. Additionally, G78, which is near the E79 also shows a R_2 dispersion curve, which supports SGE are flexible. It was also found that the loop 23 VPLI of the torpedo nAChR is in the helical conformation in WSA, however, V109 undergoes conformational exchange based on the R_2 dispersion experiments and L111 has non-zero R_{ex} term suggested by mode-free analysis. It also indicates that residues VPLI are in highly dynamic helical conformation. As discussed before, STSS exists in two different conformations based on CSI methods. It is supported by the findings that both T105 and S106 have non-zero R_{ex}, suggesting they undergo conformational exchange.

3.1.8 Conserved Pro in TM1 and its dynamics

Pro-59 is the only conserved proline in TM1 among all the members of AChR and other Cys-loop receptor family [89]. It has been proposed that the TM1 helix has an irregular structure, which may be caused by this conserved proline [90]. From our previous NMR study on the TM1 of the nAChR β_2 subunit, we found that the Pro-219 may lead to helical distortions [84]. In WSA, a more obvious kink near Pro-59, present in the center of TM1 helix, has been identified. This kink separates TM1 into two parts, the half nearer the EC domain and the C-terminal half of the TM1 helix. This separation could allow for

motion of the C-terminal half of the TM1 helix, and more importantly of the dynamic TM2 helix. In Fig. 3.1.14, τ_e indicates the local motions of the amide backbones. A close examination of τ_e data reveals two different dynamics characterizations in TM1 helix. Most residues in the C-terminal half of the TM1 helix show τ_e, while the N-terminal half shows fewer τ_e. It infers that the C-terminal half of the TM1 helix is much more flexible than the N-terminal half. As TM2 forms the channel, it is the most important domain for the channel gating, and many residues in TM2 involve conformational exchanges. TM1 is connected to TM2 and may cooperate with TM2 to gate the channel, as suggested by the higher flexibility of the C-terminal half of TM1. Pro-59 plays a role like a 'hinge', which fixes the TM2 and the mobile part of TM1 to the stable N-terminal half of TM1. It seems that the non-straight helical structure with a kink in the center might accommodate the requirement of channel gating mechanisms. A detergent-protein interacting site was identified near Pro-59, which may contribute to the stabilizing of the N-terminal half of TM1. A similar lipid-protein interaction site can also be found in GLIC [11].

3.1.9 Unique dynamics of TM2

From the cryo-EM model structure of nAChR, it has been suggested that there are two basic structural components to line the pore, inner helices and outer helices. The group of TM1, TM3 and TM4 comprises the outer helices, while TM2 of each subunit forms inner helices. The outer helices are believed to stabilize the pentameric receptor in the membrane, suggesting that TM1, TM3 and TM4 are less flexible. The inner helices, however, directly face the channel. In contrast to the dynamics of the outer helices of TM1, TM3 and TM4, TM2 dynamics feature is closely related to its important function, namely, channel gating. Therefore, the TM2 domain is considered to be the most flexible

helix, which is connected to TM1 and TM3 through two important loops, 12 and 23. Although WSA was designed and solved in a monomeric form, the intrinsic dynamics and relative helix positions of TM2 can still indicate the possible motions, which are related to the channel function. In fact, both R_2 dispersion and backbone dynamics analysis show that TM2 is more flexible compared to other TMs. For example, residues 88, 90, 95, 97, 98 and 99 in TM2 show R_{ex} terms by backbone dynamics analysis. Residues 78, 82, 85, 89, 97 and 100 involve chemical and conformational exchanges confirmed by R_2 dispersion experiments. On the contrary, only a few residues from TM1, TM3, and TM4 show the flexibility.

3.1.10 Importance of TM23 loop

The TM23 loop has been proposed as the key loop that communicates with the EC domain [7,8]. By comparing the structures of the TM23 loop between the nAChR cryo-EM model and WSA, we found that there is a notably major difference in the TM23 loop, a region believed to be important for the receptor's gating activity. Residues VPLI, which comprise the TM23 loop in the nAChR cryo-EM model structure, have undergone a notable shift toward the TM3 helix, while the residues SSTS shift the same way and become a new TM23 loop in WSA. WSA is designed as a high sequence identity to the torpedo nAChR α1 subunit; however, its structure is solved more similar to GLIC, which is in the open state. Given that the TM23 loop can directly couple with the EC domain to gate the channel, without the EC domain, WSA may represent the state of nAChR differently from the cryo-EM model for the closed state. It is possible that the presence of interactions between the TM2-3 loop and the EC region of the protein makes the TM23 loop shift toward TM2, allowing it to further interact with the Cys-loop of the EC region and serve to switch the receptor channel from open to closed. Without the restriction of

the EC domain, the TM23 loop in WSA can undergoes multiple conformations. In Fig. 3.1.5, the two conformations of the TM23 loop, identified by NMR chemical shift index method are shown. Interestingly, our previous study on the secondary TM domain of the human neuronal GlyR α1 subunit also shows two conformations for the TM23 loop residues [81]. Both WSA and the GlyR TM2 NMR studies suggest that the flexibility of two conformations is different, as indicated by CSI for WSA and backbone dynamics for glycine receptor TM2. These intrinsic pre-existing multiple conformations for the TM23 loop may relate to the channel gating mechanism. As discussed above, the TM2 helix is more flexible due to its gating function. Now, the TM23 loop exists in two conformations, further enabling the motion of the TM2 helix. Interestingly, there is only one conformation for the TM12 loop. It suggests that TM2 helix motions will not be even. The C-terminal part of the TM2 helix has more capability to move than its N-terminal counterpart. It further proves that the TM2 helix involves the channel gating by twisting or tilting around its N-terminus.

Fig. 3.1.9B show the overlap of WSA with GLIC. It appears that the highly dynamic nature of the region is responsible for the difference in loop size and arrangement of specific residues within the structure, while the specific orientation of the loop (bent toward the center of the bundle) could be a result of the lack of interactions with the EC domain. The x-ray crystal structure of the EC domain alone had similar observations: the Cys-loop region structure was significantly different from that of the cryo-EM model structure [5]. These structural differences are also believed to be a result of the lack of important interactions between the TM domain and the EC domain. Therefore, the fact that these two regions, known to strongly interact in the intact protein, both adopt different structural arrangements without the other present should be expected, and is a reasonable observation.

3.1.11 Protein-detergent interaction sites

Previous experimental and computational studies have shown that the nAChR requires the proper compositions of lipids in order to maintain proper protein function. The WSA structure has been solved in 2% lyso-lipid LPPG, which is well mimetic for the natural lipid. WSA was originally designed as a detergent-free analogue of the TM domain of the nicotine acetylcholine receptor. The location of lyso-lipid molecules in the WSA can provide us with information regarding why WSA is partially water-solubilized. Further, we can deduce what kind of protein lipid interaction may be necessary in order to for nAChR function properly. ^{15}N edited NOESY spectrum was used to identify the protein detergent interaction sites. Due to the application of the water-soluble approach on WSA, we did not observe the detergent interaction sites on the outside of WSA. However, several protein detergent interaction sites inside the WSA have been identified, as shown in Fig. 3.1.16. The most interesting one is located between TM1 and TM4. In Fig. 3.1.16, we see that there is a relatively larger space separating TM4 from all other TMs. The same space can also be found in the cryo-EM structure model of the torpedo marmorata nAChR and the X-ray structures of the two bacteria homologues, ELIC and GLIC. In WSA, the lyso-lipid LPPG was identified to be located in this large space. A very similar lipid protein interaction site is also found for the GLIC. Two lipid molecules can be found between TM4 and TM1 in its x-ray structure. These unexpected detergents for WSA and lipids for GLIC suggest that the TM4 domain may function separately or differently from other TMs. Several studies proposed that cholesterol might be located in this hydrophobic core. However, for both WSA and GLIC, there is no extra space allowed for other molecules such as cholesterol.

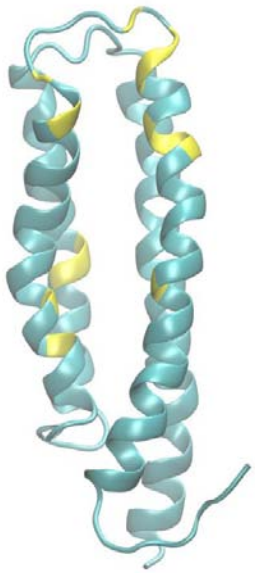

Fig. 3.1.16. Structure mapping of the detergent binding sites. Detergent-WSA interaction sites were identified based on the ^{15}N edited NOESY experiments. The residues, which show the cross peaks with the detergents, were highlighted in yellow. They are TM1 48, 50, 64, 67, TM2 88, 89, and TM4 24, 33, 34, 35, 39, 40, 41, 43.

3.1.12 Conclusion

Through mutating specific lipid-facing residues to hydrophilic ones, which greatly improved the TM protein solubility in water, the engineered water-solubilized TM domain of nicotine acetylcholine α1 subunit (WSA) was studied by NMR. The monomeric WSA structure was resolved to the backbone RMSD of 1.19 ± 0.16 Å. The overall structure is similar to the open structure of GLIC, while it disagrees with the cryo-EM model structure. In particular, the position of the TM23 loop was found to shift close to TM2. TM1 and TM2 are shorter, while TM3 and TM4 are longer in comparison to cryo-EM

model structure. In addition, STSS in TM23 region has two distinct conformations, the rigid conformation and the flexible conformation. The shifting motion of the TM23 loop with two different conformations could involve the channel gating through communicating with the EC domain. Backbone dynamics analysis of amide ^{15}N of WSA further investigated its intrinsic dynamic properties.

3.2 NMR STUDY OF TM AND IC DOMAINS OF THE HUMAN nAChR α7 SUBUNIT

3.2.1 Significance

For the first time, the novel water solubilization approach was applied to the human nAChR α 7, which mediates fast signal transduction in the central nervous system. Human nAChR α7 is a homo-pentameric ion channel and each subunit includes a large N-terminal EC domain, four TM domains and a large IC domain, which connects TM3 and TM4. Currently, most structural studies are based on the low-resolution cryo-EM model structure [7,8] from Torpedo and two X-ray structures [9-11] from the bacterial homologues of pentameric ligand-gated ion channels. However, the sequence identity between human nAChR α 7 and their homologues is low. Moreover, for both cryo-EM and X-ray structures, there is very limited or no information for the IC domain. We successfully heterologously over-expressed human nAChR α7 TM domain with (nAChRα7TM-IC) and without the IC domain (nAChRα7TM-5G) in *E. coli*. Protein expression yield for these proteins are 5 mg/l and 10 mg/l, respectively, in M9 media. The secondary structures of our recombinant proteins have been investigated by circular dichroism (CD). Both nAChRα7TM-IC and nAChRα7TM-5G folded into stable structures in ~1% empigen with helical content of 41% and 50%, respectively, which are consistent

with previous studies [91]. Highly resolved NMR HSQC spectra for these proteins have been obtained. Both CD and NMR spectra suggest that expressed proteins are well folded. Furthermore, backbone dynamics R_1, R_2, and heteronuclear NOE were performed and qualitatively analyzed using the histogram method. The comparison of the backbone dynamics of these two proteins indicate that the IC domain dramatically affects the intrinsic dynamics of the TM domain and makes the TM domain much more flexible. Further study of the human nAChR α7 using NMR will allow us to continue to investigate its function and role in ion channel gating and signaling.

3.2.2 Protein design

Human nAChR α7 DNA was first subcloned into the pTBSG1 expression vector shown in Fig. 3.2.1. Sixteen mutation sites in the TMs were experimentally implemented by PCR mutagenesis. nAChRα7TM-5G was engineered using five Glys to replace the IC domain of nAChRα7TM-IC. Both nAChRα7TM-5G and nAChRα7TM-IC were expressed with Rosetta (DE3) pLysS cell line (EMD biosciences). The specific mutation sites were identified empirically based on our novel water solubilization approach. In order to keep human nAChR α7 in a native state as much as possible, we minimized the number of mutation sites. The IC domain in the nAChRα7TM-IC was not touched, due to its high percentage of hydrophilic amino acids. The TM2 domain in both nAChRα7TM-5G and nAChRα7TM-IC were also not mutated as they face the channel pore. Particularly, it has been found that the segments of the TM2 domains of the human GlyR α1 subunit, in the same superfamily as nAChR, can form a functional homopentameric channel by themselves with reasonable conductance comparable to the authentic receptors [81,92-94]. With the native TM2s, both nAChRα7TM-5G and nAChRα7TM-IC may form homopentameric channels. Regarding the solubility of the protein, hydrophilic amino

acids were selected to replace the hydrophobic amino acids and broke down the hydrophobic patches along the lipid-facing surfaces of the TM domains (TM1, TM2 and TM3). Along these hydrophilic amino acids, the positive charged amino acids were not preferred in order to lower the isoelectric point (PI) of the recombinant protein. We found the low PI facilitates protein expression and NMR sample preparation. Finally, 16 key hydrophobic amino acids were identified and mutated.

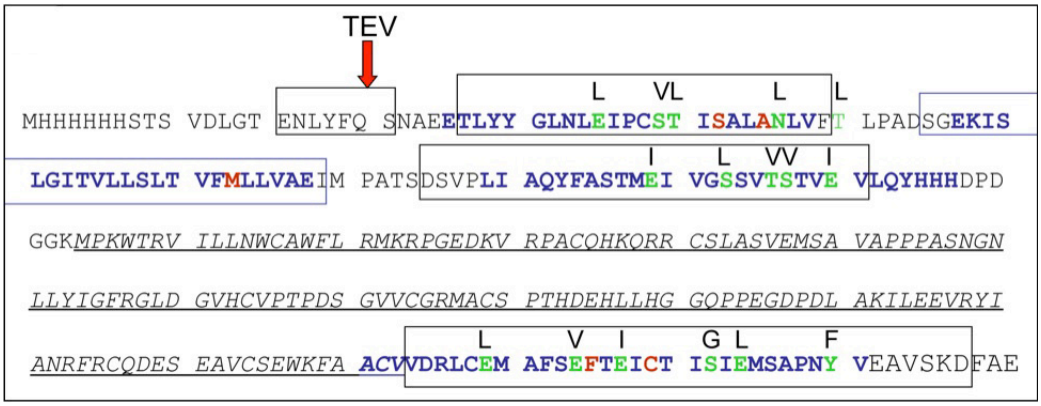

Fig. 3.2.1. Novel designed human nAChRα7TM-IC. With 300 residues, it encompasses an entire TM domain (Blue) and a long IC domain (Uderline). Sixteen mutation sites (Green) were identified and experimentally implemented on the TM1, TM3 and TM4, while TM2 and IC domains are in the native sequence. Replacing the long IC loop with a short 5-Gly linker, a TM only domain of human nAChR α7 subunit (nAChRα7TM-5G) was also reconstituted. PNU-120596 binding site is highlighted in red.

3.2.3 Protein expression and purification

Both nAChRα7TM-5G and nAChRα7TM-IC were expressed with the Rosetta (DE3) pLysS cell line (EMD biosciences). Cells were first grown at 37°C in 100 ml LB media with 100 μg/ml ampicillin and 70 mg/ml chloramphenicol overnight. Then cells were harvested and re-suspended into 1 l ^{13}C and ^{15}N rich M9 media containing 100 μg/ml ampicillin and continued to grow at 37°C until it reached OD_{600} of approximately 0.5. After one hour recovery period at 30°C, cells were induced with 0.2 mM IPTG and continued growing ~1 day.

After 1 day, cells were collected by centrifugation at 4°C and then re-suspended into the proper volume (20ml lysis buffer/1L cell culture) of lysis buffer (50 mM Tris-HCl, pH 7.5, 15% glycerol and 1 mM NaN_3). The suspended cells were incubated with 100ug/mol lysozyme and 25U/ml DNase for ~1 hour at room temperature, followed by sonication (20s on/20s off for 5mins). The lysate was centrifuged at 38724×g for 20 minutes. The supernatant was discarded and the inclusion bodies were solubilized in 0.8 ml 35% empigen (Sigma) overnight. After centrifugation at 38724×g for 20 minutes, the supernatant was diluted into 10 ml 20 mM Tris-HCl, pH 8.0 buffer and incubated with 1 ml Ni-NTA resin (Sigma) for one hour at room temperature. The resin was then washed with 40 ml of wash buffer (10 mM imidizole, 100 mM Nacl, 0.3% empigen, 20 mM Tris-HCl, pH 8.0) and eluted with 3 mL 250 mM imidazole, 0.3% empigen, 20 mM Tris-HCl, at pH 8.0. The resultant mutant (nAChRα7TM-IC) was expressed with a typical yield of 5 mg/l in M9 medium for NMR investigation. Replacing IC loop with a 5-Gly linker (nAChRα7TM-5G) increased the yield to 10 mg/l in M9.

3.2.4 NMR experiments and data processing

NMR sample preparation, and all NMR methods for the spectrum assignments were identical to those in Chapter 3, section 3.1.4. Briefly, the conventional suite of two-dimensional (2D) and three-dimensional (3D) heteronuclear, filtered experiments for spectral assignment.^{15}N- and ^{13}C-filtered NOESY was measured with a mixing time of 120 ms. NMRPipe [72] and Topspin 2.1 (Bruker NMR software) were used to process the NMR data. Sparky [73] was used to make resonance assignments.

Relaxation rate constants, R_1 and R_2 and the steady-state ^{15}N-{^{1}H} NOE were measured at 16.4 T using 4, 3, and 4 s delays respectively. The longitudinal rate constant, R_1, was recorded with 8 delay values: 10, 50, 150, 300, 500, 700, 1000, 2500 ms. The transverse relaxation constant, R_2, was recorded using 7 delay values: 16, 32, 64, 96, 128, 160, 240, and 400 ms. The steady-state ^{15}N-{^{1}H} NOE was measured with and without ^{1}H saturation in an interleaved fashion. The R_2 dispersion measurements were carried out at 16.4 T and 45 °C by using the relaxation-compensated, constant-time, Carr–Purcell–Meiboom–Gill (CPMG) sequence with the following 8 CPMG field strengths: 33.33, 66.67, 100, 166.67, 266.67, 366.67, 500.00, and 666.67 Hz [71,95]. The reference spectrum was acquired without the CPMG period. A relaxation delay of 2.5 s was used.

3.2.5 Secondary structure as determined by CD and NMR

CD measurements were performed using a Jasco Model J-810 spectrophotometer and analyzed using the K2D algorithm on the DICHROWEB server. The results are shown in Fig. 3.2.2 for both nAChRα7TM-5G and nAChRα7TM-IC. The secondary structure prediction for nAChRα7TM-5G is 50% based on the K2D output. CD result is consistent with a native acetylcholine receptor TM domain α1 subunit, given the prediction error by

circular dichroism. In the same way, the helical content of nAChRα7TM-IC was predicted to be 41%. Thus, the helical content of IC can be calculated to be at least 29%, which is in agreement with sequence-based predictions. The chemical shift index (CSI), which is commonly accepted NMR method for the identification of protein secondary structure, can provide higher resolution information of the secondary structure of the protein. A typical ^{1}H-^{15}N heteronuclear single quantum coherence spectrum (HSQC) of nAChRα7TM-5G is shown in Fig. 3.2.3A. Comparison of nAChRα7TM-5G with its wild type counterpart, the human nAChR α7 (Fig. 3.2.3B), reveals a dramatically improved NMR spectrum for membrane protein. Note that for the wild type human nAChRα7, we used 8 times more scans and the sample stability was poor. With the well resolved spectrum and other high quality of 3D spectra for nAChRα7TM-5G, a nearly complete backbone assignment of nAChRα7TM-5G was achieved, allowing us to predict the secondary structure by CSI method. Fig. 3.2.4 represents the chemical shift index for the Cα atoms. Four distinct α-helix domains with a similar position to GLIC and Torpedo nAChR can be identified, indicating that the secondary structure of native acetylcholine receptor TM domains is still retained in its water-solubilized counterpart. Overall, the α-helical content predicted by CSI is ~74%, fitting well with GLIC and the Torpedo nAChR.

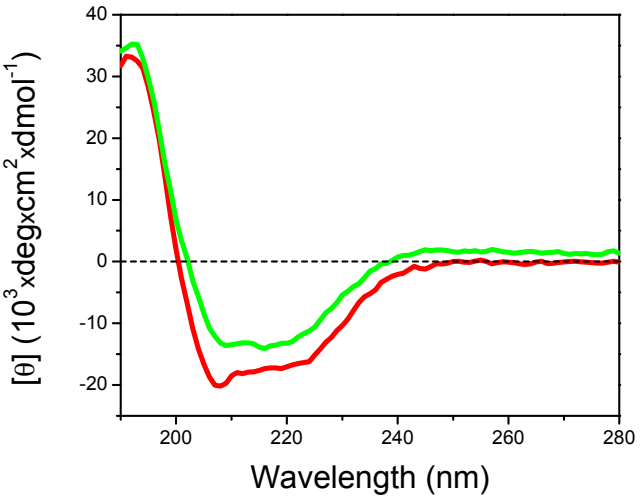

Fig. 3.2.2. **Far-UV circular dichroism spectra of nAChRα7.** Far-UV circular dichroism (CD) spectra were analyzed by online server DICHROWEB CDSSTR program, showing ~41% helical content for nAChRα7TM-IC (Green) and ~50% for nAChRα7TM-5G (Red).

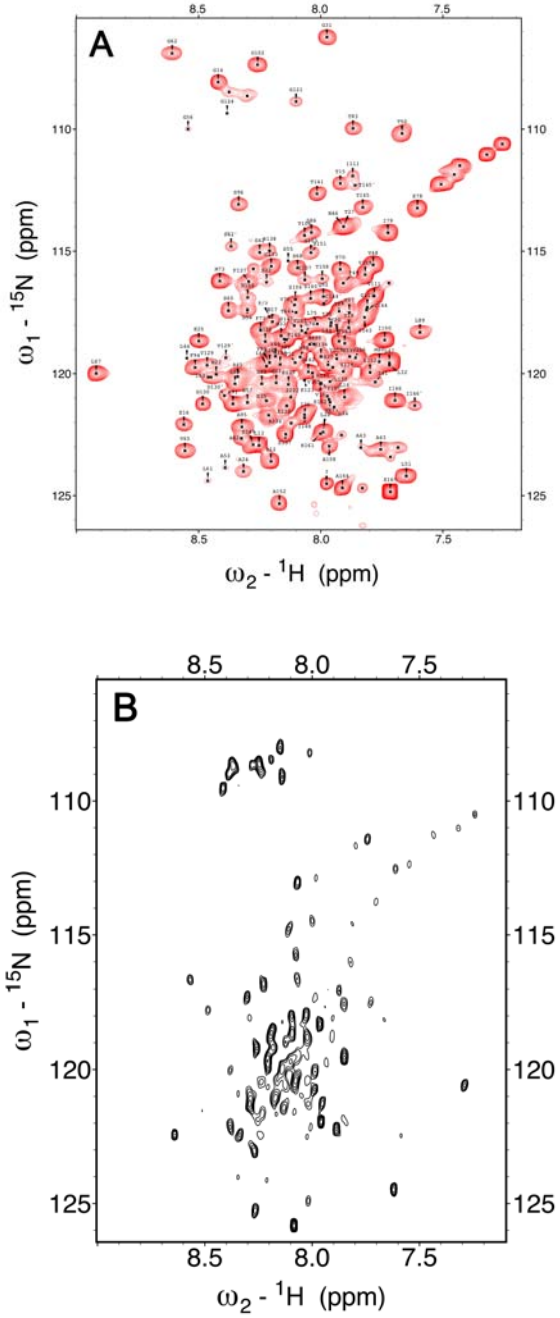

Fig. 3.2.3. **HSQC spectra of nAChRα7TM-5G and its wild-type counterpart.** Representative backbone amide proton ^{1}H-^{15}N HSQC spectrum of nAChRα7TM-5G in ~1% empigen pH 7.5 at 45˚C with 16 numbers of scans (**A**) and wild type nAChRα7TM-5G (**B**) in the comparable buffer conditions with 128 numbers of scans. The water solubilization approach dramatically improves the NMR signals and sample stability.

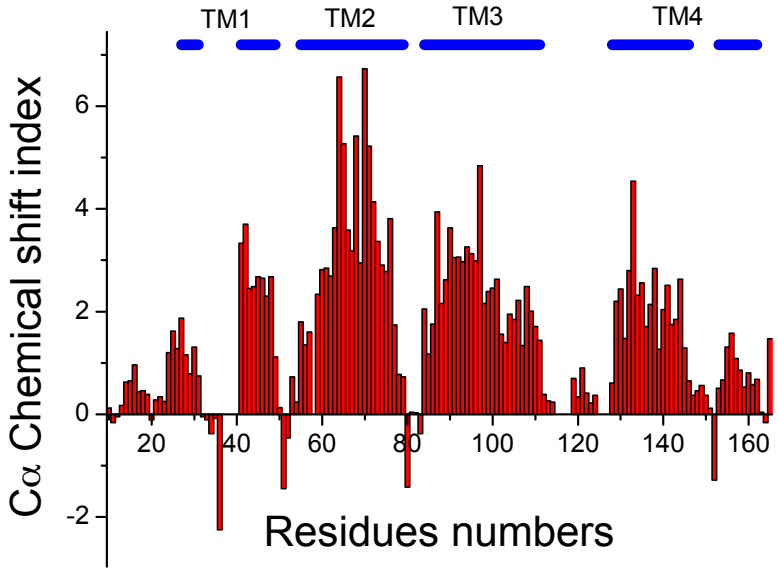

Fig. 3.2.4. **$^{13}C_{\alpha}$ chemical shift index of nAChRα7TM-5G.** The $^{13}C_{\alpha}$ chemical shift index (CSI), which was determined on the basis of Cα chemical shifts, also indicates a high helical content. Two disorder regions are observed in the middle of TM1 and TM4 domains. The residues of loop 12 and loop 23 are TLPAD and MPAT respectively, which are consistent with GLIC and WSA.

3.2.6 Backbone dynamics of TM and IC domains of human nAChR α7

R_1 and R_2 ^{15}N relaxation parameters, as well as the steady-state heteronuclear NOEs were measured for nAChRα7TM-5G at 16.4 T, corresponding to 700 MHz ^{1}H resonance. R_2/R_1 values were calculated for all residues, and all of these parameters are shown in

Fig. 3.2.5. A majority of the R_1 values are between 0.8 and 1.3 s^{-1}, and the R_2 values range from 3 to 19 s^{-1}. The NOE is higher than 0.5 for most residues in the helical regions. The hetNOE values of the residues in the polyglycine linker between TM3 and TM4 are significantly lower than those in the helices, suggesting the most flexible region of nAChRα7TM-5G is in the polyglycine linker, the same as C termini. Compared to the polyglycine linker, the native TM12 loop and TM23 loop are relative rigid. Interestingly, the R_2/R_1 for the TM2 is higher than other TMs, which suggests that the TM2 helices in this water-soluble form still form a channel. The oligomeric state cannot be simply predicted based on the R_2/R_1 ratio, if the protein involves more complicated motion [57]. R_1, R_2 and NOE experiments were also measured for nAChRα7TM-IC. Backbone dynamics analyses of nAChRα7TM-IC using our newly developed histogram method, which does not require full spectral assignment, were performed. Interestingly, for nAChRα7TM-IC, the average R_2/R_1 ratio is ~5 and most hetNOE values are negative. This indicates that most residues are very flexible. One of the possibilities is that in the low pH sample condition, the peaks from the IC loop of nAChRα7TM-IC dominate the NMR spectra.

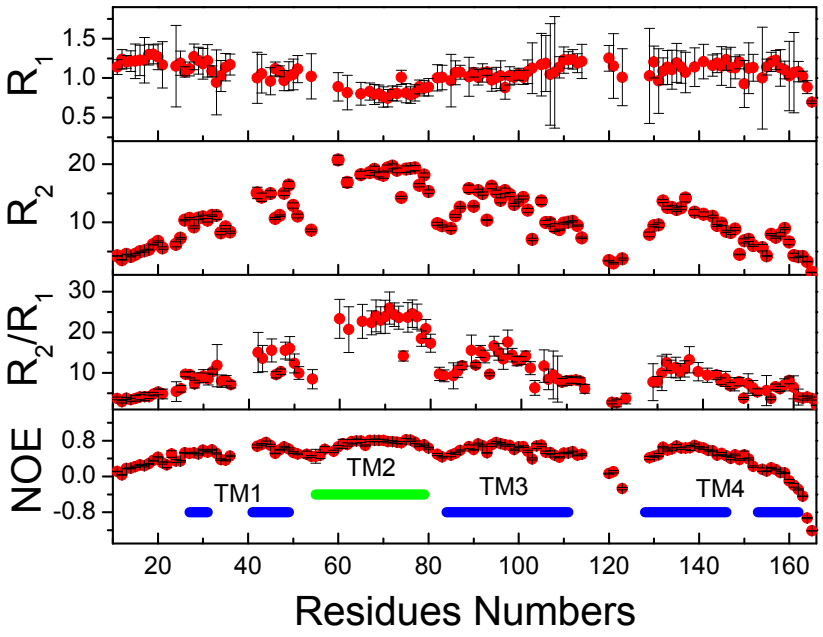

Fig. 3.2.5. Dynamics analysis of the backbone amide ^{15}N of nAChRα7TM-5G. The relaxation data were acquired at 700 MHz. Longitudinal and transverse relaxation rate constants R_1 and R_2 and ^{15}N-{^{1}H} steady-state NOE are shown. Error bars are the standard errors of the least-squares fitting to the exponential decay function for R_1 and R_2 and the calculated uncertainties for NOE. TM2 domain shows intrinsically different dynamic properties from other TM domains. R_2 dispersion experiment determined that the higher R_2/R_1 values for TM2 are contributed from anisotropic rotational diffusion.

3.2.7 IC domain effects on the TM domain

The sample nAChRα7TM-IC was prepared in two distinct pHs: pH 7.2, comparable to the sample condition for nAChRα7TM-5G and pH 4.6, the NMR preferred condition. Two ^{1}H-^{15}N heteronuclear single quantum coherence (HSQC) spectra for both sample conditions are shown in Fig. 3.2.6. In the high pH condition, the HSQC spectrum of nAChRα7TM-IC can be partially overlapped with its TM counterpart. This indicates that the TM domain itself can fold independently and the reductionist approach is valid. Some peaks in the HSQC spectrum for the TM domain of nAChRα7TM-IC disappeared. It might be due to the large protein size, aggregation or the dynamic changes, induced by the IC domain. The dynamics of the TM domain show different profiles in the absence and presence of the IC domain. The hetNOE experiments were performed for nAChRα7TM-IC in the high pH condition and the low pH condition. The two heteronuclear NOE spectra with and without saturation, measured in high pH conditions, were overlapped in Fig. 3.2.7. Compared to the same experimental results for nAChRα7TM-5G, the hetNOE values are smaller, indicating that the TM domain becomes more flexible in the presence of the IC domain.

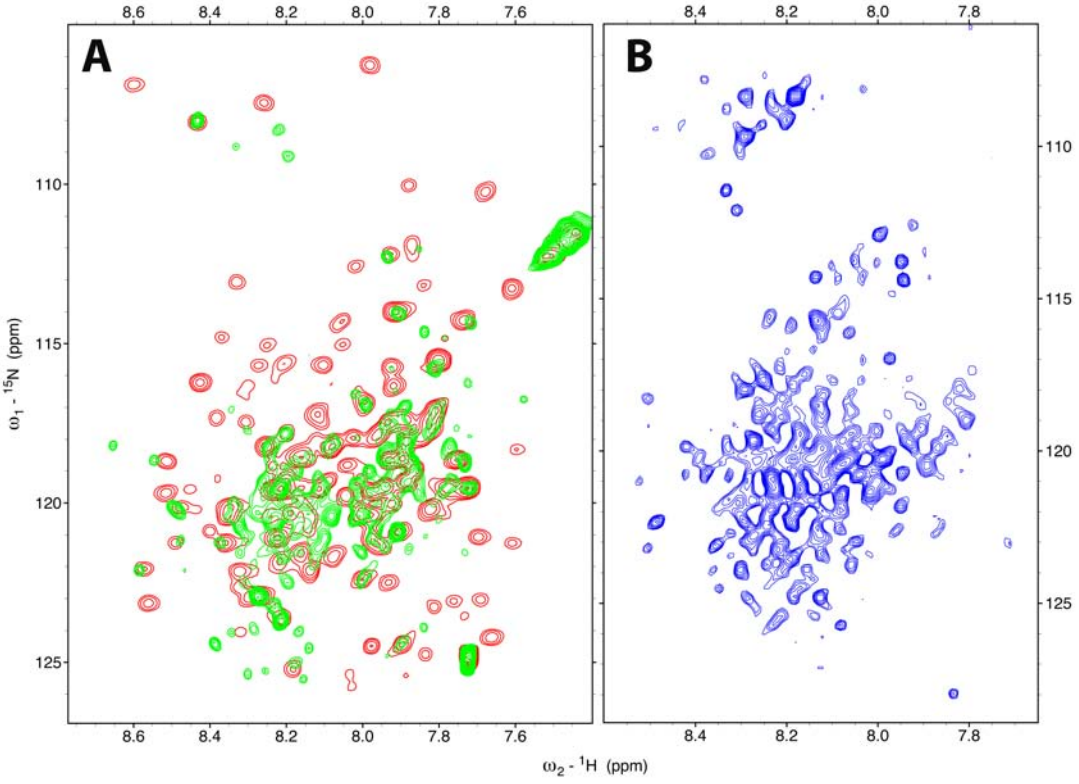

Fig. 3.2.6. **pH effects on the HSQC spectra of nAChRα7TM-IC.** (**A**) ^{1}H-^{15}N HSQC spectrum of nAChRα7TM-IC at pH 7.3 (Green) was overlapped with nAChRα7TM-5G (Red). (**B**) At pH 4.6, the peaks from the IC domain of nAChRα7TM-IC dominated the ^{1}H-^{15}N HSQC spectrum due to the intrinsic dynamics of the IC domain.

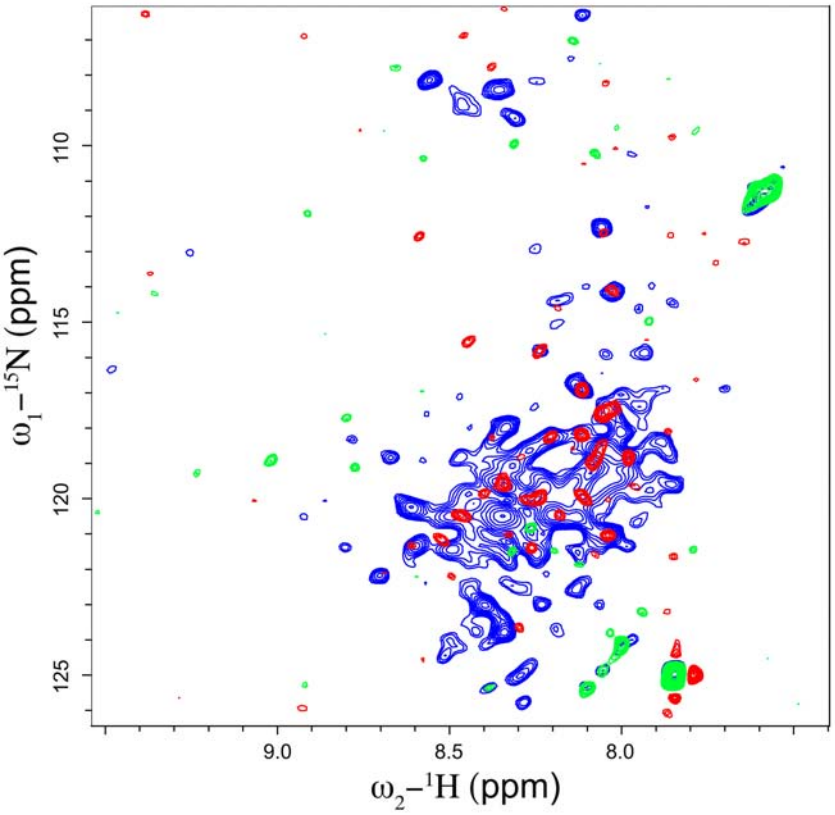

Fig. 3.2.7. **Dynamics of nAChRα7TM-IC.** ^{1}H-^{15}N heteronuclear NOE spectroscopy of nAChRα7TM-IC shows extremely dynamic domains. The spectra with (positive signals, Red; negative signals, Green) and without saturation (Blue) were overlapped. Most peaks disappeared in the saturated spectrum. This indicated that in the presence of the IC domain, the TM domain might become very flexible.

Note that for the same protein sample, the HSQC spectrum at low pH cannot be overlapped with the HSQC at high pH. Two possibilities exist. At low pH, the sample does not fold correctly. However, CD spectra in both pH conditions show no difference,

suggesting that the protein was still folded correctly at low pH. The other possibility is that at high pH, the IC domain undergoes a water exchange process, which decreases the peak intensities of the residues from the IC domain. In contrast, at low pH, the peak intensities of the residues from the IC domain start to show up and increase dramatically due to the slow water exchange process. The peak intensities for the IC domain are very strong and dominate the spectra. In this case, the most peaks in the HSQC spectrum represent the IC domain. Therefore, the histogram analysis of the backbone dynamics of nAChRα7TM-IC at low pH condition mainly reflects the IC domain dynamics.

3.2.8 Secondary structure analysis of nAChRα7TM-5G

The fully assigned backbone chemical shift of nAChRα7TM-5G allows us to predict the secondary structure accurately. The number of residues for the TM1, TM2, TM3, and TM4 of nAChRα7TM-5G is 23, 25, 27 and 35 respectively, which are similar to the numbers of each helix for the TMs in WSA (24, 22, 34 and 31) and GLIC (22, 25, 29 and 30) [9,11], but different from the cryo-EM model (27, 29, 26 and 34) [7,8]. For nAChRα7TM-5G, WSA and GLIC, TM1 and TM2 are shorter than TM3 and TM4. Therefore, the surface of the cytoplasmic side of the TM domain is not flat. With relatively longer helices, the cytoplasmic sides of TM3 and TM4 form a large empty space, which may be water accessible. On the contrary, in the cryo-EM model, with the C-terminal side titled, TM4 shares a length similar to TM1, TM2 and TM3, although TM4 is slightly longer. Therefore, the space is not observable in the cryo-EM model.

The loops connecting TMs 1 and2 (TM12 loop) and TMs 2 and 3 (TM23 loop) are also different. In the nAChRα7TM-5G, TM12 loop and TM23 loop are residue TLPAD and residue MPATS, respectively, which are also located on the homologous loop positions for WSA and GLIC. All of them contradict cryo-EM model of nAChR from

Torpedo. Compared to the cryo-EM model, both TM12 loop and TM23 loop shift to the N-terminus. One of the explanations is that nAChRα7TM-5G, WSA and GLIC represent the open state of nAChR, while the cryo-EM model represents a closed state.

It has been proposed that the TM1 helix in the nAChR has an irregular structure, which may be caused by the conserved prolines [90]. Pro-37 in nAChRα7TM and Pro-59 in WSA are the only conserved proline in TM1 among all the AChR and Cys-loop receptor members [89]. In the previous study of WSA, it was found that a clear kink near Pro-59 presents in the middle of the TM1 helix, separating TM1 into two parts, the N-terminal half and the C-terminal half of the TM1 helix. Dynamic analysis suggests that the Pro-59 may facilitate the motion of the C-terminal half of the TM1 helix and may be more important to the dynamics of the TM2 helix. Based on the CSI analysis on nAChRα7TM-5G, a clear kink can be also predicted in the TM1 helix. The residues GLNLEIPCS show different CSI values from the typical helical CSI values. Therefore, they are not in the helical conformations. Compared to the kink in the TM1 helix of WSA, the counterpart of nAChRα7TM-5G involves many more residues and is much more obvious.

Although the TM4 domain is always long among all the known structures of nAChR, the shape of TM4 is not the same. The TM4 helices in the cryo-EM model [7,8] and WSA are relative straight and less disturbed, compared to GLIC [9,11]. This is because there is a proline residue in the TM4 helix of GLIC and it bends the helix, while no proline presents in the TM4 helix of the cryo-EM model and its water-soluble analogue WSA. In the TM4 helix of nAChRα7TM-5G, the presence of Pro-153 disturbs the chemical shifts of surrounding residues. It can be predicted that there is a kink, which bends the TM4 helix of nAChRα7TM-5G. Therefore, the TM4 helix in nAChRα7TM-5G may have a similar shape as in GLIC.

3.2.9 Possible ion channel formation

It has been found that the segments of the TM2 domains of the human GlyR α1 subunit, in the same superfamily as nAChR, can form a functional homopentameric channel by themselves with reasonable conductance comparable to the authentic receptors [81,92-94]. Recently, fluorescence studies on the TM2 domain of nAChR also suggest that TM2 domains from different subunits such as α4 and β2 can form a heteropentameric channel [96]. In the nAChRα7TM-5G construct, the TM2 domain remains in the native sequence. It is highly possible that the nAChRα7TM-5G with the native TM2 domain can form a homopentameric channel.

The amide protons from NMR samples always undergo the chemical shift exchange process with water peaks (~4.6 ppm). This information could be used to probe the environment of the protein, which conversely give us the structure information. The NMR sample and experimental conditions for nAChRα7TM-5G are at pH 7.4 with a temperature of 45°C. Under the high pH and high temperature conditions, the water exchange process is more serious and can affect the amide proton chemical shifts in the HSQC spectrum and shift them to the upfield. The residues on the TM2 helix experience two distinct environments, the water-accessible environment and the non-water accessible environment. Most of the pore-lining residues are accessible to the water molecules, while other residues are not. Therefore, under the same experimental condition, the pore lining residues are affected much more by the water exchange process than others in the TM2 helix due to the ability of exchange between the pore lining residues and the water molecules. Additionally, the geometry of the pore can be predicted by the water accessibility. The residues in a large aqueous pore will undergo greater water exchange process than in a small one. In Fig. 3.2.8, the peaks in the HSQC spectrum of nAChRα7TM-5G are color-coded based on the domains they

belonged to. The peaks in the TM2 helix show larger chemical shift dispersion for the amide protons than others. The amide proton chemical shifts of the TM2 domain were plotted as a function of the residue numbers in Fig. 3.2.9. As mentioned before, most of the pore lining residues except L9' (L67) show relatively more upfield proton chemical shifts than their adjacent residues due to their particular environments. More interestingly, the residues close to the EC side in the TM2 helix show more upfield proton chemical shifts than the IC side, suggesting that C-terminal residues of the TM2 helix undergo more water exchange process than its N-terminal residues. This finding further suggests that N-terminus of the TM2 helix may form a narrower pore than its C-terminal counterpart does. It is consistent with the previous study on the Torpedo nAChR that the TM2 helices from the different subunits form a funnel-shaped channel with an ion selective filter on its IC side [97]. The gate of the pore for the α1 subunit from the nAChR in the Torpedo based on the cryo-EM model structure was identified on α-Leu 251 and α-Val 255 [7]. Residue L67 (L9') in the nAChRα7TM-5G, a homologue residue to α-Leu 251 in the cryo-EM model, shows the highest amide proton chemical shift, suggesting that L67 is well protected from the water molecules. Therefore, it can be predicted that there is also a hydrophobic gate located near L67 (L9') in the TM2 helix of the human nAChR α7.

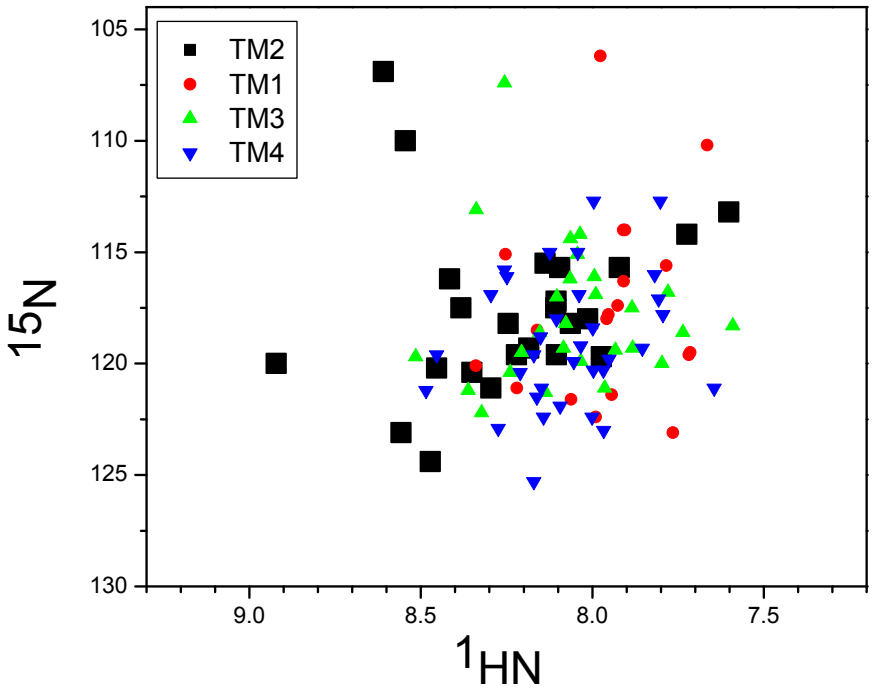

Fig. 3.2.8. Distribution map of each TM domain of nAChRα7TM-5G in a HSQC spectrum. The TM2 domain of nAChRα7TM-5G in ^{1}H-^{15}N HSQC spectrum shows a relatively large chemical shift dispersion.

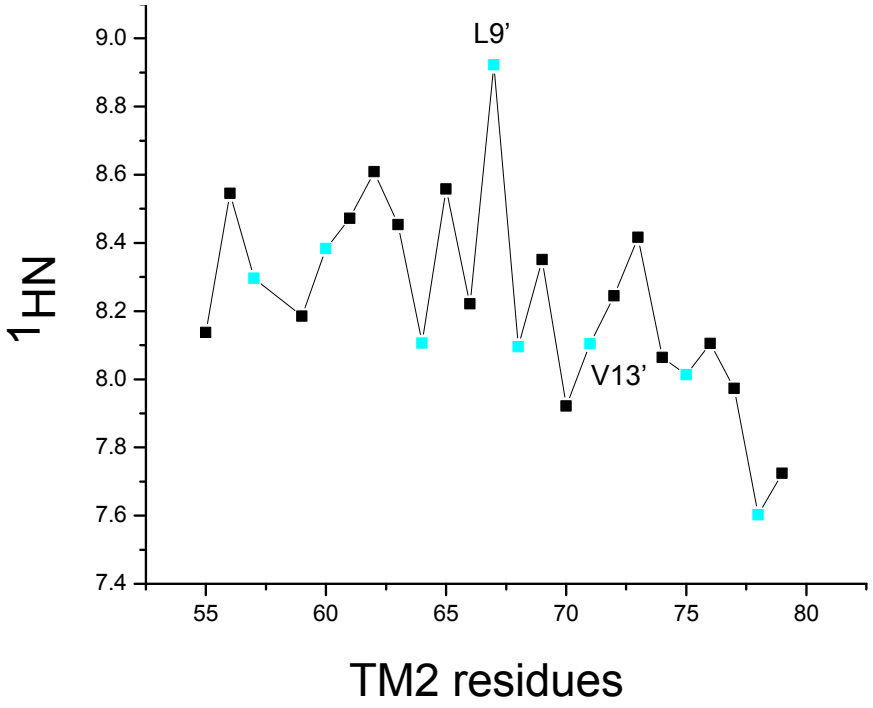

Fig. 3.2.9. **^{1}HN chemical shifts profile of the TM2 domain of nAChRα7TM-5G.** The amide proton chemical shifts (^{1}HN) of the TM2 domain of nAChRα7TM-5G were plotted as a function of the residue numbers. Most of the pore lining residues (Cyan) except L9' show relatively lower ^{1}HN than their adjacent residues. The proton chemical shifts of the EC side are lower than the IC side. Amide proton chemical shift analysis on the TM2 domain indicates TM2 domains may form a channel with the constriction site at L9'. The entire channel is in a funnel shape widely open on the EC side.

3.2.10 Unique backbone dynamics

The TM2 helix shows unusual dynamics, compared to others in Fig.3.2.5. In the hetNOE experiment, for each helix, the NOE value is similar except for the C-terminal half of the

TM4 helix, suggesting that the flexibility for each domain is comparable. However, in terms of the R_2/R_1 ratio, the value for the TM2 helix, ~25, is higher than others. Two possible reasons correspond to the high R_2/R_1 ratio, the conformational exchange or the chemical shift anisotropy. The TM2 helix has higher R_2 and lower R_1, and thereby, the chemical shift anisotropy is more possible contributing factor to the dynamics of the TM2 helix. In order to confirm this finding, CPMG R_2 dispersion measurements were performed [87,88]. There are no R2 dispersion curves identified for any residue in the TM2 helix. Therefore, the possibility of conformational exchange was rule out. As we mentioned above, the oligomerization of the native TM2 domains could lead the nAChRα7TM-5G to form a funnel-shape channel. The additional interaction along the TM2 helices may result in the chemical shift anisotropy for the nAChRα7TM-5G. If indeed, the nAChRα7TM-5G can form the homopentamer, then the R_2/R_1 ratio is too low for a typical globular protein with the molecular weight 85 kDa. In our previous study on the water-solubilized channel protein KcsA (WSK3), it also exhibits an unusual dynamic profile [57]. The nAChRα7TM-5G may experience the same situation as WSK3. A further analysis on the dynamics of the nAChRα7TM-5G will be continued.

Two prolines in the TM1 and TM2 domains not only break the helices to form a clear kink in terms of the structures, but also affect the dynamics of the TMs and cause the residues before and after the proline to behave differently in terms of the dynamics. The CSI values for them are still positive, except the residues near the kink, suggesting that they are in the helical conformation. In the TM1 helix, the R_2/R_1 ratio for the residues in the helical conformation before Pro-37 is ~8, which is lower than the ratio of the residues after the proline, ~15. A similar trend for NOE values was also observed. Both the low R_2/R_1 ratio and low NOE values indicate that the N-terminal side of the TM1 helix is more flexible than the C-terminal side. Although the TM1 helix in nAChRα7TM-5G does not connect with its native EC domain instead of a small fusion peptide for protein

purification purposes, the intrinsic flexibility of the N-terminal half of the TM1 helix may play a role in the signal transduction from the EC domain to the IC domain. Two distinct dynamic profiles can also be identified in the TM4 helix. The R_{ex} contributions to the relaxation of the C-terminal half of the TM4 helix were confirmed by the CPMG R_2 dispersion measurements.

Interestingly, the TM3 helix also has two distinct dynamics. In Fig. 3.2.5, the R_2/R_1 ratio for two regions in the TM3 helix are ~15 and ~8 respectively. In nAChRα7TM-5G, a glycine linker was used to replace the long IC loop. It is possible that this artificial linker makes the C-terminal side of the TM3 helix flexible. However, the Gly linkers have been successfully used in other proteins from our group and we have not yet observed this effect. Therefore, it could be also the intrinsic dynamics of the TM3 helix. As signal transduction is bidirectional, the signal from the IC domain is conducted through the TM3 helix to the TM2 helix and the EC domain. The intrinsic dynamics of TM3 may play an important role here.

3.2.11 Conclusion

Using the novel water solubilization approach, two new reconstituted proteins, human nAChRα7TM-5G and human nAChRα7TM-IC, were successfully expressed in E. coli. The expression levels for both of them are suitable for structure determination. Full spectrum assignment and dynamics analysis were completed for the nAChRα7TM-5G. The results indicate that the secondary structure of the nAChRα7TM-5G is consistent with GLIC and WSA, but different from the cryo-EM model for Torpedo nAChR, suggesting that the new reconstituted nAChRα7TM-5G and WSA may represent the same open state of nAChR as with GLIC. Two prolines residing in the middle of TM1 and TM4 disturbed the helix and made obvious kinks. Both the structure and the

dynamics were affected by two prolines. The partially flexible TMs near the EC side may facilitate signal transduction from the outside to the inside. The TM3 helix was also found to be partially flexible near the IC side, which may facilitate signal transduction from the inside to the outside. Without the spectrum assignment, the dynamics of nAChRα7TM-IC was analyzed by histogram method. By comparing the HSQC spectra and the backbone dynamics between nAChRα7TM-5G and nAChRα7TM-IC, the presence of the IC domain affect the dynamics of the TM domain.

CHAPTER 4

NMR STUDY OF INHALATIONAL ANESTHETIC MECHANISM

4.1 ANESTHETIC EFFECTS ON THE WATER SOLUBLE PROTEIN, FOUR-α-HELIX BUNDLE

This section has been published in *Biophys J* **94**, 4464-4472, (2008) as a full article. I am the first author. The language was directly taken from the paper.

4.1.1 Significance

A variety of small molecules, which have no common structural features and exist in different forms, can render people into a state of total unconsciousness, commonly known as general anesthesia. These small molecules are called general anesthetics. The anesthetics have been used since the 18th century; however, the molecular processes underlying this phenomenon remain unclear [21-27]. The current consensus about the anesthetic mechanism is the “protein theory”, which postulates that the anesthetics interact specifically with their target proteins. The competing “lipid theory”, which focuses on the anesthetic-induced changes in neuronal functions through nonspecific perturbation to membrane lipids in the central nervous system, remains viable [22]. Previous studies [31,32] have centered on the hypothesis that anesthetics occupy the hydrophobic pockets or cavities in the proteins to change the protein function. How

exactly it happens, however, is still a mystery.

The potential target proteins for anesthetics, ligand-gated ion channels, are membrane proteins, which are hard to study due to their intrinsic nature. The lack of structural information of ligand-protein complexes has impeded the progress of understanding as to how the anesthetics alter the biological function of protein. The water-soluble dimeric protein, (Aα_2-L1M/L38M)$_2$, was engineered to simplify this study by de novo design. The designed protein mimics ligand-gated ion channel proteins with a long hydrophobic core within a common four-α-helix bundle scaffold [98,99]. More importantly, this four-α-helix bundle has an anesthetic binding affinity in the range of clinical volatile anesthetic concentration. Therefore, it is regarded as a suitable model for the protein targets of general anesthetics [99,100]. We first completed the NMR structural and dynamical analysis of (Aα_2-L1M/L38M)$_2$ in the absence of anesthetic [34]. The apoprotein backbone structure was resolved to a root -mean-square deviation (RMSD) of 1.77 Å. As originally designed, two monomers of the helix-turn-helix motif form an anti-parallel dimer. The dimeric structure shows that two N-terminus domains from each monomer are held together and the same for two C-terminus domains by the ring stacking of F12 and W15 along the hydrophobic core and by a leucine zipper from complementary pairs of L4, L11, L18, and L25 from each monomer. By examining the high-resolution structure, we also identified a lateral access pathway near K47 between the two C-terminus domains in the dimer (helix 2 and helix 2′). This specific lateral access pathway facilitates the amphipathic anesthetic molecules to enter the hydrophobic core directly from the aqueous phase. Different from the initial design, in which two symmetrical anesthetic binding sites were intended between W15 and M38 [99], only one primary anesthetic binding pocket was identified within the hydrophobic core suggested by our NMR structure[34]. By determining the high-resolution structure of (Aα_2-L1M/L38M)$_2$ in the presence of halothane and comparing the structures and dynamics of

($A\alpha_2$-L1M/L38M)$_2$ in the presence and absence of a bound halothane molecule, we not only confirmed the binding sites of anesthetics in ($A\alpha_2$-L1M/L38M)$_2$, but also revealed that an interesting change in protein quaternary structure and in the overall dynamics of the protein in the presence of anesthetics. These results shed new light on how volatile anesthetics might potentially produce functional changes in proteins in general.

4.1.2 Materials and methods

($A\alpha_2$-L1M/L38M)$_2$ expression and purification, NMR sample preparation, and all NMR methods for structure determination have been described in detail in our previous paper [34]. Briefly, the conventional suite of 2D and 3D heteronuclear filtered experiments for spectral assignment and for TALOS dihedral angle constraints and NOESY distance restraints were carried out using the standard pulse sequences from the Bruker sequence library. ^{15}N- and ^{13}C-filtered NOESY was measured with a mixing time of 120 ms. The NOESY assignment was done initially using the Cyana program and then improved manually [74]. Because of the high helical content in ($A\alpha_2$-L1M/L38M)$_2$ and the characteristic short- and mid-range NOE connectivity to define the helix regions in the structure, the long-range inter-subunit NOEs from residues on the opposite ends of the helices can be distinctively and positively identified by the chemical shift matching with an exclusion strategy, without resorting to mixing labeled and unlabeled samples and using specific filtering or purging pulse sequences. In the halothane titration experiments, the ($A\alpha_2$-L1M/L38M)$_2$ concentration was 500 μM in 10%D_2O/90%H_2O with 0.4% 2,2-dimethyl-2-silapentane-5-sulfonic acid (DSS) and 0.02% NaN_3. Neat halothane was added in 0.3 μl increments using a Hamilton microsyringe. Because evaporation during the repeated titration procedure could not be controlled, the halothane concentrations in the NMR sample were measured by the halothane ^{1}H intensities after

each titration step and then calibrated against the final titration point, at which both ^{1}H and ^{19}F intensities were measured, with the ^{19}F intensity calibrated against known concentrations of trifluoroacetate solutions [44,45]. Based on this calibration, the halothane concentrations in the titration experiment ranged from 0 to 2.2 mM, at which point the chemical shift change started to plateau. At very low halothane concentrations, the halothane peak was too weak to be accurately measured. This technical difficulty prevents the site-specific K_d values from being accurately quantified. Therefore, the chemical shift change as a function of halothane titration is used in this study only as a qualitative indication of the halothane binding site(s). To estimate the magnitude of K_d at the binding site, non-linear regression with the following equation was used to fit the chemical shift changes as a function of halothane concentration, including the point with zero halothane [101,102]:

$$\Delta_{obs} = \frac{\Delta_{\max}}{2[P]_0}\left\{(K_D + [A]_0 + [P]_0) - \sqrt{(K_D + [A]_0 + [P]_0)^2 - 4[A]_0[P]_0}\right\} \qquad (4.1.1)$$

where $[A]_0$ and $[P]_0$ are the anesthetic and protein concentration, respectively, and Δ_{max} is the limiting chemical shift difference.

Except for temperature dependent amide proton exchange measurements, for which HSQC experiments were performed at 25, 30, 35, and 40°C to determine the temperature coefficient for hydrogen bonding constraints, all other NMR experiments were conducted at 35°C. Most of the NMR experiments were carried out using a Bruker Avance 600 spectrometer. For selected experiments, Bruker Avance 700 and 800 spectrometers were used.

Two different types of experiments were conducted to determine the halothane binding to $(A\alpha_2\text{-L1M/L38M})_2$ by measuring the inter-molecular NOE. The conventional two-dimensional ^{1}H-^{1}H NOESY was used to measure the coherent NOE build-up, whereas selective saturation transfer was used to measure the non-coherent cross

relaxation between the two interacting molecules. The ^{1}H saturation transfer NOE experiments used tr-HSQC-based pulse sequence. Selective saturation of halothane proton resonance was achieved using an IBURP2 pulse train (80-ms shaped pulses with an inter-pulse delay of 4 μ s and a total duration of 1.6 s) preceding the tr-HSQC sequence. Interleaving on-resonance and off-resonance (–5000 Hz) spectra were acquired to determine the saturation-transfer effects between halothane and individual residues.

The halothane effects on backbone dynamics were measured in the presence of 2.2 mM halothane and compared with the results obtained without halothane as described in our previous paper [34]. The ^{15}N R_1 and R_2 relaxation and ^{15}N-{^{1}H} heteronuclear NOE (hetNOE) data were analyzed using the Lipari-Szabo model-free approach with the ModelFree program [51,103,104].

The R_2 relaxation dispersion spectra were acquired at 35°C on Bruker 800 MHz NMR spectrometers with ^{15}N operating frequencies of 81.09 MHz. The spectra were recorded with 1024 t_2 and 128 t_1 data points, with spectral widths of 10 ppm for ^{1}H and 24 ppm for ^{15}N dimensions. The relaxation-compensated constant-time Carr-Purcell-Meiboom-Gill (CPMG) sequence was used [70,71]. The total CPMG constant-time delay was set to T_{CPMG} = 60 ms (two 30 ms CPMG periods). The spectra were collected with 10 different CPMG field strengths, measured by ν_{CPMG} of 33.33, 66.67, 100.00, 133.33, 200.00, 266.67, 333.33, 400.00, 500.00, and 666.67 Hz, where $\nu_{CPMG} = 1/(4t_{CPMG})$, and the separation between the centers of successive refocusing 180° pulses equals $2t_{CPMG}$. An additional reference spectrum was collected by removing the CPMG periods in the pulse sequence. A relaxation delay of 2.5 s was used. The ^{1}H chemical shifts were referenced to DSS resonance at 0 ppm, and the ^{15}N chemical shifts were indirectly referenced [105].

To analyze transverse relaxation dispersion, the intensities of cross-peaks in 2D R_2 relaxation dispersion spectra with a given CPMG field strength were measured and then converted into the ^{15}N transverse relaxation rate constant R_2 and associated uncertainties according to the well-established relations [106]:

$$R_2\left(\nu_{\mathrm{CPMG}}\right) = -\frac{1}{T_{\mathrm{CPMG}}}\ln\left(\frac{I\left(\nu_{\mathrm{CPMG}}\right)}{I_0}\right) \tag{4.1.2}$$

and

$$dR_2(\nu_{CPMG}) = \frac{1}{T_{CPMG}}\left[\left(\frac{dI(\nu_{CPMG})^2}{I(\nu_{CPMG})^2}\right)+\left(\frac{dI_0^2}{I_0^2}\right)\right]^{1/2} \tag{4.1.3}$$

where $I(\nu_{CPMG})$ and I_0 are the intensities for a given cross-peak, and $dI(\nu_{CPMG})$ and dI_0 the noise levels, in the dispersion spectra with and without the CPMG pulse trains, respectively. Three exchange parameters, R_{20}, Φ_{ex}/k_{ex} and k_{ex} were calculated using the fast exchange limit approximation ($\Delta\omega = \omega_a - \omega_b < k_{ex}$) with two exchanging sites to fit the R_2 dispersion profile $R_2(\nu_{CPMG})$ by [107]:

$$R_2(\nu_{CPMG}) = R_{20} + \frac{\Phi_{ex}}{k_{ex}}\left(1 - \frac{4\nu_{CPMG}}{k_{ex}}\tanh\left(\frac{k_{ex}}{4\nu_{CPMG}}\right)\right) \tag{4.1.4}$$

in which R_{20} is the R_2 without exchange (in the limit of $\nu_{CPMG} = \infty$), $\Phi_{ex} = (\omega_a - \omega_b)^2 p_a p_b$, p_i and ω_i are the populations and Larmor frequencies for the nuclear spin in site I; and k_{ex} is the exchange rate. It should be noted that k_{ex} describes exchange rate on the μs-ms timescale and is not the same as the phenomenological R_{ex} term used in the Model-Free approach [108,109].

4.1.3 Specific anesthetic binding

Two independent NMR methods were used to determine possible site-specific interactions between anesthetics and $(A\alpha_2\text{-L1M/L38M})_2$. The first was an anesthetic

titration experiment, in which the dependence of chemical shifts of individual residues in $(A\alpha_2\text{-L1M/L38M})_2$ was measured as a function of halothane concentration. Fig. 4.1.1 A depicts the representative overlaps of HSQC contour plots for four residues where the backbone amide ^{1}H or ^{15}N chemical shifts are profoundly affected by varying concentration of halothane. Non-linear fitting with Eq. 4.1.1, including the point without halothane, yield an estimate of K_d at W15 to be 2.6 ± 1.7 mM (R^2 = 0.996). To visualize the overall halothane effects on HSQC chemical shifts, the normalized changes in the weighted average of the ^{1}H and ^{15}N chemical shifts with and without 2.2 mM halothane are color-coded onto the protein structure (see below for structural determination), as shown in Fig. 4.1.1 B. Clearly, the most sensitive region is near W15. To further confirm that the concentration-dependent chemical shift changes are indeed due to halothane binding instead of other non-specific effects, a second, independent NMR method was used to measure the saturation transfer between halothane and various residues [110]. The percentage change in tr-HSQC peak intensity from the saturation transfer difference spectroscopy is mapped on the structure (Fig. 4.1.1 C), showing again the specific interaction between halothane and the protein near W15, A22, and A44. Neither chemical shift titration nor the saturation transfer difference spectroscopy showed significant halothane effects on M38, confirming the prediction from a computer simulation [111] and our own structural study [34] that M38 is not directly involved in the halothane binding. Thus, the 3.5-fold enhancement in the halothane binding affinity due to L38M mutation must result from allosteric effects.

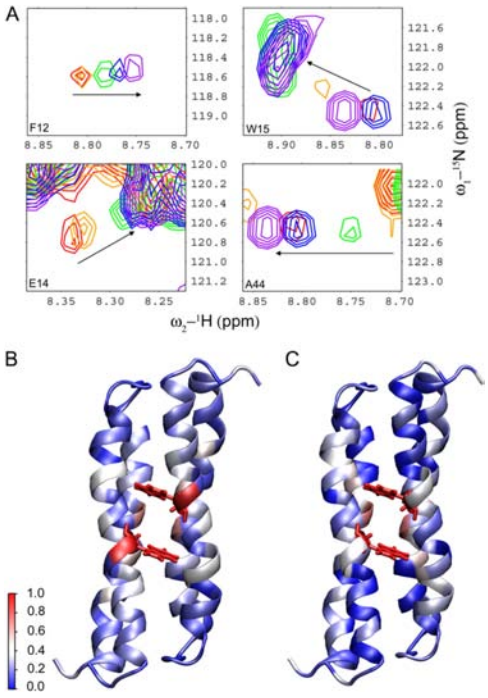

Fig. 4.1.1. Halothane binding to the four-*α*-helix bundle (Aα_2-L1M/L38M)$_2$. (**A**) Overlap of HSQC contour plots for residues F12, E14, W15, and A44 in response to halothane titration, which was done by adding neat halothane to the NMR sample in 0.3-*μ*l increments. The same contour scale is used for all peaks in each plot to show relative intensities. The peak colors in the order of red, orange, green, blue, and purple indicate increasing concentrations of halothane from 0 to 2.2 mM. In the contours for W15 and A44, the shifted A44 peaks (Blue and Purple) overlap with the unshifted W15 peak (Red). Notice that W15 shows a large chemical shift jump at the first titration point and greatly increased intensities at higher halothane concentrations. (**B**) Individual residues in the NMR-determined structure are color-coded according to their normalized chemical shift sensitivities to halothane titration, with blue to red representing the least to most sensitive, respectively. (**C**) Normalized saturation transfer NOE is mapped onto the NMR structure of (Aα_2-L1M/L38M)$_2$ using the blue-white-red color code. This figure was reproduced from *Biophys J* **94**, 4464-4472, (2008)

4.1.4 High-resolution structure with a bound halothane

Parallel to the studies without anesthetics as described in the previous study [34], the same batch of the expressed proteins was used in the present study to determine the $(A\alpha_2\text{-L1M/L38M})_2$ structure in the presence of halothane. The same suite of heteronuclear, multidimensional NMR experiments was performed for assignment and structure determination. The NOE connectivity and chemical shift index (CSI) pattern resemble those shown in Figure 3 of the previous study [34]. Again, two helical segments, from R5 to E27 and from E36 to R58, are readily identifiable in the NOE connectivity and CSI. The two termini and the glycine linker between the two helices appear to be unstructured based on the CSI and dynamics results (see below). The statistics of the 20 structures with the lowest target function is given in Table 4.1.2. The overall backbone RMSD is 1.72 ± 0.39 Å; the backbone RMSD of the helical regions is 1.05 ± 0.28 Å. The insignificant difference in RMSD between the apo and halothane-bound protein structures is likely due to the difference in the spectral quality and the different numbers of total constraints available for the structural calculation. In the presence of halothane, at least two inter-molecular NOE peaks were positively identified in 2D NOESY between halothane and L18 and A44 (Fig. 4.1.3). Structural calculations with the inclusion of a halothane molecule clearly define the halothane binding pocket, which is shown to be bordered by the aromatic side chains of W15 and the hydrophobic side chains of L18 and A44 in the dimeric form (see Fig. 4.1.4 E). Fig. 4.1.4 A and Fig. 4.1.4 B show the superposition of the structures with and without halothane in the monomer and dimer form, respectively, exhibiting nearly the same secondary and tertiary monomer structures and pronounced quaternary structural changes after the addition of halothane. The side-chain arrangements surrounding the primary halothane binding site without and with a bound halothane are depicted in Fig. 4.1.4 C and D, respectively, and the packing

details of halothane interaction with the protein at the binding site are shown in Fig. 4.1.4 E. While the halothane orientation in the pocket is not fixed, there is a clear orientation preference in binding interaction in the bundle of structures (Fig. 4.1.5) due to cation-pi type of interaction between the partial positive charge on the hydrogen atom of halothane [112] and the aromatic ring of W15. Among the 20 lowest-energy structures, 12 have a halothane orientation as shown in Fig. 4.1.4E, with halothane's Br and Cl each interacting with one of the two hydrophobic side chains of L18, and the hydrogen and the CF_3 moiety orienting towards the W15 aromatic ring and the A44 side chain, respectively. In the remaining 8 structures, the halothane flips about 180° to point the proton to the aromatic ring of the other W15.

Table 4.1.2. Structural statistics of 20 ($A\alpha_2$-L1M/L38M)$_2$ structures with halothane

NMR structure	**Statistic**
Restraints per monomer	
NOE distances	
Intraresidue	144
Short range (i-j = 1)	128
Medium range (1 < i-j ≤ 4)	96
Long range (i-j > 4)	15
Dimer (intermonomer)	6
Dihedral angles	72
Hydrogen bonds	20
Residual upper limit constraints violations number > 0.5 Å	0
Residual dihedral angle constraints violations number > 5°	0
Backbone RMSD	
Residues 5-27, 36-58, 205-227, 236-258	1.05 ± 0.28 Å
All residues (1-62, 201-262)	1.72 ± 0.39 Å
Heavy atom RMSD	
Residues 5-27, 36-58, 206-226, 236-258	1.56 ± 0.32 Å
All residues (1-62, 201-262)	2.07 ± 0.36 Å
Ramachandran plot	
Residues in most favored regions	91.0%
Residues in allowed regions	8.9%
Residues in disallowed regions	0.2%

This table was reproduced from *Biophys J* **94**, 4464-4472, (2008)

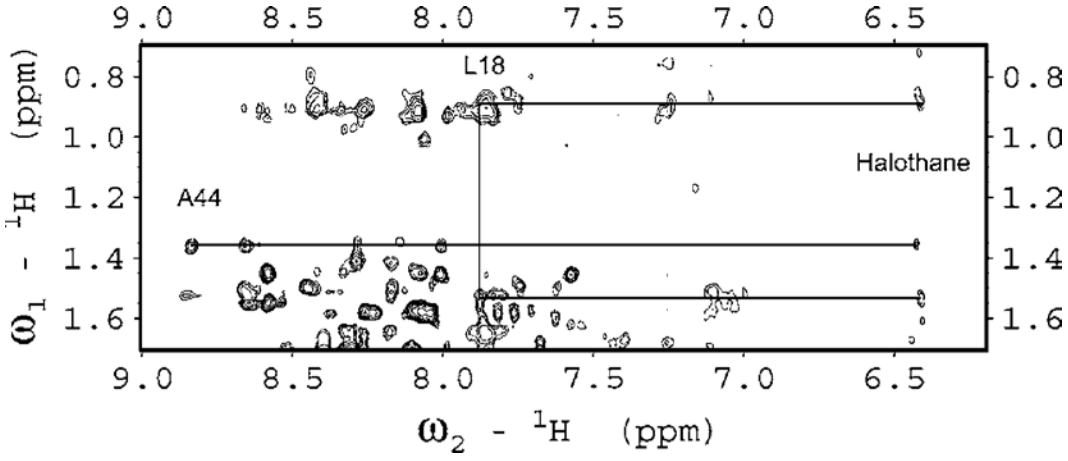

Fig. 4.1.3. A contour plot of a ^{1}H-^{1}H 2D NOESY spectrum. It shows unambiguous crosspeaks between halothane resonance at 6.4 ppm and the side chains of L18 and A44. This figure was reproduced from *Biophys J* **94**, 4464-4472, (2008)

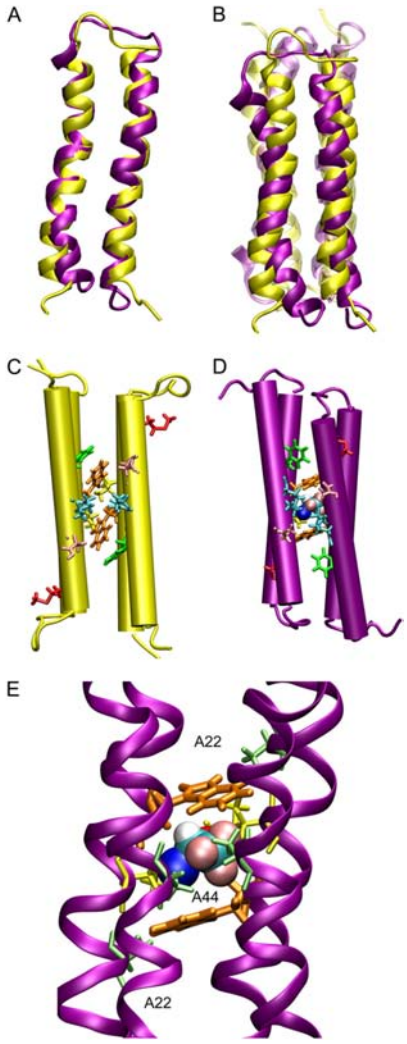

Fig. 4.1.4. **Comparison of high-resolution NMR structures of (Aα_2-L1M/L38M)$_2$ determined with and without halothane.** (**A**) The monomer structure determined in the presence of halothane (Purple) is superimposed onto the structure of the apoprotein (Yellow). (**B**) Superposition of the dimer structures. Notice the quaternary structural changes and supercoiling of the helices in the presence of halothane. (**C**) Side view of hydrophobic core of the four-*α*-helix bundle in the absence of halothane. (**D**) Side view of hydrophobic core of the four-*α*-helix bundle with a halothane bound in the primary binding site. (**E**) Detailed interactions between halothane and the residues surrounding the anesthetic binding pocket. In C, D, and E, important side chains are shown in licorice

representation: W15 (Orange); K47 (Cyan); E43 (Pink); F12 (Green); and A22 and A44 (Lime). The halothane molecule is shown in VDW spheres: C (Cyan); H (White); Cl (Blue); Br (Red); and F (Pink). This figure was reproduced from *Biophys J* **94**, 4464-4472, (2008)

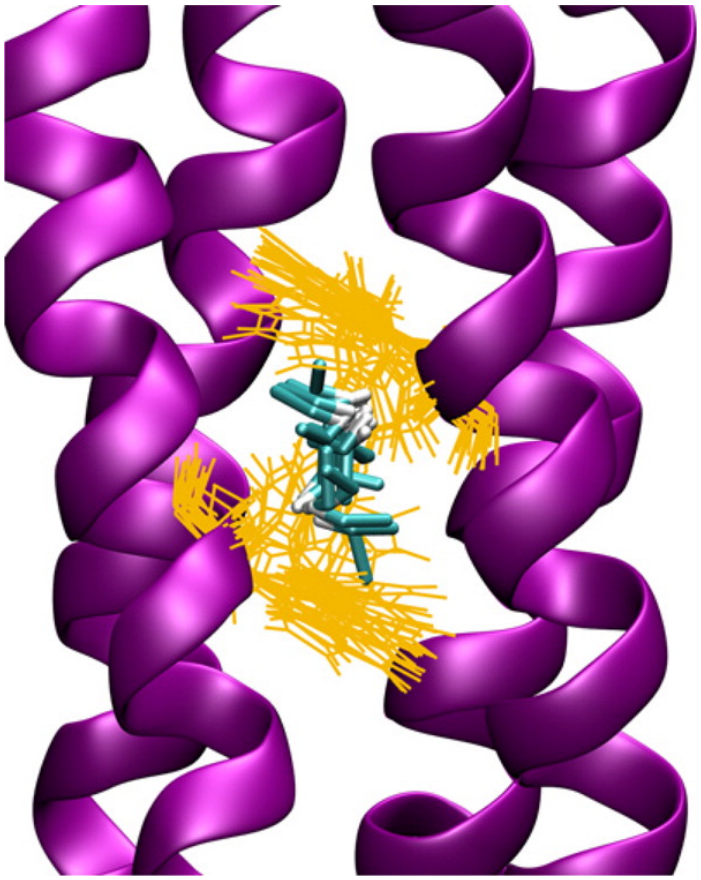

Fig. 4.1.5. **Orientations of halothane molecules in the binding pocket.** A bundle of 20 halothane molecules (C-C bond (Cyan); C-H bond (White)) is depicted in relation to the bundle of W15 side chains (Orange) in the 20 lowest energy structures. Although the halothane orientation is not fixed, the hydrogen, with partial positive charge, has the

tendency to point to the aromatic ring of W15 due to cation-pi type of interaction. This figure was reproduced from *Biophys J* **94**, 4464-4472, (2008)

4.1.5 Anesthetic effects on the backbone dynamics

The backbone dynamics was determined by analyzing the R_1, R_2, and hetNOE of the backbone amide ^{15}N with and without halothane using the Model-Free approach [103,104]. In addition, the conformation exchange on the μs-ms timescale was examined using the CPMG R_2 dispersion measurements. The effects of halothane binding on the local and global dynamics are depicted in Fig. 4.1.6 and Fig. 4.1.7. Fig. 4.1.6 shows the conventional Model-Free analysis, depicting the generalized order parameter, the correlation time of the fast local motion (τ_e), the exchange contribution to the relaxation (R_{ex}) [113], and the model number used to fit the data. As in the case without anesthetics, the two termini and the loop regions are significantly more flexible with order parameters lower than 0.5. The loop region does not meet the basic Lipari-Szabo assumption and can only be fitted with Model 5. In the presence of halothane, the residues in the immediate vicinity of the binding site showed slightly elevated order parameters, becoming more ordered than without halothane. The most profound changes are seen in the global distribution of the R_{ex} term in the helical regions. Overall, R_{ex} is reduced upon halothane binding, suggesting a lesser degree of conformational exchange. The involvement of non-zero R_{ex} terms in many residues is confirmed by the R_2 dispersion measurements, which are independent of the model selection or the spectral density mapping. As shown in Fig. 4.1.7, many residues exhibit the R_2 dependence on the CPMG frequencies. The ΔR_2 values, which are estimated from the R_2 values at the two extreme CPMG frequencies achievable with our NMR hardware, display the same distribution pattern as R_{ex} along the protein sequence (Fig. 4.1.7B). It should be noted

that the ΔR_2 measured by the relaxation dispersion underlies the phenomenological non-zero R_{ex} term in the Model-Free analysis, albeit the two are not expected to be identical [108] because the two experimental methods are sensitive to motions on different timescales. Nevertheless, the overall trend is clear, and the binding of halothane reduces the conformational exchange on the global scale. The significance of this reduction in R_{ex} (or ΔR_2) will be discussed below. As in the case without halothane, two residues, M38 and C41, still show a larger R_{ex} than other residues, albeit halothane reduced the R_{ex} values by a factor of 2. There seems to be also a slight tendency that halothane binding makes the loop region more ordered as shown in the S^2 values. This is supported by the slightly elevated R_2 values for some of the loop residues in the R_2 dispersion measurements (e.g., G30 in Fig. 4.1.7A). However, since the R_2 dispersion method is prone to artifacts when R_2 is not significantly larger than R_1 [114], which is indeed the case for the loop residues, the small difference in the R_2 dispersion with and without halothane should be taken with caution for the loop and terminal residues. Using the same method as in the previous paper [34] to search for the best-fitted τ_m value, the ModelFree calculations yielded the global tumbling time of 5.00 ± 0.08 ns, in agreement with the global tumbling time of the apo protein.

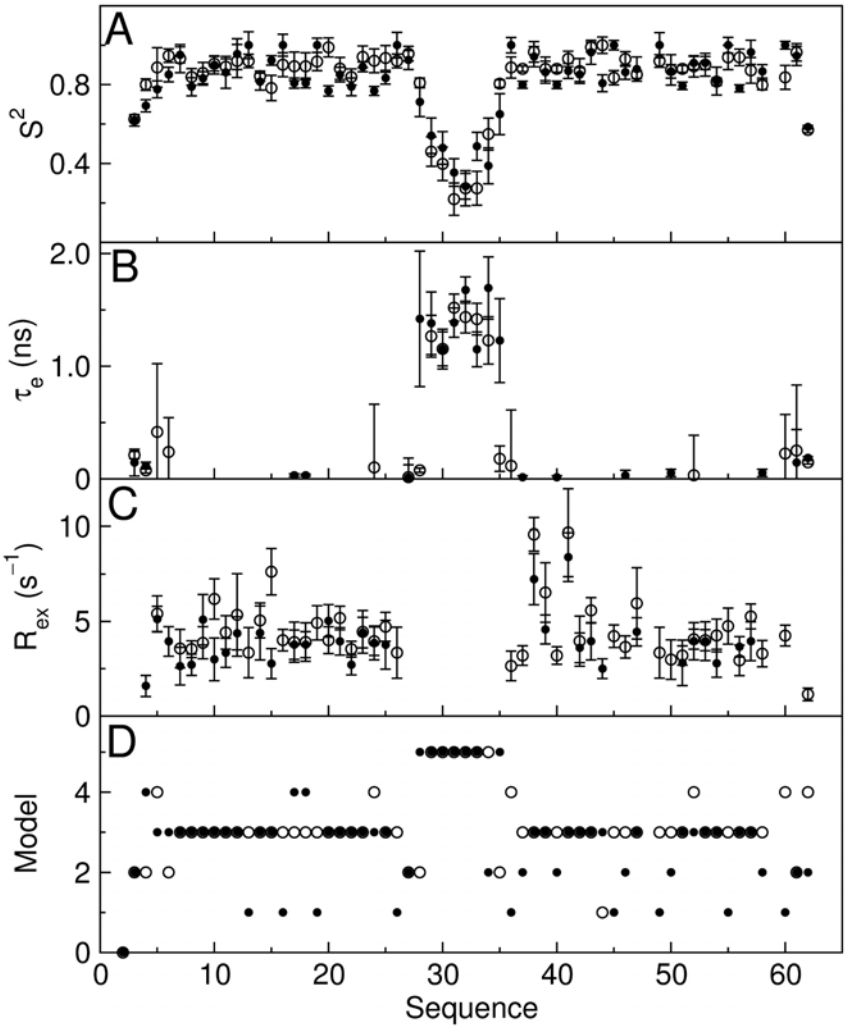

Fig. 4.1.6. **Comparison of (Aα_2-L1M/L38M)$_2$ dynamics in the presence and absence of halothane binding.** (**A**) The squared order parameter (S^2), (**B**) the local correlation time (τ_e), (**C**) the exchange contribution (R_{ex}), and (**D**) model number used in the model-free analysis are plotted as a function of the residue numbers of the four-α-helix bundle, depicting the dynamics in the absence (○) and presence (●) of 2.2 mM of halothane. Notice that halothane stabilizes overall protein motion as evidenced by the increased S^2 in the immediate vicinity of W15 and the globally reduced R_{ex} terms at many residues. This figure was reproduced from *Biophys J* **94**, 4464-4472, (2008)

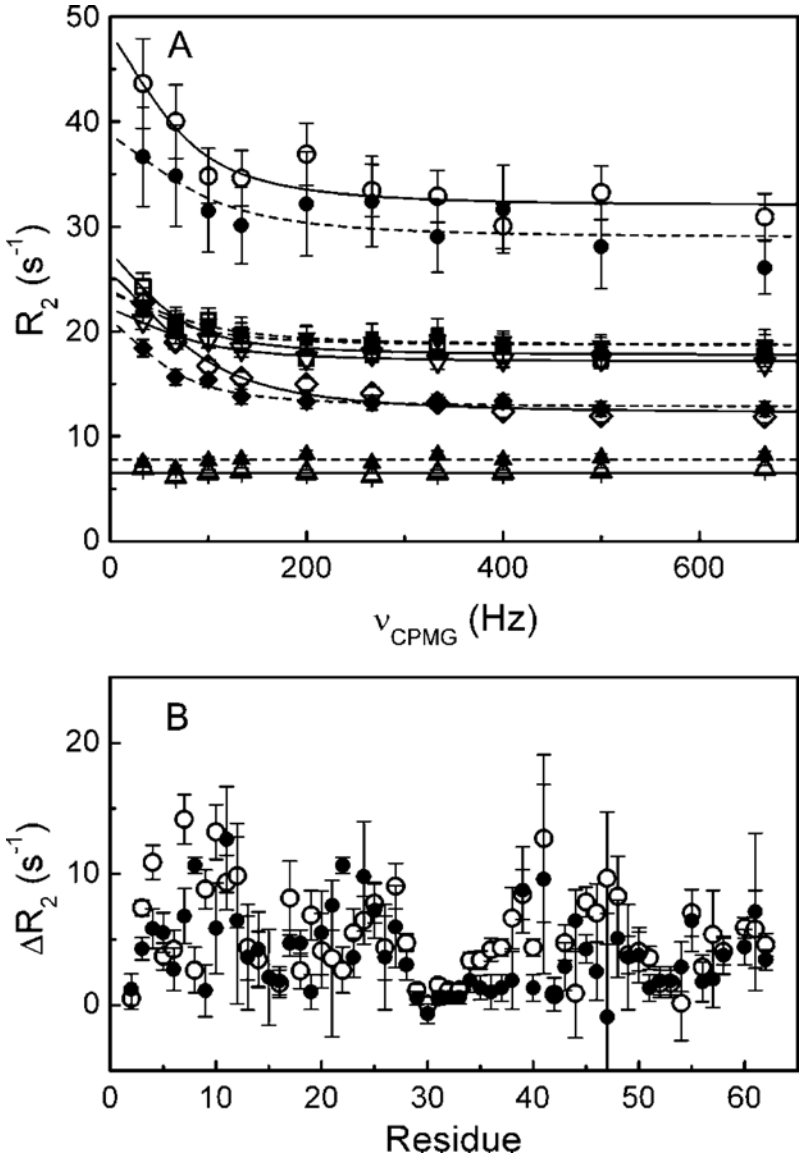

Fig. 4.1.7. **Backbone ^{15}N relaxation dispersion profile of (Aα_2-L1M/L38M)$_2$.** (**A**) Representative plots of the ^{15}N transverse relaxation rate, R_2, as a function of the CPMG field strength, ν_{CPMG}, for L4 (◊), G30 (Δ), M38 (□), C41 (○), and E50 (∇) in (Aα_2-L1M/L38M)$_2$ without (Open symbols) and with (Solid symbols) 2.2 mM halothane at 18.8 T (800 MHz). Uncertainties in R_2 were determined from the signal/noise ratio using Eq.

4.1.3. The $R_2(\nu_{CPMG})$ dispersion profiles for L4, M38, C41, and E50 demonstrate the contribution of conformation exchange to the ^{15}N transverse relaxation rate. The solid and dash lines are the best fit to the data for the protein in the absence and presence of the anesthetic, respectively, using Eq. 4.1.4. G30 shows no conformation exchange and is presented here as a reference. (**B**) Values of $\Delta R_2 = R_2(\nu_{CPMG}=33.3\ \text{Hz}) - R_2(\nu_{CPMG}=666.7\ \text{Hz})$ are plotted as a function of residue numbers in $(A\alpha_2\text{-L1M/L38M})_2$ without (○) and with (●) halothane at 18.8 T. Most residues show a decreased ΔR_2 in the presence of halothane, indicating that halothane suppresses the global conformational exchange in the protein. This figure was reproduced from *Biophys J* **94**, 4464-4472, (2008)

4.1.6 Primary anesthetic binding site in the four-α-helix bundle

Four-α-helix bundle is a common scaffold found in many important functional proteins. For example, the TM domains of anesthetic-sensitive superfamily of Cys-loop receptors are composed of pseudosymmetric pentamers of four-α-helix bundles. Serving as a model for anesthetic protein targets, $(A\alpha2\text{-L1M/L38M})_2$ was designed with a few iterations of design changes aimed at improving the binding affinity for volatile anesthetics [98,99]. Our structural studies of $(A\alpha2\text{-L1M/L38M})_2$ in the absence of a bound anesthetic, as detailed in previous study [34] , suggested a primary binding site between the two W15 side chains in a dimer and an amphipathic lateral access pathway from the aqueous phase through the flexible C-terminal helix interface into this binding site. These findings are somewhat unexpected because the intended binding sites by design are closer to the two ends of the hydrophobic core of the four-helix bundle, and thus

there should be two sites that are mirror images of each other. In the present structural study with halothane, we confirmed that the main halothane binding site is indeed sandwiched between the two W15 residues. The chemical shift changes in response to titration with varying concentrations of halothane, the saturation transfer experiment, and 2D NOESY experiment all indicate that the preferred halothane interaction site are in the middle section of the four-helix bundle, instead of between W15 and M38 as the latest iteration of design had intended. The apparent dissociation constant for halothane binding to $(A\alpha2\text{-}L1M/L38M)_2$ is estimated to be in the submillimolar range based on the fluorescence quenching on $(A\alpha2\text{-}L38M)_2$ [99]. Our chemical shift titration experiments, which measure the halothane influence on the protein backbone amide nitrogen and proton chemical shifts, probe the relative involvement of individual residues in the anesthetic binding. Since the side chains at the binding site are more directly involved in the interaction than the backbone, the site-specific Kd determined from the backbone chemical shifts does not necessarily reflect the true binding affinity at the interaction site. Nevertheless, the approximate Kd value obtained from the chemical shift titration measurements is consistent with the apparent Kd from the fluorescence quenching experiments [99].

It is interesting to note that when the experimental structures were used in a docking search for potential halothane binding sites, we found that the site between two W15 side chains is highly preferred (~98%) but not exclusive in the apoprotein. In contrast, with the lowest energy structure determined in the presence of halothane, Autodock [115] found the halothane-binding site to be exclusively between W15 side chains. The estimated free energy of binding from Autodock is –3.35 kcal/mol (4.89 mM), which is in agreement with the experimental titration data.

4.1.7 An induced fit for anesthetic binding

Detailed structural analysis revealed that the monomeric helix-turn-helix fold is very similar in the two structural bundles with and without a bound anesthetic, as shown in Fig. 4.1.4 A. When fitting the helical regions of the monomers, the RMSD between the two structural bundles is ~1.5 Å, which is only slightly larger than the RMSD of the monomers among the 20 lowest-energy structures of each bundle. Thus, halothane binding did not greatly affect the monomer (secondary and tertiary) structure. As shown in Fig. 4.1.4 B, the most significant structural change upon halothane binding is the quaternary association of the four helices in the dimer. There is a vertical shift of the monomers relative to each other by approximately half a helix turn and a super-coil twisting of the helices when a halothane molecule is bound at the site between the two W15s. These quaternary structural changes removed the asymmetry found in the apoprotein due to wider separation between helix 2 and helix 2′. The halothane-induced quaternary changes led to a better fitting between halothane and the amphipathic cavity of the binding site. Measured by the Q-SiteFinder program [116], the binding cavity bordered primarily by the side chains of W15, L18, and A44 (Fig. 4.1.4, D and E) reduces its size from ~381 $Å^3$ in the structures without halothane to ~162 $Å^3$ in the structures determined with halothane (after removing halothane from the structure). The latter value better matches the molecular volume of halothane (~130 $Å^3$ [117,118]). Thus, our structural data suggest an induced fit between halothane and its binding site. The high structural flexibility of the apoprotein, the lateral opening between helix 2 and helix 2′ for direct access to the binding site from the aqueous phase, and the quaternary structural re-arrangement for an induced fit can all contribute to an increase in the binding on-rate. As evidenced in the packing between the halothane molecule and the residues surrounding the binding pocket (Fig. 4.1.4 E), the interaction at the binding site is both

hydrophobic and electrostatic in nature. Optimization of the fitting in the binding site and the closure of the lateral pathway as a result of the twisting of helices 2 and 2′ relative to helices 1 and 1′ will likely decrease the binding off-rate, thereby achieving the high-affinity specific binding of halothane in this designed protein.

4.1.8 Implications of anesthetic effects on local and global dynamics

In addition to the structural changes, halothane binding to the four-α-helix bundle also resulted in profound changes in the protein dynamics, not only locally but also globally at residues remote from the binding site. This finding is important because protein function always involves protein motion. Thus, the four-α-helix bundle offers more than just a structural model. The characteristics of halothane effects on the dynamics of (Aα2-L1M/L38M)$_2$ may have universal implications on how anesthetic binding to protein ultimately leads to changes in protein functions [23,24,26,27,119-121].

In the absence of halothane, (Aα2-L1M/L38M)$_2$ appears extremely dynamic on the NMR timescale [34]. Model-free analysis showed that many residues in the helical regions contain the Rex contribution to the backbone amide 15N relaxation, suggesting the presence of a conformational exchange process at these residues [104,112,122]. This finding is confirmed in this study by the R2 dispersion measurements. By comparing the model-free analyses of the relaxation data with and without halothane as shown in Fig. 4.1.6 and of the R2 dispersion data as shown in Fig. 4.1.7, it is clear that halothane binding not only stabilizes the residues in direct contact with halothane, but also reduces the Rex (or ΔR2) on a global scale. The most noticeable Rex changes in (Aα2-L1M/L38M)$_2$ are at W15 and near M38 and C41. In the apoprotein, W15 signal is relatively weak (hence precluding the R2 dispersion measurement), presumably due to an intermediate exchange. Indeed, when the site is not occupied, there is a large degree

of orientation freedom for the W15 side chains within the hydrophobic core. The NMR structure of the apoprotein suggests that W15 side chains tend to swing toward F12 to form an aromatic ring stack within the long stretch of hydrophobic core, leaving a large space between the W15 side chains to accept halothane. When the site is occupied, the two W15 side chains are locked into a parallel configuration (Fig. 4.1.4, D and E) with reduced local flexibility, as indicated by the increased order parameter at W15 and nearby residues. This not only changes the chemical shift but also increases the intensity of W15 in HSQC (Fig. 4.1.1 A). One of the direct consequences of the reduced W15 side chain flexibility—in addition to the induced fitting for high-affinity halothane binding as discussed above—is the largest decrease of the Rex term associated with W15 (Fig. 4.1.4 E).

As discussed previously [34], another dynamic hotspot in $(A\alpha 2\text{-}L1M/L38M)_2$ is located near M38 and C41. Both of these residues showed a large Rex term compared to the rest of the protein when no halothane is bound. It is known that a point mutation at residue 38 from Leu to Met can result in a 3.5-fold increase in halothane binding [99]. Such an increase could be due to changes in either structure or dynamics, or both. Structurally, Leu-Met mutation has been shown to be well tolerated by numerous studies [99,100]. Because M38 (or L38) is not even part of the halothane binding site according to the NMR structure, local steric effects in a structural sense are unlikely to be the cause of the increased binding affinity after the mutation. In searching for other possible explanations, we believe that global dynamics is an obvious candidate, given the unusual dynamics property near the mutation site. The allosteric coupling between W15 and M38 is clearly evident in the large reduction of the Rex term at M38 and C41 on halothane binding at W15. This suggests that residue 38 is situated at a pivotal point to control the global dynamics of the protein. Although Leu and Met are close on the

hydrophobicity scale [123], methionine's side chain is longer and narrower than leucine's side chain. Residue 38 is at the first heptad g position in the first turn of helix 2 after the flexible glycine linker. From the apoprotein structure, it can be seen clearly that the M38 side chain is sandwiched between the adjacent L37 and the more distant E27 and A23, all of which congregate at the two ends of the flexible glycine loop. The long and linear M38 side chain can either point toward the glycine loop or toward the lateral aqueous phase, depending on the glycine loop orientation. If L38 resumes the same local structure as M38, its side chain has predictably less orientation freedom relative to the glycine loop due to its bulkier branching methyl groups. Therefore, it is conceivable that the mobility at residue 38 in relation to the flexible linker is critical to the opening and closing of the lateral pathway between helix 2 and helix 2′. The higher halothane binding affinity found in the L38M mutation can be explained by the increased on-rate, whereas the off-rate should be dictated by the W15 ring stacking and induced fit after halothane has occupied the binding site, which would be similar irrespective of L38 or M38.

In support of this viewpoint is the dynamics change at E43 and K47, where sizeable Rex terms can be seen when halothane is absent. After halothane binding, the high-resolution NMR structures reveal that the quaternary structural changes shift E43 of one monomer to almost the same level as K47 of the other monomer. The super-coil twisting brings E43 at heptad b position closer to K47 at heptad e position of the opposing helix. The electrostatic interaction stabilizes E43 and closes the interface (and thus the lateral access pathway) between helices 2 and 2′. As a consequence, both E43 and K47 show a significantly reduced Rex term after halothane binding.

Our results suggest an interesting interplay between structural fitting and dynamical contribution to anesthetic binding at protein targets. From a pure structural viewpoint without considering protein mobility, the space between two W15 side chains in the apoprotein would not seem ideal for halothane binding. As discussed above, there

is a large discrepancy between the cavity size (381 $Å^3$) and the volume of the anesthetic molecule (130 $Å^3$) for a snug structural fit. However, the opening between helices 2 and 2′ and their conformational flexibility create an easy access directly from the aqueous phase to this site. The intrinsic global mobility of this dimeric protein and the interaction-induced structural fitting between halothane and the key residues at the binding site make this site more favorable than other potential sites. For example, the minor sites found by the Autodock program in the apoprotein between F12 and F52 would be theoretically suitable for halothane binding. These minor sites, however, are not occupied with high affinity due to divergence of the structural and dynamical factors at these sites. As discussed in the previous study [34], the side chain of F52 seems to be "out of place" in the aqueous phase. Although the local rotational freedom of F12 and F52 side chains would allow halothane to bind, the absence of a consequent structural change to secure the binding would render any halothane occupancy between F12 and F52 short-lived. Similarly, Q-SiteFinder revealed two amphipathic pockets bordered mainly by A8, F12, L51, L54, and R58 of one monomer and L26, E27, L37, M38, and C41 of the other monomer, along with three residues from the glycine loop. These pockets have a volume of 303 $Å^3$ but show no interaction with halothane experimentally and yield no population by flexible docking. The controlling factor in this later case is likely to be the protein dynamics. Thus, when searching for important anesthetic interaction site or sites in neuronal proteins to understand the molecular mechanisms of general anesthesia, one must analyze and differentiate the structural and dynamical contributions to the functional consequences of anesthetic-protein interactions.

4.1.9 Conclusion

In conclusion, we identified a novel anesthetic binding site in the designed four-α-helix bundle $(Aα2\text{-}L1M/L38M)_2$ by solving its high-resolution structure in the presence of halothane. Different from the designed locations, this site becomes preferred over other potential sites, including the two designed sites, for anesthetic binding after the interaction between the anesthetic and protein has occurred. The intrinsic global dynamics characteristics of this protein make the induced fitting possible, and the induced structural fitting upon anesthetic binding, in turn, modifies the local and global dynamics of the protein. For neuronal proteins, the latter aspect is likely to account for functional change of the proteins, ultimately leading to the anesthetizing effects. It is consistent with what we have proposed more than a decade ago, based on the analysis of xenon [25], that some molecules would not normally be classified as general anesthetics due to their lack of basic properties found in common anesthetizing agents, but they nevertheless can produce anesthesia by gaining these properties after interactions with their targets takes place (e.g., induced dipole in xenon). We now show an example of a related phenomenon, namely, that the protein targets can be turned into relevant to anesthetic action only after the interaction between anesthetic and protein has taken place. The value of the designed four-α-helix bundle as a model for anesthetic targets lies not only in its structural resemblance to the ubiquitous scaffold found in many functional proteins, but also in its dynamics characteristics that are perhaps more relevant to the functional response to anesthetics [23,24].

4.2 ANESTHETIC EFFECTS ON THE MEMBRANE PROTEIN, MISTIC

This section has been published in *J Phys Chem B* **112**, 14312-14318, (2008) as a full article. I am the co-author. I rewrote it based on the paper.

4.2.1 Significance

The current consensus about the mechanism of general anesthesia is that inhaled anesthetics act on the membrane proteins in the central nervous system (CNS) and affect neural networks. A wealth of molecular biology and electrophysiology studies have demonstrated that neurotransmitter-gated ion channels, particularly Cys-loop receptors [21,30], are plausible targets for general anesthetics. These ion channels are sensitive to volatile anesthetics at clinically relevant concentrations. However, it is still unclear where anesthetic binding sites reside and whether the induce fit between anesthetics and their target proteins, such as what we have found in the four-α-helix bundle [34], is still applicable for anesthetics interacting with proteins. Furthermore, we have recently proposed that anesthetics exert their action on proteins through disrupting the modes of global motion essential to protein functions [24].

To experimentally validate our hypothesis, directly obtaining structural and dynamic information of neuronal proteins with atomic resolution is often challenged by technical obstacles, such as limitations of protein size and low expression yields, for nuclear magnetic resonance (NMR) spectroscopy or X-ray crystallography. Instead, a membrane model protein (membrane integrating sequence for translation of integral membrane protein constructs, Mistic) that mimics certain properties of Cys-loop channel receptors was investigated in the absence and presence of general anesthetics by NMR spectroscopy. Mistic shares four-α-helix bundle structural motif with other TM domains of Cys-loop receptors. It has been shown that general anesthetics are presumed to binding

to the TM domain of Cys-loop receptors [124]. And a de novo designed prototype protein with specific anesthetic binding pocket [32,34,98] and a natural soluble protein (ferritin) [125], both of them with such a special four-α-helix bundle motif, served previously as models for investigating the structural basis of inhaled anesthetic binding in proteins. Mistic was chosen not only because it naturally folds into a four-α-helix bundle motif in micelles, but also the structure of Mistic has been previously determined by NMR spectroscopy in lauryl dimethylamine oxide (LDAO) micelles [47]. High-quality NMR spectra of Mistic facilitate us to explore molecular details of anesthetic and Mistic interaction at atomic resolution. The information obtained from these studies could be applicable for understanding molecular insight on anesthetics in much more complex membrane proteins, neurotransmitter-gated ion channels and further validate our working hypothesis that inhaled general anesthetics act on proteins via altering protein motions, especially motions in the flexible loops, which connects different TM helices.

Halothane binding sites were identified mostly in the interfacial loop regions. Although halothane had little effect on Mistic structure, R_2 relaxation dispersion experiments revealed that halothane affected Mistic's motion on the microsecond-millisecond time scale. Compared to the absence of anesthetics, halothane can affect the equilibrium of chemical exchange in some residues. It is also shown that the motion of the microsecond-millisecond time scale was suppressed and disappeared for several residues. Most residues show the obvious chemical shift changes in the presence of halothane, while their dynamics were modulated by halothane at the same time. It indicates that halothane modulates the dynamics of the protein through directly interacting with these residues. In addition to the direct interaction, allosteric modulation by halothane was also found to contribute to dynamics changes. For example, I52 and Y82 do not experience chemical shift changes but show the dynamics changes. In conclusion, general anesthetics could act on the target protein by modulating its motion

on microsecond-millisecond time scale. The most profound region is located in the flexible loops, which connect with different TM helices. Interestingly, the corresponding loop region is critical for signal transduction in Cys-loop receptors. And many biochemical events occur on microsecond-millisecond time scale. Therefore, we propose that anesthetics modulate the microsecond-millisecond time scale motion that is correlated with protein function and it may be a critical step in the mechanisms of anesthesia.

4.2.2 Materials and methods

The gene-encoding Mistic was cloned from B. subtilis into the expression vector pTBSG1 (a gift from Prof. Timothy A. Cross' laboratory at Florida State University). Mistic was expressed in strain BL21(DE3) CodonPlus cells (EMD biosciences) using the Marley protocol [126]. Typically, expression was induced with 0.2 mM isopropyl β-d-1-thiogalactopyranoside and kept in M9 minimal medium at 12 °C for about 80 h. The protein was purified using published procedures [47]. A yield of 120 mg of purified Mistic was obtained from each liter of M9 minimal media. In order to extend the stability of Mistic samples, Mistic was exchanged into DPC during purification. The samples for NMR experiments typically contained 0.5 mM of either 15N-labeled or 13C/15N-labeled Mistic, 30 mM DPC, 0.2 mM dithiotreitol, 50 mM KCl, and 10 mM potassium phosphate buffer at pH 6.0.

All ^{1}H, ^{15}N, and ^{13}C NMR experiments were performed at 30 °C on Bruker Avance 600 or 700 or 800 MHz NMR spectrometers equipped with cryoprobes (Bruker Instruments, Billerica, MA). The ^{1}H chemical shifts were referenced to the 2,2-dimethyl-2-silapentene-5-sulfonate resonance at 0 ppm, and the 15N/13C chemical shifts were indirectly referenced. 19F NMR experiments were performed on a Bruker Avance 600

spectrometer with a Bruker TXO probe to determine halothane concentrations in reference to a solution with 10 mM trifluoroacetic acid (TFA). Although the chemical shifts assignments of Mistic in LDAO were done previously [47] and the $^{1}H-^{15}N$ TROSY-HSQC spectra of Mistic in DPC showed high similarity to that in LDAO, we repeated the same two-dimensional (2D) and three-dimensional (3D) NMR experiments [47] for the 13C and 15N chemical shift assignments of Mistic in DPC. A series of $^{1}H-^{15}N$ TROSY-HSQC spectra were collected on samples with five different halothane concentrations, ranging from 0 to 13 mM, to determine site-specific dissociation constants. The CBCA(CO)NH and HBHA(CO)NH spectra were acquired in the absence and presence of halothane so that the chemical shifts of Cα, Cβ, Hα, and Hβ at these two different conditions were obtained for comparison. $^{1}H-^{15}N$ residual dipolar couplings (RDCs) of Mistic were measured using a TROSY-IPAP-HSQC pulse sequence with 1024 (^{1}H) × 256 (^{15}N) complex points. A weak alignment of 15N-labeled Mistic in DPC micelles was achieved in both compressed and stretched charged polyacrylamide gel. The degree of alignment for each sample was checked using one-dimensional (1D) 2H NMR experiments.

To confirm anesthetic direct interaction with Mistic, ^{1}H saturation transfer difference (STD) NMR [127] was performed on a 0.5 mM 15N-labeled Mistic sample in 30 mM DPC in the presence of 10 mM halothane. As a control, the same experiment was also performed on a similar sample but without Mistic. The spectra were obtained in an interleaved manner using irradiation of 50 ms Gaussian pulses applied on-resonance at 0.58 ppm, corresponding to Mistic methyl protons, and off-resonance at 40 ppm. The pulse sequence utilized the WATERGATE water suppression and spoil sequence to destroy unwanted magnetization [128]. A series of STD spectra were acquired within a range of saturation times: 0.5, 1, 3, 5, 10, 20, and 40 s. Each spectrum had 64 scans with a relaxation delay of 40 s. The STD ($\Delta I = I_{off} - I_{on}$) was calculated by subtraction of

the intensities of the on-resonance peak (I_{on}) from those of the off-resonance peak (I_{off}) [40,129].

To characterize the dynamic property of Mistic, spin−lattice (R_1) and spin−spin (R_2) ^{15}N relaxation rate constants were measured with 512 (^1H) × 128 (^{15}N) complex points using standard pulse sequences with echo−antiecho gradient selection [130]. Nine (ranging from 10−1800 ms) or 10 (16−160 ms) variable delays were used for the R_1 or R_2 measurements, respectively. The effective transverse relaxation rate was also measured using relaxation-compensated Carr−Purcell−Meiboom−Gill (CPMG) experiments as a function of CPMG field strength (ν_{CPMG}) [71,109]. The ^{15}N R_2 relaxation dispersion data are suited to determine Mistic's conformation exchange on the microsecond−millisecond time scale in the presence and absence of halothane. The R_2 relaxation dispersion profiles were recorded at two different magnetic field strengths corresponding to ^1H frequencies of 600 and 800 MHz. The experiments were performed in a constant time manner (T_{CP} = 60 ms) on uniformly ^{15}N-labeled Mistic samples. The CPMG field strength, ν_{CPMG}, was varied to 33.33, 66.67, 100.00, 133.33, 200.00, 266.67, 333.33, 400.00, 500.00, and 666.67 Hz.

All NMR data were processed using NMRPipe [72] and analyzed with Sparky [73]. The chemical shift assignments were accomplished with the aid of AutoAssign [131] and manual comparison to the assignments of Mistic in LDAO [47]. The structure of Mistic in DPC micelles was obtained through refinement of the lowest-energy structures (PDB: 1YGM) of Mistic in LDAO micelles [47] using dihedral angle restraints obtained from Cα and Cβ chemical shift index (CSI) processed using Talos [75] and RDC data of helical regions obtained from two different alignment mediums. The refinement used the slow cooling simulated annealing protocol in Xplor-NIH [132]. The axial (Da) and rhombic (R) components of the alignment tensor in RDC experiments were determined using the histogram method [133], producing Da = −10.8 and R = 0.23 for samples in compressed

gel and Da = −10.0, R = 0.27 for samples in stretched charged gel, respectively. A total of 100 structures were produced in the refinement, and half of them with lower energies were used for an averaged structure. The best-fit comparison between experimental RDCs and the refined structures were performed using the program MODULE 1.0 [134]. ^{15}N relaxation dispersion data were analyzed using Eq. 4.2.1, which encompasses all chemical exchange timescales: [135]

$$R_2 = [R_{20} + (k_{ex}/2) - v_{CPMG}\cosh^{-1}(D_+\cosh(\eta_+) - D_-\cos(\eta_-))] \quad (4.2.1)$$

where $D_\pm = 1/2(\pm 1 + (\psi + 2\Delta\omega^2)/(\psi^2 + \xi^2)^{1/2})$, $\eta_\pm = (v_{CPMG}/2(2)^{1/2})(\pm\psi + (\psi^2 + \xi^2)^{1/2})^{1/2}$, $\psi = k_{ex}^2 - \Delta\omega^2$, $\xi = -2\Delta\omega(p_a k_{ex} - p_b k_{ex})$, R_{20} is the intrinsic transverse relaxation rate, k_{ex} is the exchange rate, Δω is the difference of chemical shifts between exchange sites a and b, the population of site a is denoted by $p_a = (1 - p_b)$, vCPMG = 1/(2τ), and τ is the time between centers of successive 180° pulses in the CPMG pulse sequence.

4.2.3 Halothane interaction site in Mistic

Halothane and Mistic direct interaction was confirmed by the STD experiments shown in Fig. 4.2.1. A halothane peak obviously appeared in STD spectra in the presence of Mistic (fig. 4.2.1A), while in the absence of protein the halothane peak cannot be observed in the same experimental conditions (fig. 4.2.1B). The on-resonance saturation frequency was set at 0.58 ppm, which is a frequency far away from halothane proton but near the methyl group of the protein side chain. The halothane binding sites in Mistic were studied by halothane titration experiments, shown Fig. 4.2.2.

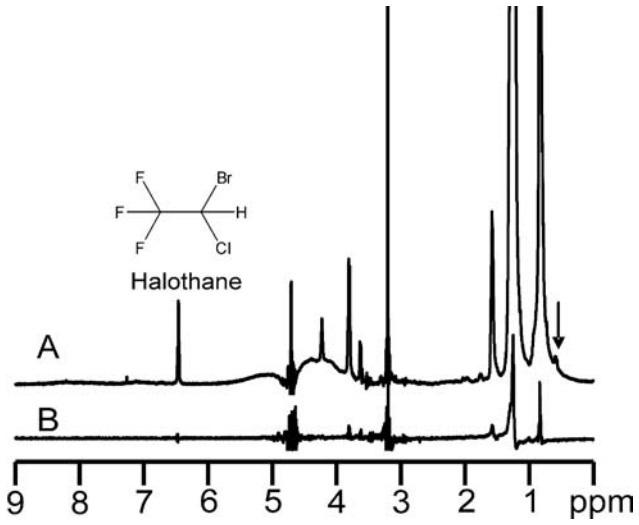

Fig. 4.2.1. Halothane Mistic interaction. ^{1}H STD NMR spectra of 10 mM halothane (resonance at 6.48 ppm) in (**A**) 30 mM DPC with 0.5 mM Mistic and (**B**) 50 mM DPC without Mistic. The arrow indicates the frequency for on-resonance saturation at 0.58 ppm that is near the Hδ resonance of Leu and Ile residues in Mistic. Note that the halothane signal was not observed in panel B under the same NMR conditions as in A, but without Mistic, indicating a direct interaction between halothane and Mistic. A stick chemical structure of halothane is inserted for reference. This figure was reproduced from *J Phys Chem B* **112**, 14312-14318, (2008)

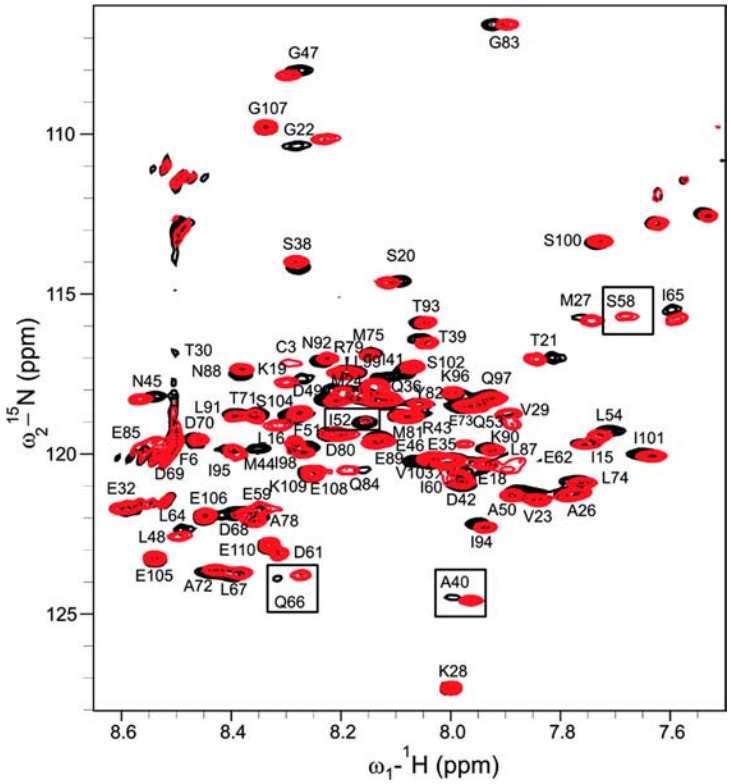

Fig. 4.2.2. NMR mapping of halothane effects on Mistic. Overlay of ^{1}H−^{15}N TROSY-HSQC spectra of 0.5 mM Mistic in 30 mM DPC micelles in the absence (Black) and presence (Red) of 10 mM halothane. The spectra were acquired at 30 °C. Despite many residues being undisturbed by the addition of halothane, some residues experienced significant chemical shift changes and/or intensity changes of their resonance signals. A few examples are highlighted in small boxes. This figure was reproduced from *J Phys Chem B* **112**, 14312-14318, (2008)

A number of residues showed profound chemical shift changes in the presence of halothane. For some residues, such as A40 and Q66, both chemical shifts and peak intensity changed after the addition of halothane. The S58 signal became much stronger, while the I52 peak intensity became much weaker. The peak intensity changes suggest that there may be the dynamic modulation in the region where the residue resided. Fig. 4.2.3 highlights Mistic residues that experienced obvious changes in chemical shift (HN > 0.05 ppm, Cα and Cβ > ± 1 ppm, Hα and Hβ > ± 0.1 ppm) upon halothane titration. The chemical shifts of most residues in helices were insensitive to anesthetics, except for some residues in the middle of α2 helix or adjacent to the loop regions. And both N- and C-terminal residues of Mistic do not respond to the addition of anesthetics, suggesting they may be buried in the similar hydrophobic environment as most helical residues do. It was confirmed by detergent exchange experiments. Most helical residues and both N- and C-terminal residues were insensitive to the different types of detergents. In contrast to less sensitive helical residues, all loop residues were more or less perturbed by halothane. Thee loop residues were identified to be located in the aqueous phase in the micelle, because they are sensitive to the head group of the detergents. A40 and M44, near to the kink in α2 helix, were affected by halothane, suggesting they may form a specific pocket for anesthetics.

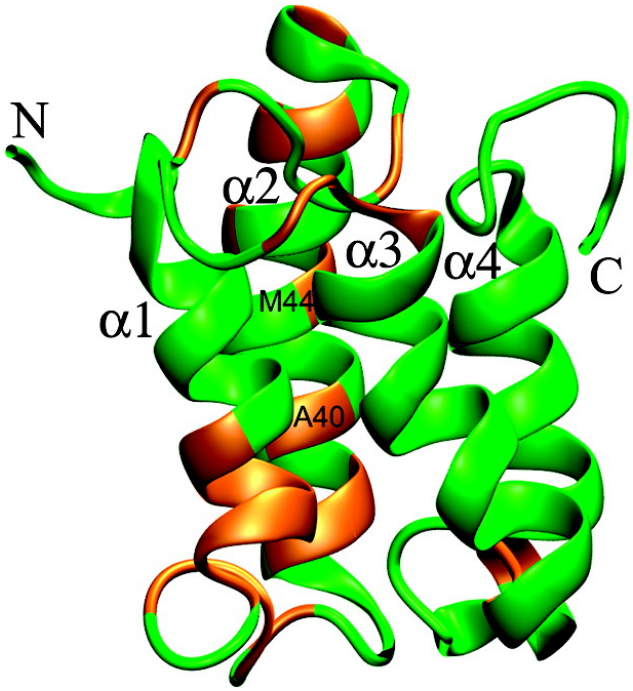

Fig. 4.2.3. Halothane interaction sites in Mistic. The residues whose chemical shifts were significantly perturbed by halothane are highlighted in orange color. The four TM helices are marked as α1−α4. This figure was reproduced from *J Phys Chem B* **112**, 14312-14318, (2008)

Halothane dissociation constants in the loop regions were determined. Halothane interaction with Mistic loop residues at aqueous interface of the micelle indicates that general anesthetics prefer to the amphipathic environment, water−lipid interfaces [25,40,42]. As we know, protein loops play a certain role in the protein function. The role will be more critical, when the loop is located in the aqueous phase. For example, a point mutation introduced in the TM2-3 loop in the α 1 subunit of the GABA receptor can prohibit the correct communication between the TM domain and the EC domain, which

further affect the channel conductivity [136]. Halothane prefers to interfering with the loop regions in Mistic, which suggests that anesthetic act on the protein through modulating the residues having important function such as loop residues. The significance of this finding lies not only in revealing the nature of anesthetic interaction sites, but also in suggesting potential anesthetic modulation to protein regions at the water-lipid interface that play critical roles in protein functions.

4.2.4 Halothane had minimal anesthetic effect on Mistic structure

The structure of Mistic in DPC micelles was obtained through refinement of Mistic structure in LDAO [47] by using the RDC constraints of Mistic in DPC. The generated structure of Mistic in DPC has a similar folding as original Mistic in LDAO.

The addition of halothane into Mistic in DPC micelle did not change the overall structure of Mistic. The comparison of the CSIs of Cα, Cβ, and Hα chemical shifts in the absence and presence of 10 mM halothane indicates that general anesthetics do not alter the secondary structure of Mistic, shown in Fig. 4.2.4. Halothane effect on Mistic tertiary structure was examined via measuring backbone RDCs of Mistic in the absence and presence of 5 mM halothane. Only a small change observed after addition of halothane, shown in Fig.4.2.5. It suggests that the overall tertiary structure of Mistic is well preserved upon the addition of halothane.

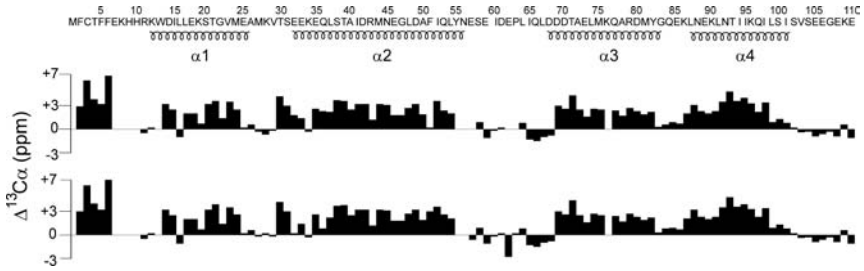

Fig. 4.2.4. **Halothane effects on the secondary structure of Mistic.** The similarity of ^{13}Cα CSI of Mistic residues in the absence (top) and presence (bottom) of 10 mM halothane indicated that halothane does not interfere the secondary structure of Mistic. The Cα chemical shifts were referenced with respect to random coil values at 0 ppm. This figure was reproduced from *J Phys Chem B* **112**, 14312-14318, (2008)

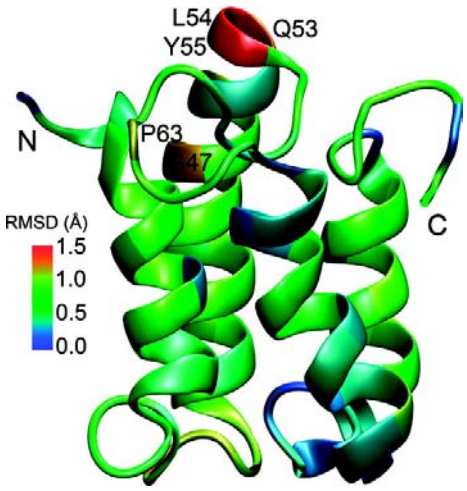

Fig. 4.2.5. Refined structure of Mistic in DPC on the basis of RDC NMR measurements. The RMSD (Å) of Mistic structure in the absence and presence of 10 mM halothane is presented using a color scale. Residues that showed the largest RMSD are labeled. This figure was reproduced from *J Phys Chem B* **112**, 14312-14318, (2008)

Previously studies [24,40,42] show that structures of TM peptides remained unchanged in the presence of general anesthetics. It has been also reported that the overall structures of several globular proteins do not change with general anesthetics at low millimolar concentrations [28,125,137,138]. Mistic in micelles shares the same structural motif, four TM domains, with a subunit in the Cys-loop receptors. Therefore, the structure of Mistic insensitivity to anesthetics may also exist in the Cys-loop receptors. It suggests that anesthetic action on these Cys-loop receptors is unlikely through significantly altering receptor structures.

4.2.5 Halothane had profound effects on MISTIC motion

Halothane-induced changes in Mistic motion were confirmed by at least two experimental evidences. First, in HSQC experiment, some residues showed profound changes in their peak intensities (or line widths) after adding halothane. Second, in ^{15}N relaxation dispersion experiments indicated that halothane can modulate the motion on the microsecond-millisecond time scale in some regions of Mistic.

As shown in Fig. 4.2.2, residues S58, Q66, and A40 peak intensities increased (peak line width decreased) in the $^{1}H-^{15}N$ HSQC NMR spectra in the presence of halothane. It is also happened to several Cα resonance peaks such as loop residues S58−L67, which changed from weak to strong after the addition of halothane, as shown in Fig. 4.2.4. In contrast, I52 peak intensity decreased significantly after the addition of halothane (Fig.4.2.2). Backbone dynamics in the picosecond-nanosecond time scale, longitudinal (R1) and transverse (R2) relaxation rates, as well as 1H−15N heteronuclear NOE, show that they are not sensitive to anesthetics. It indicates that anesthetics have almost no effect on the motion of protein in the picosecond-nanosecond time scale.

However, the peak intensities for several residues were observed, which suggests that anesthetics may modulate on the motion of the protein in different time scale such as microsecond-millisecond time scale. In this case, anesthetic protein interaction may interfere with the conformational exchange process in Mistic. In order to know whether anesthetics potentiate or inhibit the exchange process, quantitative measurements were achieved through ^{15}N R_2 CPMG relaxation dispersion experiments.

For the majority of Mistic residues, their transverse relaxation rates were not affected by a systematic variation of CPMG pulse. This indicates that most residues do not involve the motion on the microsecond-millisecond time scale. However, R_2 dispersion curves were observed for a number of residues located at the loop 23 (S58, D61, Q66, and D68), loop12 (V29), helix α2 (T39 and N45), and loop34 (Y82). The R_2 dispersion profiles for two representative residues, D61 and N 45, in the absence and presence of 10 mM halothane was shown in Fig. 4.2.6. It is clear that halothane inhibited the exchange contribution to R_2 on residue N45 and suppressed the exchange on D61. It is consistent with what we concluded based on the changes of peak intensities and line widths. The R_2 relaxation dispersion experimental data was fitted to Eq. 4.1.1 by using a two-site exchange model, which provided us estimated exchange parameters, including the difference of chemical shifts between two exchanging sites (Δω), the exchange rate (k_{ex}), the relative population of a conformation (p_a or p_b), and the intrinsic transverse relaxation rate (R_{2o}). Table 4.2.7 summarizes these fitting parameters in the absence and presence of 10 mM halothane. The population of the major conformation, p_a, was close to, or over, 90% and it increased 0−3% after the addition of halothane. Δω remained the same for most residues, which is consistent with the result that Mistic structure remained the same in the presence of halothane.

Table 4.2.7. ^{15}N Relaxation Dispersion Parameters[a] of Exchanging Residues of Mistic in the Absence and Presence of 10 mM Halothane

Residues		R_{ex} (s^{-1})[b]	R_{20} (s^{-1})	k_{ex} (s^{-1})	p_a	$\Delta\omega$ (s^{-1})
V29	−	7.8	16.4±0.7	532±290	0.97±0.02	508±59
	+	4.2	16.9±0.2	154±22	0.97±0.02	523±69
T39	−	3.9	20.7±0.3	1455±296	0.98±0.08	588±65
	+	NA[c]				
N45	−	5.2	27.3±0.4	635±197	0.92±0.02	258±28
	+	NA				
I52	−	6.2	23.7±0.4	722±200	0.90±0.02	241±30
	+	ND[d]				
S58	−	6.4	15.8±0.3	217±83	0.91±0.03	205±12.5
	+	4.8	17.2±0.5	551±270	0.91±0.03	189±33
D61	−	26.7	13.5±0.9	468±144	0.89±0.02	529±26
	+	17.9	13.2±0.5	199±22	0.90±0.01	550±50
Q66	−	12.9	17.0±0.7	376±99	0.90±0.03	362±18
	+	12.0	17.1±0.6	174±33	0.92±0.01	486±74
D68	−	3.5	17.9±0.2	279±120	0.97±0.02	317±25
	+	3.3	16.3±0.1	482±84	0.97±0.02	300±15
Y82	−	11.5	25.0±1.1	267±148	0.87±0.17	244±24
	+	NA				

a Equation 1 was used for fitting of these parameters.

b $R_{ex} = R_2(\nu_{cp} \rightarrow 0) - R_2(\nu_{cp} \rightarrow \infty)$.

c NA: no relaxation dispersion.

d ND: the signal was too weak to determine relaxation dispersion parameters.

Absence (−) and presence (+) of halothane

This table was reproduced from *J Phys Chem B* **112**, 14312-14318, (2008)

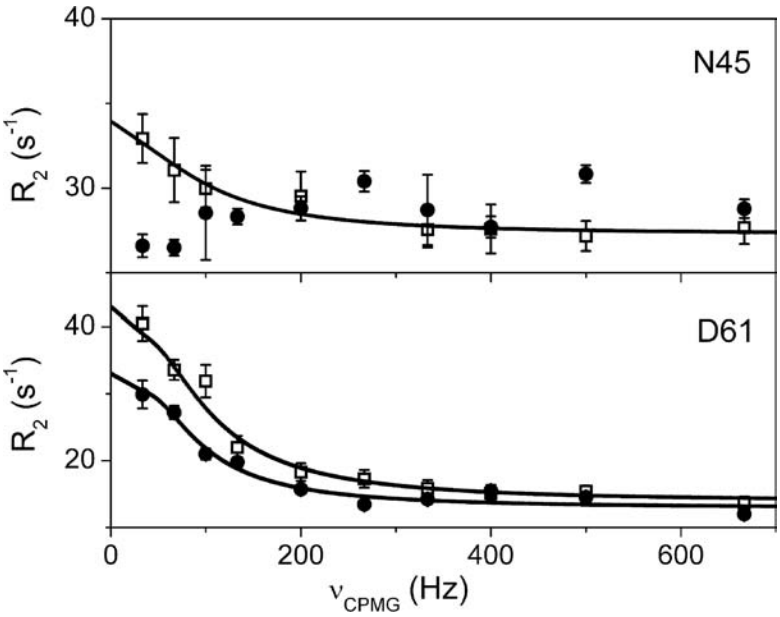

Fig. 4.2.6. **Backbone ^{15}N relaxation dispersion curves of Mistic.** Two representative residues, N45 and D61, were shown in the absence (□) and presence (●) of 10 mM halothane. This figure was reproduced from *J Phys Chem B* **112**, 14312-14318, (2008)

The exchange rate k_{ex} varied to a different extent on different residues. Because these residues resided in the specific joints connecting a rigid region with a flexible region, they likely experienced the chemical exchange on the microsecond−millisecond time scale in the absence of halothane, as shown in Table 4.2.7. For example, both residues T39 and N45 reside in the middle part of helix α2, where a helical kink is located between these two residues. Residue Y82 resides at the end of helix α3. Interestingly, the exchange disappeared in the presence of halothane. In these cases, the anesthetic halothane inhibited the conformational exchange process. For residue V29 located at the end of helix α1, the Rex value of V29 was reduced almost by half,

and the exchange rate k_{ex} became less than 1/3 of its original value after addition of halothane. Residue I52, at the end of helix α 2, experienced fast exchange in the absence of halothane, since k_{ex} is much greater than Δω (Table 4.2.7). It makes I52 give a relatively strong peak in $^{1}H-^{15}N$ HSQC (Fig. 4.2.2). However, the resonance peak of I52 vanished as a result of addition of halothane.

Residue Q66 is located at the beginning of helix α3 or end of the loop connecting α2 and α 3, whose side chain is a few angstroms away from the side chain of Q66. Therefore, both Q66 and D61 can have similar exchange rates that became much slower after the addition of halothane. It is a similar case for residue S58 and D68. S58 resides at the middle of the loop 23 close to D68 at the beginning of helix α3. For these two residues, they also show very similar kinetic parameters. By comparing the fitting results between Q66 and D61 with D68 and S58, we can find that these two pairs show opposite trends of rate changes in the presence of halothane. A close inspection of Mistic structure revealed that the pair of D68 and S58 is oriented inward to helices, while the pair of Q66 and D61 is directed outward in the loop and pointed to the water phase. This phenomenon is also observed in the previous study on the kinetics of SH2 protein [139]. The residues near to ligand binding sites show distinctive kinetics, similar to what we found in Mistic.

Our previous study [32] shows that the dynamical changes due to the addition of halothane may not necessarily result from direct halothane interaction with individual residues. Allosteric effect may play an important role in term of the mechanism of anesthesia. In Mistic, most of the residues listed in Table 4.2.7 showed significant chemical shifts due to halothane titration, while neither I52 nor Y82 demonstrated obvious changes in their chemical shifts. It suggests that both I52 and Y82 had no close or direct interaction with halothane molecules. Therefore, the dynamical alternation of these residues may result from halothane allosteric modulation. The present study in

Mistic confirmed that anesthetic molecules could induce changes in protein motions on the microsecond−millisecond time scale either through direct interaction with specific residues or through allosteric modulation.

4.2.6 Conclusion

In the present study, we confirmed what we found in the previous study on the water-soluble anesthetic-binding model protein, the four-α-helix bundle [32]. In this work, it was found that inhaled general anesthetics were bound to the designed amphipathic pocket and anesthetics could modulate protein slow dynamics. Similar to the four-α-helix bundle, Mistic, a real membrane protein with a similar structural motif to the TM domain of Cys loop receptors, also served as a model protein for the study of anesthetic mechanism. What we found is that inhaled general anesthetics can also modulate its motion on the microsecond-millisecond time scale and especially motion close to the flexible loops. These loops are usually located in the surface of the detergent micelles, which is also considered as the amphipathic environments. Additionally, the inhaled general anesthetics perturb Mistic slow dynamics not only to residues that might interact directly with halothane molecules, but also to residues that may be remote from halothane. Allosteric effect may also play an important role. By collecting more experimental data demonstrating anesthetic modulation on protein dynamics, we can significantly advance our understanding of molecular mechanisms of general anesthesia.

4.3 ANESTHETIC EFFECTS ON THE TM2 DOMAIN OF nAChR α4β2

This section has been published in *Biochim Biophys Acta* **1798**, 161-166, (2010) as a full article. I am the first author. The language was directly taken from the paper.

4.3.1 Significance

nAChRs belong to a superfamily of ligand gated ion channels involving the rapid chemical transmission of nerve impulses at synapses. Previous studies found that some subtypes of nAChRs might be potential targets of general anesthetics and their normal channel functions could be inhibited by general anesthetics [140-146]. Neuronal α4β2 nAChR is one of the subtypes sensitive to general anesthetics [35,143-145]. It is also one of the most abundant nAChR subtypes in the brain [147]. Despite ample evidence showing that general anesthetics could alter α4β2 nAChR functions [35], it remains largely unclear how anesthetics perturb the protein structures and dynamics that ultimately affect the protein functions. Therefore, the insights of anesthetic modulation on the structure and dynamics of the α4β 2 nAChR are valuable to resolve a long time mystery of the molecular mechanisms of general anesthesia [21,30].

A comprehensive understanding of anesthetic action on α4β2 nAChR or other nAChR subtypes has often been restricted by limited available structural information of nAChRs in the past. The structural models of the closed- and open-channel α4β2 nAChR have been generated [49] recently via computations using the known structure of the *Torpedo* nAChR as a template [8]. More recent X-ray structures of pentameric ion channels in closed- and open-channel forms from *Erwinia chrysanthemi* and *Gloeobacter violaceus* provide high-resolution structural information relevant to nAChRs [9,10,49]. These new developments certainly facilitate the understanding of anesthetic action on α4β 2 nAChR, but experimental studies of structural and dynamic effects of

anesthetics on α4β2 nAChR may lead directly to insights into how anesthetics act on α4β2 nAChR and alter the protein function.

Solid-state NMR spectroscopy is a powerful technique for the characterization of membrane protein structures and dynamics and for the investigation of ligand–protein interactions [148-156]. The polarization Inversion and Spin Exchange at the Magic Angle (PISEMA) experiment [53] is particularly useful for the determination of topological structures and dynamics of helical proteins in a well-oriented lipid environment [157-160]. Ligand binding to the *Torpedo* nAChR was comprehensively analyzed using static ^{2}H and cross polarization magic angle spinning (CPMAS) ^{13}C solid-state NMR experiments [161,162]. The structures of the TM domains of the *Torpedo* nAChR were also examined by various solid-state NMR methods [48,163,164], including PISEMA [48]. However, no solid-state NMR study on neuronal nAChR has been reported previously. In the present study, we embedded the TM2 domains of α4β2 nAChR in lipid bicelles, which served as membrane mimetic media and magnetically aligned the protein. The structural and dynamic properties of the TM2 α4β2 nAChR in the absence and presence of anesthetics halothane or isoflurane were investigated using solid state NMR, especially PISEMA experiments. Anesthetics were found to affect both helical tilting and rotational motions that have been identified computationally as critical elements for ion channel functions. This study suggested that anesthetics could alter these motions to modulate channel functions.

4.3.2 Materials and methods

Sample preparation

The TM2 domains of the human nAChR were obtained by solid phase synthesis [40,82]. The α_4 and β_2 TM2 domains have the sequences of EKIT***L***CISV***LL***S***L***TVF***LLL***ITE

and EKMTLCISVLLALTVFLLLISK, respectively. In order to simplify the studies, only seven leucine residues in α_4 TM2 domain, as indicated in bold letters, were ^{15}N labeled.

Lipids were purchased from Avanti Polar Lipids (Alabaster, AL). A conventional protocol of bicelle preparation [165] was followed. 1,2-dimyristoyl-sn-glycero-3-phosphocoline (DMPC) and 1,2-dihexyl-sn-glycero-3-phosphocholine (DHPC) were mixed in a desired molar ratio (q=3.2). Lipid concentration was 28% of sample volume (typically 220μL). To extend sample stability for samples containing the nAChR TM2 domains, 1,2-O-ditetradecyl-sn-glycero-3-phosphocoline (14-O-PC)) and 1,2-O-dihexyl-sn-glycero-3-phosphocholine (6-O-PC) replaced DMPC and DHPC, respectively. A small amount of deuterated $DMPC_{d54}$ (~1mg) was added to each sample for ^2H NMR. The α4 or β2 TM2 was dissolved in 100μL trifluoroethanol and added to the 6-O-PC-chloroform solution. The organic solvents were removed under a stream of nitrogen gas, followed by further evaporation under high vacuum overnight. The aqueous solutions were prepared by adding 110μL of deuterium-depleted water to dried 14-O-PC and 6-O-PC/peptide. The 14-O-PC suspension was vortexed extensively followed by three freeze/thaw cycles (liquid nitrogen/42°C). The 14-O-PC suspension at 42°C was then added to the 6-O-PC/peptide, followed by vortexing and three freeze/thaw cycles. Slow-speed centrifugation was sometimes necessary to remove air bubbles in the sample. A transparent solution was obtained that was viscous at 38°C and fluid at 4°C. Parallel-oriented peptide-containing bicelles were prepared by adding 100 mM $YbCl_3 \cdot 6H_2O$ to the peptide-bicelle solution to reach a final lanthanide concentration of 3 mM. The sample was transferred to a 5-mm OD glass tube (New Era Enterprises, Newfield, NJ) using a pre-cooled pipette tip at 4°C. The glass tube was sealed with a tight fitting rubber cap and further sealed with hard bees wax. The α4-TM2 concentration was 7.4 mM in the α4 samples and 3 mM in the α4β2 samples. The molar ratio of β2 to α4 was 1.5 in the α4β2 samples to ensure a formation of $(\alpha4)_2(\beta2)_3$. The peptide to lipid ratio is ~1:60.

Anesthetics halothane (2-bromo-2-chloro-1,1,1-trifluoro-ethane) and isoflurane (2-chloro-2-(difluoromethoxy)-1,1,1-trifluoro-ethane) were added directly to the NMR tube (pre-cooled in an ice bath) and mixed thoroughly with the samples. The anesthetic concentrations were determined using ^{19}F NMR with 5 mM trifluoroacetic acid (TFA) as a reference.

NMR spectroscopy

All solid state NMR experiments were performed at 40°C on a Bruker Avance 600MHz NMR spectrometer equipped with a ^{1}H/^{31}P/^{15}N(^{2}H) Bruker flat-coil probe. ^{19}F NMR experiments were performed on a Bruker Avance 600 spectrometer with a Bruker TXO probe. The 1-D ^{15}N cross-polarization experiments were conducted using a ^{1}H 90° pulse of 5.1μs, a 49kHz ^{1}H-decoupling field, 1ms contact time, 3s recycle delay, and 10,000 scans. The same cross-polarization parameters were used in the 2-D ^{15}N-^{1}H PISEMA [166]. Other parameters included ±35kHz frequency jumps for the Lee-Goldberg condition, 400–1000 scans, and 6–8 s recycle delay. The ^{1}H carrier frequency was set at 4.5 ppm on parallel oriented bicelle samples. The ^{15}N chemical shift frequencies were referenced to solid ammonium sulfate at 26.8 ppm (relative to liquid ammonia at 0 ppm). The ^{2}H NMR experiments were performed using a solid echo sequence ((π/2) − τ − (π/2) − τ). The 90° pulse length was 2 μs and τ values were 40μs (perpendicular bicelle) and 20μs (parallel bicelle). The recycle delay of 0.5 s and the scans of 256 to 10,000 were used.

NMR data processing

All NMR spectra were processed using NMRPipe [167] and analyzed using Sparky [73]. The data from PISEMA experiments were fitted to the PISA (Polarity Index Slant Angle) [168,169] wheels using the program developed by Veglia's group [158]. The tilt angle (θ) of the helix axis with respect to the bicelle normal, rotation angle (ρ) of the helix around its axis, the angle between the N-H bond and helix axis (δ), and the dipolar coupling

constant (K_{DD}) were determined via fittings. The principal values of the ^{15}N chemical shift tensors [53] for non-glycine residues, σ11=64 ppm, σ22=77 ppm, and σ33=217 ppm, were adopted for the fittings. These values were multiplied uniformly by a factor of 0.95 to accommodate reduced ^{15}N chemical shift anisotropy of proteins in bicelles, as reflected in the reduction of spectral span of the same proteins in bicelles in comparison to those in mechanically aligned lipids.

The TM2 chemical shift assignments were accomplished by combining several sources of information, including the previous assignments of δ–TM2 nAChR [48], the solution NMR structure of β2-TM2 nAChR [82], and the best fitting of PISA wheel. L19 is distinctly separated from the rest of leucine residues in a top view of the NMR structure (pdb code: 2K59) [82]. L19 also has weaker NMR signal than other leucines, presumably because it is located at the lipid-water interface and has less protection from solvent exchange. The distinct location and intensity of L19 convinced us to assign L19 to the most downfield peak in the α4-TM2 PISEMA spectra. Once L19 is defined, the rest of peaks were assigned automatically by PISA wheel fitting. The final assignment of our α4-TM2 PISEMA spectra matches very well with a 2-D projection of the leucine distribution along helical axis from N- to C-terminus in the solution NMR structure [82]. The assignment also agrees well with that for δ–TM2 nAChR [48].

The orientational order parameter, S_i^{CD}, of the ith CD bond vector can relate to the residual quadrupolar splitting, $\Delta\nu_Q^i$, in a ^2H NMR spectrum using the equation [170]

$$\Delta\nu_Q^i = \tfrac{3}{2} A_Q \frac{3\cos^2\theta - 1}{2} S_i^{CD} \qquad (4.3.1)$$

where $A_Q=e^2Qq/h=167kHz$ is the static deuterium quadrupolar coupling constant for aliphatic CD bonds, θ is the angle between the bilayer normal and the magnetic field.

Na^+ flux assay and confocal fluorescence microscopy

The Na^+ flux assay, as measured by the enhancement of Sodium Green™ dye

(Invitrogen, Carlsbad, CA) fluorescence due to Na^+ entry into vesicles through open nAChR channels, is an effective way to assess nAChR activity macroscopically. We prepared 30 mM large lamellar vesicles with 250μM α4β2. The vesicles contain phosphatidylcholine (PC) and phosphatidylglycerol (PG) in a 4:1 molar ratio [41]. PC and PG were mixed in chloroform. α4 and β2 were mixed in a molar ratio of 2:3 and dissolved in TFE. The dissolved lipids and α4β2 were mixed and dried to a thin film. Residual organic solvent was removed by vacuum overnight. The lipid–protein mixture was hydrated with a buffer solution at pH 7.5 containing 20 mM Tris, 50 mM $CaCl_2$, and 6 uM membrane impermeable Sodium Green™. The vesicles were obtained by incubating the lipid–protein solution at 42°C overnight and subsequent multiple cycles of freeze and thaw. An extensive dialysis was performed to remove Sodium Green™ dye outside the vesicles.

The Na^+ flux assay was performed using an Olympus Fluoview300 Confocal Laser Scanning head with an Olympus IX70 inverted microscope (Olympus, Melville, NY). Sodium Green™ was excited by the 488nm argon laser line and the emission was detected using sharp cutoff 510IF long-pass and BA530RIF short-pass filters. For each measurement, 50μL vesicles containing α4β2 were added into a tray coated with poly-lysine that facilitated vesicle adhesion due to the interactions between negatively charged PG and positively charged poly-lysine. The image acquisition began before the addition of an isotonic 100 mM NaCl solution to the media outside the vesicles and continued for 200 s after the exposure to Na^+. The program MetaMorph was used for analyzing the image data.

4.3.3 Anesthetic effects on the bicelles

Solid-state ^{2}H NMR spectra of bicelles with deuterated $DMPC_{d54}$, as shown in Fig. 4.3.1, provided insight of lipid alignment and dynamics. The high-resolution ^{2}H NMR spectra with distinguished quadrupolar splittings in Fig. 4.3.1A and B attested that the bicelles, without incorporating proteins, were well oriented. The quadrupolar splitting of individual ^{2}H peaks corresponding to carbon positions close to the tail of the aliphatic chains showed little difference in Fig. 4.3.1A and B, suggesting that anesthetic halothane molecules had no access to the hydrophobic tail region. However, halothane diffused to the carbon positions close to the glycerol group, as evidenced by significantly broadened ^{2}H signals of the region in Fig. 4.3.1B. The order parameters of individual C-^{2}H bonds of $DMPC_{d54}$, S_{CD}, were calculated using Eq. 4.3.1 in the presence and absence of 6 mM halothane. S_{CD} normally contains information on (a) collective motions of lipids, including bicelle wobbling, (b) trans-gauche isomerizations around C-C bonds of lipids, and (c) the anisotropic reorientation of a whole lipid molecule. Collective motions of lipids were small in our systems, in which a 72% hydration level was remained and bicelles were well magnetically oriented. A recent comprehensive NMR analysis also suggested a good bicelle alignment at such a hydration level [171]. The contribution of anisotropic lipid reorientation to S_{CD} was expected to be uniform for all C–^{2}H bonds linked to a rigid structure. Therefore, a small increase in S_{CD} values in the presence of halothane in Fig. 4.3.2 predominately resulted from orientation of the C–^{2}H bonds with respect to the principal axis of motion of individual lipid molecule. However, since only the readable quadrupolar splitting was used for S_{CD} calculations, the disordered component reflected in the broader peaks might be underestimated in Fig. 4.3.2.

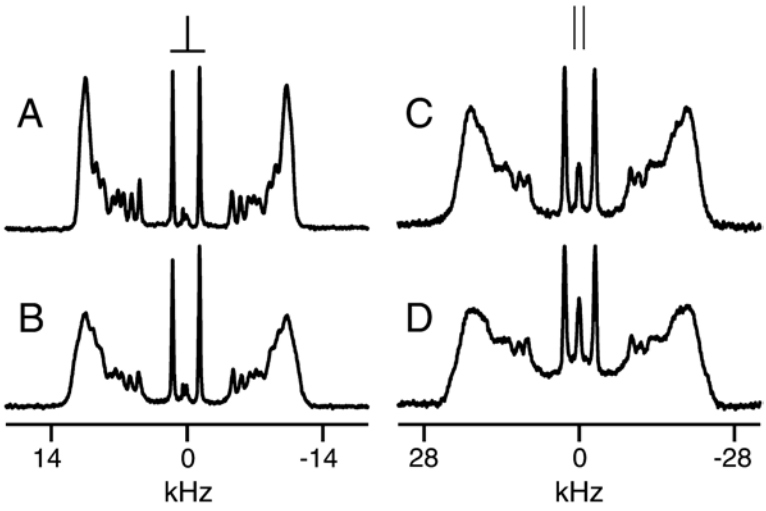

Fig. 4.3.1. ^{2}H NMR spectra of perdeuterated DPMC$_{d54}$ phospholipids. The DPMC phospholipids were embedded in (**A**) a pure DMPC/DHPC (q = 3.2) bicelle system; (**B**) after adding 6 mM halothane to the system in (**A**); (**C**) the 14OPC/6OPC bicelle system incorporated with $(\alpha 4)_2(\beta 2)_3$ nAChR TM2 domains; (**D**) after adding 6 mM halothane to the system in (**C**). The bicelle normal was perpendicular to the magnetic field in (**A**) and (**B**), parallel to the magnetic field in (**C**) and (**D**) due to the addition of 3 mM lanthanide. The spectra were acquired with the solid echo pulse sequence at 40 °C. The spectrum center was arbitrarily set to 0 Hz. This figure was reproduced from *Biochim Biophys Acta* **1798**, 161-166, (2010)

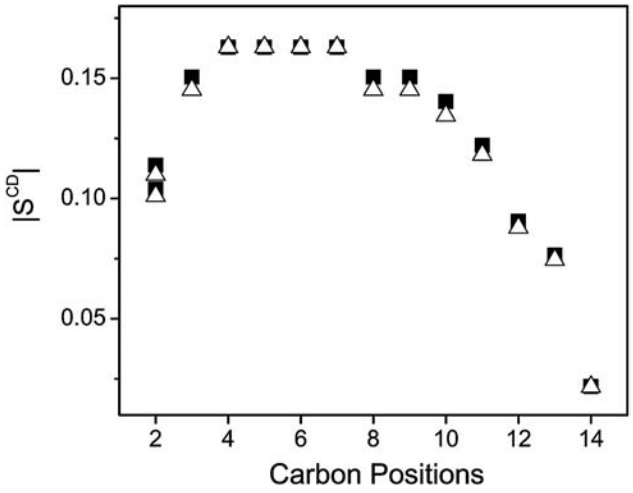

Fig. 4.3.2. **C-^{2}H order parameter S_{CD} as a function of DPMC$_{d54}$ carbon positions.** The absence (△) and presence (■) of 6 mM anesthetic halothane were investigated. This figure was reproduced from *Biochim Biophys Acta* **1798**, 161-166, (2010)

Fig. 4.3.1C and D shows the solid-state ^{2}H NMR spectra of the bicelles incorporated with the $(\alpha4)_2(\beta2)_3$ TM2 in the absence and presence of 6 mM anesthetic isoflurane, respectively. The bicelles were flipped 90° by $YbCl_3$ so that their quadrupolar splittings were double of that in Fig. 4.3.1A and B. The presence of the $(\alpha4)_2(\beta2)_3$ TM2 made the ^{2}H peaks much broader, presumably because the lipid bilayer was severely disturbed by the insertion of the TM2 domains. A small amount of lipids were in isotropic phase after incorporating TM2 domains into the bicelles and the amount increased upon addition of 6 mM isoflurane, as reflected in the peak at zero frequency. The degree of anesthetics-induced ^{2}H peak broadening in Fig. 4.3.1D seemed to be more severe than that in Fig. 4.3.1B, especially to the carbon positions at the middle of DMPC aliphatic chains. Formation of the $(\alpha4)_2(\beta2)_3$ channels might facilitate anesthetic diffusion into the

deep bilayer where anesthetics normally have less access. Direct interactions between anesthetics and TM proteins were observed previously [25,31,40,44]. Anesthetics could modulate protein dynamics directly and allosterically [31]. Such changes in protein motions could affect lipids surrounding proteins and contribute to the observed lipid peak broadening in Fig. 4.3.1D.

4.3.4 TM2 domain in channel and non-channel forms

The α4 and β2 subunits of nAChR need to be in 2:3 stoichiometry to form pentameric channels [172]. Our Na^+ flux experiments confirmed that ion channels could be formed by combining the α4 and β2 TM2 domains in a 2:3 molar ratio, but not by the α4 TM2 domain alone. As shown in Fig. 4.3.3, large vesicles made of phosphatidylcholine (PC) and phosphatidylglycerol (PG) with $(\alpha4)_2(\beta2)_3$ TM2 could be easily identified. A time-dependent increase of sodium green fluorescence intensity upon injection of 10μl 100 mM NaCl signaled channel formation. Control vesicles without channels showed no increase in fluorescence intensity, nor did the channel-containing vesicles when isotonic $CaCl_2$ was added instead of the NaCl solution. The same experiment was also performed on the PC-PG vesicles containing the α4 TM2 domain alone and found no indication of channel formation, suggesting different topology and dynamics of the α4 and $(\alpha4)_2(\beta2)_3$ TM2 assemblies.

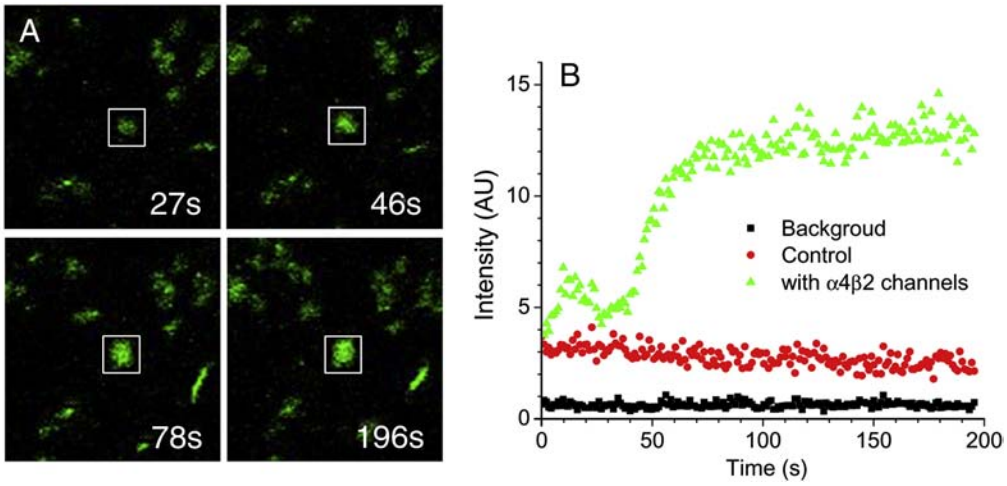

Fig. 4.3.3. **Functional assay of TM2 domains of α 4β2 nAChR.** (**A**) Confocal fluorescence images of large unilamellar vesicles (LUV) made of phosphatidylcholine and phosphatidylglycerol containing α4β2 nAChR channels after exposure to 100 mM NaCl solution at different time points. Membrane-impermeable Sodium Green fluorescent dyes were enclosed and trapped inside the LUVs to indicate intra-vesicle Na^+ concentration. The fluorescence intensity of the vesicles with α4β2 channels increased significantly within a short period of time after exposure to extra-vesicle NaCl, indicating an influx of Na^+ through the channels. (**B**) The intensity changes in the circled vesicles over time after the exposure to extra-vesicle Na^+**.** The background refers to the region without vesicles. The control refers to vesicles without channels, whose fluorescence intensity remained constant before and after exposure to extra-vesicle Na^+. This figure was reproduced from *Biochim Biophys Acta* **1798**, 161-166, (2010)

4.3.5 PISEMA: Effect of β2 TM2 on α4 TM2

The solid state ^{1}H-^{15}N dipolar /^{15}N chemical shift correlation PISEMA spectra of the ^{15}N-Leu labeled α4 TM2 in Fig. 4.3.4 demonstrated distinct differences in the absence and presence of the unlabeled β2 TM2. Wheel-like patterns in the PISEMA spectra of parallel 14-O-PC/6-O-PC bicelles confirmed the TM helical structure of the TM2 domains [82]. Six out of seven total leucine residues of the α4 TM2 showed amide ^{15}N resonances between 180 and 200 ppm. Their resonance patterns are similar to those composed by the TM2 of the δ nAChR [48]. Leu 5 at the N-terminus of the TM2 did not show up in this region of PISEMA spectra, confirming our early solution NMR finding that Leu 5 was not part of the TM2 helix [82]. Leu 19 resides close to the C terminus of the TM2. Its relatively weak intensity in the PISEMA spectra is probably due to a conformational exchange and less efficient cross-polarization in the dynamic C-terminal region. The most downfield ^{15}N chemical shift in the PISEMA spectra is 12 ppm smaller than the conventional value of σ33 (217 ppm), suggesting a more dynamical environment in bicelles.

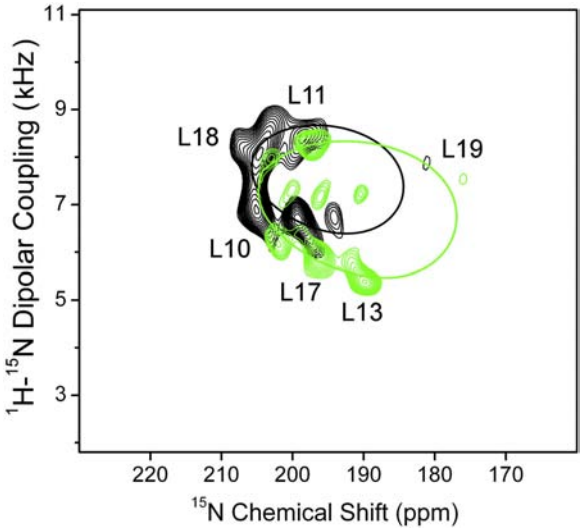

Fig. 4.3.4. **PISEMA spectra of the ^{15}N-Leu labeled α4 TM2 in the absence (Black) and presence (Green) of unlabeled β2 TM2.** Best fit simulations to the PISEMA data reveal the helical tilt angles of 12 ± 1° and 16 ± 1° of the α4 TM2 and the $(\alpha4)_2(\beta2)_3$ TM2, respectively. The notable difference between two PISEMA spectra suggests that the α4 TM2 must have experienced the existence of the β2 TM2 in the $(\alpha4)_2(\beta2)_3$ TM2 sample. This figure was reproduced from *Biochim Biophys Acta* **1798**, 161-166, (2010)

Although the α4 TM2 had a single set of ^{15}N-Leu resonances in the PISEMA spectrum in Fig. 4.3.4, the presence of unlabeled β2 TM2 brought up several minor resonances for the $(\alpha4)_2(\beta2)_3$ TM2. Leu10, Leu17, and Leu13 showed almost the same ^{15}N chemical shifts in both major and minor resonances, but their dipolar couplings were about 1kHz greater in the minor resonances. Although it was almost impossible to accurately define topology of the minor conformation due to too few numbers of resonances, the chemical shift and dipolar coupling data suggested that the helix tilt

angle relative to the bicelle normal must be smaller in the minor conformation than in the major population [168,169]. The minor peaks might also result from a sub-population α4 TM2 in a slightly different motional environment.

A more noticeable difference between the α4 and $(\alpha4)_2(\beta2)_3$ spectra in Fig. 4.3.4 is the shift of the amide resonances along both ^{15}N chemical shift and ^{1}H-^{15}N dipolar coupling axis. Leu11 and Leu18 of the α4 TM2 experienced relatively small shifts before and after mixing with the β2 TM2, but Leu10, Leu13, Leu17 and Leu19 had more profound changes. It is plausible that Leu11 and Leu18 have experienced little interaction with residues in other helices. The best fitting of all downfield resonances to ideal PISA wheels revealed the helical tilt angles of 12 ±1° and 16 ±1° of the α4 TM2 and the $(\alpha4)_2(\beta2)_3$ TM2, respectively. The rotation angle, ρ, was 65° for both α4 and $(\alpha4)_2(\beta2)_3$. The tilt angle of 12° for the α4 TM2 in bicelles agrees with the result of the δ nAChR [48], where the δ TM2 helix was also tilted 12° relative to the normal of mechanically oriented DMPC bilayers. Neither α4 nor δ subunit could form nAChR channels without partitioning of other subunit types [172]. The tilt angle of 16 ± 1° of the $(\alpha4)_2(\beta2)_3$ TM2 is comparable to the tilt angle of 15 ± 2° found for the $GABA_A$ receptor TM2 domain, an anion channel-forming peptide, by a recent solid-state NMR study [151].

It is worth mentioning that all the resonances in our PISEMA spectra resulted solely from the ^{15}N-Leu residues of the α4 TM2. The unlabeled β2 TM2 did not generate ^{15}N NMR signals. If the α4 TM2 was isolated from the β2 TM2, the $(\alpha4)_2(\beta2)_3$ TM2 would give the same PISEMA spectrum as the α4 TM2. The notable difference between the two spectra in Fig. 4.3.4 prove that the α4 TM2 must have interacted with the β2 TM2 in the $(\alpha4)_2(\beta2)_3$ TM2 sample. A thorough NMR characterization of oligomerization states of ^{2}H selective labeled TM peptides in oriented lipid bilayers was demonstrated previously [173]. The same method can also be applied to the α4 and β2 TM2 if proper labeled samples become available. Nevertheless, the data in Fig. 4.3.4 indicate that interaction

between α4 and β2 subunits that might be the driving force for assembling a functional channel. The larger helix tilt angle found in the $(\alpha4)_2(\beta2)_3$ TM2 supported the previous prediction that channel opening might involve tilting of pore lining helices [10,49,81,121].

4.3.6 PISEMA: Anesthetic effect on TM2 domains

Fig. 4.3.5 displays an overlay of the PISEMA spectra of the α4 TM2 in the absence and presence of 6 mM halothane. Halothane lowered ^{1}H-^{15}N dipolar coupling and ^{15}N chemical shift of six leucine residues noticeably. The data fitting into PISA wheels provided a helical tilt angle of 14° in the presence of halothane. The dipolar coupling constant, K_{DD}, decreased from 8700 to 8100 KHz, but the rotational angle (ρ=65°) and the angle between N-H bone and helix axis (δ=13°) remained the same in the absence and presence of 6 mM halothane.

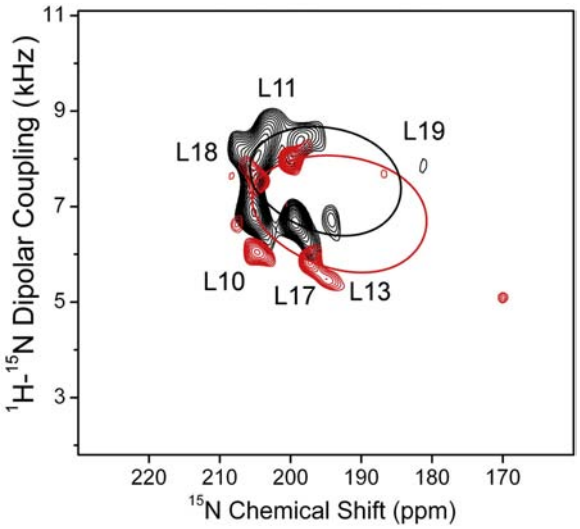

Fig. 4.3.5. **Overlay of PISEMA spectra of the α4 TM2 in the absence (Black) and presence (Red) of 6 mM halothane.** PISA wheel fitting of the α4 TM2 in the presence

of 6 mM halothane reveals an increase in tilt angle from 12° ± 1° to 14° ± 1°. This figure was reproduced from *Biochim Biophys Acta* **1798**, 161-166, (2010)

In comparison to the α4 TM2, the $(\alpha4)_2(\beta2)_3$ TM2 seemed less susceptible to anesthetics. Fig. 4.3.6 shows the PISEMA spectra of the $(\alpha4)_2(\beta2)_3$ TM2 before and after adding 12 mM anesthetic isoflurane. The helix tilt angle of the $(\alpha4)_2(\beta2)_3$ TM2 with respect to the bicelle normal changed less than 1° (θ =16.5°). The K_{DD} value changed from 8400 to 7900 KHz. The other two parameters, ρ=65° and δ=13°, remain unchanged. To the majority of the $(\alpha4)_2(\beta2)_3$ TM2 in the sample, anesthetic isoflurane had a subtle but real impact on their helical orientation in bicelles. The anesthetic-induced changes in the major resonance pattern also implicate the possibility of a wobbling motion of the helix axis with respect to the bicelle normal [174]. Those aforementioned minor resonances of Leu10, Leu13, and Leu17 shown in Fig. 4.3.4 disappeared after adding 6 mM isoflurane to the sample (see the on-line supporting information). However, another subset of minor resonances appeared upon further increasing the isoflurane concentration to 12 mM, as shown in Fig. 4.3.6. The new minor peaks, labeled as L19′, L11′, L13′ L17′, and L19′ in Fig. 4.3.6, appeared as if they resulted from corresponding major resonances rotating 50° counterclockwise around the helical axis. Distinct major and minor resonances signify that the helix rotational motion was on a time scale slower than 10^{-4} s [175]. Both tilting and rotational motions of the TM2 helices are critical elements for channel functions [49]. Our data reveal that anesthetic molecules are able to alter motions of the TM2 helices that could account, at least partially, for anesthetic inhibition effects on the α4β2 nAChR [35].

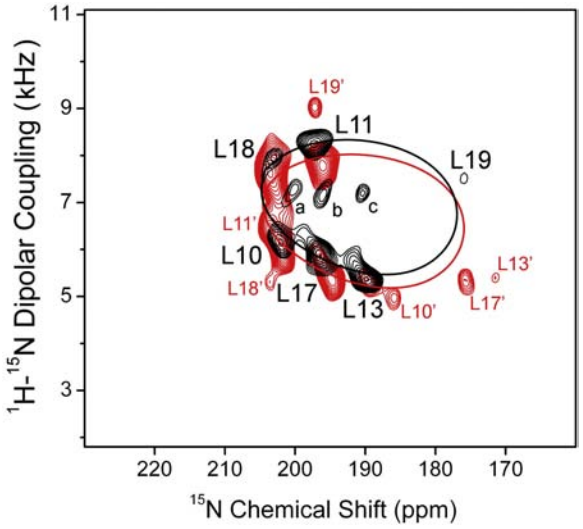

Fig. 4.3.6. **Overlay of PISEMA spectra of the $(\alpha4)_2(\beta2)_3$ TM2 in the absence (Black) and presence (Red) of 12 mM anesthetic isoflurane.** Notice the appearance of subset resonance peaks (a, b, c in black and L19′, L11′, L18′, L19′, L13′, L17′ in red). The minor resonance peaks in red seem to result from rotating corresponding major resonances 50° counterclockwise around the helical axis. This figure was reproduced from *Biochim Biophys Acta* **1798**, 161-166, (2010)

It is not surprising to observe different responses of the α4 TM2 and the $(\alpha4)_2(\beta2)_3$ to anesthetics, considering that one might exist as monomer but the other could form channels. Without the presence of the β2 TM2, the α4 TM2 interacted loosely with other α4 TM2 helices so that individual helix orientation was affected by anesthetics more severely. In a pentameric $(\alpha4)_2(\beta2)_3$ TM2, the helix tilting in respect to the bicelle normal became less sensitive to the addition of anesthetics, presumably due to stronger interaction between the α4 TM2 and its adjacent β2 TM2. One may wonder if small

changes in helix orientation induced by anesthetics, either through tilting or rotational motion, are significant enough to alter channel functions. The X-ray structures of pentameric ion channels from bacterial demonstrated that the pore-lining TM2 domains in closed- and open-channel conformations differ by merely 9° rotation around an axis that is parallel to the membrane normal [9-11], suggesting that a small change in the TM2 orientation could elicit a sizable change in channel functions. Although further structural and dynamical investigations on integral α4β2 nAChR are necessary to define a final answer, the present study highlights the possibility that anesthetics may modulate the channel function via altering the motion as well as orientation of the pore-ling domain.

4.3.7 Conclusion

Several key findings emerged from the current study. First, TM proteins could facilitate anesthetic diffusion into deep membrane bilayers even though anesthetics normally prefer amphiphilic lipid-water interface region [43]. Consequently, anesthetics affected lipid alignment and conformation more severely in bicelles containing proteins. Secondly, the α4 TM2 could not form channels unless it had been mixed with the β2 TM2. The interactions between the α4 and β2 TM2 subunits do exist and such interactions may be essential to drive channel formation. Thirdly, general anesthetics could perturb orientations of the TM helices in lipid bilayers and introduce changes in helical motions. The observed anesthetic effects on the tilt and rotational angles of pore lining TM2 helices reveal a potential pathway for anesthetic inhibition of channel functions. A more challenging question has arisen based on the current study: how do anesthetics make changes in TM protein orientations and motions that are related to protein functions? This is certainly a question worth further investigation.

CHAPTER 5

FUNCTIONAL STUDIES AND INHALATIONAL ANESTHETIC EFFECTS ON TRANSMEMBRANE PROTEINS

5.1 PROTEIN FUNCTIONAL STUDY BY ^{35}Cl NMR SPECTROSCOPY

5.1.1 Significance

The structural study of proteins by high resolution NMR is often limited by the protein size. GlyRs belong to a superfamily of ligand-gated ion channels, involving in rapid inhibitory chemical transmission of nerve impulses at synapses. These receptors are typically pentameric ion channels formed by either one or a combination of various subunits. Each subunit is comprised of a large EC domain, a four-helix TM bundle, and an IC domain region. The GlyR's molecular mass is ~240-290 kDa and each subunit is ~48 (α-subunit)-58 (β-subunit) kDa [176].

Taking into consideration the presence of the detergent to solubilize the receptors for NMR study, the molecular mass is increased to ~80 kDa, even for a single

subunit. The larger the protein size, the weaker the NMR signals are detected and the more severe peak overlaps are observed. Therefore, it is very challenging to study proteins with such large molecular mass by NMR. Not only the protein size but also the dynamic properties in the protein are critical in NMR studies. The dynamics could be wildly different among different domains in a protein. These inhomogeneous dynamic properties also weaken the NMR signals and cause additional peak overlaps.

A feasible approach is to use the reductionist approach. In order to study a large complicated system such as GlyRs or nAChRs, we decompose the complex into several small units. As a consequence, each unit with a smaller molecular mass and homogeneous motion is suitable for structural studies. In the present study, the EC domains were truncated, and the specific TM domains were isolated with the IC domain replaced by a glycine linker. The legitimate question is whether in the reduced system, TM domains themselves can still represent the large complicated system. In other words, whether the TM domains by themselves form a correct channel with the relevant biology is critical for this reductionist approach. The truncated GlyR TM domain, GlyRα1TM-5G (where 5G indicates five glycine linker in place of the long IC loop), was selected and its channel activity was studied using ^{35}Cl NMR. By using magnetization inversion transfer (MIT) experiments, the transport of chloride ion across the truncated GlyR channel was investigated [177,178]

5.1.2 Materials and sample preparation

L-α phosphatidylcholine (PC) and L-α phosphatidylglycerol (PG) were purchased from Avanti Polar Lipids (Alabaster, AL). The vesicles contained PC and PG in a 3:1 molar

ratio [41]. Approximately 25 mM large lamellar vesicles (LUV) with ~26 uM GlyRα1TM-5G were prepared. The lipid to channel ratio was ~4800:1. It was optimized based on the sample stability and MIT signal intensity. PC and PG were mixed in chloroform first and the GlyRα1TM-5G was dissolved in TFE. The dissolved lipids and GlyRs were mixed and dried to a thin film under N_2 gas. Residual organic solvent was removed by high vacuum overnight. Large unilamellar vesicles were prepared based on the previous protocol [179]. The lipid–protein mixture was first hydrated with 5 mM Tris-HCl buffer solution (buffer A) at pH 7.2 in 1/5 the final volume. After thoroughly vortexing and sonicating, the ion strength was increased to a concentration of 0.4 M by adding buffer A in the presence of 0.5 M KCl. This new high salt buffer was added into the vesicle sample in two successive steps. 1/5 the final volume of high salt buffer was first added into the vesicle sample and thoroughly vortexing and approximately sonicating was done. This was repeated using 3/5 of the final volume of high salt buffer. The reconstituted vesicles were frozen slowly in an -80°C freezer for more than 30 min. The frozen vesicles were then thawed at room temperature without agitation. This “freeze and thaw” procedure was done twice. In order to achieve expanded larger vesicles, the concentrated vesicles were further diluted 2-fold by very carefully adding buffer A. The final KCl concentration was 200 mM in 5 mM Tris-HCl.

Picrotoxin (PTX) was purchased from Tocris Bioscience. A 50-mM PTX stock solution in pure DMSO was prepared. In the experiment of PTX effect on GlyRs, two-microliter PTX solution was first titrated into the mixture of the GlyRα1TM-5G and the lipid PC/PG in chloroform solution. The dissolved PTX, lipids and GlyRs were well mixed and then dried to a thin film under N_2 gas. Residual organic solvent was further removed by high vacuum overnight. Unilamellar vesicle preparation was the same as above.

The chloride chemical shift reagent ($Co(II)(gly)_3^-$) was prepared as previously described [180]. Cobalt chloride was mixed with Gly in a ratio 1:3 in buffer A. The sample

pH after the addition of 20 mM chemical shift reagent changed to pH ~4.3. For higher pH experiment, the sample pH was adjusted to pH 7.2 by titrating 1 M KOH solution.

5.1.3 NMR measurements

The NMR experiments were performed at 30°C using a 4-mm MAS probe on Bruker Avance 600 MHz spectrometer. The resonance frequency for ^{35}Cl is 58.8 MHz at 14.4T. In the absence of the chloride chemical shift reagent, there was only one peak and it was manually assigned to 0 ppm. In the presence of 20 mM $Co(II)(gly)_3^-$ shift reagent, the ^{35}Cl peak outside the vesicles ($^{35}Cl_{out}$), which experienced the shift reagent, was separated from the peak inside the vesicles ($^{35}Cl_{in}$). The chemical shift difference is ~25 ppm between $^{35}Cl_{out}$ and $^{35}Cl_{in}$. The normal 90° pulse is ~5 us and the power level is 0 dB. The duration t_1 is equal to the reciprocal of twice the chemical shift difference between $^{35}Cl_{out}$ and $^{35}Cl_{in}$. The mixing time t_2 was set from 10 us to 0.5 ms and a total of 13-14 mixing times were used in the MIT experiments. The recycle delay d_1 was 0.5 s with 256 scans for 1D ^{35}Cl experiments and 1 s with 512/1024 scans for MIT experiments. The resulting MIT spectra were further deconvoluted by using the software, MestReNova NMR (mestrelab reseach).

The Solomon equation was modified to fit the MIT results as previously described [178].

$$\frac{dI}{dt} = -\frac{1}{T_1}(I - I_0) - k_e I + k_i S \quad (5.1.1)$$

$$\frac{dS}{dt} = -\frac{1}{T_1'}(S - S_0) - k_i S + k_e I \quad (5.1.2)$$

where I and S are inside and outside spins, respectively, T_1 and T_1' are the longitudinal relaxation for the spin *I* and *S,* respectively. k_e and k_i are the apparent unidirectional efflux and influx rate with the boundary condition $k_e I_0 = k_i S_0$ (5.1.3) based on the thermal

equilibrium relationship. From Eq. (5.1.1), (5.1.2) and (5.1.3), we can get the solutions:

$$I = I_0\left[1 - \frac{2k_e}{k_i + k_e}e^{-(t/T_1)}(1 - e^{-(k_i + k_e)t})\right] \quad (5.1.4)$$

$$S = S_0\left[1 - \frac{2}{k_i + k_e}e^{-(t/T_1)}(k_e + k_i e^{-(k_i + k_e)t})\right] \quad (5.1.5)$$

Here, spin *S* was selected to invert and $T_1 \approx T'$ was assumed, which was measured from the conventional inversion-recovery experiments with the control sample (no proteins). I_0 and S_0 were measured by the fully recovered spectra. Other parameters were determined by non-linear fitting, using Eq. (5.1.4) and (5.1.5).

5.1.4 1D ^{35}Cl experiment

In the presence and absence of GlyRα1TM-5G, the $^{35}Cl_{out}$ and $^{35}Cl_{in}$ peaks were examined by a 1D ^{35}Cl NMR experiment.

Fig. 5.1.1 shows a typical micrograph of a LUV sample used in the NMR experiments. In the absence of GlyRα1TM-5G, the addition of 20 mM chemical shift reagent (SR) ($Co(II)(gly)_3^-$) separated the ^{35}Cl peak into two peaks, $^{35}Cl_{out}$ and $^{35}Cl_{in}$, which were overlapped in the absence of SR, shown in Fig. 5.1.2A. In the presence of SR, the $^{35}Cl_{out}$ peak became broader and the chemical shift difference between $^{35}Cl_{out}$ and $^{35}Cl_{in}$ peaks was ~25 ppm. In the above experiment, the sample pH was changed to pH 4.3 instead of the original pH 7.2, after the addition of SR. The KOH solution was then titrated into the same sample to bring pH back to 7.2. Two separated ^{35}Cl peaks were still observed. Due to the pH effect on the SR, the $^{35}Cl_{out}$ became sharp and was shifted to the highfield, while the $^{35}Cl_{in}$ was unchanged, as shown in Fig. 5.1.2B.

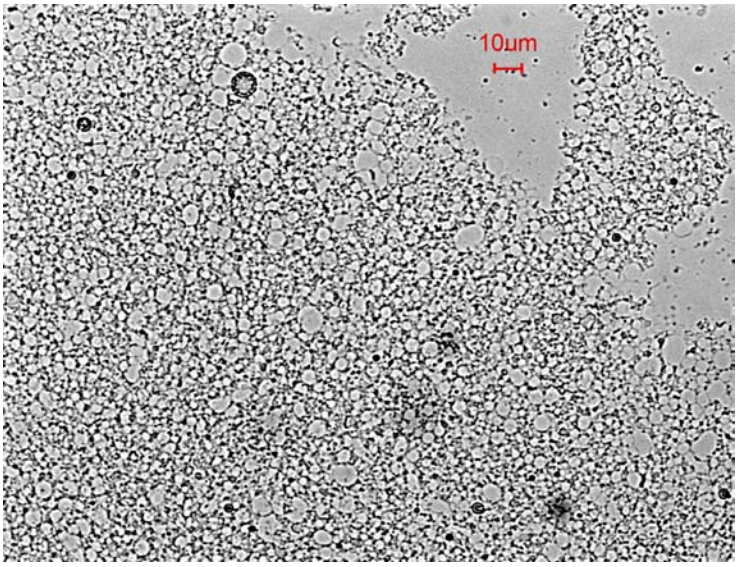

Fig. 5.1.1. Bright field phase-contrast image of a typical large vesicle sample. The vesicles contained PC and PG in a 3:1 molar ratio. The large lamellar vesicles with ~26 uM GlyRα1TM-5G in approximately 25 mM lipid were prepared. A 10um scale was label in red.

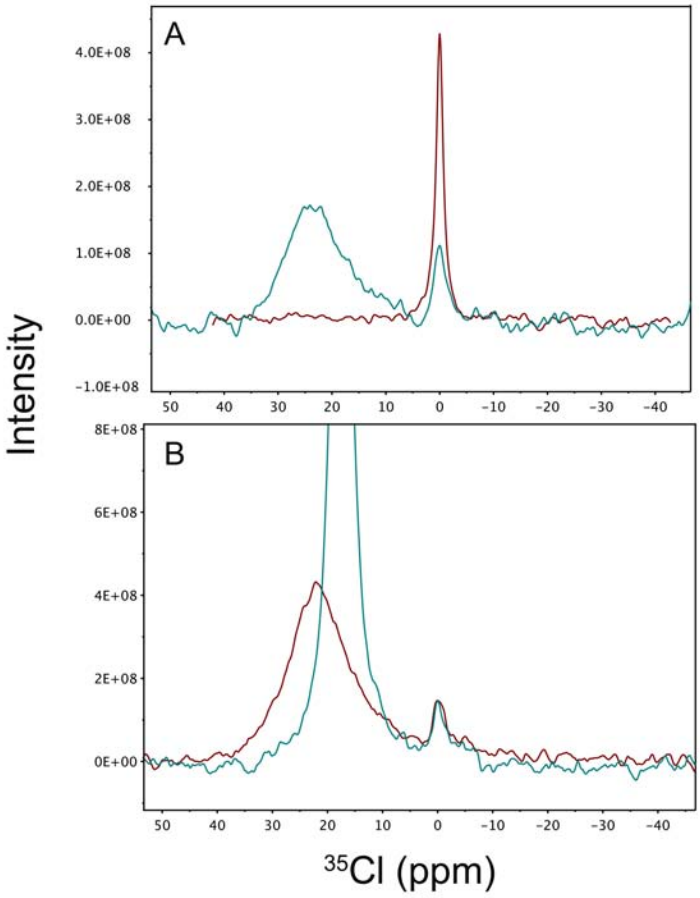

Fig. 5.1.2. 1D ^{35}Cl spectra in the absence of GlyRα1TM-5G. The $^{35}Cl_{in}$ peak was manually assigned to 0 ppm. (**A)** In the absence of chemical shift reagent SR (Brown), the $^{35}Cl_{out}$ and $^{35}Cl_{in}$ peaks were overlapped together at 0 ppm. At low pH, the chemical shift of $^{35}Cl_{out}$ ion in the presence of SR (Cyan) was shifted to downfield, comparing to $^{35}Cl_{out}$ ion in the absence of SR (Brown), while the chemical shift of $^{35}Cl_{in}$ ion remained the same at 0 ppm. The brown peak was scaled down ~2.5-fold for clarification. (**B**) At high pH (Cyan), the $^{35}Cl_{out}$ peak became sharp and was shifted to highfield, comparing to the low pH result (Brown). The sample pH was adjusted to high pH by titrating KOH solution into the sample. The $^{35}Cl_{in}$ remain untouched.

Interestingly, in the presence of GlyRα1TM-5G, only one ^{35}Cl peak can be detected at high pH in Fig. 5.1.3B. Based on its chemical shift, peak intensity and peak width, this peak was assigned to both $^{35}Cl_{out}$ and $^{35}Cl_{in}$. This indicates that the truncated GlyR with the TM domain alone (GlyRα1TM-5G), likely formed a large open channel, which allowed the $^{35}Cl_{in}$ to experience very fast exchange with $^{35}Cl_{out}$. In this case, only one peak ^{35}Cl was detected on the NMR timescale. In our previous study with gramicidin [178], two separated peaks, $^{23}Na_{out}$ and $^{23}Na_{in}$, were always present, regardless of the channel formation by the gramicidin. The different phenomena between the GlyRα1TM-5G and the gramicidin may suggest that the GlyRα1TM-5Gs oligomerized in the open conformation and may form a much large pore in the vesicle, while the gramicidin can form a small pore or a transit channel. This large pore formed by the GlyRα1TM-5G may be the intrinsic large conductance property of GlyR channel, or due to the truncation of the EC and IC domains.

The pH effect on the ^{35}Cl transport across the GlyRα1TM-5G channel was investigated. In order to observe two peaks, lower concentration of GlyRα1TM-5G (thus, less channels per vesicle) was reconstituted on the vesicles at pH ~4.3. In Fig. 5.1.3A, two distinct peaks for $^{35}Cl_{in}$ and $^{35}Cl_{in}$ were observed. This pH dependence may be due to the conserved Arg-252 residing in the terminus of the TM2 domain of the GlyRα1TM-5G. At low pH, the Arg-252 was always protonated with positive charges. A ring of positively charged side chains, formed by the Arg-252 from each subunit, might be essential to the pH dependence of the channel conductance. The charged ring creates a deep energy well to trap Cl^-, thus the transport slows down. In the slow exchange state, it allowed us to observe two distinct ^{35}Cl peaks by NMR. In contrast, partial deprotonation at high pH allows Cl^- to leave the region at the fast rate. In such a case, only one peak was detected shown in Fig. 5.1.3B.

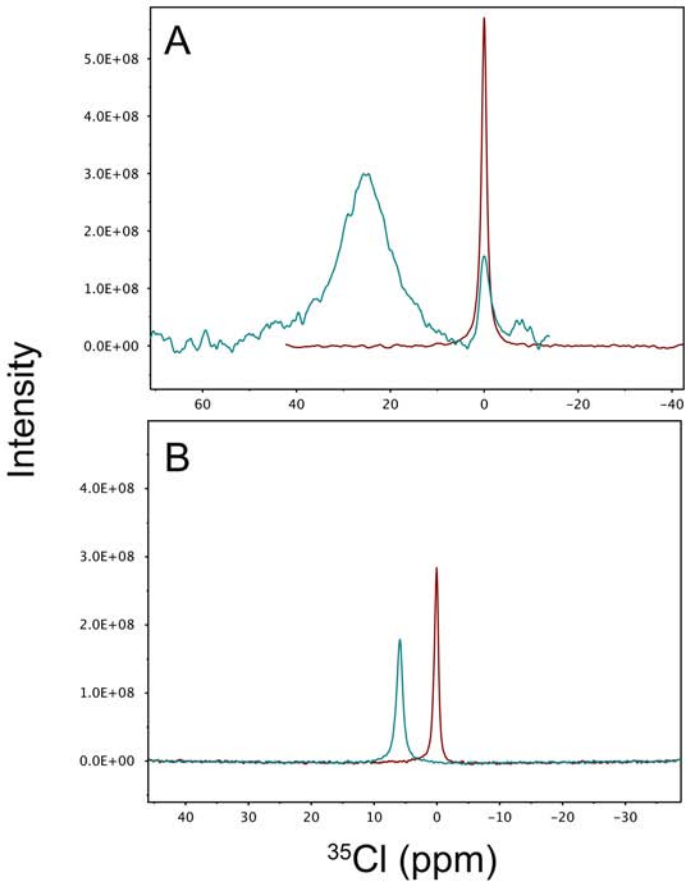

Fig. 5.1.3. 1D ^{35}Cl spectra in the presence of GlyRα1TM-5G with (Cyan) and without SR (Brown). (**A**) At low pH, two individual peaks were observed in the presence of SR. The chemical shift splitting between $^{35}Cl_{out}$ and $^{35}Cl_{in}$ is ~25 ppm. It indicated that they were in the slow exchange state. The brown peak was scaled down for the clarification. (**B**) At high pH, one single peak was observed in the presence of SR (Cyan). It indicated that a fast exchange occurred between $^{35}Cl_{out}$ and $^{35}Cl_{in}$.

5.1.5 MIT experiments

At low pH, in the case of slow exchange, the flow rate of the ^{35}Cl transport across the GlyRα1TM-5G channel can be estimated by MIT experiments. Fig. 5.1.4 shows two stack plots of ^{35}Cl NMR spectra of MIT experiments and their fitting results. In the absence of the channel protein, the $^{35}Cl_{in}$ peak was not affected (Fig. 5.1.4.A), while the $^{35}Cl_{out}$ was selectively inverted and gradually returned to its thermal equilibrium state. This suggested that the ^{35}Cl transport was negligible on the NMR time scale when there were no channels formed in the vesicles. Basically, the MIT cure was flat (Fig. 5.1.4C). However, in the presence of the GlyRα1TM-5G, the $^{35}Cl_{in}$ peak was modulated by the inverted $^{35}Cl_{out}$ peak, which strongly suggested the channel formation, shown in Fig. 5.1.4B. The apparent rate constants k_i and k_e were estimated to be 562.2±292.4s^{-1} and 1345.9±464.2s^{-1}, by using Eq. 5.1.4, shown in Fig. 5.1.C. Here, in the fitting, T_1 was fixed to 21.3 ms, which was independently measured from MIT experiment of the vesicles in the absence of GlyRα1TM-5G. The relatively large fitting error was due to sample stability and experimental errors. Therefore, the values for the apparent rate constants are more qualitative than quantitative. If comparing these results with the previous study with gramicidin, the apparent rate constants of the channels formed by GlyRα1TM-5G were much larger. The apparent rate constants for the gramicidin channels were 182±15.4 (k_i) and 149.7±7.2 (k_e) [178].

Picrotoxin (PTX) is a 1:1 mixture of picrotoxinin and picrotin. It is a poisonous crystalline compound that is used as a stimulant in the central nervous system (CNS). It has been reported that PTX is a non-competitive channel blocker, which interacts with the TM2 domain of the receptors and thereby inhibit ion flows of the α homo-oligomeric GlyRs [181]. In our experiments, 1 mM PTX was added to over saturate the GlyRα1TM-5G sample. The presence of PTX successfully blocked ^{35}Cl ion flow in the MIT experiments,

shown in Fig. 5.1.4C. These results indicated that the quaternary association of GlyRα1TM-5G monomers is essentially the same as in the authentic channel.

5.1.6 Conclusion

The channel functions of the truncated GlyR, GlyRα1TM-5G, were examined by using ^{35}Cl NMR. GlyRα1TM-5Gs themselves do form a channel in the vesicles. Cryo-EM experiments with these TM segments also confirmed the formation of oligomers with pentamers being dominant. The transport rates were measured by the MIT experiments. PTX, a channel blocker for the GlyRs, can also inhibit the Cl^- ion flows of GlyRα1TM-5G. This indicated that GlyRα1TM-5G channel has the correctly folded quaternary structure. More interestingly, we found that this specific GlyR channel formed by the TM domain alone is pH dependent. At low pH, the transport rate is lower than at high pH.

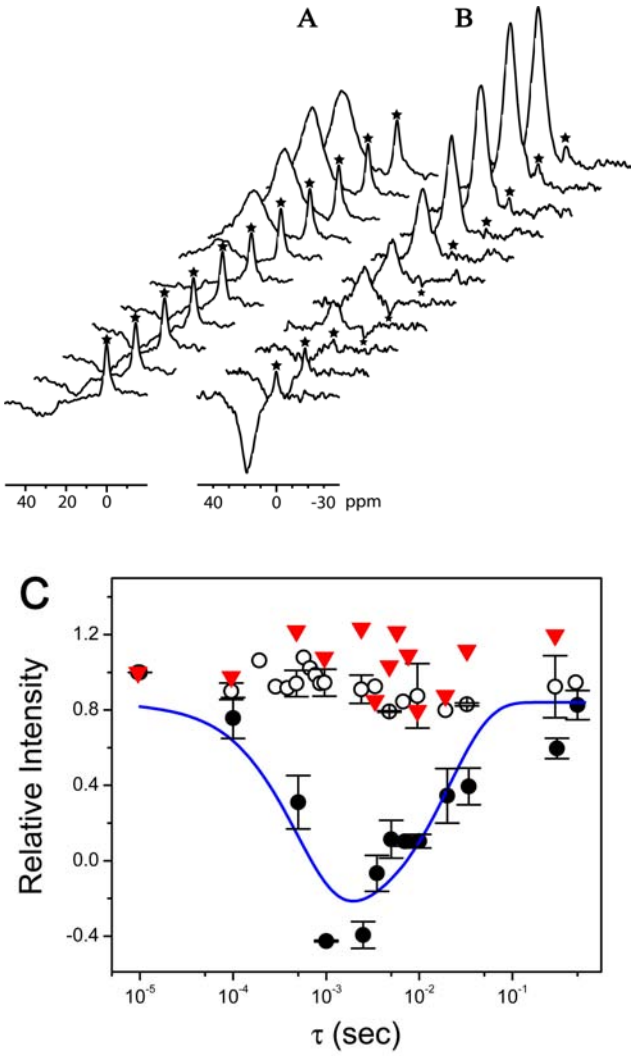

Fig. 5.1.4. Stack plots of ^{35}Cl magnetization inversion transfer spectra. The absence (**A**) and presence (**B**) of GlyRα1TM-5G channels were investigated respectively. $^{35}Cl_{in}$ and $^{35}Cl_{out}$ were separated by 20 mM $Co(II)(gly)_3^-$ shift reagent. (**C**) The peak intensity profiles of $^{35}Cl_{in}$ were plotted as a function of the inversion recovery time, τ. In the presence of GlyRα1TM-5G (Filled circles), the peak intensity profile was best fit using Eq. 5.1.4. The fitting result was a V-shaped curve. The apparent influx rate k_i was estimated to be 562.2±292.4 s^{-1} and the apparent efflux rate k_e was 1345.9±464.2

s^{-1}. T_1 was fixed to be 21.3 ms as determined under the control condition. In the absence of GlyRα1TM-5G (Open Circles), no V-shaped curve was observed. In the GlyRα1TM-5G sample, the presence of 1 mM picrotoxin (Red triangles) eliminated the V-shaped curve and a relatively flat curve was observed. This indicated that there were no ^{35}Cl ions across the membranes of the vesicles. Error bars show the standard error of the mean.

5.2 PROTEIN FUNCTIONAL ASSAY AND FUNCTIONAL STUDY OF ANESTHETIC EFFECT ON THE TM DOMAINS OF nAChR BY FLUORESCENCE MICROSCOPY

5.2.1 Significance

Fluorescence microscopy is also a straightforward method to address whether reconstituted proteins still retain their native function. nAChRs are made of five subunits with a molecular mass of ~290 kDa [12]. This receptor is in the same superfamily as the GlyRs. The large molecular mass and various dynamics in each domain also complicate the structural study of nAChRs. Using the reductionist approach, the TM domain of nAChR was isolated and studied independently. Whether the reduced nAChR is functionally relevant is addressed by fluorescence microscopy. In the present study, the channel activities of nAChRα4β2TM-5Gs and nAChRα7TM-5Gs were studied by fluorescence microscopy.

Cys-loop receptors have been proposed as the main targets for general anesthetics. In previous studies from our group [31-33], anesthetic effects on the TM

domain of the nAChRs and their analogues have been intensely studied on the molecular basis, such as the preferred binding sites of anesthetics and the effects of anesthetics on the structure and dynamics of the protein targets. In these studies, the reductionist approach was applied. Whether the results from the various studies on the reduced nAChR are functionally valid still need to be addressed.

Electrophysiology studies show that the different types of full-length nAChRs respond differently to general anesthetics. The full-length nAChR α4β2 is sensitive to general anesthetics and they can be inhibited by general anesthetics, whereas the full-length nAChR α7 is insensitive to volatile anesthetics [35]. In the present study of TM domains, the anesthetic effect on the channel functions was investigated by fluorescence microscopy. Similar results to the full-length proteins were observed, suggesting that the previous studies of the anesthetic effects on the TM domains are physiologically relevant. This finding also suggested that the TM domains of nAChRs were the main targets of general anesthetics, since their responses to the general anesthetics were in the same trends as with the full-length nAChRs.

5.2.2 Materials and sample preparation

Sample preparation has been described in the previous chapters. Briefly, we prepared the vesicles with 30 mM lipids and 150 μM receptors. The ratio between the lipid and receptors was 200:1 and the PC/PG ratio was 4:1 for the nAChR [41]. For the TM domains of nAChR, the purified samples, α 4 and β 2 in the lauryldimethylamine-oxide (Ldao) micelles, were first mixed in a molar ratio of 2:3 and dialyzed against the water to remove the detergents. The precipitated proteins were re-dissolved in the tetrafluoroethylene (TFE) organic solvent. The dissolved protein sample in TFE was mixed with the lipid in chloroform and dried to a thin film. The dried mixture of the lipids

and proteins were further re-hydrated in 200 mM NaCl buffered at 20 mM Tris buffer pH 7.5. Basically, the same protocol as described before was followed to prepare the vesicles for fluorescence microscopy. The same protocol was followed to prepare the nAChR α7 sample.

For the anesthetic studies, 2 ul net isoflurane solution was equilibrated with 1ml 200 mM NaCl at 20 mM Tris buffer pH 7.5. The vesicle sample was pre-mixed with an equal volume of the above isoflurane solution for 0.5 h before the measurements. The final isoflurane concentration in the vesicles was ~0.2 mM, confirmed by ^{19}F NMR.

In order to observe the correct fluorescence signal that corresponds to the channel function, specific dyes were selected. The nAChRs form cation channels, which allow the positively charged Na^+ ion to pass through the channel. Sodium Green (Invitrogen, Carlsbad, CA) is a sodium enhancement dye, which increases the fluorescence intensity as the Na^+ concentration rises inside the vesicles. 5 uM Sodium Green dyes were added into the samples during the rehydration process. The dyes outside the vesicles were removed by overnight dialysis.

5.2.3 Vesicle-channel activity assay

Fig. 5.2.1A shows that, when 10 mM NaCl was carefully replacing the extra-vesicle 100 mM Na^+ ion in the nAChR samples, the fluorescence intensities decreased rapidly, suggesting that the truncated nAChRs formed the functional channels to allow the intra-vesicle Na^+ to flow out. For the control experiment, the intensity kept constant during the experiment (Fig. 5.2.1B). This indicated that the intensity decay observed in Fig. 5.2.1A was not due to fluorescence bleaching. Fig. 5.2.1C shows the typical curves of the fluorescence intensities as a function of time. The fluorescence data were best fitted to

Eq. 5.2.1 and the average transport rate can be determined as ~2 s^{-1} for the nAChR α4β2.

$$F(t) = A_1 \cdot \exp(-k \cdot t) + A_2 \quad (5.2.1)$$

where F is the fluorescence intensity, t the experimental time in sec, and k the apparent transport rate, respectively, and A_1 and A_2 are constants.

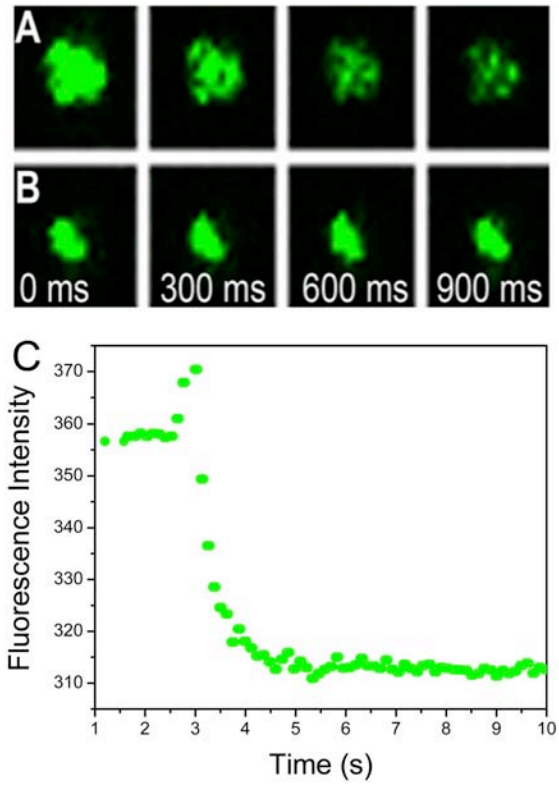

Fig. 5.2.1. Functional assay of TM domains of α4β2 nAChR. (**A**) Zoom-in confocal fluorescence images of unilamellar vesicles containing α4β2 nAChR channels, after rapidly exchanging extra-vesicular Na^+ concentration from 100 mM to 10 mM at different time points. Membrane-impermeable Sodium Green fluorescent dyes were enclosed and trapped inside the vesicles to indicate intra-vesicle Na+ concentration. The fluorescence

intensity of the vesicles with α4β2 channels decreased significantly within a short period of time after dilution of extra-vesicle NaCl, indicating an enflux of Na+ through the channels. (**B**) A control experiment to show that the intensity decay observed in **(A)** was not due to fluorescence bleaching. (**C**) The intensity changes in the vesicles over time after the exposure to extra-vesicle Na+.

The flow rates determined by nonlinear fitting on the fluorescence intensity profiles show the difference along the channel types. The flow rate determined by a single event is only valid for that particular sample under that particular experimental condition because the flux depends on the channel density in the vesicles. Therefore, based on a single experiment, we cannot tell the difference between the α7 channel and the α4β2 channel with regard to the flow rates. In order to compare them, the average flow rates were obtained through using the histogram method to analyze multiple independent experiments. Fig. 5.2.2 shows the histogram of Na^+ efflux rates for α4β2 and α7 nAChR channels. In general, the efflux rates were similar to each other. The flow rate of the nAChR α7 may be smaller than the nAChR α4β2.

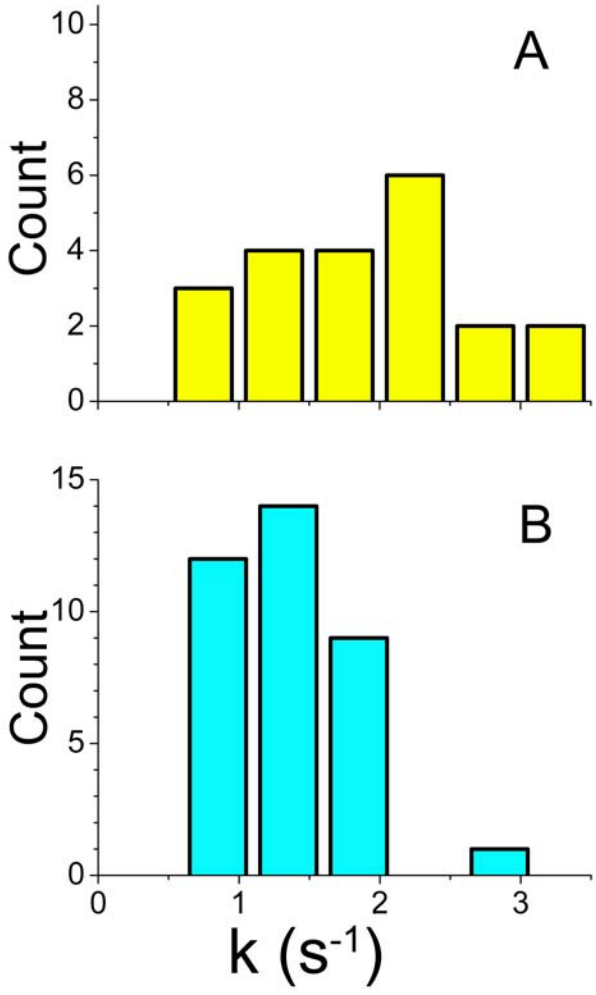

Fig. 5.2.2. Vesicle-channel activity assay of nAChR α4β2 and α7. (**A**) Histogram of apparent Na^+ efflux rate constants in α4β2 TM1234 channels. **(B)** Histogram of apparent Na^+ efflux rate constants in α7 TM1234 channels.

The flow rates determined by fluorescence microscopy are expected to be much slower than the transport rates measured by the MIT experiments. In the MIT experiment, the ^{35}Cl ions were in the equilibrium state. Therefore, the changes

measured by NMR must be due to the ^{35}Cl ion across the channel. However, in the fluorescence experiment, when the extra buffer was added into the sample, the equilibrium state was broken and needed a rebuilt. During this time, the fluorescence intensity started to change correspondingly. It resulted that the flow rates determined by fluorescence microcopy combined both the time for rebuilding the equilibrium and the time for the ions to cross the channel.

5.2.4 Isoflurane effects on the TM domain of nAChR α4β2 and α7

The vesicle samples of nAChR α4β2 and α7 were prepared as previously described. Similar experiments, using fluorescence microscopy, were performed for both α4β2 and α7 in the presence of isoflurane. The flow rates were determined by fitting the data using Eq. 5.2.1. The histogram method was further used to analyze the distribution of the flow rates.

For the TM domains of nAChR α4β2, in the absence of isoflurane, the apparent flow rates were distributed between 0.5 s^{-1} and 3.5 s^{-1}, as shown in Fig. 5.2.2A. In the presence of ~2 mM isoflurane, the histogram bars shifted to the left. The flow rates were obviously decreased by the addition of the isoflurane (Fig. 5.2.3A). This suggested that the general anesthetics inhibited the channel activities. However, for the TM domains of nAChR α7, we did not observe the same trend in the presence of the isoflurane (Fig. 5.2.3B). The TM domains of α7 are insensitive to the isoflurane. These findings are consistent with previous studies based on the full-length nAChR α4β2 and α7. Without the EC domain and IC domain, the TM domains of nAChR themselves can resemble the native nAChR responses to the general anesthetics, therefore the TM domains may be the main targets for the anesthetic. Our studies based on the truncated nAChR are valid and functionally important.

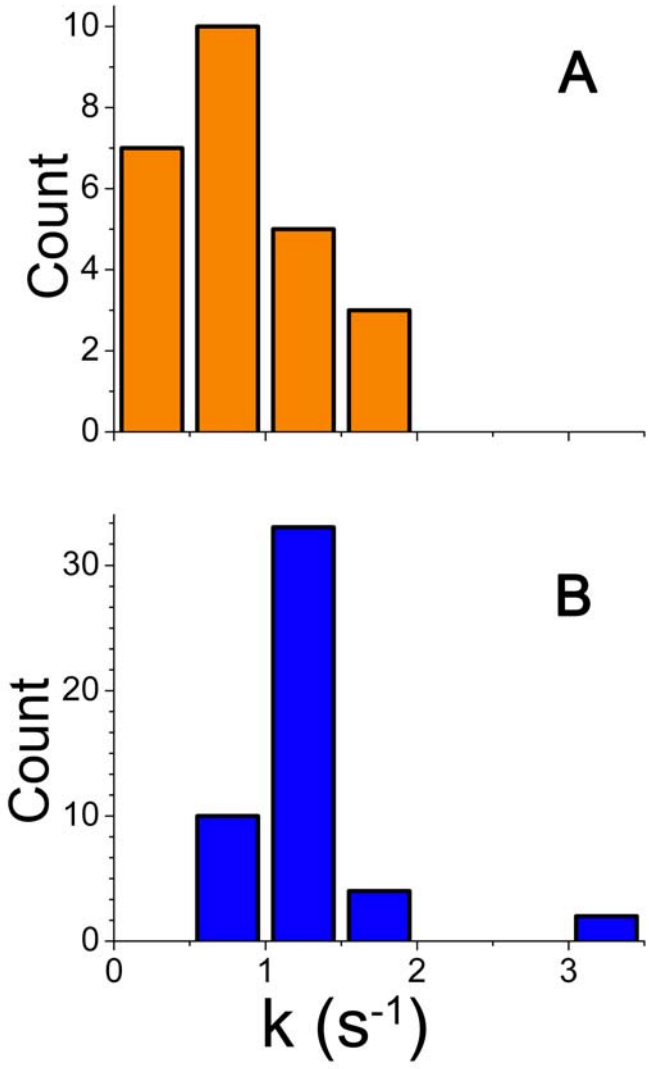

Fig. 5.2.3. Anesthetic effect on the TM domains of nAChRs. Histogram of apparent Na^+ efflux rate constants in α4β2 (**A**) and α7 (**B**) channels in the presence of ~0.2 mM isoflurane.

5.2.5. Conclusion

The vesicle-channel activities of nAChR α4β2 and α7 were examined by fluorescence microscopy. The fluorescence intensity reduction in response to the decreases of the Na^+ concentrations outside the vesicles indicated the channel formations of nAChR α4β2 and α7. The flow rates were estimated to be 0.5~3.5 s^{-1} for α4β2 and 0.5~2.2 s^{-1} for α7. In the presence of isoflurane, the observed flow rate of nAChR α4β2 was decreased to 0~2 s^{-1}, while it remained the same for nAChR α7. These results were consistent with the responses of full-length nAChR α4β2 and α7 to the anesthetic. nAChR α4β2 is sensitive to isoflurane and α7 is not. Therefore, our previous anesthetic studies on the TM domains of nAChR α4β2 and α7 were functionally relevant.

CHAPTER 6

SUMMARY OF CONCLUSIONS AND FUTURE DIRECTIONS

6.1 STRUCTURAL STUDIES OF nAChR AND FUTURE DIRECTIONS

6.1.1 Structural studies

The TM domains of a water-soluble acetylcholine receptor (WSA), human nAChR TM domains with and without the IC domain (nAChRα7TM-IC and nAChRα7TM-5G, respectively) were successfully constructed and heterologously over-expressed in *E. coli*.

The monomer structure of WSA and the secondary structure of nAChRα7TM-5G were determined by NMR. Both WSA and nAChRα7TM-5G show a secondary structure more similar to the bacterial analogues of the pentameric channels, GLIC and ELIC, than to the cryo-EM structure model of the parent nAChR, on which WSA was designed. The monomer structure of WSA was resolved to the backbone RMSD of ~1.1 Å. The overall tertiary structure of WSA is also more similar to the X-ray structures of GLIC and ELIC than to the cryo-EM structure of nAChR. The dynamics of WSA, nAChRα7TM-5G

and nAChRα7TM-IC, which provided more detailed information about protein motion, were investigated by NMR. The dynamics of the IC domain was first characterized using our newly developed histogram method. It revealed that the presence of the IC domain dramatically affects the intrinsic dynamics of the TM domains.

6.1.2 Future directions

This thesis has focused on the monomeric WSA, nAChRα7TM-5G and nAChRα7TM-IC. However, based on our previous study on WSK3 and several lines of other evidence in the thesis, we believe that these water –solubilized proteins might exist in a channel-like oligomeric state. The structure determination for them will be very critical to the understanding of the channel gating mechanism of Cys-loop receptors.

For the membrane proteins used in this thesis, we used a novel water solubilization approach. We mutated putatively lipid-facing residues to hydrophilic ones for the entire TM domains in order to make the target protein water-soluble. However, fewer mutation sites than we reported here may be sufficient to make the protein over-express in *E*.coli and yield a sufficient mount of proteins for the structure determination.

The IC domains are intrinsically flexible, making it hard to be characterized structurally. Because IC domains are usually involved in downstream signal transduction by interacting with other soluble protein in the cytoplasm, such interactions may facilitate the structure determination or crystallization.

6.2 INHALATIONAL ANESTHETIC MECHANISMS AND FUTURE DIRECTIONS

6.2.1 Anesthetic mechanism

In this thesis, we focused on the mechanism of general anesthesia by studying a water-soluble dimeric protein, $(A\alpha_2\text{-L1M/L38M})_2$, a membrane protein, Mistic, and TM2 domains of nAChR. It revealed that general anesthetics always prefer amphipathic environments. Compared to the effect on the structures of proteins, general anesthetics show stronger effect on the dynamics. The effects on the dynamics of proteins can manifest directly or allosterically.

6.2.2 Future directions

In the thesis, we investigated several model proteins and the TM2 domain of nAChR by NMR. WSA, nAChRα7TM-5G and nAChRα7TM-IC are all larger and more complete domains of nAChR. General anesthetic effects on these proteins will further advance our understanding of the mechanism of the general anesthesia.

APPENDIX

See blow for the four published papers.

Cui, T., Bondarenko, V., Ma, D., Canlas, C., Brandon, N. R., Johansson, J. S., Xu, Y. & Tang, P. Four-alpha-helix bundle with designed anesthetic binding pockets. Part II: halothane effects on structure and dynamics.

Ma, D., Brandon, N. R., **Cui, T.**, Bondarenko, V., Canlas, C., Johansson, J. S., Tang, P. & Xu, Y. Four-alpha-helix bundle with designed anesthetic binding pockets. Part I: structural and dynamical analyses.

Canlas, C. G., **Cui, T.**, Li, L., Xu, Y. & Tang, P. Anesthetic modulation of protein dynamics: insight from an NMR study.

Cui, T., Canlas, C. G., Xu, Y. & Tang, P. Anesthetic effects on the structure and dynamics of the second transmembrane domains of nAChR alpha4beta2.

Four-α-Helix Bundle with Designed Anesthetic Binding Pockets. Part II: Halothane Effects on Structure and Dynamics

Tanxing Cui,* Vasyl Bondarenko,* Dejian Ma,* Christian Canlas,* Nicole R. Brandon,* Jonas S. Johansson,[§¶] Yan Xu,*[†] and Pei Tang*[†‡]

*Department of Anesthesiology, [†]Department of Pharmacology, and [‡]Department of Computational Biology, University of Pittsburgh School of Medicine, Pittsburgh, Pennsylvania 15260; [§]Department of Anesthesiology and Critical Care, and [¶]Johnson Research Foundation, Department of Biochemistry and Biophysics, University of Pennsylvania, Philadelphia, Pennsylvania 19104

ABSTRACT As a model of the protein targets for volatile anesthetics, the dimeric four-α-helix bundle, (Aα_2-L1M/L38M)$_2$, was designed to contain a long hydrophobic core, enclosed by four amphipathic α-helices, for specific anesthetic binding. The structural and dynamical analyses of (Aα_2-L1M/L38M)$_2$ in the absence of anesthetics (another study) showed a highly dynamic antiparallel dimer with an asymmetric arrangement of the four helices and a lateral accessing pathway from the aqueous phase to the hydrophobic core. In this study, we determined the high-resolution NMR structure of (Aα_2-L1M/L38M)$_2$ in the presence of halothane, a clinically used volatile anesthetic. The high-solution NMR structure, with a backbone root mean-square deviation of 1.72 Å (2JST), and the NMR binding measurements revealed that the primary halothane binding site is located between two side-chains of W15 from each monomer, different from the initially designed anesthetic binding sites. Hydrophobic interactions with residues A44 and L18 also contribute to stabilizing the bound halothane. Whereas halothane produces minor changes in the monomer structure, the quaternary arrangement of the dimer is shifted by about half a helical turn and twists relative to each other, which leads to the closure of the lateral access pathway to the hydrophobic core. Quantitative dynamics analyses, including Modelfree analysis of the relaxation data and the Carr-Purcell-Meiboom-Gill transverse relaxation dispersion measurements, suggest that the most profound anesthetic effect is the suppression of the conformational exchange both near and remote from the binding site. Our results revealed a novel mechanism of an induced fit between anesthetic molecule and its protein target, with the direct consequence of protein dynamics changing on a global rather than a local scale. This mechanism may be universal to anesthetic action on neuronal proteins.

INTRODUCTION

A diverse range of molecules, from structurally featureless noble gases to complex steroids, can render people into a state of mind commonly known as general anesthesia. The molecular processes underlying this phenomenon remain unclear (1–7). Although modulation of neuronal protein functions through nonspecific anesthetic perturbation to the lipids in the central nervous system remains a distinct possibility, the current consensus is that anesthetic molecules, despite their structural diversity, interact specifically with proteins (5). Extensive investigations, particularly with biophysics, electrophysiology, and mutagenesis approaches, have centered on the hypothesis that anesthetics occupy the hydrophobic pockets or cavities in the proteins to change the protein function. How exactly such a change is achieved, however, is still a mystery.

The dimeric protein, (Aα_2-L1M/L38M)$_2$, was engineered by de novo design to create a long hydrophobic core within a common four-α-helix bundle scaffold (8,9). This four-α-helix bundle has an anesthetic binding affinity in the anesthetizing concentration range of clinical volatile anesthetics (9,10) and thus is regarded as a suitable model for the protein targets of general anesthetics. In our Part I article in this issue (11), we presented the NMR structural and dynamical analysis of (Aα_2-L1M/L38M)$_2$ in the absence of anesthetic binding. The apoprotein backbone structure was resolved to a root mean-square deviation (RMSD) of 1.77 Å. As originally designed, two monomers of the helix-turn-helix motif form an antiparallel dimer. The dimeric structure shows that two helices from the N-terminus to the linker (helix 1 and helix 1′) are held together by the ring stacking of F12 and W15 along the hydrophobic core and by a leucine zipper from complementary pairs of L4, L11, L18, and L25 at the heptad *e* position of each monomer. The high-resolution structure also shows a lateral access pathway near K47 between the two second helices in the dimer (helix 2 and helix 2′) such that the amphipathic anesthetic molecules can enter the hydrophobic core directly from the aqueous phase. Departing from the initial design, however, is the number of anesthetic binding pockets identifiable within the hydrophobic core. Whereas the original design intended to create two sites with mirror images of each other between W15 and M38 of each monomer (9), the NMR structure suggests only one primary anesthetic binding site between the aromatic rings of W15 in the dimer, and two possible minor binding sites between the ring stacking of F12 and F52 (11).

In this study, we experimentally measured the halothane binding to (Aα_2-L1M/L38M)$_2$ and determined the

Submitted July 19, 2007, and accepted for publication January 18, 2008.

Address reprint requests to Professor Pei Tang or Professor Yan Xu, 2049 Biomedical Science Tower 3, 3501 Fifth Avenue, Pittsburgh, PA 15260. Tel.: 412-383-9798; Fax: 412-648-8998; E-mail: tangp@anes.upmc.edu or xuy@anes.upmc.edu.

Editor: Susan P. Gilbert.

0006-3495/08/06/4464/09 $2.00

doi: 10.1529/biophysj.107.117853

high-resolution structure of $(A\alpha_2\text{-L1M/L38M})_2$ in the presence of halothane. Comparison of the structures and dynamics of $(A\alpha_2\text{-L1M/L38M})_2$ in the presence and absence of a bound halothane molecule revealed an interesting change in protein quaternary structure and in the overall dynamics of the protein. These results shed new light on how volatile anesthetics might potentially produce functional changes in proteins in general.

MATERIALS AND METHODS

$(A\alpha_2\text{-L1M/L38M})_2$ expression and purification, NMR sample preparation, and all NMR methods for structure determination have been described in detail in Part I (11). Briefly, the conventional suite of two-dimensional (2D) and three-dimensional (3D) heteronuclear, filtered experiments for spectral assignment, TALOS dihedral angle constraints, and NOESY distance constraints were carried out using the standard pulse sequences from the Bruker sequence library. ^{15}N- and ^{13}C-filtered NOESY was measured with a mixing time of 120 ms. The NOESY assignment was done initially using the Cyana program (12) and then improved manually. Because of the high helical content in $(A\alpha_2\text{-L1M/L38M})_2$ and the characteristic short- and mid-range NOE connectivity to define the helix regions in the structure, the long-range intersubunit NOEs from residues on the opposite ends of the helices can be distinctively and positively identified by the chemical shift matching with an exclusion strategy, without resorting to mixing labeled and unlabeled samples and using specific filtering or purging pulse sequences. In the halothane titration experiments, the $(A\alpha_2\text{-L1M/L38M})_2$ concentration was 500 μM in 10%D_2O/90%H_2O with 0.4% 2,2-dimethyl-2-silapentane-5-sulfonic acid (DSS) and 0.02% NaN_3. Neat halothane was added in 0.3 μl increments using a Hamilton microsyringe. Because evaporation during the repeated titration procedure could not be controlled, the halothane concentrations in the NMR sample were measured by the halothane ^{1}H intensities after each titration step and then calibrated against the final titration point, at which both ^{1}H and ^{19}F intensities were measured, with the ^{19}F intensity calibrated against known concentrations of trifluoroacetate solutions (13,14). Based on this calibration, the halothane concentrations in the titration experiment ranged from 0 to 2.2 mM, at which point the chemical shift change started to plateau. At very low halothane concentrations, the halothane peak was too weak to be accurately measured. This technical difficulty prevents the site-specific K_d values from being accurately quantified. Therefore, the chemical shift change as a function of halothane titration is used in this study only as a qualitative indication of the halothane binding site(s). To estimate the magnitude of K_d at the binding site, nonlinear regression with the following equation (15,16) was used to fit the chemical shift changes as a function of halothane concentration, including the point with zero halothane:

$$\Delta_{obs} = \frac{\Delta_{max}}{2[P]_0}\left\{\left(K_D + [A]_0 + [P]_0\right) - \sqrt{\left(K_D + [A]_0 + [P]_0\right)^2 - 4[A]_0[P]_0}\right\}, \quad (1)$$

where $[A]_0$ and $[P]_0$ are the anesthetic and protein concentration, respectively, and Δ_{max} is the limiting chemical shift difference.

Except for temperature dependent amide proton exchange measurements, for which HSQC experiments were performed at 25, 30, 35, and 40°C to determine the temperature coefficient for hydrogen bonding constraints, all other NMR experiments were conducted at 35°C. Most of the NMR experiments were carried out using a Bruker Avance 600 spectrometer. For selected experiments, Avance 700 and 800 spectrometers were used.

Two different types of experiments were conducted to determine the halothane binding to $(A\alpha_2\text{-L1M/L38M})_2$ by measuring the intermolecular NOE. The conventional 2D ^{1}H-^{1}H NOESY was used to measure the coherent NOE build-up, whereas selective saturation transfer was used to measure the noncoherent cross relaxation between the two interacting molecules. The ^{1}H saturation transfer NOE experiments used tr-HSQC-based pulse sequence. Selective saturation of halothane proton resonance was achieved using an IBURP2 pulse train (80-ms shaped pulses with an interpulse delay of 4 μs and a total duration of 1.6 s) preceding the tr-HSQC sequence. Interleaving on-resonance and off-resonance (–5000 Hz) spectra were acquired to determine the saturation-transfer effects between halothane and individual residues.

The halothane effects on backbone dynamics were measured in the presence of 2.2 mM halothane and compared with the results obtained without halothane as described in Part 1 (11). The ^{15}N R_1 and R_2 relaxation and ^{15}N-{^{1}H} heteronuclear NOE (hetNOE) data were analyzed using the Lipari-Szabo model-free approach (17,18) with the Modelfree program (19).

The R_2 relaxation dispersion spectra were acquired at 35°C on Bruker 800 MHz NMR spectrometers with ^{15}N operating frequencies of 81.09 MHz. The spectra were recorded with 1024 t_2 and 128 t_1 data points, with spectral widths of 10 ppm for ^{1}H and 24 ppm for ^{15}N dimensions. The relaxation-compensated constant-time Carr-Purcell-Meiboom-Gill (CPMG) sequence was used (20,21). The total CPMG constant-time delay was set to T_{CPMG} = 60 ms (two 30 ms CPMG periods). The spectra were collected with 10 different CPMG field strengths, measured by ν_{CPMG} of 33.33, 66.67, 100.00, 133.33, 200.00, 266.67, 333.33, 400.00, 500.00, and 666.67 Hz, where $\nu_{CPMG} = 1/(4\tau_{CPMG})$, and the separation between the centers of successive refocusing 180° pulses equals $2\tau_{CPMG}$. An additional reference spectrum was collected by removing the CPMG periods in the pulse sequence. A relaxation delay of 2.5 s was used. The ^{1}H chemical shifts were referenced to DSS resonance at 0 ppm, and the ^{15}N chemical shifts were indirectly referenced (22).

To analyze transverse relaxation dispersion, the intensities of crosspeaks in 2D R_2 relaxation dispersion spectra with a given CPMG field strength were measured and then converted into the ^{15}N transverse relaxation rate constant R_2 and associated uncertainties according to the well-established relations (23):

$$R_2(\nu_{CPMG}) = -\frac{1}{T_{CPMG}}\ln\left(\frac{I(\nu_{CPMG})}{I_0}\right) \quad (2)$$

and

$$dR_2(\nu_{CPMG}) = \frac{1}{T_{CPMG}}\left[\left(\frac{dI(\nu_{CPMG})^2}{I(\nu_{CPMG})^2}\right) + \left(\frac{dI_0^2}{I_0^2}\right)\right]^{1/2}, \quad (3)$$

where $I(\nu_{CPMG})$ and I_0 are the intensities for a given crosspeak, and $dI(\nu_{CPMG})$ and dI_0 are the noise levels in the dispersion spectra with and without the CPMG pulse trains, respectively. Three exchange parameters, R_{20}, Φ_{ex}/k_{ex} and k_{ex} were calculated using the fast exchange limit approximation ($\Delta\omega = \omega_a - \omega_b < k_{ex}$) with two exchanging sites to fit the R_2 dispersion profile $R_2(\nu_{CPMG})$ by (24):

$$R_2(\nu_{CPMG}) = R_{20} + \frac{\Phi_{ex}}{k_{ex}}\left(1 - \frac{4\nu_{CPMG}}{k_{ex}}\tanh\left(\frac{k_{ex}}{4\nu_{CPMG}}\right)\right), \quad (4)$$

in which R_{20} is the R_2 without exchange (in the limit of $\nu_{CPMG} = \infty$), $\Phi_{ex} = (\omega_a - \omega_b)^2 p_a p_b$, p_i and ω_i are the populations and Larmor frequencies for the nuclear spin in site i; and k_{ex} is the exchange rate. It should be noted that k_{ex} describes exchange rate on the μs-ms timescale and is not the same as the phenomenological R_{ex} term used in the Modelfree approach (24,25).

RESULTS

Site-specific anesthetic binding

Two independent NMR methods were used to determine possible site-specific interactions between anesthetics and $(A\alpha_2\text{-L1M/L38M})_2$. The first was an anesthetic titration ex-

periment, in which the dependence of chemical shifts of individual residues in (Aα_2-L1M/L38M)$_2$ was measured as a function of halothane concentration. Fig. 1 *A* depicts the representative overlaps of HSQC contour plots for four residues where the backbone amide ^{1}H or ^{15}N chemical shifts are profoundly affected by varying concentration of halothane. Nonlinear fitting with Eq. 1, including the point without halothane, yield an estimate of K_d at W15 to be 2.6 ± 1.7 mM (R^2 = 0.996). To visualize the overall halothane effects on HSQC chemical shifts, the normalized changes in the weighted average of the ^{1}H and ^{15}N chemical shifts with

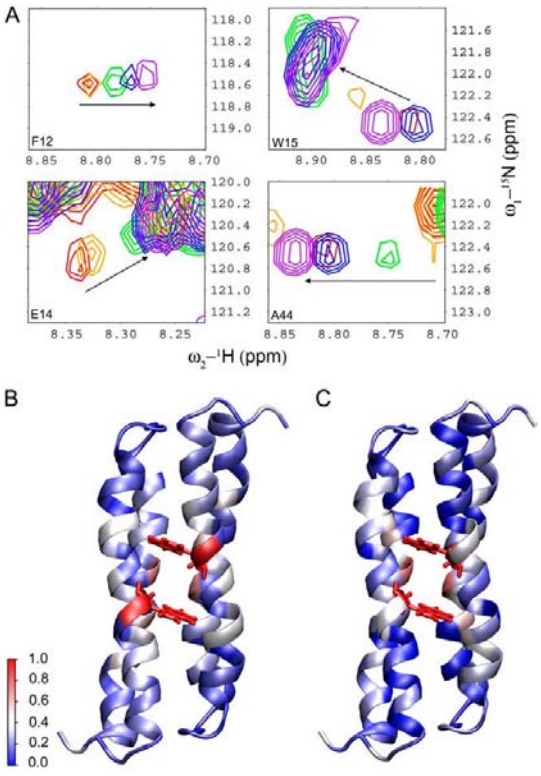

FIGURE 1 Halothane binding to the four-α-helix bundle (Aα_2-L1M/L38M)$_2$. (*A*) Overlap of HSQC contour plots for residues F12, E14, W15, and A44 in response to halothane titration, which was done by adding neat halothane to the NMR sample in 0.3-μl increments. The same contour scale is used for all peaks in each plot to show relative intensities. The peak colors in the order of red, orange, green, blue, and purple indicate increasing concentrations of halothane from 0 to 2.2 mM. In the contours for W15 and A44, the shifted A44 peaks (*blue* and *purple*) overlap with the unshifted W15 peak (*red*). Notice that W15 shows a large chemical shift jump at the first titration point and greatly increased intensities at higher halothane concentrations. (*B*) Individual residues in the NMR-determined structure are color-coded according to their normalized chemical shift sensitivities to halothane titration, with blue to red representing the least to most sensitive, respectively. (*C*) Normalized saturation transfer NOE is mapped onto the NMR structure of (Aα_2-L1M/L38M)$_2$ using the blue-white-red color code.

and without 2.2 mM halothane are color coded onto the protein structure (see below for structural determination), as shown in Fig. 1 *B*. Clearly, the most sensitive region is near W15. To further confirm that the concentration-dependent chemical shift changes are indeed a result of halothane binding instead of other nonspecific effects, a second, independent NMR method was used to measure the saturation transfer (26) between halothane and various residues. The percentage change in tr-HSQC peak intensity from the saturation transfer difference spectroscopy is mapped on the structure (Fig. 1 *C*), showing again the specific interaction between halothane and the protein near W15, A22, and A44. Neither chemical shift titration nor the saturation transfer difference spectroscopy showed significant halothane effects on M38, confirming the prediction from a computer simulation (27) and our own structural study (Part I (11)) that M38 is not directly involved in the halothane binding. Thus, the 3.5-fold enhancement in the halothane binding affinity due to L38M mutation must result from allosteric effects.

High-resolution structures with a bound halothane

Parallel to the studies without anesthetics as described in Part I (11)), the same batch of the expressed proteins was used in this study to determine the (Aα_2-L1M/L38M)$_2$ structure in the presence of halothane. The same suite of heteronuclear, multidimensional NMR experiments was performed for assignment and structure determination. The NOE connectivity and chemical shift index (CSI) pattern resemble those shown in Fig. 3 of Part I (11)). Again, two helical segments, from R5 to E27 and from E36 to R58, are readily identifiable in the NOE connectivity and CSI. The two termini and the glycine linker between the two helices appear to be unstructured based on the CSI and dynamics results (see below). The statistics of the 20 structures with the lowest target function is given in Table 1. The overall backbone RMSD is 1.72 ± 0.39 Å; the backbone RMSD of the helical regions is 1.05 ± 0.28 Å. The insignificant difference in RMSD between the apo- and halothane-bound protein structures is likely due to the difference in the spectral quality and the different numbers of total constraints available for the structural calculation. In the presence of halothane, at least two intermolecular NOE peaks were positively identified in 2D NOESY between halothane and L18 and A44 (Fig. 2). Structural calculations with the inclusion of a halothane molecule clearly define the halothane binding pocket, which is shown to be bordered by the aromatic side chains of W15 and the hydrophobic side chains of L18 and A44 in the dimeric form (Fig. 3 *E*). Fig. 3, *A* and *B*, show the superposition of the structures with and without halothane in the monomer and dimer forms, respectively, exhibiting nearly the same secondary and tertiary monomer structures and pronounced quaternary structural changes after the addition of halothane. The side-chain arrangements surrounding the primary halothane binding site

TABLE 1 Structural statistics of 20 ($A\alpha_2$-L1M/L38M)$_2$ structures with halothane

NMR structure	Statistic
Restraints per monomer	
NOE distances	
Intraresidue	144
Short range (i-j = 1)	128
Medium range (1< i-j ≤ 4)	96
Long range (i-j > 4)	15
Dimer (intermonomer)	6
Dihedral angles	72
Hydrogen bonds	20
Residual upper limit constraints violations number > 0.5 Å	0
Residual dihedral angle constraints violations number > 5°	0
Backbone RMSD	
Residues 5-27, 36-58, 205-227, 236-258	1.05 ± 0.28 Å
All residues (1-62, 201-262)	1.72 ± 0.39 Å
Heavy atom RMSD	
Residues 5-27, 36-58, 206-226, 236-258	1.56 ± 0.32 Å
All residues (1-62, 201-262)	2.07 ± 0.36 Å
Ramachandran plot	
Residues in most favored regions	91.0%
Residues in allowed regions	8.9%
Residues in disallowed regions	0.2%

without and with a bound halothane are depicted in Fig. 3, *C* and *D*, respectively, and the packing details of halothane interaction with the protein at the binding site are shown in Fig. 3 *E*. Whereas the halothane orientation in the pocket is not fixed, there is a clear orientation preference in binding interaction in the bundle of structures (Fig. 4) because of cation-pi type of interaction between the partial positive charge on the hydrogen atom of halothane (28) and the aromatic ring of W15. Among the 20 lowest-energy structures, 12 have a halothane orientation as shown in Fig. 3 *E*, with halothane's Br and Cl each interacting with one of the two hydrophobic side chains of L18, and the hydrogen and the $-CF_3$ moiety orienting toward the W15 aromatic ring and the A44 side chain, respectively. In the remaining 8 structures, the halothane flips ~180° to point the proton to the aromatic ring of the other W15.

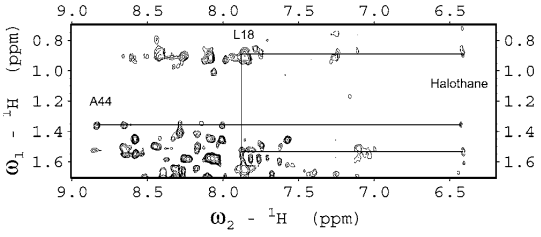

FIGURE 2 A contour plot of a ^{1}H-^{1}H 2D NOESY spectrum showing unambiguous crosspeaks between halothane resonance at ~6.4 ppm and the side chains of L18 and A44.

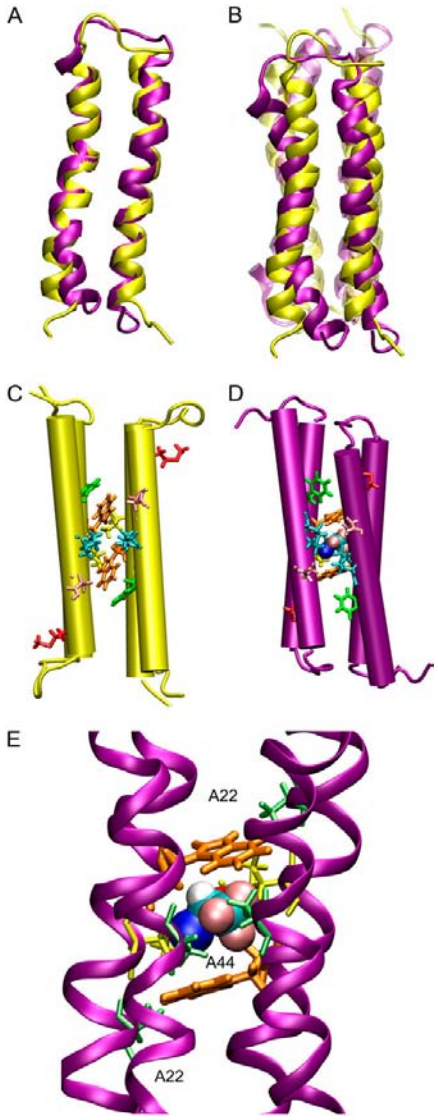

FIGURE 3 Comparison of high-resolution NMR structures of ($A\alpha_2$-L1M/L38M)$_2$ determined with and without halothane. (*A*) The monomer structure determined in the presence of halothane (purple) is superimposed onto the structure of the apoprotein (*yellow*). (*B*) Superposition of the dimer structures. Notice the quaternary structural changes and supercoiling of the helices in the presence of halothane. (*C*) Side view of hydrophobic core of the four-α-helix bundle in the absence of halothane. (*D*) Side view of hydrophobic core of the four-α-helix bundle with a halothane bound in the primary binding site. (*E*) Detailed interactions between halothane and the residues surrounding the anesthetic binding pocket. In *C*, *D*, and *E*, important side chains are shown in licorice representation: W15 (*orange*); K47 (*cyan*); E43 (*pink*); F12 (*green*); and A22 and A44 (*lime*). The halothane molecule is shown in VDW spheres: C (*cyan*); H (*white*); Cl (*blue*); Br (*red*); and F (*pink*).

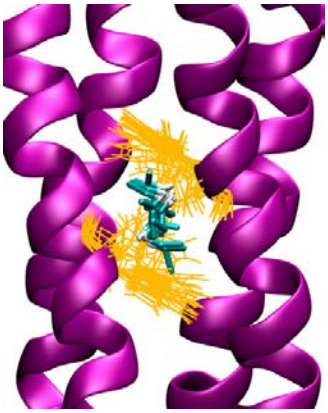

FIGURE 4 Orientations of halothane molecules in the binding pocket. A bundle of 20 halothane molecules (C-C bond (*cyan*); C-H bond (*white*) is depicted in relation to the bundle of W15 side chains (*orange*) in the 20 lowest energy structures. Although the halothane orientation is not fixed, the hydrogen, with partial positive charge, has the tendency to point to the aromatic ring of W15 due to cation-pi type of interaction.

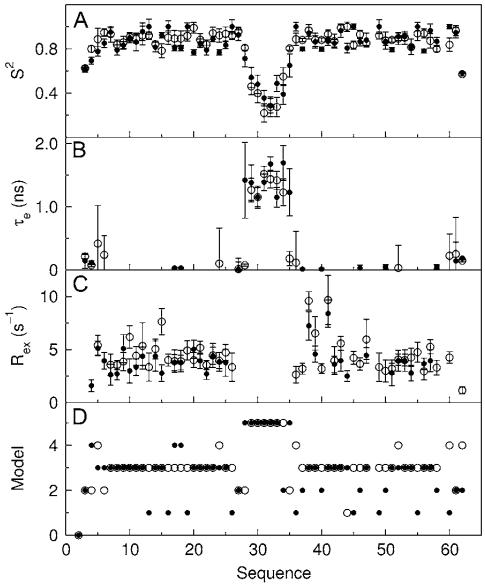

FIGURE 5 Comparison of $(A\alpha_2\text{-L1M/L38M})_2$ dynamics in the presence and absence of halothane binding. (*A*) The squared order parameter (S^2), (*B*) the local correlation time (τ_e), (*C*) the exchange contribution (R_{ex}), and (*D*) model number used in the model-free analysis are plotted as a function of the residue numbers of the four-α-helix bundle, depicting the dynamics in the absence (○) and presence (●) of 2.2 mM of halothane. Notice that halothane stabilizes overall protein motion as evidenced by the increased S^2 in the immediate vicinity of W15 and the globally reduced R_{ex} terms at many residues.

Anesthetic effects on backbone dynamics

The backbone dynamics was determined by analyzing the R_1, R_2, and hetNOE of the backbone amide ^{15}N with and without halothane using the Modelfree approach (17,18). In addition, the conformation exchange on the μs-ms timescale was examined using the CPMG R_2 dispersion measurements. The effects of halothane binding on the local and global dynamics are depicted in Figs. 5 and 6. Fig. 5 shows the conventional Modelfree analysis, depicting the generalized order parameter, the correlation time of the fast local motion (τ_e), the exchange contribution to the relaxation (R_{ex}) (29), and the model number used to fit the data. As in the case without anesthetics, the two termini and the loop regions are significantly more flexible, with order parameters lower than 0.5. The loop region does not meet the basic Lipari-Szabo assumption and can only be fitted with Model 5. In the presence of halothane, the residues in the immediate vicinity of the binding site showed slightly elevated order parameters, becoming more ordered than without halothane. The most profound changes are seen in the global distribution of the R_{ex} term in the helical regions. Overall, R_{ex} is reduced upon halothane binding, suggesting a lesser degree of conformational exchange. The involvement of nonzero R_{ex} terms in many residues is confirmed by the R_2 dispersion measurements, which are independent of the model selection or the spectral density mapping. As shown in Fig. 6, many residues exhibit the R_2 dependence on the CPMG frequencies. The ΔR_2 values, which are estimated from the R_2 values at the two extreme CPMG frequencies achievable with our NMR hardware, display the same distribution pattern as R_{ex} along the protein sequence (Fig. 6 *B*). It should be noted that the ΔR_2 measured by the relaxation dispersion underlies the phenomenological nonzero R_{ex} term in the Modelfree analysis, albeit the two are not expected to be identical (25) because the two experimental methods are sensitive to motions on different timescales. Nevertheless, the overall trend is clear, and the binding of halothane reduces the conformational exchange on the global scale. The significance of this reduction in R_{ex} (or ΔR_2) will be discussed below. As in the case without halothane, two residues, M38 and C41, still show a larger R_{ex} than other residues, albeit halothane reduced the R_{ex} values by a factor of 2. Exchange parameters, R_{20}, Φ_{ex}/k_{ex}, and k_{ex}, determined for several residues using the fast exchange limit approximation (Eq. 4) to fit the R_2 dispersion data, are shown in Supplementary Material, Table S1. There seems to be also a slight tendency that halothane binding makes the loop region more ordered as shown in the S^2 values. This is supported by the slightly elevated R_2 values for some of the loop residues in the R_2 dispersion measurements (e.g., G30 in Fig. 6 *A*). However, since the R_2 dispersion method is prone to artifacts when R_2 is not significantly larger than R_1 (30), which is indeed the case for the loop residues, the small difference in the R_2 dispersion with and without halothane should be taken with caution for the loop and terminal residues. Using the same method as in Part

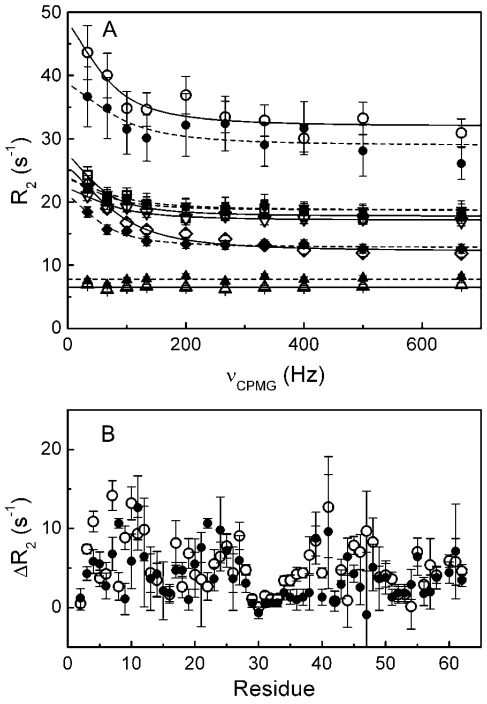

FIGURE 6 (*A*) Representative plots of the ^{15}N transverse relaxation rate, R_2, as a function of the CPMG field strength, ν_{CPMG}, for L4 (◇), G30 (Δ), M38 (□), C41 (○), and E50 (∇) in (Aα_2-L1M/L38M)$_2$ without (*open symbols*) and with (*solid symbols*) 2.2 mM halothane at 18.8 T (800 MHz). Uncertainties in R_2 were determined from the signal/noise ratio using Eq. 3. The $R_2(\nu_{CPMG})$ dispersion profiles for L4, M38, C41, and E50 demonstrate the contribution of conformation exchange to the ^{15}N transverse relaxation rate. The solid and dash lines are the best fit to the data for the protein in the absence and presence of the anesthetic, respectively, using Eq. 4. G30 shows no conformation exchange and is presented here as a reference. (*B*) Values of $\Delta R_2 = R_2(\nu_{CPMG}=33.3\text{Hz}) - R_2(\nu_{CPMG} = 666.7\text{Hz})$ are plotted as a function of residue numbers in (Aα_2-L1M/L38M)$_2$ without (○) and with (●) halothane at 18.8 T. Most residues show a decreased ΔR_2 in the presence of halothane, indicating that halothane suppresses the global conformational exchange in the protein.

I (11) to search for the best-fitted τ_m value, the Modelfree calculations yielded the global tumbling time of 5.00 ± 0.08 ns, in agreement with the global tumbling time of the apo protein.

DISCUSSION

Primary anesthetic binding site in the four-α-helix bundle

Four-α-helix bundle is a common scaffold found in many important functional proteins. For example, the transmembrane domains of anesthetic-sensitive superfamily of Cys-loop receptors are composed of pseudosymmetric pentamers of four-α-helix bundles. Serving as a model for anesthetic protein targets, (Aα_2-L1M/L38M)$_2$ was designed with a few iterations of design changes aimed at improving the binding affinity for volatile anesthetics (8,9). Our structural studies of (Aα_2-L1M/L38M)$_2$ in the absence of a bound anesthetic, as detailed in Part I (11) suggested a primary binding site between the two W15 side chains in a dimer and an amphipathic lateral access pathway from the aqueous phase through the flexible C-terminal helix interface into this binding site. These findings are somewhat unexpected because the intended binding sites by design are closer to the two ends of the hydrophobic core of the four-helix bundle, and thus there should be two sites that are mirror images of each other. In the present structural study with halothane, we confirmed that the main halothane binding site is indeed sandwiched between the two W15 residues. The chemical shift changes in response to titration with varying concentrations of halothane, the saturation transfer experiment, and 2D NOESY experiment all indicate that the preferred halothane interaction site are in the middle section of the four-helix bundle, instead of between W15 and M38 as the latest iteration of design had intended. The apparent dissociation constant for halothane binding to (Aα_2-L1M/L38M)$_2$ is estimated to be in the submillimolar range based on the fluorescence quenching on (Aα_2-L38M)$_2$ (9). Our chemical shift titration experiments, which measure the halothane influence on the protein backbone amide nitrogen and proton chemical shifts, probe the relative involvement of individual residues in the anesthetic binding. Since the side chains at the binding site are more directly involved in the interaction than the backbone, the site-specific K_d determined from the backbone chemical shifts does not necessarily reflect the true binding affinity at the interaction site. Nevertheless, the approximate K_d value obtained from the chemical shift titration measurements is consistent with the apparent K_d from the fluorescence quenching experiments (9).

It is interesting to note that when the experimental structures were used in a docking search for potential halothane binding sites, we found that the site between two W15 side chains is highly preferred (~98%) but not exclusive in the apoprotein. In contrast, with the lowest energy structure determined in the presence of halothane, Autodock (31) found the halothane binding site to be exclusively between W15 side chains. The estimated free energy of binding from Autodock is –3.35 kcal/mol (4.89 mM), which is in agreement with the experimental titration data.

An induced fit for anesthetic binding

Detailed structural analysis revealed that the monomeric helix-turn-helix fold is very similar in the two structural bundles with and without a bound anesthetic, as shown in Fig. 3 *A*. When fitting the helical regions of the monomers, the RMSD between the two structural bundles is ~1.5 Å, which is only slightly larger than the RMSD of the monomers

among the 20 lowest-energy structures of each bundle. Thus, halothane binding did not greatly affect the monomer (secondary and tertiary) structure. As shown in Fig. 3 *B*, the most significant structural change upon halothane binding is the quaternary association of the four helices in the dimer. There is a vertical shift of the monomers relative to each other by approximately half a helix turn and a super-coil twisting of the helices when a halothane molecule is bound at the site between the two W15s. These quaternary structural changes removed the asymmetry found in the apoprotein due to wider separation between helix 2 and helix 2′. The halothane-induced quaternary changes led to a better fitting between halothane and the amphipathic cavity of the binding site. Measured by the Q-SiteFinder program (32), the binding cavity bordered primarily by the side chains of W15, L18, and A44 (Fig. 3, *D* and *E*) reduces its size from ~381 Å^3 in the structures without halothane to ~162 Å^3 in the structures determined with halothane (after removing halothane from the structure). The latter value better matches the molecular volume of halothane (~130 Å^3 (33,34)). Thus, our structural data suggest an induced fit between halothane and its binding site. The high structural flexibility of the apoprotein, the lateral opening between helix 2 and helix 2′ for direct access to the binding site from the aqueous phase, and the quaternary structural re-arrangement for an induced fit can all contribute to an increase in the binding on-rate. As evidenced in the packing between the halothane molecule and the residues surrounding the binding pocket (Fig. 3 *E*), the interaction at the binding site is both hydrophobic and electrostatic in nature. Optimization of the fitting in the binding site and the closure of the lateral pathway as a result of the twisting of helices 2 and 2′ relative to helices 1 and 1′ will likely decrease the binding off-rate, thereby achieving the high-affinity specific binding of halothane in this designed protein.

Implications of anesthetic effects on local and global dynamics

In addition to the structural changes, halothane binding to the four-α-helix bundle also resulted in profound changes in the protein dynamics, not only locally but also globally at residues remote from the binding site. This finding is important because protein function always involves protein motion. Thus, the four-α-helix bundle offers more than just a structural model. The characteristics of halothane effects on the dynamics of (Aα_2-L1M/L38M)$_2$ may have universal implications on how anesthetic binding to protein ultimately leads to changes in protein functions (1–3,7,35–37).

In the absence of halothane, (Aα_2-L1M/L38M)$_2$ appears extremely dynamic on the NMR timescale (11). Model-free analysis showed that many residues in the helical regions contain the R_{ex} contribution to the backbone amide ^{15}N relaxation, suggesting the presence of a conformational exchange process at these residues (18,28,38). This finding is confirmed in this study by the R_2 dispersion measurements. By comparing the model-free analyses of the relaxation data with and without halothane as shown in Fig. 5 and of the R_2 dispersion data as shown in Fig. 6, it is clear that halothane binding not only stabilizes the residues in direct contact with halothane, but also reduces the R_{ex} (or ΔR_2) on a global scale. The most noticeable R_{ex} changes in (Aα_2-L1M/L38M)$_2$ are at W15 and near M38 and C41. In the apoprotein, W15 signal is relatively weak (hence precluding the R_2 dispersion measurement), presumably due to an intermediate exchange. Indeed, when the site is not occupied, there is a large degree of orientation freedom for the W15 side chains within the hydrophobic core. The NMR structure of the apoprotein suggests that W15 side chains tend to swing toward F12 to form an aromatic ring stack within the long stretch of hydrophobic core, leaving a large space between the W15 side chains to accept halothane. When the site is occupied, the two W15 side chains are locked into a parallel configuration (Fig. 3, *D* and *E*) with reduced local flexibility, as indicated by the increased order parameter at W15 and nearby residues. This not only changes the chemical shift but also increases the intensity of W15 in HSQC (Fig. 1 *A*). One of the direct consequences of the reduced W15 side chain flexibility—in addition to the induced fitting for high-affinity halothane binding as discussed above—is the largest decrease of the R_{ex} term associated with W15 (Fig. 3 *E*).

As discussed in Part I (11), another dynamic hotspot in (Aα_2-L1M/L38M)$_2$ is located near M38 and C41. Both of these residues showed a large R_{ex} term compared to the rest of the protein when no halothane is bound. It is known that a point mutation at residue 38 from Leu to Met can result in a 3.5-fold increase in halothane binding. Such an increase could be due to changes in either structure or dynamics, or both. Structurally, Leu-Met mutation has been shown to be well tolerated by numerous studies. Because M38 (or L38) is not even part of the halothane binding site according to the NMR structure, local steric effects in a structural sense are unlikely to be the cause of the increased binding affinity after the mutation. In searching for other possible explanations, we believe that global dynamics is an obvious candidate, given the unusual dynamics property near the mutation site. The allosteric coupling between W15 and M38 is clearly evident in the large reduction of the R_{ex} term at M38 and C41 on halothane binding at W15. This suggests that residue 38 is situated at a pivotal point to control the global dynamics of the protein. Although Leu and Met are close on the hydrophobicity scale (39), methionine's side chain is longer and narrower than leucine's side chain. Residue 38 is at the first heptad *g* position in the first turn of helix 2 after the flexible glycine linker. From the apoprotein structure, it can be seen clearly that the M38 side chain is sandwiched between the adjacent L37 and the more distant E27 and A23, all of which congregate at the two ends of the flexible glycine loop. The long and linear M38 side chain can either point toward the glycine loop or toward the lateral aqueous phase, depending on the glycine loop orientation. If L38 resumes the same local

structure as M38, its side chain has predictably less orientation freedom relative to the glycine loop due to its bulkier branching methyl groups. Therefore, it is conceivable that the mobility at residue 38 in relation to the flexible linker is critical to the opening and closing of the lateral pathway between helix 2 and helix 2′. The higher halothane binding affinity found in the L38M mutation can be explained by the increased on-rate, whereas the off-rate should be dictated by the W15 ring stacking and induced fit after halothane has occupied the binding site, which would be similar irrespective of L38 or M38.

In support of this viewpoint is the dynamics change at E43 and K47, where sizeable R_{ex} terms can be seen when halothane is absent. After halothane binding, the high-resolution NMR structures reveal that the quaternary structural changes shift E43 of one monomer to almost the same level as K47 of the other monomer. The super-coil twisting brings E43 at heptad *b* position closer to K47 at heptad *e* position of the opposing helix. The electrostatic interaction stabilizes E43 and closes the interface (and thus the lateral access pathway) between helices 2 and 2′. As a consequence, both E43 and K47 show a significantly reduced R_{ex} term after halothane binding.

Our results suggest an interesting interplay between structural fitting and dynamical contribution to anesthetic binding at protein targets. From a pure structural viewpoint without considering protein mobility, the space between two W15 side chains in the apoprotein would not seem ideal for halothane binding. As discussed above, there is a large discrepancy between the cavity size (381 $Å^3$) and the volume of the anesthetic molecule (130 $Å^3$) for a snug structural fit. However, the opening between helices 2 and 2′ and their conformational flexibility create an easy access directly from the aqueous phase to this site. The intrinsic global mobility of this dimeric protein and the interaction-induced structural fitting between halothane and the key residues at the binding site make this site more favorable than other potential sites. For example, the minor sites found by the Autodock program in the apoprotein between F12 and F52 would be theoretically suitable for halothane binding. These minor sites, however, are not occupied with high affinity due to divergence of the structural and dynamical factors at these sites. As discussed in Part I (11), the side chain of F52 seems to be ''out of place'' in the aqueous phase. Although the local rotational freedom of F12 and F52 side chains would allow halothane to bind, the absence of a consequent structural change to secure the binding would render any halothane occupancy between F12 and F52 short-lived. Similarly, Q-SiteFinder revealed two amphipathic pockets bordered mainly by A8, F12, L51, L54, and R58 of one monomer and L26, E27, L37, M38, and C41 of the other monomer, along with three residues from the glycine loop. These pockets have a volume of 303 $Å^3$ but show no interaction with halothane experimentally and yield no population by flexible docking. The controlling factor in this later case is likely to be the protein dynamics. Thus, when searching for important anesthetic interaction site or sites in neuronal proteins to understand the molecular mechanisms of general anesthesia, one must analyze and differentiate the structural and dynamical contributions to the functional consequences of anesthetic-protein interactions.

In conclusion, we identified a novel anesthetic binding site in the designed four-α-helix bundle $(A\alpha_2\text{-L1M/L38M})_2$ by solving its high-resolution structure in the presence of halothane. Different from the designed locations, this site becomes preferred over other potential sites, including the two designed sites, for anesthetic binding after the interaction between the anesthetic and protein has occurred. The intrinsic global dynamics characteristics of this protein make the induced fitting possible, and the induced structural fitting upon anesthetic binding, in turn, modifies the local and global dynamics of the protein. For neuronal proteins, the latter aspect is likely to account for functional change of the proteins, ultimately leading to the anesthetizing effects. It should be pointed out also that we proposed more than a decade ago, based on the analysis of xenon (6), that some molecules would not normally be classified as general anesthetics due to their lack of basic properties found in common anesthetizing agents, but they nevertheless can produce anesthesia by gaining these properties after interactions with their targets takes place (e.g., induced dipole in xenon). We now show an example of a related phenomenon, namely, that the protein targets can be turned into relevant to anesthetic action only after the interaction between anesthetic and protein has taken place. The value of the designed four-α-helix bundle as a model for anesthetic targets lies not only in its structural resemblance to the ubiquitous scaffold found in many functional proteins, but also in its dynamics characteristics that are perhaps more relevant to the functional response to anesthetics (1,2).

SUPPLEMENTARY MATERIAL

To view all of the supplemental files associated with this article, visit www.biophysj.org.

The authors thank Professor Rieko Ishima for her valuable suggestions and stimulating discussions on R2 relaxation dispersion studies.

This work was supported in part by grants from the National Institutes of Health (R37GM049202 to Y.X. and P.T., R01GM056257 to PT, and P01GM055876 to Y.X. and J.S.J.).

REFERENCES

1. Szarecka, A., Y. Xu, and P. Tang. 2007. Dynamics of firefly luciferase inhibition by general anesthetics: Gaussian and anisotropic network analyses. *Biophys. J.* 93:1895–1905.
2. Tang, P., and Y. Xu. 2002. Large-scale molecular dynamics simulations of general anesthetic effects on the ion channel in the fully hydrated membrane: the implication of molecular mechanisms of general anesthesia. *Proc. Natl. Acad. Sci. USA.* 99:16035–16040.

3. Yonkunas, M. J., Y. Xu, and P. Tang. 2005. Anesthetic interaction with ketosteroid isomerase: insights from molecular dynamics simulations. *Biophys. J.* 89:2350–2356.
4. Campagna, J. A., K. W. Miller, and S. A. Forman. 2003. Mechanisms of actions of inhaled anesthetics. *N. Engl. J. Med.* 348:2110–2124.
5. Eckenhoff, R. G., and J. S. Johansson. 1997. Molecular interactions between inhaled anesthetics and proteins. *Pharmacol. Rev.* 49:343–367.
6. Xu, Y., and P. Tang. 1997. Amphiphilic sites for general anesthetic action? Evidence from 129Xe-[1H] intermolecular nuclear Overhauser effects. *Biochim. Biophys. Acta.* 1323:154–162.
7. Xu, Y., P. Tang, and S. Liachenko. 1998. Unifying characteristics of sites of anesthetic action revealed by combined use of anesthetics and non-anesthetics. *Toxicol. Lett.* 100–101:347–352.
8. Johansson, J. S., B. R. Gibney, F. Rabanal, K. S. Reddy, and P. L. Dutton. 1998. A designed cavity in the hydrophobic core of a four-α-helix bundle improves volatile anesthetic binding affinity. *Biochemistry.* 37:1421–1429.
9. Johansson, J. S., D. Scharf, L. A. Davies, K. S. Reddy, and R. G. Eckenhoff. 2000. A designed four-α-helix bundle that binds the volatile general anesthetic halothane with high affinity. *Biophys. J.* 78: 982–993.
10. Pidikiti, R., M. Shamim, K. M. Mallela, K. S. Reddy, and J. S. Johansson. 2005. Expression and characterization of a four-α-helix bundle protein that binds the volatile general anesthetic halothane. *Biomacromolecules.* 6:1516–1523.
11. Ma, D., N. R. Brandon, T. Cui, V. Bondarenko, C. Canlas, J. S. Johansson, P. Tang, and Y. Xu. 2008. Four-α-helix bundle with designed anesthetic binding pockets. Part I: Structural and dynamical analyses. *Biophys. J.* 94:4454–4463.
12. Guntert, P., C. Mumenthaler, and K. Wuthrich. 1997. Torsion angle dynamics for NMR structure calculation with the new program DYANA. *J. Mol. Biol.* 273:283–298.
13. Xu, Y., P. Tang, L. Firestone, and T. T. Zhang. 1996. 19F nuclear magnetic resonance investigation of stereoselective binding of isoflurane to bovine serum albumin. *Biophys. J.* 70:532–538.
14. Xu, Y., T. Seto, P. Tang, and L. Firestone. 2000. NMR study of volatile anesthetic binding to nicotinic acetylcholine receptors. *Biophys. J.* 78:746–751.
15. Fielding, L. 2003. NMR methods for the determination of protein-ligand dissociation constants. *Curr. Top. Med. Chem.* 3:39–53.
16. Morton, C. J., D. J. Pugh, E. L. Brown, J. D. Kahmann, D. A. Renzoni, and I. D. Campbell. 1996. Solution structure and peptide binding of the SH3 domain from human Fyn. *Structure.* 4:705–714.
17. Lipari, G., and A. Szabo. 1982. Model-free approach to the interpretation of nuclear magnetic resonance relaxation in macromolecules. 1. Theory and range of validity. *J. Am. Chem. Soc.* 104:4546–4559.
18. Lipari, G., and A. Szabo. 1982. Model-Free Approach to the Interpretation of Nuclear Magnetic Resonance Relaxation in Macromolecules. 2. Analysis of Experimental Results. *J. Am. Chem. Soc.* 104:4559–4570.
19. Mandel, A. M., M. Akke, and A. G. Palmer III. 1995. Backbone dynamics of *Escherichia coli* ribonuclease HI: correlations with structure and function in an active enzyme. *J. Mol. Biol.* 246:144–163.
20. Loria, J. P., M. Rance, and A. G. Palmer. 1999. A Relaxation-Compensated Carr-Purcell-Meiboom-Gill Sequence for Characterizing Chemical Exchange by NMR Spectroscopy. *J. Am. Chem. Soc.* 121:2331–2332.
21. Tollinger, M., N. R. Skrynnikov, F. A. Mulder, J. D. Forman-Kay, and L. E. Kay. 2001. Slow dynamics in folded and unfolded states of an SH3 domain. *J. Am. Chem. Soc.* 123:11341–11352.
22. Wishart, D. S., C. G. Bigam, J. Yao, F. Abildgaard, H. J. Dyson, E. Oldfield, J. L. Markley, and B. D. Sykes. 1995. 1H, 13C and 15N chemical shift referencing in biomolecular NMR. *J. Biomol. NMR.* 6:135–140.
23. Mulder, F. A., N. R. Skrynnikov, B. Hon, F. W. Dahlquist, and L. E. Kay. 2001. Measurement of slow (micros-ms) time scale dynamics in protein side chains by (15)N relaxation dispersion NMR spectroscopy: application to Asn and Gln residues in a cavity mutant of T4 lysozyme. *J. Am. Chem. Soc.* 123:967–975.
24. Luz, Z., and S. Meiboom. 1963. Nuclear magnetic resonance study of the protolysis of trimethylammonium ion in aqueous solution—order of the reaction with respect to solvent. *J. Chem. Phys.* 39:366–370.
25. Perazzolo, C., M. Verde, S. W. Homans, and G. Bodenhausen. 2007. Evidence of chemical exchange in recombinant major urinary protein and quenching thereof upon pheromone binding. *J. Biomol. NMR.* 38:3–9.
26. Meyer, B., and T. Peters. 2003. NMR spectroscopy techniques for screening and identifying ligand binding to protein receptors. *Angewandte Chemie International ed.* 42:864–890.
27. Davies, L. A., Q. Zhong, M. L. Klein, and D. Scharf. 2000. Molecular dynamics simulation of four-α-helix bundles that bind the anesthetic halothane. *FEBS Lett.* 478:61–66.
28. Tang, P., I. Zubryzcki, and Y. Xu. 2001. Ab initio calculation of structures and properties of halogenated general anesthetics: halothane and sevoflurane. *J. Comput. Chem.* 22:436–444.
29. Kneller, J. M., M. Lu, and C. Bracken. 2002. An effective method for the discrimination of motional anisotropy and chemical exchange. *J. Am. Chem. Soc.* 124:1852–1853.
30. Ishima, R., and D. A. Torchia. 2003. Extending the range of amide proton relaxation dispersion experiments in proteins using a constant-time relaxation-compensated CPMG approach. *J. Biomol. NMR.* 25:243–248.
31. Morris, G. M., D. S. Goodsell, R. S. Halliday, R. Huey, W. E. Hart, R. K. Belew, and A. J. Olson. 1998. Automated docking using a Lamarckian genetic algorithm and an empirical binding free energy function. *J. Comput. Chem.* 19:1639–1662.
32. Laurie, A. T., and R. M. Jackson. 2005. Q-SiteFinder: an energy-based method for the prediction of protein-ligand binding sites. *Bioinformatics.* 21:1908–1916.
33. Lopez, M. M., and D. Kosk-Kosicka. 1997. Entropy-driven interactions of anesthetics with membrane proteins. *Biochemistry.* 36:8864–8872.
34. Eckenhoff, M. F., K. Chan, and R. G. Eckenhoff. 2002. Multiple specific binding targets for inhaled anesthetics in the mammalian brain. *J. Pharmacol. Exp. Ther.* 300:172–179.
35. Liu, Z., Y. Xu, and P. Tang. 2005. Molecular dynamics simulations of C2F6 effects on gramicidin A: implications of the mechanisms of general anesthesia. *Biophys. J.* 88:3784–3791.
36. Liu, Z., Y. Xu, and P. Tang. 2006. Steered molecular dynamics simulations of Na+ permeation across the gramicidin A channel. *J. Phys. Chem.* 110:12789–12795.
37. Szarecka, A., Y. Xu, and P. Tang. 2007. Dynamics of heteropentameric nicotinic acetylcholine receptor: implications of the gating mechanism. *Proteins.* 68:948–960.
38. Krizova, H., L. Zidek, M. J. Stone, M. V. Novotny, and V. Sklenar. 2004. Temperature-dependent spectral density analysis applied to monitoring backbone dynamics of major urinary protein-I complexed with the pheromone 2- sec-butyl-4,5-dihydrothiazole. *J. Biomol. NMR.* 28:369–384.
39. Kyte, J., and R. F. Doolittle. 1982. A simple method for displaying the hydropathic character of a protein. *J. Mol. Biol.* 157:105–132.

Four-α-Helix Bundle with Designed Anesthetic Binding Pockets. Part I: Structural and Dynamical Analyses

Dejian Ma,* Nicole R. Brandon,* Tanxing Cui,* Vasyl Bondarenko,* Christian Canlas,* Jonas S. Johansson,[§¶] Pei Tang,*[†‡] and Yan Xu*[†]

*Department of Anesthesiology, [†]Department of Pharmacology, and [‡]Department of Computational Biology, University of Pittsburgh School of Medicine, Pittsburgh, Pennsylvania, 15260; [§]Department of Anesthesiology and Critical Care, and [¶]Johnson Research Foundation, Department of Biochemistry and Biophysics, University of Pennsylvania, Philadelphia, Pennsylvania 19104

ABSTRACT The four-α-helix bundle mimics the transmembrane domain of the Cys-loop receptor family believed to be the protein target for general anesthetics. Using high resolution NMR, we solved the structure (Protein Data Bank ID: 2I7U) of a prototypical dimeric four-α-helix bundle, $(A\alpha_2\text{-L1M/L38M})_2$, with designed specific binding pockets for volatile anesthetics. Two monomers of the helix-turn-helix motif form an antiparallel dimer as originally designed, but the high-resolution structure exhibits an asymmetric quaternary arrangement of the four helices. The two helices from the N-terminus to the linker (helices 1 and 1′) are associated with each other in the dimer by the side-chain ring stacking of F12 and W15 along the long hydrophobic core and by a nearly perfect stretch of hydrophobic interactions between the complementary pairs of L4, L11, L18, and L25, all of which are located at the heptad *e* position along the helix-helix dimer interface. In comparison, the axes of the two helices from the linker to the C-terminus (helices 2 and 2′) are wider apart from each other, creating a lateral access pathway around K47 from the aqueous phase to the center of the designed hydrophobic core. The site of the L38M mutation, which was previously shown to increase the halothane binding affinity by ~3.5-fold, is not part of the hydrophobic core presumably involved in the anesthetic binding but shows an elevated transverse relaxation (R_2) rate. Qualitative analysis of the protein dynamics by reduced spectral density mapping revealed exchange contributions to the relaxation at many residues in the helices. This observation was confirmed by the quantitative analysis using the Modelfree approach and by the NMR relaxation dispersion measurements. The NMR structures and Autodock analysis suggest that the pocket with the most favorable amphipathic property for anesthetic binding is located between the W15 side chains at the center of the dimeric hydrophobic core, with the possibility of two additional minor binding sites between the F12 and F52 ring stacks of each monomer. The high-resolution structure of the designed anesthetic-binding protein offers unprecedented atomistic details about possible sites for anesthetic-protein interactions that are essential to the understanding of molecular mechanisms of general anesthesia.

INTRODUCTION

Recent mutagenesis and biophysics investigations have led to the belief that general anesthetics, although structurally diverse, can interact with proteins in a specific manner (1–7). Among the proteins that are essential for neurological functions, a superfamily of neurotransmitter-gated postsynaptic receptors, known as the Cys-loop receptors, has been shown to be particularly sensitive to volatile anesthetics (8). The Cys-loop receptors are ion channels that, on activation by neurotransmitter binding, respond to fast synaptic transmissions in the central and peripheral nervous systems (9). These ion channels are formed by association of five subunits, each of which has four transmembrane (TM) domains, traversing the membrane four times as a four-α-helix bundle. Point mutations in the TM domains of the Cys-loop receptors have been found to significantly alter the receptors' sensitivity to volatile anesthetics (10), implicating certain specific interactions between the anesthetics and the TM four-α-helix bundles.

Despite numerous functional investigations, the current knowledge on the structure-function relationship of anesthetic-protein interactions is limited. This is largely because of the technical difficulties in studying membrane proteins. Although significant progress has been made in recent years (11–17), no structure at the atomistic resolution is currently available for the four-α-helix bundle TM domains of the Cys-loop receptors.

To understand the structural basis of anesthetic-protein interactions, de novo designs of prototype four-α-helix bundles with specific anesthetic binding pockets have been proposed (18,19). The original design, denoted as $(L\alpha_2)_2$, was composed of a Leu-rich hydrophobic core as part of an anesthetic binding pocket. The pocket was later modified with six Leu-to-Ala mutations (denoted as $(A\alpha_2)_2$), leading to a factor of 4.4 improvement in the halothane binding affinity. Further optimization with an additional 3.5-fold binding affinity increase was achieved in $(A\alpha_2)_2$ with the L38M point mutation (19). This newer generation four-α-helix bundle protein has a halothane dissociation constant, K_d, of 0.2 mM, which is essentially the same as the clinical concentration for halothane. Thus, $(A\alpha_2\text{-L38M})_2$ is considered one of the most

Submitted July 19, 2007, and accepted for publication January 18, 2008.

Address reprints to Professor Yan Xu or Professor Pei Tang, 2048 Biomedical Science Tower 3, 3501 Fifth Avenue, Pittsburgh, PA 15260. Tel.: 412-648-9922; Fax: 412-648-8998; E-mail: xuy@anes.upmc.edu or tangp@anes.upmc.edu.

Editor: Susan P. Gilbert.

0006-3495/08/06/4454/10 $2.00

doi: 10.1529/biophysj.107.117838

suitable models for the volatile anesthetic binding targets in the four-α-helix bundle scaffold proteins.

Because of the size difference between the Leu and Ala side chains, the improvement in anesthetic binding due to the Leu-to-Ala mutations in $(A\alpha_2)_2$ was interpreted intuitively as the result of the steric effects, namely, a possibly better fit between anesthetic molecules and their binding pockets. Nearly the same degree of improvement seen in the L38M mutation, however, was not expected fully by design. Molecular dynamics simulations of a structure model for $(A\alpha_2$-L38M$)_2$ showed that M38 was not even part of the hydrophobic core (20), suggesting that factors other than simple geometric fitting or steric restrictions between anesthetic molecules and protein pockets might be at play in determining the anesthetic binding affinity. To better understand these factors, we determined the high-resolution structure and dynamics of the bacterial-expressed $(A\alpha_2$-L1M/L38M$)_2$, which has compatible anesthetic-binding properties to the early chemically synthesized $(A\alpha_2$-L38M$)_2$ (21). The sequence of this 62-residue peptide and the heptad repeat assignments used to design the amphiphilic α-helices are shown in Fig. 1. We present here the results of our investigation in the absence of any anesthetic binding and emphasize the intrinsic structural and dynamical properties of this designed anesthetic-binding protein. The parallel studies of the same protein in the presence of halothane are presented in our Part II article in this issue (22).

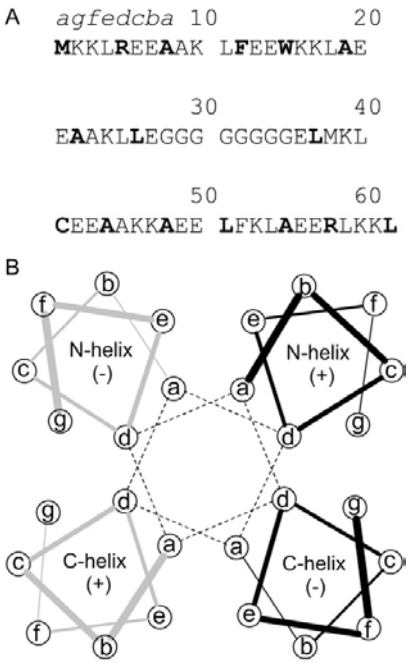

FIGURE 1 (*A*) The primary structure of $(A\alpha_2$-L1M/L38M$)_2$ four-α-helix bundle protein with the heptad position *a* and *d* positions highlighted in boldface. (*B*) Wheel diagram showing a single cycle of the heptad repeat. The left two helices belong to a monomer (*gray*) with the linker below the plane of the page, and the right two helices belong to another monomer (*black*) with the linker above the plane of the page. The direction of the helices is indicated by the + and – signs. The *a* and *d* positions on the helices form the hydrophobic core of the four-α-helix bundle.

MATERIALS AND METHODS

Sample preparation

$(A\alpha_2$-L1M/L38M$)_2$ was expressed using BL21 codon plus (DE3)-RP competent *Escherichia coli* cells in M9 minimal media and purified using reversed-phase HPLC, as described previously (21). The L1M mutation was required for the bacteria to express the protein without a fusion protein. The M9 medium contained $(^{15}NH_4)_2SO_4$ and ^{13}C-glucose as the sole ^{15}N and ^{13}C sources for uniform ^{15}N and ^{13}C labeling, respectively. The purified protein was lyophilized and stored at –20°C until use. NMR samples were prepared by dissolving lyophilized protein in a 10% D_2O/90% H_2O solution to a monomer concentration of 0.5 mM in a total volume of 300–400 μL. Approximately 1 μL of 100 mM 2,2-dimethyl-2-silapentane-5-sulfonate (DSS) sodium salt was added as an internal chemical shift reference. Typically, the unbuffered sample has a pH of 4.5. Samples prepared in this way have been stable for several months if stored at 4°C.

NMR experiments

A suite of two-dimensional and three-dimensional (3D) NMR experiments for spectral assignment, including ^{1}H-^{15}N HSQC, HNCO, HNCA, HN(CO)CA, HNCACB, CBCA(CO)NH, HBHANH, and HBHA(CO)NH, was performed at 35°C using a Bruker Avance 600 MHz spectrometer equipped with a cryoprobe (Bruker Instruments, Billerica, MA). The ^{13}C-decoupled ^{1}H-^{15}N HSQC was acquired in 1024 (^{1}H) × 128 (^{15}N) complex points, with a spectral width of 10 ppm for ^{1}H and 23 ppm for ^{15}N, and averaged for 16 scans. The HNCACB was acquired in 512 (^{1}H) × 24 (^{15}N) × 64 (^{13}C) complex points, with spectral widths of 10 ppm (^{1}H), 22 ppm (^{15}N), and 64 ppm (^{13}C), and 32 scans. The CBCA(CO)NH, HNCO, HNCA, and HN(CO)CA were each acquired in 512 (^{1}H) × 30 (^{15}N) × 64 (^{13}C) complex points, with spectral widths of 10 ppm (^{1}H) and 22 ppm (^{15}N), and 16 scans. The ^{13}C spectral widths were 64 ppm (CBCA(CO)NH), 20 ppm (HNCO and HNCA), or 24 ppm (HN(CO)CA).

The 3D HCCH-TOCSY was acquired at 35°C on a Bruker Avance 700 MHz spectrometer with a cryoprobe using the following parameters: 1024(^{1}H) × 64(^{13}C) ×128(^{1}H-indirect) points, spectral widths of 10 ppm for ^{1}H and 75 ppm for ^{13}C, carrier at H_2O resonance for ^{1}H and 41.65 ppm for ^{13}C, and 16 transients for each time increment. To assist with manual assignments and to obtain distance constraints for the structure calculation, ^{15}N-edited 3D NOESY (mixing time of 120 ms and 150 ms) and ^{13}C-edited 3D NOESY (mixing time of 75 ms and 150 ms) were performed. All four NOESY experiments had 512 (^{1}H) × 30 (^{15}N) × 64 (^{13}C) complex points and 16 scans. The spectral widths were 10 ppm for ^{1}H, 22 PM for ^{15}N, and 40 ppm for ^{13}C.

To measure the temperature effects, a series of ^{1}H-^{15}N HSQC experiments were performed at 25, 30, 35, and 40°C. The same sample as the one for the assignment experiments was used. The experiments were performed on a Bruker Avance 600 MHz spectrometer with a TXI probe. At least 30 min were given between each temperature change for the sample to equilibrate before proceeding with the experiment. HSQC at 35°C was repeated to verify that the protein had not irreversibly changed at different temperature steps. Each ^{1}H-^{15}N HSQC was acquired with 16 scans in 512 (^{1}H) × 64 (^{15}N) complex points and spectral widths of 10 ppm (^{1}H) and 22 ppm (^{15}N).

The four-α-helix bundle dynamics was measured at 35°C using ^{15}N R_1 and R_2 relaxation and ^{15}N-{^{1}H} heteronuclear NOE experiments. A Bruker

Avance 600 MHz spectrometer with a TXI probe and the Bruker standard pulse sequences were used. In the R_2 measurements, the interpulse delay between two adjacent ^{15}N 180 pulses in the CPMG sequence was 1000 μs (including a 100-μs pulse width), and thus the field strength of the CPMG refocusing pulses was 1.0 kHz. 512 (^1H) × 128 (^{15}N) complex points were taken, interleaving with and without ^1H saturation. The spectral widths were 10 ppm for ^1H and 22 ppm for ^{15}N, with 88 scans for hetNOE and 24 scans for R_1 and R_2 measurements. The R_1 was determined using 8 delay values: 20, 50, 100, 200, 400, 600, 1100, 2000 ms. The R_2 experiments used eight delay values: 17, 34, 51, 68, 85, 119, 153, 221 ms. The relaxation rate constants were obtained by exponential fitting. The hetNOE values were defined as the ratios of peak intensities with and without proton saturation. The uncertainties of hetNOE values, ΔNOE, were calculated using the well-established method (23):

$$\frac{\Delta NOE}{NOE} = \sqrt{\left(\frac{\Delta I_{sat}}{I_{sat}}\right)^2 + \left(\frac{\Delta I_{unsat}}{I_{unsat}}\right)^2}, \quad (1)$$

where I_{sat} and I_{unsat} are the peak intensities with and without proton saturation, respectively. Their uncertainties were determined from the root mean-square noise in the background regions.

Data processing and structure calculations

Data were processed using NMRPipe (24) and analyzed with NMRView (One Moon Scientific, Westfield, NJ) (25) or Sparky (26). Because of the repetitive nature of the designed amino acid sequence, the backbone spectral assignments were done semimanually with the aid of the automatic spectral assignment software packages AutoAssign (27) and MONTE (28,29). Structure calculations were performed using CYANA v2.1 (30) based on NOE restraints and Talos dihedral angle restraints from CSI (31). Hydrogen bonding restraints were added for those residues that showed not only slow exchange with water based on the small amide proton chemical shift dependence on temperature (32), but also the helical ^{13}C CSI as well as the helical backbone NOE connectivities. To calculate the dimeric structures, the restraints were duplicated for the two monomers, including 15 intermonomer long-range NOEs observed in the ^{15}N- or ^{13}C-edited NOESY spectra. The intermonomer NOEs were assigned by matching chemical shifts using an exclusion strategy. A total of 100 structures were initially calculated by CYANA. A bundle of 20 structures with the lowest target function is presented. Structures were analyzed using VMD (33) and Molmol (34).

The reduced spectral density mapping method (35) was used to qualitatively evaluate the dynamic characteristics of the protein. The reduced spectral density functions at three frequencies, $J(0)$, $J(\omega_N)$, and $J(0.87\omega_H)$, were calculated from ^{15}N R_1, R_2, and ^{15}N-{^1H} hetNOE by the following matrix conversion (35):

$$\begin{pmatrix} J(0) \\ J(\omega_N) \\ J(0.87\omega_H) \end{pmatrix} = \begin{pmatrix} -0.75\times F & 1.5\times F & -0.9\times F \\ F & 0 & -1.4\times F \\ 0 & 0 & 0.2\times B \end{pmatrix} \times \begin{pmatrix} R_1 \\ R_2 \\ \dfrac{\gamma_N\times(NOE-1)\times R_1}{\gamma_H} \end{pmatrix}, \quad (2)$$

where

$$\frac{1}{B} = \frac{\gamma_{H^N}^2\times\gamma_N^2\times h^2}{4\times r_{NH^N}^6\times 4\pi^2}\times\left(\frac{\mu_0}{4\pi}\right), \quad (3)$$

and

$$\frac{1}{F} = \frac{3}{B} + \frac{\Delta^2\times\omega_N^2}{3}. \quad (4)$$

The ^{15}N-^1H internuclear bond distance (r_{NH}) of 1.02 Å and the ^{15}N chemical shift anisotropy (Δ) of −160 ppm were assumed in the calculation of the matrix elements (35). General classification of the spectral densities was done by comparing the experimental spectral density values with the theoretical curves for the single Lorentzian motion (36):

$$J(0)\times J(\omega) = \frac{J(0)^2}{1+\left[\frac{5}{2}\times\omega\times J(0)\right]^2}. \quad (5)$$

Deviations from the single Lorentzian motion were used to determine qualitatively whether there is an exchange contribution to the relaxation at each residue. In addition, we also employed a similar qualitative method proposed earlier (37) to use $R_1\times R_2$ to effectively discriminate chemical exchange contribution from the motional anisotropy contribution in the R_2 relaxation. This method takes the advantage of the fact that the anisotropy effects on correlation times are greatly attenuated in $R_1\times R_2$ when $\omega\tau \gg 1$. After calculating the theoretical curve of $R_1\times R_2$ as a function of R_2/R_1 using the full spectral density expressions for R_1 and R_2, we compared the experimental data with the theoretical curve in the $R_1\times R_2$ dimension. Any residues with excess $R_1\times R_2$ values above the theoretical curve would suggest a nonzero R_{ex} term for those residues. To quantitatively analyze the ^{15}N relaxation parameters and ^{15}N-{^1H} heteronuclear NOE, the model-free approach (38–41) and the Modelfree program (41) were used. The model selection was first done based on the F-statistics in the R_2/R_1 diffusion analysis. Because qualitative $R_1\times R_2$ vs. R_2/R_1 analysis suggests that many residues have nonzero R_{ex} contribution in the R_2 relaxation (see Results), the global tumbling correlation time (τ_m) was determined by extensive search for the τ_m value that gives the minimum reduced χ^2 value and the least number of nonfitted residues in the Modelfree data fitting, instead of estimating from the R_2/R_1 ratio.

RESULTS

Spectral assignments

As shown in Fig. 1, this designed protein has 14 Es, 12 Ks, 11 Ls, 9 As, 8 Gs, 2 Fs, 2 Ms, 2 Rs, and one C and W, with a significant amount of segment repetitiveness (e.g., 3 EEAAK segments, 7 KL pairs, 6 EE pairs, etc.). Such sequence degeneracy made the NMR spectral assignment difficult. Fig. 2 shows a typical ^1H-^{15}N HSQC spectrum of (Aα_2-L1M/L38M)$_2$. A total of 115 peaks can be found in this spectrum, nearly twice as many as expected. It is clear that the peaks can be classified into two sets based roughly on the intensities, corresponding to two different conformations. From a suite of triple-resonance NMR experiments, 61 out of the 62 residues (except M1) for the major conformation could be positively identified and assigned (see Supplementary Material, Table S1). The final assignments were marked in Fig. 2. Approximately 90% of the side-chain resonances in the major conformation were assigned by using the 3D HCCH-TOCSY. Because many peaks in the 3D spectra for the minor conformation are too weak to be measured, only ~50% of

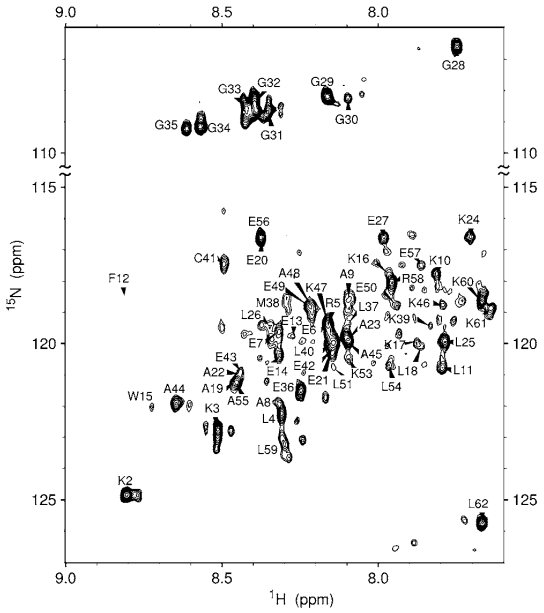

FIGURE 2 [^{1}H, ^{15}N]-HSQC of ^{13}C/^{15}N-labeled four-α-helix bundle in 90% H_2O/10% D_2O with a monomer concentration of 0.5 mM at 35°C and pH 4.5. Sixty-one of 62 backbone resonances of the major conformation are assigned with the exception of M1. F12 is visible when the contour level is lowered. On addition of anesthetics, these resonances become stronger, which allows their assignments to be easily confirmed in 3D experiments. Assignments of the major conformation are labeled using the one-letter amino acid code and the sequence number.

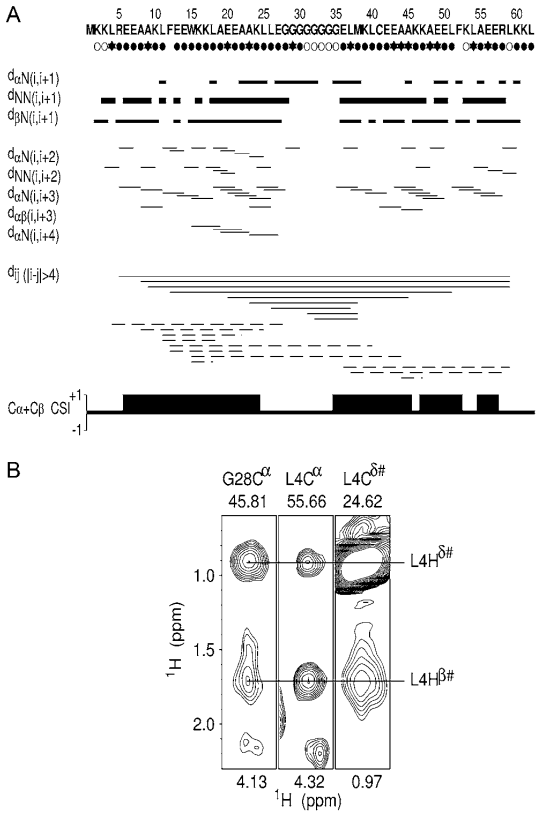

FIGURE 3 (*A*) Summary of NMR restraints determined for (Aα_2-L1M/L38M)$_2$ four-α-helix bundle. Sequential and midrange NOE connectivity is linked by the line segments, with the line thickness proportional to the crosspeak intensity. For the long-range NOE [$dij(|i-j| > 4)$], the solid lines represent intramonomer NOEs, and the dashed lines represent intermonomer NOEs. The chemical shift index obtained from combining C_α and C_β shifts is also shown. The amide proton chemical shift dependence on temperature is marked under the sequence. Solid circle, solid star, and open circle represent slow, medium, and fast exchange, respectively. (*B*) An example of intersubunit NOESY assignment. Shown here are strip plots from ^{13}C-edited 3D NOESY showing intersubunit NOE crosspeaks between G28 and L4. Such crosspeaks cannot arise from the same subunit.

reliable assignments for the second set of signals can be made. Therefore, the current NMR data set does not allow a complete structure and dynamics characterization of the minor conformation. Possible sources of some of the minor peaks include residual impurity in the protein preparation, a very small population of the four-α-helix in the monomer state, or different forms of dimers (e.g., parallel instead of antiparallel dimers). In this study, we focus only on the major conformation.

High-resolution structures of four-α-helix bundle

The sequential and midrange NOE connectivity in the major conformation, the chemical shift indices (CSI), and the temperature dependence of amide proton chemical shift are summarized in Fig. 3. Similar to using line segments for short- and mid-range NOEs, long-range NOEs ($|i-j| > 4$) are also indicated by lines connecting the two interacting residues. Solid and dashed lines are used to distinguish the intra- and inter-monomer long-range NOEs, respectively. Two helical segments, from E7 to E27 and from E36 to R58, are clearly discernible from the NOE connectivity. The C_α and C_β CSI confirms that at least the segments from E6 to K24 and from E36 to E57 are helical. The first 5 residues from the N-terminus, the last 5 residues to the C terminus, and 11 residues in the center from L25 to G35 have C_α and C_β chemical shifts not significantly different from the random-coil values. The CSI data also suggest a certain degree of disruption in the α-helicity near F52.

Fig. 4 *A* shows a bundle of 20 structures calculated using the restraints derived from the NMR peaks in the major conformation. The atomic coordinates of the structures have been deposited in Protein Data Bank (PDB: 2I7U). The statistics of the structural calculation are given in Table 1. The overall backbone RMSD, including the flexible and less-

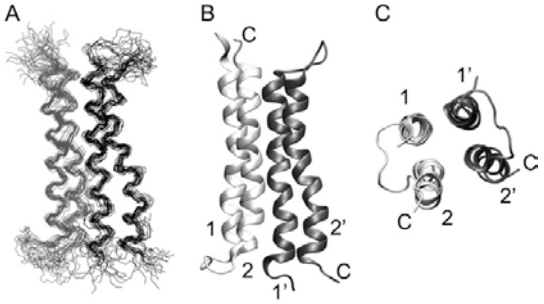

FIGURE 4 (*A*) The backbones of 20 lowest-energy structures of ($A\alpha_2$-L1M/L38M)$_2$, fitted from E6 to E27 and from E36 to E57. Two monomers are colored gray and black for distinction. (*B*) Side view of ($A\alpha_2$-L1M/L38M)$_2$ structure in ribbon representation, showing distortion in helix 2 and helix 2′. (*C*) Top view of ($A\alpha_2$-L1M/L38M)$_2$ structure in ribbon representation. Notice the overall asymmetry in the arrangement of the four helices. The N-terminal helices are labeled as 1 and 1′, and the C-terminal helices as 2 and 2′.

structured terminal and linker regions, is 1.77 ± 0.24 Å. The backbone RMSD for all four helical regions combined is 0.82 ± 0.17 Å. Further improvement of backbone RMSD by residual dipole coupling (RDC) was not attempted because high sequence redundancy and spectral overlap in the IPAP-type spectra would not provide the needed accuracy in the RDC frequency difference measurements.

Several features are readily apparent in the calculated structures: 1), Because of the random-coil structures at the two termini, the helical segments are somewhat shorter than initially designed. 2), The dimer is antiparallel based on the long-range NOEs between the two monomers (Fig. 3, *dashed lines*). 3), There is a super-helical twist (coiled-coil) leading to slight deformation of the helices (Fig. 4 *B*). 4), As originally designed, the first helix from the N-terminus to the linker (helix 1) is associated with the other first helix (helix 1′) in the dimer in an antiparallel fashion (likewise, helix 2 and helix 2′ are associated with each other), such that the hydrophobic surfaces composed of the *a* and *d* positions in the helical heptad are facing each other in the hydrophobic core. 5), The tertiary and quaternary arrangements of the four helices are not completely symmetrical (Fig. 4 *C*). Helices 1 and 1′ are closer to each other than helices 2 and 2′. As will be discussed later, this feature might be essential for creating a lateral pathway for amphiphilic anesthetics to enter the designed hydrophobic core.

TABLE 1 Statistics of 20 NMR structures with the lowest target functions

NMR structure	Statistic
Restraints per monomer	
NOE distances	
Intraresidue	168
Short range (|i–j| = 1)	133
Medium range (1 < | i–j| ≤ 4)	82
Long range (|i–j| > 4)	17
Dimer (intermonomer)	15
Dihedral angles	90
Hydrogen bonds	40
Residual upper limit constraint violations > 0.5 Å	0
Residual dihedral angle constraint violations > 5°	0
Backbone RMSD	
Residues in helical regions only (6–27, 36–58)	0.82 ± 0.17 Å
All residues (1–62)	1.77 ± 0.24 Å
Heavy atom RMSD	
Residues in helical regions only (6–27, 36–58)	1.38 ± 0.20 Å
All residues (1–62)	2.22 ± 0.27 Å
Ramachandran plot	
Residues in most favored regions	92.8%
Residues in allowed regions	6.5%
Residues in disallowed regions	0.7%

Changes in chemical shifts of the amide protons at different temperatures are consistent with both the NOE connectivity and the CSI result. As expected, the slope of chemical shift change with temperature is small for residues in the helical regions, indicating the existence of backbone hydrogen bonding (32), whereas those with large chemical shift changes with temperature are in the glycine linker region. Among the residues associated with the helices, those whose chemical shifts are least sensitive to temperature tend to be in the hydrophobic core of the protein. These data further validate the spectral assignments and confirm that the four-α-helix bundle is a dimer with hydrophobic faces of the monomers associating with each other to exclude the water in the hydrophobic core.

Backbone dynamics

The R_1, R_2, and hetNOE data for the backbone amide ^{15}N of ($A\alpha_2$-L1M/L38M)$_2$, the reduced spectral density mapping results, the R_2/R_1 ratio, and the graphical analyses of $J(\omega_N)$ as a function $J(0)$ and $R_1 \times R_2$ as a function of R_2/R_1 are shown in Fig. 5. The dynamics in the two termini and the loop regions are significantly different from that in the helices. The R_1 values cluster in the 1.8–2.3 s^{-1} range throughout the sequence, with only small variations in the loop region and near the termini. In contrast, R_2 and hetNOE values are significantly smaller in these regions (3.0–6.3 s^{-1}) than in the helices (10.1–13.7 s^{-1}), suggesting considerable backbone flexibility in the loop and the termini. Two residues, M38 and C41, have noticeably higher R_2 values than their adjacent residues (17.5 and 17.3 s^{-1}, respectively), indicating considerable contributions from exchange in the R_2 relaxation for these residues. The hetNOE values are above 0.7 for all residues in the α-helical regions. Initial estimates of the τ_m value of the four-α-helix bundle, based on the R_2/R_1 ratio and averaged over the residues in the α-helical regions, is 5.6 ± 0.5 ns at 600 MHz. Because many residues have nonzero R_{ex} contributions to the R_2 relaxation (see below). The τ_m value should be determined independent of the R_2/R_1 ratio.

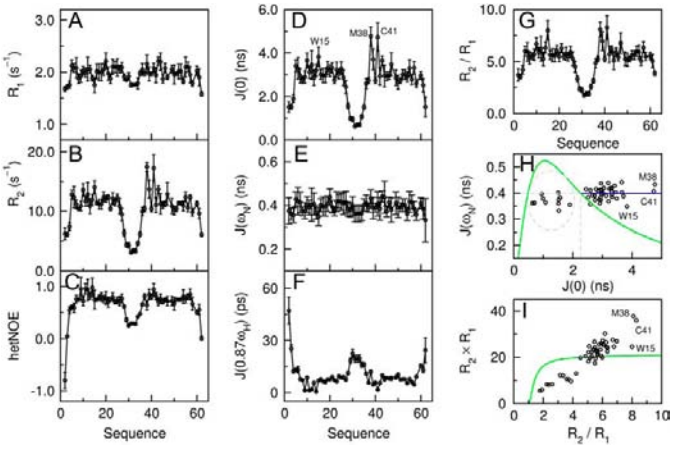

FIGURE 5 Dynamics analysis of the backbone amide ^{15}N of (Aα_2-L1M/L38M)$_2$ in H_2O at 35°C. Longitudinal and transverse relaxation rate constants, R_1 and R_2, and ^{15}N-{^1H} NOE values are shown in *A*, *B*, and *C*, respectively. The reduced spectral density functions, $J(0)$, $J(\omega_N)$, and $J(0.87\omega_H)$, are shown in *D*, *E*, and *F*, respectively. R_2/R_1 ratio and the correlation between $J(\omega_N)$ and $J(0)$ and between $R_1 \times R_2$ and R_2/R_1 are shown in *G*, *H*, and *I*, respectively. The relaxation data were acquired at 600 MHz. Error bars are either the standard errors in the least-squares fit to the exponential decay function (for R_1 and R_2) or the calculated uncertainties (for NOE). (*H*) residues inside the dashed ellipse are from the loop region and the termini. The solid green curves describe the dependence of $J(\omega_N)$ on $J(0)$ in the limiting case of single Lorentzian motion. Points to the right of the green curve suggest the presence of exchange and/or anisotropic contribution to the relaxation. (*I*) the contribution of exchange and anisotropy can be effectively isolated because the dependence of $R_1 \times R_2$ on correlation times is greatly attenuated. Experimental data above the theoretical curve (*solid green curve*) suggest the presence of R_{ex} contribution to the R_2 relaxation.

Qualitative analysis of the relaxation data using the reduced spectral density mapping method clearly indicates a complex dynamics profile of the dimeric (Aα_2-L1M/L38M)$_2$. The points within the dashed ellipse in Fig. 5 *H* are those from the loop and terminal residues, which are less structured and highly flexible. Many residues in the helices exhibit a rightward shift from the theoretical single Lorentzian $J(\omega_N)$ vs. $J(0)$ curve, which is equivalent to the case of isotropic tumbling in the model-free analysis. The rightward shift is an indication that other motions, either anisotropic motion and/or chemical and conformational exchange, contribute to the R_2 relaxation in addition to the global tumbling and internal local motion. Since $J(\omega_N)$ is dominated by R_1 and hetNOE and is independent of R_{ex} (see Eq. 2), the intersection between the single Lorentzian curve and the average $J(\omega_N)$ values (horizontal line in Fig. 5 *H*) yields a $J(0)$ value corresponding to an apparent correlation time should the protein tumble isotropically. This estimate also gives a τ_m value of ~5.6 ns. To distinguish exchange from anisotropy contributions, we compared experimental $R_1 \times R_2$ with the corresponding theoretical values (Fig. 5 *I*). If $R_{ex} = 0$, the experimental $R_1 \times R_2$ would be smaller than the theoretical values by a factor of S^4, where S^2 is the generalized order parameter. A nonzero R_{ex} would displace the experimental values vertically by $R_1 \times R_{ex}$. As shown in Fig. 5 *I*, many residues have nonzero R_{ex} contributions to R_2, with M38 and C41 being distinctly different from the others. We confirmed the presence of exchange contribution to relaxation by the R_2 dispersion measurements, in which the relaxation-compensated, constant-time Carr-Purcell-Meiboom-Gill (CPMG) sequences (42,43) were used to determine the R_2 dependence on the CPMG frequency. Detailed analyses of the relaxation dispersion data and of the anesthetic effects on the conformational exchange are discussed in Part II (22). Quantitative analyses using the Lipari-Szabo model-free approach with the NMR structure and the relaxation data as input are depicted in Fig. 6. The model selection criteria based on F-statistics suggested that the isotropic tumbling model fit the relaxation data of the apo protein better than the anisotropic model. In agreement with the qualitative assessment, the majority of residues in the helical region can be fit best with

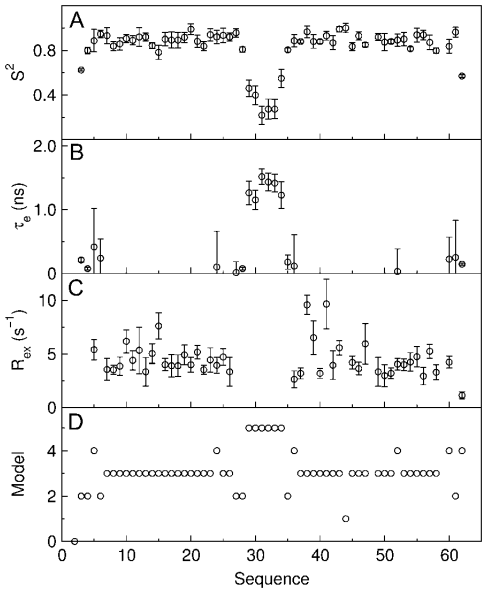

FIGURE 6 Quantitative model-free analyses of the dynamics of (Aα_2-L1M/L38M)$_2$ using Modelfree program: (*A*) the generalized squared-order parameter (S^2); (*B*) the local correlation time (τ_e), (*C*) the exchange term (R_{ex}), and (*D*) the models used to fit the data for each residue. Error bars are standard errors from the fitting.

Model 3, which includes a nonzero R_{ex} term indicative of exchange contribution to the dynamics. Again, the most noticeable dynamical hotspot is the large R_{ex} term for residues M38 and C41, suggesting that the L38M mutation that renders a 3.5-fold increase in halothane binding affinity is at an intrinsically dynamic site of the protein. Note also that the entire loop region can be described only by Model 5, which assumes internal backbone motions on multiple timescales. Thus, the basic assumption for the model-free approach does not strictly apply to the residues in the loop region. By searching for the τ_m value that gives the minimum reduced χ^2 value and the least number of nonfitted residues, Modelfree calculations yielded a global tumbling time of 5.1 $\pm$ 0.1 ns, corresponding to a protein size of 11–12 kDa. Because the (Aα_2-L1M,L38M) monomer has a molecular mass of 6.86 kDa, the dynamics data confirm that the major peaks used for the model-free calculations indeed arise from the dimeric form of the four-α-helix bundle.

DISCUSSION

We have solved the high-resolution structure of a designed dimeric four-α-helix-bundle protein that was found previously to interact specifically with volatile anesthetics with relatively high binding affinities. Since the four-α-helix bundle is a ubiquitous scaffold in functional proteins, our designed protein is considered to be a suitable model for anesthetic binding targets. The high and specific anesthetic binding affinity to (Aα_2-L1M/L38M)$_2$ suggests that certain intrinsic structural and dynamical features of this particular protein are essential for volatile anesthetic-protein interaction. Our NMR structure and the dynamics data have revealed some of these features that might be important for anesthetic-protein interaction in general.

Spatial asymmetry of the four helices

An unexpected feature in the high-resolution structure is the overall asymmetry in the spatial arrangement of the four helices. Although the final structures show a two-fold symmetry, which is consistent with the fact that the NMR peaks in the helical region give a tumbling rate of a dimer and that each peak arises from the same residue in the two monomers, the quaternary arrangement of helices 1 and 1′ is different from that of helices 2 and 2′, as shown in Fig. 4 *C*. Careful examinations of the detailed side-chain packing of helices 1 and 1′ shows a stack of aromatic rings from two F12 and two W15 residues in the hydrophobic core, as shown in Fig. 7 *A*. Moreover, there is excellent steric complementarity of eight leucine residues (L4, L11, L18, and L25), all of which occupy the heptad *e* position at the interface of helices 1 and 1′ (Fig. 7 *A*). The accumulation of van der Waals interactions, in addition to the hydrophobic interactions, holds helices 1 and 1′ together in an antiparallel fashion. In contrast, helices 2 and 2′ are wider apart from each other. The complementarity between the hydrophobic side chains of helices 2 and 2′ is disrupted in the middle of the helical interface because K47 is at the heptad *e* position. The side chains of the two K47 collide at nearly the same level (see Fig. 7). The electrostatic repulsion of the charged side chains forces helix 2 to distort slightly. Deformation of helix 2 is also clearly evident in the CSI result in Fig. 3.

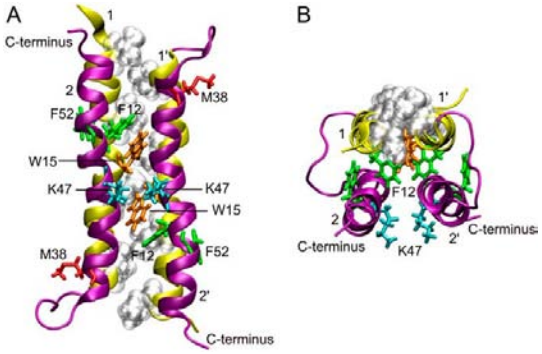

FIGURE 7 Side view (*A*) and top view (*B*) of the (Aα_2-L1M/L38M)$_2$ structure in ribbon representation, showing the relationship of important side chains. Helices 1 and 1′ are colored in yellow and helices 2 and 2′ are colored in purple. The complementary L4, L11, L18, and L25 are depicted in gray in van der Waals spheres representation. F12, F52, W15, M38, and K47 are shown in licorice representation. F12 and F52 are shown in green, W15 in orange, M38 in red, and K47 in cyan.

Lateral accessibility to binding site

It is very likely that the two K47 in the middle of helix 2 play an important role in the high-affinity anesthetic binding in this designed four-α-helix bundle. One of the most essential properties of general anesthetics is their tendency to preferentially interact with amphipathic molecular targets (4,44,45). As shown in Fig. 7, two K47 residues in the dimeric (Aα_2-L1M/L38M)$_2$ are at the level midpoint to the two W15 side chains. This creates an ideal amphipathic environment. Most importantly, the opening in the middle of the helices 2 and 2′ interface creates a lateral access pathway for anesthetics from the aqueous phase to enter the site between the two W15 side chains in the center of the long hydrophobic core without passing through either end of the four helix bundle. Thus, the predominant anesthetic binding site, which has now been confirmed experimentally (see Part II (22)), is between the two W15 aromatic side chains, bordered additionally by A44 and A48 at the heptad *a* and *e* positions at the same level. A closer examination of this particular binding pocket also predicts that among the six L-to-A mutations to convert (Lα_2)$_2$ to (Aα_2)$_2$ (18), the two L44A and the two L48A are the most crucial ones responsible for the increase in the halothane binding affinity. The bulkier side chains of leucine would require significantly larger distortion

of helix 2 to accommodate a halothane molecule in this pocket.

Importance of aromatic side chains

It is interesting to further analyze the orientations of aromatic side chains from F12, W15, and F52 in the structure. All three residues are located in the helical region. The intensities of these residues in the HSQC spectrum are significantly weaker than other resonances in the major conformation, indicative of intermediate conformational exchange. It is likely that, in response to helix-2 global movement at the level of K47, W15 side chains adapt different orientations in the hydrophobic core when the cavity between the two W15 side chains is not occupied, as suggested previously by a fluorescence quenching study (21). This re-orientation of the bulky W15 side chains will inevitably affect W15 backbone dynamics. As we have found in the study with halothane (see Part II (22)), the presence of a bound halothane stabilizes the W15 side chains, resulting in not only halothane concentration-dependent shift of W15 backbone amide ^{1}H and ^{15}N resonance, but also an increase in peak intensity for W15 in the HSQC spectrum with halothane. The increases in peak intensity after halothane binding strongly suggest that the weak intensity of W15 in the absence of halothane is indeed the result of intermediate conformation exchange.

In the NMR structure, F52 seems to be ''out of place''. Although it is designed to be at the heptad *g* position, which is supposed to be at the interface between helix 1 and helix 2 of the same monomer, the F52 side chain is extended outward, pointing into the aqueous phase. This is the direct consequence of the helix 2 distortion from K47 to the C-terminus. Having a highly hydrophobic side chain oriented into the aqueous phase is energetically unfavorable. Hence, it is expected that the F52 side chain experiences a tremendous amount of fluctuations, which leads to greatly reduced F52 resonance in HSQC.

Because of its ''odd'' location, the F52 side chain can only be stabilized by the ring stacking with the side chain of F12 in the same monomer. This affords the possibility of another two plausible anesthetic binding sites in $(A\alpha_2\text{-L1M/L38M})_2$, namely, the space sandwiched by the F12 and F52 side chains. However, because of the extremely hydrophobic rather than amphipathic nature of the phenylalanine residues, these two additional anesthetic binding sites would be not as favorable as the major binding site between the two W15 side chains.

Implications of dynamics in anesthetic binding

$(A\alpha_2\text{-L1M/L38M})_2$ exhibits a very interesting motional profile as measured by the ^{15}N backbone dynamics. As shown in Fig. 6, our designed four-α-helix bundle is a very dynamic protein in the absence of a bound anesthetic. Judged by the nonzero R_{ex} terms, it can be concluded that neither of the two helices behave like a rigid rod. Instead, as discernible in the NMR structure, the well known coiled-coil structural twist commonly found in four-α-helix bundles might result from the underlying superhelical twist motion. Indeed, when we subject the NMR structure of $(A\alpha_2\text{-L1M/L38M})_2$ to normal mode analysis using ElNemo (46,47), we found that the global mode (the first nonzero mode) is dominated by a large-amplitude winding and unwinding helical twist motion. Such coiled-coil twist may prove to be the universal dynamic characteristic of four-α-helix bundles. The fact that so many structurally diverse anesthetics can interact with so many proteins in a similar way suggests the possibility of an ''induced fit'' between small volatile anesthetic molecules and their protein targets. The protein's intrinsic ability to be flexible enough to accommodate necessary conformational changes upon anesthetic binding is exemplified in $(A\alpha_2\text{-L1M/L38M})_2$. It is tempting to speculate that the coupling between the supercoil twisting global dynamics and the structurally defined amphipathic lateral pathway leading to the binding pocket will facilitate the binding on-rate when the binding site(s) are empty. As will be shown in the study with anesthetics (see Part II (22)), the presence of halothane in the binding site reduces the dynamics of $(A\alpha_2\text{-L1M/L38M})_2$, thus decreasing the off-rate of the bound halothane. Our structural and dynamic data on the apo protein seem to suggest the possibility of interplay between structural and global dynamics as contributing factors for anesthetic-protein interactions. This possibility is further explored in Part II (22).

In conclusion, to our knowledge, we have solved the first high-resolution structure of a designed anesthetic-binding protein having the common four-α-helix bundle scaffold. In the apo form, the protein is highly dynamic, with a clear indication of conformational heterogeneity on the NMR timescale. The major conformation is an antiparallel dimer showing two helices from the N-terminus to the linker packed neatly with a long stretch of eight complementary leucine side chains at the heptad *e* positions and four aromatic rings in the hydrophobic core. The two helices from the linker to the C-terminus are less well packed because of two charged K47 side chains being too close to each other. The distortion of the second helix from a straight helix creates a lateral access pathway for general anesthetics to reach the amphipathic binding site between the two W15 side chains. The global protein dynamics, coupled with the mobility near the flexible glycine linker, seems to contribute to the specific anesthetic binding affinity to this designed protein.

SUPPLEMENTARY MATERIAL

To view all of the supplemental files associated with this article, visit www.biophysj.org.

This work was supported in part by grants from the National Institutes of Health (R37GM049202 to Y.X. and P.T., R01GM056257 to P.T., and P01GM055876 to Y.X. and J.S.J.).

REFERENCES

1. Tang, P., and Y. Xu. 2002. Large-scale molecular dynamics simulations of general anesthetic effects on the ion channel in the fully hydrated membrane: the implication of molecular mechanisms of general anesthesia. *Proc. Natl. Acad. Sci. USA.* 99:16035–16040.
2. Szarecka, A., Y. Xu, and P. Tang. 2007. Dynamics of firefly luciferase inhibition by general anesthetics: Gaussian and anisotropic network analyses. *Biophys. J.* 93:1895–1905.
3. Yonkunas, M. J., Y. Xu, and P. Tang. 2005. Anesthetic interaction with ketosteroid isomerase: insights from molecular dynamics simulations. *Biophys. J.* 89:2350–2356.
4. Xu, Y., P. Tang, and S. Liachenko. 1998. Unifying characteristics of sites of anesthetic action revealed by combined use of anesthetics and non-anesthetics. *Toxicol. Lett.* 100–101:347–352.
5. Xu, Y., V. E. Yushmanov, and P. Tang. 2002. NMR studies of drug interaction with membranes and membrane-associated proteins. *Biosci. Rep.* 22:175–196.
6. Campagna, J. A., K. W. Miller, and S. A. Forman. 2003. Mechanisms of actions of inhaled anesthetics. *N. Engl. J. Med.* 348:2110–2124.
7. Eckenhoff, R. G., and J. S. Johansson. 1997. Molecular interactions between inhaled anesthetics and proteins. *Pharmacol. Rev.* 49:343–367.
8. Franks, N. P., and W. R. Lieb. 1994. Molecular and cellular mechanisms of general anaesthesia. *Nature.* 367:607–614.
9. Karlin, A. 2002. Emerging structure of the nicotinic acetylcholine receptors. *Nat. Rev. Neurosci.* 3:102–114.
10. Mihic, S. J., Q. Ye, M. J. Wick, V. V. Koltchine, M. D. Krasowski, S. E. Finn, M. P. Mascia, C. F. Valenzuela, K. K. Hanson, E. P. Greenblatt, R. A. Harris, and N. L. Harrison. 1997. Sites of alcohol and volatile anaesthetic action on GABA(A) and glycine receptors. *Nature.* 389:385–389.
11. Unwin, N. 2005. Refined structure of the nicotinic acetylcholine receptor at 4A resolution. *J. Mol. Biol.* 346:967–989.
12. Ma, D., Z. Liu, L. Li, P. Tang, and Y. Xu. 2005. Structure and dynamics of the second and third transmembrane domains of human glycine receptor. *Biochemistry.* 44:8790–8800.
13. Opella, S. J., and F. M. Marassi. 2004. Structure determination of membrane proteins by NMR spectroscopy. *Chem. Rev.* 104:3587–3606.
14. Yushmanov, V. E., Y. Xu, and P. Tang. 2003. NMR structure and dynamics of the second transmembrane domain of the neuronal acetylcholine receptor β 2 subunit. *Biochemistry.* 42:13058–13065.
15. Yushmanov, V. E., P. K. Mandal, Z. Liu, P. Tang, and Y. Xu. 2003. NMR structure and backbone dynamics of the extended second transmembrane domain of the human neuronal glycine receptor α1 subunit. *Biochemistry.* 42:3989–3995.
16. Tang, P., P. K. Mandal, and Y. Xu. 2002. NMR structures of the second transmembrane domain of the human glycine receptor α (1) subunit: model of pore architecture and channel gating. *Biophys. J.* 83:252–262.
17. Szarecka, A., Y. Xu, and P. Tang. 2007. Dynamics of heteropentameric nicotinic acetylcholine receptor: implications of the gating mechanism. *Proteins.* 68:948–960.
18. Johansson, J. S., B. R. Gibney, F. Rabanal, K. S. Reddy, and P. L. Dutton. 1998. A designed cavity in the hydrophobic core of a four-α-helix bundle improves volatile anesthetic binding affinity. *Biochemistry.* 37:1421–1429.
19. Johansson, J. S., D. Scharf, L. A. Davies, K. S. Reddy, and R. G. Eckenhoff. 2000. A designed four-α-helix bundle that binds the volatile general anesthetic halothane with high affinity. *Biophys. J.* 78:982–993.
20. Davies, L. A., Q. Zhong, M. L. Klein, and D. Scharf. 2000. Molecular dynamics simulation of four-α-helix bundles that bind the anesthetic halothane. *FEBS Lett.* 478:61–66.
21. Pidikiti, R., M. Shamim, K. M. Mallela, K. S. Reddy, and J. S. Johansson. 2005. Expression and characterization of a four-α-helix bundle protein that binds the volatile general anesthetic halothane. *Biomacromolecules.* 6:1516–1523.
22. Cui, T., V. Bondarenko, D. Ma, C. Canlas, N. R. Brandon, J. S. Johansson, Y. Xu, and P. Tang. Four-α-helix bundle with designed anesthetic binding pockets. Part II: Halothane effects on structure and dynamics. *Biophys. J.* 94:4464–4472.
23. Farrow, N. A., R. Muhandiram, A. U. Singer, S. M. Pascal, C. M. Kay, G. Gish, S. E. Shoelson, T. Pawson, J. D. Forman-Kay, and L. E. Kay. 1994. Backbone dynamics of a free and phosphopeptide-complexed Src homology 2 domain studied by 15N NMR relaxation. *Biochemistry.* 33:5984–6003.
24. Delaglio, F., S. Grzesiek, G. W. Vuister, G. Zhu, J. Pfeifer, and A. Bax. 1995. NMRPipe: a multidimensional spectral processing system based on UNIX pipes. *J. Biomol. NMR.* 6:277–293.
25. Johnson, B. A. 2004. Using NMRView to visualize and analyze the NMR spectra of macromolecules. *Methods Mol. Biol.* 278:313–352.
26. Goddard, T. D., and D. G. Kneller. SPARKY 3. University of California, San Francisco.
27. Huang, Y. J., G. V. Swapna, P. K. Rajan, H. Ke, B. Xia, K. Shukla, M. Inouye, and G. T. Montelione. 2003. Solution NMR structure of ribosome-binding factor A (RbfA), a cold-shock adaptation protein from *Escherichia coli*. *J. Mol. Biol.* 327:521–536.
28. Hitchens, T. K., J. A. Lukin, Y. Zhan, S. A. McCallum, and G. S. Rule. 2003. MONTE: an automated Monte Carlo based approach to nuclear magnetic resonance assignment of proteins. *J. Biomol. NMR.* 25:1–9.
29. Hitchens, T. K., S. A. McCallum, and G. S. Rule. 2003. Data requirements for reliable chemical shift assignments in deuterated proteins. *J. Biomol. NMR.* 25:11–23.
30. Guntert, P., C. Mumenthaler, and K. Wuthrich. 1997. Torsion angle dynamics for NMR structure calculation with the new program DYANA. *J. Mol. Biol.* 273:283–298.
31. Cornilescu, G., F. Delaglio, and A. Bax. 1999. Protein backbone angle restraints from searching a database for chemical shift and sequence homology. *J. Biomol. NMR.* 13:289–302.
32. Baxter, N. J., and M. P. Williamson. 1997. Temperature dependence of 1H chemical shifts in proteins. *J. Biomol. NMR.* 9:359–369.
33. Humphrey, W., A. Dalke, and K. Schulten. 1996. VMD: visual molecular dynamics. *J. Mol. Graph.* 14:33–38.
34. Koradi, R., M. Billeter, and K. Wuthrich. 1996. MOLMOL: a program for display and analysis of macromolecular structures. *J. Mol. Graph.* 14:51–55.
35. Lefevre, J. F., K. T. Dayie, J. W. Peng, and G. Wagner. 1996. Internal mobility in the partially folded DNA binding and dimerization domains of GAL4: NMR analysis of the N-H spectral density functions. *Biochemistry.* 35:2674–2686.
36. Krizova, H., L. Zidek, M. J. Stone, M. V. Novotny, and V. Sklenar. 2004. Temperature-dependent spectral density analysis applied to monitoring backbone dynamics of major urinary protein-I complexed with the pheromone 2- sec-butyl-4,5-dihydrothiazole. *J. Biomol. NMR.* 28:369–384.
37. Kneller, J. M., M. Lu, and C. Bracken. 2002. An effective method for the discrimination of motional anisotropy and chemical exchange. *J. Am. Chem. Soc.* 124:1852–1853.
38. Fushman, D., S. Cahill, and D. Cowburn. 1997. The main-chain dynamics of the dynamin pleckstrin homology (PH) domain in solution: analysis of 15N relaxation with monomer/dimer equilibration. *J. Mol. Biol.* 266:173–194.
39. Lipari, G., and A. Szabo. 1982. Model-free approach to the interpretation of nuclear magnetic resonance relaxation in macromolecules. 1. Theory and range of validity. *J. Am. Chem. Soc.* 104:4546–4559.
40. Lipari, G., and A. Szabo. 1982. Model-free approach to the interpretation of nuclear magnetic resonance relaxation in macromolecules. 2. Analysis of experimental results. *J. Am. Chem. Soc.* 104:4559–4570.
41. Mandel, A. M., M. Akke, and A. G. Palmer III. 1995. Backbone dynamics of *Escherichia coli* ribonuclease HI: correlations with structure and function in an active enzyme. *J. Mol. Biol.* 246:144–163.

42. Loria, J. P., M. Rance, and A. G. Palmer. 1999. A relaxation-compensated Carr-Purcell-Meiboom-Gill sequence for characterizing chemical exchange by NMR spectroscopy. *J. Am. Chem. Soc.* 121:2331–2332.

43. Tollinger, M., N. R. Skrynnikov, F. A. Mulder, J. D. Forman-Kay, and L. E. Kay. 2001. Slow dynamics in folded and unfolded states of an SH3 domain. *J. Am. Chem. Soc.* 123:11341–11352.

44. Tang, P., J. Hu, S. Liachenko, and Y. Xu. 1999. Distinctly different interactions of anesthetic and nonimmobilizer with transmembrane channel peptides. *Biophys. J.* 77:739–746.

45. Xu, Y., and P. Tang. 1997. Amphiphilic sites for general anesthetic action? Evidence from ^{129}Xe-{^{1}H} intermolecular nuclear Overhauser effects. *Biochim. Biophys. Acta.* 1323:154–162.

46. Suhre, K., J. Navaza, and Y. H. Sanejouand. 2006. NORMA: a tool for flexible fitting of high-resolution protein structures into low-resolution electron-microscopy-derived density maps. *Acta Crystallogr.* 62:1098–1100.

47. Suhre, K., and Y. H. Sanejouand. 2004. ElNemo: a normal mode web server for protein movement analysis and the generation of templates for molecular replacement. *Nucleic Acids Res.* 32:W610–W614.

Anesthetic Modulation of Protein Dynamics: Insight from an NMR Study

Christian G. Canlas,[†] Tanxing Cui,[†] Ling Li,[†] Yan Xu,[†,‡] and Pei Tang*[,†,‡,§]

Departments of Anesthesiology, Pharmacology and Chemical Biology, and Computational Biology, University of Pittsburgh School of Medicine, Pittsburgh, Pennsylvania 15261

Received: July 6, 2008; Revised Manuscript Received: August 12, 2008

Mistic (membrane integrating sequence for translation of integral membrane protein constructs) comprises the four-α-helix bundle scaffold found in the transmembrane domains of the Cys-loop receptors that are plausible targets for general anesthetics. Nuclear magnetic resonance (NMR) studies of anesthetic halothane interaction with Mistic in dodecyl phosphocholine (DPC) micelles provide an experimental basis for understanding molecular mechanisms of general anesthesia. Halothane was found to interact directly with Mistic, mostly in the interfacial loop regions. Although the presence of halothane had little effect on Mistic structure, ^{15}N NMR relaxation dispersion measurements revealed that halothane affected Mistic's motion on the microsecond−millisecond time scale. Halothane shifted the equilibrium of chemical exchange in some residues and made the exchange faster or slower in comparison to the original state in the absence of halothane. The motion on the microsecond−millisecond time scale in several residues disappeared in response to the addition of halothane. Most of the residues experiencing halothane-induced dynamics changes also exhibited profound halothane-induced changes in chemical shift, suggesting that dynamics modification of these residues might result from their direct interaction with halothane molecules. Allosteric modulation by halothane also contributed to dynamics changes, as reflected in residues I52 and Y82 where halothane introduction brought about dynamics changes but not chemical shift changes. The study suggests that inhaled general anesthetics could act on proteins via altering protein motion on the microsecond−millisecond time scale, especially motion in the flexible loops that link different alpha helices. The validation of anesthetic effect on protein dynamics that are potentially correlated with protein functions is a critical step in unraveling the mechanisms of anesthetic action on proteins.

Introduction

The molecular mechanism of general anesthesia remains unsolved. The current consensus is that inhaled anesthetics act on the central nervous system (CNS) and affect neural networks. A wealth of molecular biology and electrophysiology data has demonstrated that neurotransmitter-gated ion channels, particularly Cys-loop receptors,[1,2] are plausible targets for general anesthetics. These ion channels are sensitive to volatile anesthetics at clinically effective concentrations. The channel functions could be inhibited or potentiated significantly by general anesthetics in the excitatory (nicotinic acetylcholine and serotonin type 3) or inhibitory ($GABA_A$ and glycine) receptors, respectively.[1,2] It is, however, still debatable where anesthetic binding sites reside and whether the traditional lock-and-key-binding paradigm is applicable for anesthetics interacting with proteins. We have recently proposed a hypothesis of anesthetic action based on protein global dynamics[3] and contend that the *necessary* and *sufficient* condition for general anesthetics, as well as other low-affinity drugs, to exert their action on proteins is to disrupt the modes of motion essential to protein functions. Experimental evidence, in addition to computational studies, is critical to further validate the hypothesis.[3,4]

Directly obtaining information with atomic resolution concerning anesthetic modulation on the structures and dynamics of neuronal proteins is often prohibited by technical obstacles, such as limitations of protein size for nuclear magnetic resonance (NMR) spectroscopy or challenges regarding crystallization of membrane proteins for X-ray crystallography. As an alternative approach, model proteins that mimic certain properties of neuronal ion channels have been used to understand the structural basis of anesthetic−protein interaction. Proteins of four-α-helix bundle structural motif are useful models because binding pockets of inhaled anesthetics are presumed to be within transmembrane four-α-helix bundles of Cys-loop receptors.[5] A de novo designed prototype four-α-helix bundle with specific anesthetic binding pockets[6−8] and a natural soluble four-α-helix bundle protein (ferritin)[9] served previously as models for investigating the structural basis of inhaled anesthetic binding in proteins with such a special structural motif. The knowledge gained from these studies could be applicable for understanding molecular insight on anesthetics in much more complex neurotransmitter-gated ion channels.

Our recent NMR studies[7,8] on a water-soluble, de novo designed, prototype four-α-helix bundle indicated that the motion of the four-α-helix bundle could be modulated by halothane, an inhaled general anesthetic. This inspired us to look into similar anesthetic effects on other four-α-helix bundle proteins and to investigate whether there are any common anesthetic effects on four-α-helix bundle proteins. Mistic was chosen for the present study because it could naturally fold into a four-α-helix bundle motif in micelles. The structure of this 110-amino acid (13 kD) *Bacillus subtilis* protein was previously

* To whom correspondence should be addressed. Mailing address: 2049 Biomedical Science Tower 3, 3501 Fifth Avenue, University of Pittsburgh, Pittsburgh, Pennsylvania 15260. Tel (412) 383-9798. Fax (412) 648-8998. E-mail: tangp@anes.upmc.edu.
† Department of Anesthesiology.
‡ Department of Pharmacology and Chemical Biology.
§ Department of Computational Biology.

10.1021/jp805952w CCC: $40.75
Published on Web 09/27/2008

determined with NMR in lauryl dimethylamine oxide (LDAO) micelles.[10] High-quality NMR spectra of Mistic (membrane integrating sequence for translation of integral membrane protein constructs) allow for exploring molecular details of anesthetic and Mistic interaction at atomic resolution. Conformational flexibility of Mistic offers a possibility to assess potential structural and dynamical changes as a consequence of the interaction with halothane. The working hypothesis of our study on Mistic is that volatile general anesthetics act on proteins via altering protein motions, especially motions in the flexible loops, which link different α helices.

Materials and Methods

Sample Preparation. The gene-encoded Mistic was cloned from the *B. subtilis* into the expression vector pTBSG1 (a gift from Prof. Timothy A. Cross' laboratory at Florida State University). The Mistic was expressed in strain BL21(DE3) CodonPlus cells using the Marley protocol.[11] Typically, the expression was induced with 0.2 mM isopropyl β-D-1-thiogalactopyranoside (IPTG) and kept in M9 minimal medium at 12 °C for about 80 h. The protein was purified using published procedures.[10] A yield of ∼120 mg of purified Mistic was obtained from each liter of M9 minimal media.

Mistic is insoluble in water. The presence of detergent is essential for solubilizing Mistic. Mistic is stable in LDAO for ∼5 days, but for more than 5 months in dodecyl phosphocholine (DPC). The exchange of DPC for LDAO was performed at the protein elution from the Ni-NTA resin in order to extend the stability of Mistic samples.

The samples for NMR experiments typically contained 0.5 mM of either ^{15}N-labeled or ^{13}C/^{15}N-labeled Mistic, 30 mM DPC, 0.2 mM dithiotreitol (DTT), 50 mM KCl, and 10 mM potassium phosphate buffer at pH 6.0.

NMR Experiments. All ^{1}H, ^{15}N, and ^{13}C NMR experiments were performed at 30 °C on Bruker Avance 600 or 700 or 800 MHz NMR spectrometers equipped with cryoprobes (Bruker Instruments, Billerica, MA). The ^{1}H chemical shifts were referenced to the 2,2-dimethyl-2-silapentene-5-sulfonate resonance at 0 ppm, and the ^{15}N/^{13}C chemical shifts were indirectly referenced. ^{19}F NMR experiments were performed on a Bruker Avance 600 spectrometer with a Bruker TXO probe to determine halothane concentrations in reference to a solution with 10 mM trifluoroacetic acid (TFA). Although the chemical shifts assignments of Mistic in LDAO were done previously[10] and the ^{1}H−^{15}N TROSY-HSQC spectra of Mistic in DPC showed high similarity to that in LDAO, we repeated the same two-dimensional (2D) and three-dimensional (3D) NMR experiments[10] for the ^{13}C and ^{15}N chemical shift assignments of Mistic in DPC. A series of ^{1}H−^{15}N TROSY-HSQC spectra were collected on samples with five different halothane concentrations, ranging from 0 to 13 mM, to determine site-specific dissociation constants. The CBCA(CO)NH and HBHA(CO)NH spectra were acquired in the absence and presence of halothane so that the chemical shifts of Cα, Cβ, Hα, and Hβ at these two different conditions were obtained for comparison. ^{1}H−^{15}N residual dipolar couplings (RDCs) of Mistic were measured using a TROSY-IPAP-HSQC pulse sequence with 1024 (^{1}H) × 256 (^{15}N) complex points. A weak alignment of ^{15}N-labeled Mistic in DPC micelles was achieved in both compressed and stretched charged polyacrylamide gel.[12] The degree of alignment for each sample was checked using one-dimensional (1D) ^{2}H NMR experiments.

To confirm anesthetic direct interaction with Mistic, ^{1}H saturation transfer difference (STD)[13] NMR was performed on a 0.5 mM ^{15}N-labeled Mistic sample in 30 mM DPC in the presence of 10 mM halothane. As a control, the same experiment was also performed on a similar sample but without Mistic. The spectra were obtained in an interleaved manner using irradiation of 50 ms Gaussian pulses applied on-resonance at 0.58 ppm, corresponding to Mistic methyl protons, and off-resonance at 40 ppm. The pulse sequence utilized the WATERGATE water suppression and spoil sequence to destroy unwanted magnetization.[14] A series of STD spectra were acquired within a range of saturation times: 0.5, 1, 3, 5, 10, 20, and 40 s. Each spectrum had 64 scans with a relaxation delay of 40 s. The STD ($\Delta I = I_{off} - I_{on}$) was calculated by subtraction of the intensities of the on-resonance peak (I_{on}) from those of the off-resonance peak (I_{off}).[15,16]

To characterize the dynamic property of Mistic, spin−lattice (R_1) and spin−spin (R_2) ^{15}N relaxation rate constants were measured with 512 (^{1}H) × 128 (^{15}N) complex points using standard pulse sequences with echo−antiecho gradient selection.[17] Nine (ranging from 10−1800 ms) or 10 (16−160 ms) variable delays were used for the R_1 or R_2 measurements, respectively. The effective transverse relaxation rate was also measured using relaxation-compensated Carr−Purcell−Meiboom−Gill (CPMG) experiments as a function of CPMG field strength (ν_{CPMG}).[18,19] The ^{15}N R_2 relaxation dispersion data are suited to determine Mistic's conformation exchange on the microsecond−millisecond time scale in the presence and absence of halothane. The R_2 relaxation dispersion profiles were recorded at two different magnetic field strengths corresponding to ^{1}H frequencies of 600 and 800 MHz. The experiments were performed in a constant time manner (T_{CP} = 60 ms) on uniformly ^{15}N-labeled Mistic samples. The CPMG field strength, ν_{CPMG}, was varied to 33.33, 66.67, 100.00, 133.33, 200.00, 266.67, 333.33, 400.00, 500.00, and 666.67 Hz.

Data Process and Structure Refinement. All NMR data were processed using NMRPipe[20] and analyzed with Sparky.[21] The chemical shift assignments were accomplished with the aid of AutoAssign[22] and manual comparison to the assignments of Mistic in LDAO.[10]

The structure of Mistic in DPC micelles was obtained through refinement of the lowest-energy structures (PDB: 1YGM) of Mistic in LDAO micelles[10] using dihedral angle restraints obtained from Cα and Cβ chemical shift index (CSI)[23] processed using Talos[24] and RDC data of helical regions obtained from two different alignment mediums. The refinement used the slow cooling simulated annealing protocol in Xplor-NIH.[25] The axial (Da) and rhombic (R) components of the alignment tensor in RDC experiments were determined using the histogram method,[26] producing Da = −10.8 and R = 0.23 for samples in compressed gel and Da = −10.0, R = 0.27 for samples in stretched charged gel, respectively. A total of 100 structures were produced in the refinement, and half of them with lower energies were used for an averaged structure. The best-fit comparison between experimental RDCs and the refined structures were performed using the program MODULE 1.0.[27]

^{15}N relaxation dispersion data were analyzed using eq 1, which encompasses all chemical exchange timescales:[28]

$$R_2(\nu_{CPMG}) = [R_{20} + (k_{ex}/2) - \nu_{CPMG}\cosh^{-1}(D_+\cosh(\eta_+) - D_-\cos(\eta_-))] \quad (1)$$

where $D_\pm = 1/2(\pm 1 + (\psi + 2\Delta\omega^2)/(\psi^2 + \xi^2)^{1/2})$, $\eta_\pm = (\nu_{CPMG}/2(2)^{1/2})(\pm\psi + (\psi^2 + \xi^2)^{1/2})^{1/2}$, $\psi = k_{ex}^2 - \Delta\omega^2$, $\xi = -2\Delta\omega(p_a k_{ex} - p_b k_{ex})$, R_{20} is the intrinsic transverse relaxation rate, k_{ex} is the exchange rate, $\Delta\omega$ is the difference of chemical shifts between exchange sites a and b, the population of site a

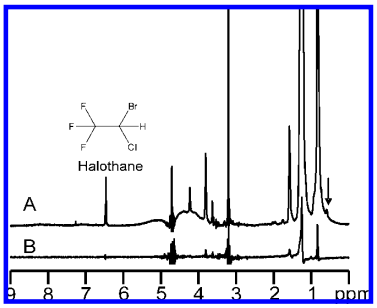

Figure 1. ^{1}H STD NMR spectra of 10 mM halothane (resonance at 6.48 ppm) in (A) 30 mM DPC with 0.5 mM Mistic and (B) 50 mM DPC without Mistic. The arrow indicates the frequency for on-resonance saturation at 0.58 ppm that is near the Hδ resonance of Leu and Ile residues in Mistic. Note that the halothane signal was not observed in panel B under the same NMR conditions as in A, but without Mistic, indicating a direct interaction between halothane and Mistic. A stick chemical structure of halothane is inserted for reference.

is denoted by $p_a = (1 - p_b)$, $\nu_{CPMG} = 1/(2\tau)$, and τ is the time between centers of successive 180° pulses in the CPMG pulse sequence.

Results and Discussion

For increased readability, we present here only the primary results that are intimately related to our discussion. Other supporting data are provided in the Supporting Information as references.

Halothane Interaction Sites in Mistic. Direct halothane interaction with Mistic was evidenced in the STD experiments based on the nuclear Overhauser effect between bound halothane proton and Mistic protons. As shown in Figure 1A, a halothane signal became observable in STD spectra when the on-resonance saturation frequency was set at 0.58 ppm, a frequency far away from halothane proton but near Hδ of Leu and Ile. The halothane signal in Figure 1A critically depended on the presence of Mistic. Under the same NMR experimental condition (0.58 ppm for the on-resonance saturation), but without Mistic, there was no observable halothane signal (Figure 1B), indicating that direct interaction between halothane and Mistic certainly exists. The halothane interacting sites in Mistic were examined by monitoring chemical shift changes of Mistic backbones and sidechains in response to halothane titrations. Figure 2 shows a representative overlay of Mistic's ^{1}H$-^{15}$N TROSY-HSQC spectra in the presence and absence of halothane. A number of residues showed profound chemical shift changes after the addition of halothane. Some residues, such as A40 and Q66, had changes not only in their chemical shifts, but also in their signal intensities. After the addition of halothane, the S58 signal became much stronger, but the I52 peak intensity became much weaker. The peak intensity signified plausible dynamics alternation in the region where the residue resided. Figure 3 highlights Mistic residues that experienced obvious changes in chemical shift (HN $>$ 0.05 ppm, Cα and Cβ $>$ $\pm$ 1 ppm, Hα and Hβ $>$ $\pm$ 0.1 ppm) upon halothane titration. The α2 helix had several residues in the middle of the helix that were sensitive to halothane. The location of residues affected by halothane coincided with the helix kink near A40 and M44, suggesting the possibility that the helical kink acted as a pocket for halothane binding. The chemical shifts of residues in other helices were largely insensitive to anesthetics, except for some residues adjacent to or in loop regions. In contrast to helical residues, all loop residues were more or less perturbed by halothane. These loop residues were located at the micelle headgroup region, as evidenced by high sensitivity of their chemical shifts to the headgroup changes in micelles from 100% DPC to 40% LDAO/60% DPC (see Figure 1S in the Supporting Information). Most helical residues or N- and C-terminal residues maintained the same chemical shifts when DPC was partially replaced by LDAO, confirming that they were embedded in the micelle hydrocarbon regions or exposed to bulk water.

Halothane dissociation constants in the loop regions were estimated in the range of a few millimolars (Figure 2S in the Supporting Information). The observation of halothane attraction to Mistic loop residues at the micelle$-$water interface is consistent with the notion that general anesthetics prefer amphipathic water$-$lipid interfaces.[15,29,30] The significance of this idea lies not only in revealing the nature of anesthetic interaction sites, but also in suggesting potential anesthetic modulation to protein regions at the water$-$lipid interface that play critical roles in protein functions. Anesthetics could disrupt normal residues' interactions within the same loop or between different loops. Anesthetic disruption on residues interactions between different loops can be more vital. Proper couplings of loop residues in agonist-binding extracellular and transmembrane domains at the water$-$lipid interface are often crucial for functions of plausible anesthetic targeting channels.[1,2] Modification of interfacial electrostatic interactions by point mutations induced profound changes in channel functions.[31] Because of their preferred interaction with residues at an interface, it is conceivable that anesthetics could also affect receptor interfacial interactions and ultimately alter functions of Cys-loop receptors. Such a possibility will be discussed further in the following sections.

The halothane concentration of $\sim$10 mM was suitable for observing halothane effects in our NMR experiments, but one might wonder if this concentration is pharmacologically relevant. A clinically relevant concentration of volatile general anesthetics is often quoted as being in the submillimolar ($\sim$0.1$-$1 mM) range. The strict meaning of this range refers to what is measured in saline. For volatile anesthetics administered in patients, the only entity that is constant throughout the body under equilibrium is partial pressure. The concentration in any given compartment depends on the partition coefficient in that compartment. Under the same partial pressure, a 100 μM concentration of halothane in saline translates as $\sim$12 mM concentration in lipids, given a 1:124 saline/lipid partition coefficient of halothane at 30 °C.[32] Note that our reported concentration was measured in an excess amount of detergent for stabilizing Mistic. Therefore, the halothane concentration of 10 mM used in our NMR measurements is not as high as it appears and is pharmacologically relevant.

Halothane Had Minimal Effects on Mistic Structure. The structure of Mistic in DPC micelles was obtained through refinement of Mistic structure in LDAO[10] using our RDC data attained on Mistic in DPC. We found that Mistic had virtually the same folding in DPC and LDAO. Details of the structure refinement are provided in the Supporting Information (Figure 3S).

The introduction of halothane to Mistic in DPC did not change the overall structure of Mistic. The CSIs of Cα, Cβ, and Hα, characterizing the secondary structures of Mistic, were largely unchanged in the absence and presence of 10 mM halothane, especially in helical regions. Figure 4 displays a comparison of the Cα CSI before (top) and after (bottom) the addition of halothane, showing that halothane had a minute impact on the secondary structure of Mistic. Halothane effects on Mistic

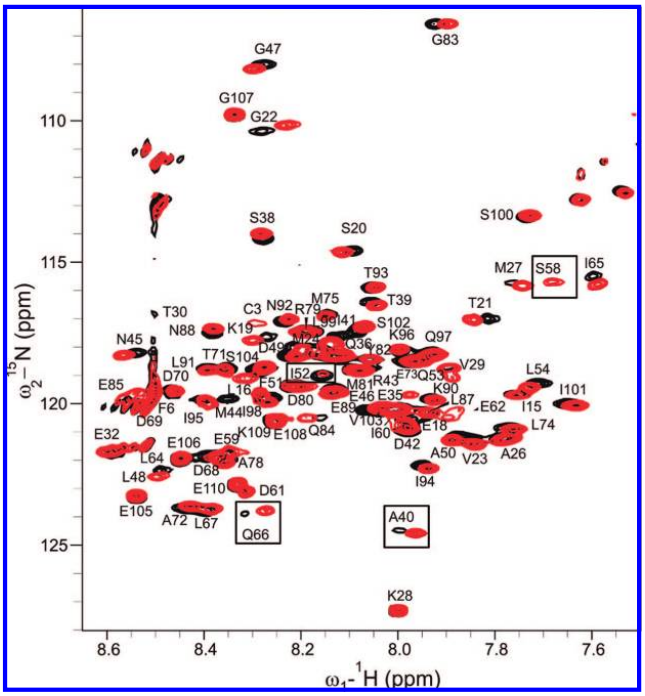

Figure 2. Overlay of $^{1}H-^{15}N$ TROSY-HSQC spectra of 0.5 mM Mistic in 30 mM DPC micelles in the absence (black) and presence (red) of 10 mM halothane. The spectra were acquired at 30 °C. Despite many residues being undisturbed by the addition of halothane, some residues experienced significant chemical shift changes and/or intensity changes of their resonance signals. A few examples are highlighted in small boxes.

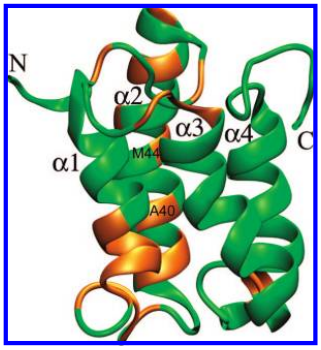

Figure 3. Halothane interaction sites in Mistic. The residues whose chemical shifts were significantly perturbed by halothane are highlighted in orange color. The four transmembrane helices are marked as α1−α4.

tertiary structure were determined via measuring backbone RDCs of Mistic in the absence and presence of 5 mM halothane. The structures of Mistic without and with halothane were both refined using RDC data. Relatively small values of root-mean-square deviations (rmsd's) of the refined structures in the absence and presence of halothane, as color coded in the Mistic structure in Figure 5, suggest that the overall tertiary structure of Mistic is well preserved upon the addition of halothane.

It was reported previously[15,33,34] that structures of transmembrane peptides remained unchanged in the presence of general anesthetics. Several studies on globular proteins with general anesthetics also found remarkable tolerance of overall protein structures to the added anesthetics at low millimolar concentrations.[9,35−37] Since the folding of Mistic in micelles resembles the structural motif of four transmembrane domains of a subunit in the Cys-loop receptors, the observed structure insensitivity to anesthetic perturbation in the present study may also occur in the Cys-loop receptors. Therefore, it is reasonable to speculate that anesthetic action on those Cys-loop receptors is unlikely via significantly altering receptor structures, although more experimental data should be collected for a final conclusion.

Halothane Had Profound Effects on Mistic Motion. Halothane-induced changes in Mistic motion were confirmed by at least two lines of experimental evidence. First, some residues showed profound changes in their NMR signal intensities (or line widths) after adding halothane. Second, ^{15}N relaxation dispersion experiments indicated that motion on the microsecond−millisecond time scale existed in some regions of Mistic, and halothane could alter such motion.

As shown in Figure 2, residues S58, Q66, and A40 gained higher peak intensities and narrower peak line-widths in the $^{1}H-^{15}N$ HSQC NMR spectra in the presence of halothane. Several Cα resonance peaks of loop residues S58−L67 also changed from weak to strong after the addition of halothane, as summarized in Figure 4. In contrast, I52 peak intensity dropped significantly after the addition of halothane (Figure 2). These observations could not be adequately explained by the halothane effect on Mistic motion in the picosecond−nanosecond time scale. Changes in longitudinal (R_1) and transverse (R_2) relaxation rates, as well as $^{1}H-^{15}N$ heteronuclear NOE due to the presence of halothane, seem relatively small (see Figure 4S in the Supporting Information). Intrinsically weak intensity of

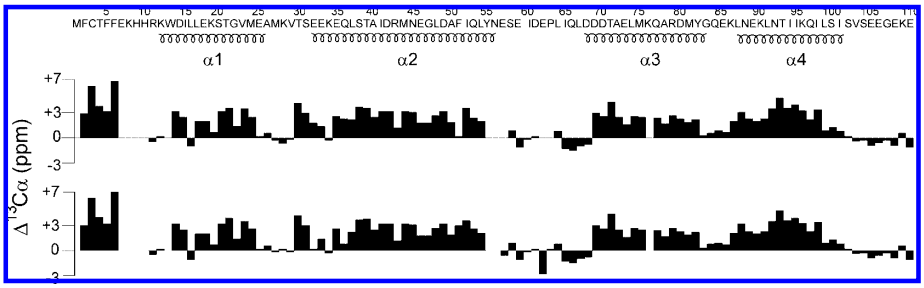

Figure 4. The $^{13}C\alpha$ CSI of Mistic residues in the absence (top) and presence (bottom) of 10 mM halothane. The Cα chemical shifts were referenced with respect to random coil values at 0 ppm.

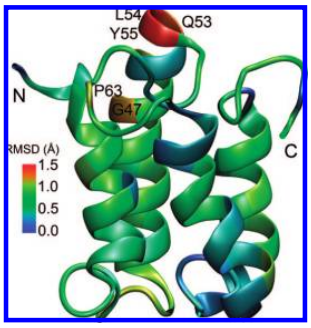

Figure 5. The refined structure of Mistic in DPC on the basis of RDC NMR measurements. The rmsd (Å) of Mistic structure in the absence and presence of 10 mM halothane is presented using a color scale. Residues that showed the largest rmsd are labeled.

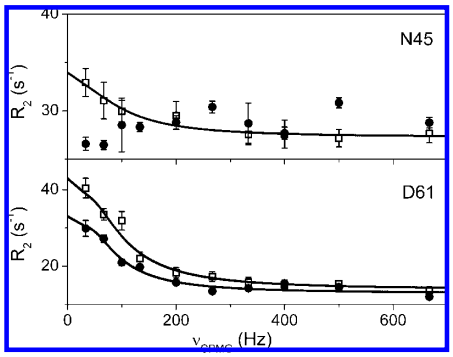

Figure 6. Backbone^{15}N relaxation dispersion curves of two representative Mistic residues, N45 and D61, in the absence (□) and presence (●) of 10 mM halothane.

some NMR peaks could result from conformational-exchange broadening in the microsecond−millisecond time scale. The increasing intensity of these peaks after the addition of halothane might be the consequence of changes in exchange process,[38] though alternation in peak intensity alone would not provide specific information regarding whether halothane had a potentiation or inhibition effect on the exchange.

Quantitative characterization of Mistic's motion on the microsecond−millisecond time scale was achieved through ^{15}N R_2 relaxation dispersion measurements. Majority residues of Mistic showed no motion on the microsecond−millisecond time scale, and their transverse relaxation rates were not affected by a systematical variation of the CPMG field strength, ν_{CPMG}. However, R_2 dispersion dependence on the ν_{CPMG} variation was observed for a number of residues located at the loop connecting α2 and α3 helices (residues S58, D61, Q66, and D68), at the loop connecting α1 and α2 helices (residues V29), along helix α2 (T39 and N45), and at the loop connecting α3 and α4 (Y82) helices. Figure 6 depicts relaxation dispersion profiles for two representative residues, D61 and N45, in the absence and presence of 10 mM halothane. Halothane quenched the exchange contribution to R_2 on residue N45 and suppressed the exchange on D61. This is consistent with the aforementioned increase of peak intensity and decrease of line widths in some residues upon the addition of halothane. The fitting of relaxation dispersion data using eq 1 for a two-site (a and b) exchange model[28] provided estimation of exchange parameters, including differences in chemical shifts between exchanging sites ($\Delta\omega$), the exchange rate (k_{ex}), the relative population of a conformation (p_a or p_b), and the intrinsic transverse relaxation rate (R_{20}) in the absence of chemical exchange. Table 1 summarizes these parameters for several residues in the absence and presence of 10 mM halothane. The population of the major conformation, p_a was close to, or over, 90% for all these residues and had 0−3% increase after the addition of halothane. $\Delta\omega$ remained virtually the same for most residues, which is consistent with the aforementioned result that Mistic structure remained the same before and after adding halothane. The exchange rate k_{ex} varied to a different extent on different residues.

Both residues T39 and N45 reside in the middle part of helix α2, where a helical kink occurs between these two residues. Residue Y82 resides at the end of helix α3. Although these residues experienced the chemical exchange on the microsecond−millisecond time scale in the absence of halothane, the exchange disappeared in the presence of halothane, as shown in Table 1. In all these cases, anesthetic halothane suppressed exchange motion. Residue V29 is located at the end of helix α1. Halothane did not completely remove the exchange contribution, but the R_{ex} value of V29 was reduced almost by half, and the exchange rate k_{ex} became less than 1/3 of its original value. Residue I52 is located at the end of helix α2. It experienced fast exchange in the absence of halothane (Table 1) and possessed a relatively strong $^1H-^{15}N$ HSQC resonance peak (Figure 2). However, the resonance peak of I52 virtually vanished as a result of intermediate exchange induced by halothane. Q66 resides at the beginning of helix α3 or end of the loop connecting α2 and α3. The side chain of Q66 is within a few angstroms of the D61 side chain. Both Q66 and D61 had similar exchange rates that became much slower after the addition of halothane. Interestingly, the α2−α3 loop folds in such a way that S58 at the middle of the loop is not far away from D68, which resides at the beginning of helix α3. The kinetic data also suggest that S58 and D68 share similar exchange rates, and both rates became greater in the presence of halothane. One may wonder if it is possible that these two

TABLE 1: ^{15}N Relaxation Dispersion Parameters[a] of Exchanging Residues of Mistic in the Absence and Presence of 10 mM Halothane

residues	absence (−) and presence (+) of halothane	R_{ex} (s^{-1})[b]	R_{20} (s^{-1})	k_{ex} (s^{-1})	p_a	Δw (s^{-1})
V29	−	7.8	16.4 ± 0.7	532 ± 290	0.97 ± 0.02	508 ± 59
	+	4.2	16.9 ± 0.2	154 ± 22	0.97 ± 0.02	523 ± 69
T39	−	3.9	20.7 ± 0.3	1455 ± 296	0.98 ± 0.08	588 ± 65
	+	NA[c]				
N45	−	5.2	27.3 ± 0.4	635 ± 197	0.92 ± 0.02	258 ± 28
	+	NA				
I52	−	6.2	23.7 ± 0.4	722 ± 200	0.90 ± 0.02	241 ± 30
	+	ND[d]				
S58	−	6.4	15.8 ± 0.3	217 ± 83	0.91 ± 0.03	205 ± 12.5
	+	4.8	17.2 ± 0.5	551 ± 270	0.91 ± 0.03	189 ± 33
D61	−	26.7	13.5 ± 0.9	468 ± 144	0.89 ± 0.02	529 ± 26
	+	17.9	13.2 ± 0.5	199 ± 22	0.90 ± 0.01	550 ± 50
Q66	−	12.9	17.0 ± 0.7	376 ± 99	0.90 ± 0.03	362 ± 18
	+	12.0	17.1 ± 0.6	174 ± 33	0.92 ± 0.01	486 ± 74
D68	−	3.5	17.9 ± 0.2	279 ± 120	0.97 ± 0.02	317 ± 25
	+	3.3	16.3 ± 0.1	482 ± 84	0.97 ± 0.02	300 ± 15
Y82	−	11.5	25.0 ± 1.1	267 ± 148	0.87 ± 0.17	244 ± 24
	+	NA				

[a] Equation 1 was used for fitting of these parameters. [b] $R_{ex} = R_2(\nu_{cp} \rightarrow 0) - R_2(\nu_{cp} \rightarrow \infty)$. [c] NA: no relaxation dispersion. [d] ND: the signal was too weak to determine relaxation dispersion parameters.

nearby pairs of residues, Q66 and D61 vs D68 and S58, have different directions of rate change upon addition of halothane. A close inspection of Mistic structure revealed that both D68 and S58 were oriented inward to helices, while Q66 and D61 were directed outward in the loop and pointed to the water phase (see Figure 5S in the Supporting Information). Distinctive motional characteristics of nearby residues upon ligand binding were also observed previously in SH2 protein.[39]

Several features can be extracted from the ^{15}N relaxation dispersion data presented above. First, residues carrying motion on the microsecond−millisecond time scale are often in loop edges or helical ends (V29, I52, Q66, D68, Y82). Second, helical residues are often not involved in slow (microsecond−millisecond) dynamics, except those (T39 and N45) in helical kink regions. Third, residues far away from each other in primary sequence but close in space (Q66 and D61 vs D68 and S58) exhibit concerted motion. Last, but most importantly for this study, anesthetic halothane could alter the slow dynamics. Anesthetic molecules could make protein motion faster in one region but slower in another region. The exchange rate k_{ex} decreased in most of the aforementioned Mistic residues, but increased in some residues. R_{ex} values of the majority of residues in the presence of halothane decreased to different degrees, indicating that halothane suppressed motion of these residues on the microsecond−millisecond time scale. An opposite effect might also exist. The NMR intensity of residue I52 was severely decreased after adding halothane, indicating an intermediate exchange promoted by halothane. However, a systematic evaluation of the slow dynamics of I52 in the presence of 10 mM halothane was prohibited by the weak signal of this residue.

We want to point out that the aforementioned dynamical changes due to the addition of halothane may not necessarily result from direct halothane interaction with individual residues. Most of the residues listed in Table 1 showed obvious chemical shifts in response to halothane titration. However, neither I52 nor Y82 demonstrated significant changes in their chemical shifts, suggesting that these two residues had no close interaction with halothane molecules. The dynamical alternation of these residues must result from halothane allosteric modulation. Therefore, anesthetic molecules could induce changes in protein motions on the microsecond−millisecond time scale either through direct interaction with specific residues or through allosteric modulation.

Conclusions

The most significant contribution of the present study is providing unequivocal experimental evidence that inhaled general anesthetics can modulate protein slow dynamics, especially motion in the flexible loops that link different alpha helices. It is well-known that protein motion on the microsecond−millisecond time scale often couples with protein functions.[40] Low affinity drugs, such as volatile general anesthetics, do not usually interact with proteins in a lock-and-key fashion.[41] Therefore, it is rational for us to determine how anesthetics alter protein functions via altering protein motion. Our previous computational studies established a theoretical basis for anesthetic action on protein global dynamics.[3,4] Experimental evidence is critical for validating the theory of anesthetic action on protein dynamics. Our study demonstrates that halothane perturbed slow dynamics of Mistic, indicating the plausibility that changes in protein functions by general anesthetic can be achieved by interrupting the mode of protein motion[4] instead of tight bindings with number of protein hydrophobic pockets. These findings on Mistic certainly encourage us to look further into anesthetic effects on protein motion in other functional proteins. By collecting enough experimental data demonstrating anesthetic modulation on protein dynamics, we can significantly advance our understanding of molecular mechanisms of general anesthesia.

Identification of the halothane interaction sites on Mistic in this study supports our view that anesthetics prefer to interact with amphipathic sites of proteins.[7,15,29,30] Although halothane interaction occurred at multiple sites of Mistic, it did not introduce significant secondary and tertiary structure changes. This observation is consistent with our previous findings on other proteins.[15,29,34]

One may wonder if the anesthetic effects, such as those observed here on Mistic, are large enough to account for anesthetic action on proteins. Because of the low affinity nature of inhaled general anesthetics (submillimolar), their interaction with proteins should not be expected to cause structural and

dynamical effects on proteins as great as those high-affinity ligands or substrates. We are still in the process of determining how large an anesthetic effect on protein structures and dynamics is required to produce protein functional changes which ultimately contribute to general anesthesia. Experiments on model proteins are only the starting point of this process. The demonstration of halothane perturbation to dynamics of Mistic in the microsecond−millisecond time scale is such a starting point.

Halothane perturbation on Mistic slow dynamics happened not only to residues that might interact directly with halothane molecules, but also to residues that seemed to be remote from halothane, signifying halothane allosteric modulation on protein dynamics. It is conceivable that the impact of general anesthetic modulation on protein dynamics, be it direct or indirect through allosteric effects, will be amplified on much larger protein complexes, such as Cys-loop receptors, in which the concerted motion among different subunits regulates the protein functions. Normally, several different conformers of these protein complexes coexist dynamically, and each conformer determines different functional states. Anesthetic perturbation in a few critical sites could introduce vital disturbance to highly coupled motion in these molecular machineries, shift the equilibrium of conformational states, and ultimately alter protein functions. When a large enough number of proteins in the CNS are dynamically perturbed by general anesthetics, even though the perturbation on individual proteins is rather small, the cumulative effects on the CNS could lead to the phenomena of general anesthesia. The study on Mistic provides encouraging evidence for pursuing a dynamical view of molecular mechanisms of general anesthesia. Further investigation on other proteins is necessary to confirm that anesthetic modulation to functionally important motion in proteins contributes to general anesthesia.

Acknowledgment. The authors would like to thank Prof. Rieko Ishima for the stimulating discussions and her input into the application of the R_2 dispersion relaxation all-time scale fitting program. The assistance from Dr. Tommy S. Tillman in Mistic expression, Ms. Nicole Brandon in gel preparations for RDC measurements, and Mrs. Sandra C. Hirsch in manuscript editing is highly appreciated. This work was supported in part by grants from the National Institute of Health (R01GM56257 and R01GM66358 to P.T. and R37GM049202 to Y.X.).

Supporting Information Available: Effect of detergent ratio on Mistic; calculation of K_d; Mistic structure refinement using RDCs; ^{15}N R_1, R_2, NOE data; residues showing conformational exchange superimposed in the structure; and RDC data table. This material is free of charge via the Internet at http://pubs.acs.org.

References and Notes

(1) Franks, N. P.; Lieb, W. R. *Nature* **1984**, *310*, 599.
(2) Campagna, J. A.; Miller, K. W.; Forman, S. A. *N. Engl. J. Med.* **2003**, *348*, 2110.
(3) Tang, P.; Xu, Y. *Proc. Natl. Acad. Sci. U.S.A.* **2002**, *99*, 16035.
(4) Szarecka, A.; Xu, Y.; Tang, P. *Biophys. J.* **2007**, *93*, 1895.
(5) Mihic, S. J.; Ye, Q.; Wick, M. J.; Koltchine, V. V.; Krasowski, M. D.; Finn, S. E.; Mascia, M. P.; Valenzuela, C. F.; Hanson, K. K.; Greenblatt, E. P.; Harris, R. A.; Harrison, N. L. *Nature* **1997**, *389*, 385.
(6) Johansson, J. S.; Gibney, B. R.; Rabanal, F.; Reddy, K. S.; Dutton, P. L. *Biochemistry* **1998**, *37*, 1421.
(7) Cui, T.; Bondarenko, V.; Ma, D.; Canlas, C.; Brandon, N. R.; Johansson, J. S.; Xu, Y.; Tang, P. *Biophys. J.* **2008**, *94*, 4464.
(8) Ma, D.; Brandon, N. R.; Cui, T.; Bondarenko, V.; Canlas, C.; Johansson, J. S.; Tang, P.; Xu, Y. *Biophys. J.* **2008**, *94*, 4454.
(9) Liu, R.; Loll, P. J.; Eckenhoff, R. G. *FASEB J.* **2005**, *19*, 567.
(10) Roosild, T. P.; Greenwald, J.; Vega, M.; Castronovo, S.; Riek, R.; Choe, S. *Science* **2005**, *307*, 1317.
(11) Marley, J.; Lu, M.; Bracken, C. *J. Biomol. NMR* **2001**, *20*, 71.
(12) Cierpicki, T.; Bushweller, J. H. *J. Am. Chem. Soc.* **2004**, *126*, 16259.
(13) Moriz Mayer, B. M. *Angew. Chem., Int. Ed.* **1999**, *38*, 1784.
(14) Hwang, T. L.; Shaka, A. J. *J. Magn. Reson., Ser. A* **1995**, *112*, 275.
(15) Bondarenko, V.; Yushmanov, V. E.; Xu, Y.; Tang, P. *Biophys. J.* **2008**, *94*, 1681.
(16) Streiff, J. H.; Juranic, N. O.; Macura, S. I.; Warner, D. O.; Jones, K. A.; Perkins, W. J. *Mol. Pharmacol.* **2004**, *66*, 929.
(17) Farrow, N. A.; Muhandiram, R.; Singer, A. U.; Pascal, S. M.; Kay, C. M.; Gish, G.; Shoelson, S. E.; Pawson, T.; Forman-Kay, J. D.; Kay, L. E. *Biochemistry* **1994**, *33*, 5984.
(18) Tollinger, M.; Skrynnikov, N. R.; Mulder, F. A.; Forman-Kay, J. D.; Kay, L. E. *J. Am. Chem. Soc.* **2001**, *123*, 11341.
(19) Loria, J. P.; Rance, M.; Palmer, A. G. *J. Am. Chem. Soc.* **1999**, *121*, 2331.
(20) Delaglio, F.; Grzesiek, S.; Vuister, G. W.; Zhu, G.; Pfeifer, J.; Bax, A. *J. Biomol. NMR* **1995**, *6*, 277.
(21) Goddard, T. D.; Kneller, D. G. *Sparky 3*; University of California: San Francisco.
(22) Zimmerman, D. E.; Kulikowski, C. A.; Huang, Y.; Feng, W.; Tashiro, M.; Shimotakahara, S.; Chien, C.; Powers, R.; Montelione, G. T. *J. Mol. Biol.* **1997**, *269*, 592.
(23) Wishart, D. S.; Sykes, B. D.; Richards, F. M. *J. Mol. Biol.* **1991**, *222*, 311.
(24) Cornilescu, G.; Delaglio, F.; Bax, A. *J. Biomol. NMR* **1999**, *13*, 289.
(25) Schwieters, C. D.; Kuszewski, J. J.; Tjandra, N.; Clore, G. M. *J. Magn. Reson.* **2003**, *160*, 65.
(26) Clore, G. M.; Gronenborn, A. M.; Bax, A. *J. Magn. Reson.* **1998**, *133*, 216.
(27) Dosset, P.; Hus, J. C.; Marion, D.; Blackledge, M. *J. Biomol. NMR* **2001**, *20*, 223.
(28) Carver, J. P.; Richards, R. E. *J. Magn. Reson.* **1969**, *1972* (6), 89.
(29) Tang, P.; Simplaceanu, V.; Xu, Y. *Biophys. J.* **1999**, *76*, 2346.
(30) Xu, Y.; Tang, P. *Biochim. Biophys. Acta* **1997**, *1323*, 154.
(31) Kash, T. L.; Jenkins, A.; Kelley, J. C.; Trudell, J. R.; Harrison, N. L. *Nature* **2003**, *421*, 272.
(32) Smith, R. A.; Porter, E. G.; Miller, K. W. *Biochim. Biophys. Acta* **1981**, *645*, 327.
(33) Tang, P.; Hu, J.; Liachenko, S.; Xu, Y. *Biophys. J.* **1999**, *77*, 739.
(34) Tang, P.; Mandal, P. K.; Zegarra, M. *Biophys. J.* **2002**, *83*, 1413.
(35) Kruse, S. W.; Zhao, R.; Smith, D. P.; Jones, D. N. *Nat. Struct. Biol.* **2003**, *10*, 694.
(36) Colloc'h, N.; Sopkova-de Oliveira Santos, J.; Retailleau, P.; Vivares, D.; Bonnete, F.; Langlois d'Estainto, B.; Gallois, B.; Brisson, A.; Risso, J. J.; Lemaire, M.; Prange, T.; Abraini, J. H. *Biophys. J.* **2007**, *92*, 217.
(37) Franks, N. P.; Jenkins, A.; Conti, E.; Lieb, W. R.; Brick, P. *Biophys. J.* **1998**, *75*, 2205.
(38) Rao, B. D. *Methods Enzymol.* **1989**, *176*, 279.
(39) Mittag, T.; Schaffhausen, B.; Gunther, U. L. *Biochemistry* **2003**, *42*, 11128.
(40) Ishima, R.; Torchia, D. A. *Nat. Struct. Biol.* **2000**, *7*, 740.
(41) Xu, Y.; Seto, T.; Tang, P.; Firestone, L. *Biophys. J.* **2000**, *78*, 746.

JP805952W

Biochimica et Biophysica Acta 1798 (2010) 161–166

Contents lists available at ScienceDirect

Biochimica et Biophysica Acta

journal homepage: www.elsevier.com/locate/bbamem

Anesthetic effects on the structure and dynamics of the second transmembrane domains of nAChR α4β2

Tanxing Cui [a,1], Christian G. Canlas [a,1], Yan Xu [a,b], Pei Tang [a,b,c,*]

[a] Department of Anesthesiology, University of Pittsburgh School of Medicine, Pittsburgh, PA 15261
[b] Department of Pharmacology and Chemical Biology, University of Pittsburgh School of Medicine, Pittsburgh, PA 15261
[c] Department of Computational Biology, University of Pittsburgh School of Medicine, Pittsburgh, PA 15261

ARTICLE INFO

Article history:
Received 4 February 2009
Received in revised form 31 July 2009
Accepted 12 August 2009
Available online 26 August 2009

Keywords:
Mechanisms of general anesthesia
Halothane
Isoflurane
Volatile anesthetics
PISEMA
Solid state NMR
nAChR
a4b2
Neuronal nAChR

ABSTRACT

Channel functions of the neuronal α4β2 nicotinic acetylcholine receptor (nAChR), one of the most widely expressed subtypes in the brain, can be inhibited by volatile anesthetics. Our Na^+ flux experiments confirmed that the second transmembrane domains (TM2) of α4 and β2 in 2:3 stoichiometry, $(\alpha4)_2(\beta2)_3$, could form pentameric channels, whereas the α4 TM2 alone could not. The structure, topology, and dynamics of the α4 TM2 and $(\alpha4)_2(\beta2)_3$ TM2 in magnetically aligned phospholipid bicelles were investigated using solid-state NMR spectroscopy in the absence and presence of halothane and isoflurane, two clinically used volatile anesthetics. ^{2}H NMR demonstrated that anesthetics increased lipid conformational heterogeneity. Such anesthetic effects on lipids became more profound in the presence of transmembrane proteins. PISEMA experiments on the selectively ^{15}N-labeled α4 TM2 showed that the TM2 formed transmembrane helices with tilt angles of $12^\circ \pm 1^\circ$ and $16^\circ \pm 1^\circ$ relative to the bicelle normal for the α4 and $(\alpha4)_2(\beta2)_3$ samples, respectively. Anesthetics changed the tilt angle of the α4 TM2 from $12^\circ \pm 1^\circ$ to $14^\circ \pm 1^\circ$, but had only a subtle effect on the tilt angle of the $(\alpha4)_2(\beta2)_3$ TM2. A small degree of wobbling motion of the helix axis occurred in the $(\alpha4)_2(\beta2)_3$ TM2. In addition, a subset of the $(\alpha4)_2(\beta2)_3$ TM2 exhibited counterclockwise rotational motion around the helix axis on a time scale slower than 10^{-4} s in the presence of anesthetics. Both helical tilting and rotational motions have been identified computationally as critical elements for ion channel functions. This study suggested that anesthetics could alter these motions to modulate channel functions.

1. Introduction

Nicotinic acetylcholine receptors (nAChRs) belong to a superfamily of ligand gated ion channels involving the rapid chemical transmission of nerve impulses at synapses. Previous studies found that some subtypes of nAChRs might be potential targets of general anesthetics and their normal channel functions could be inhibited by general anesthetics [1-6]. Neuronal α4β2 nAChR is one of the subtypes sensitive to general anesthetics [4,5,7]. It is also one of the most abundant nAChR subtypes in the brain. Despite ample evidence showing that general anesthetics could alter α4β2 nAChR functions, it remains largely unclear how anesthetics perturb the protein structures and dynamics that ultimately affect the protein functions. Therefore, the insights of anesthetic modulation on the structure and dynamics of the α4β2 nAChR are valuable to resolve a long time mystery of the molecular mechanisms of general anesthesia [8,9].

A comprehensive understanding of anesthetic action on α4β2 nAChR or other nAChR subtypes has often been restricted by limited available structural information of nAChRs in the past. The structural models of the closed- and open-channel α4β2 nAChR have been generated [10] recently via computations using the known structure of the *Torpedo* nAChR as a template [11]. More recent X-ray structures of pentameric ion channels in closed- and open-channel forms from *Erwinia chrysanthemi* and *Gloeobacter violaceus* provide high-resolution structural information relevant to nAChRs [12–14]. These new developments certainly facilitate the understanding of anesthetic action on α4β2 nAChR, but experimental studies of structural and dynamic effects of anesthetics on α4β2 nAChR may lead directly to insights into how anesthetics act on α4β2 nAChR and alter the protein function.

Solid-state NMR spectroscopy is a powerful technique for the characterization of membrane protein structures and dynamics and for the investigation of ligand–protein interactions [15-23]. The polarization Inversion and Spin Exchange at the Magic Angle (PISEMA) experiment [24] is particularly useful for the determination of topological structures and dynamics of helical proteins in a well-oriented lipid environment [25-29]. Ligand binding to the *Torpedo* nAChR was comprehensively analyzed using static ^{2}H and cross polarization magic angle spinning (CPMAS) ^{13}C solid-state NMR

* Corresponding author. 2049 Biomedical Science Tower 3, 3501 Fifth Avenue, University of Pittsburgh, Pittsburgh, PA 15260. Tel.: +1 412 383 9798; fax: +1 412 648 8998.
E-mail address: tangp@anes.upmc.edu (P. Tang).
[1] Both authors contribute equally to the work.

0005-2736/$ – see front matter © 2009 Elsevier B.V. All rights reserved.
doi:10.1016/j.bbamem.2009.08.009

experiments [30,31]. The structures of the transmembrane domains of the *Torpedo* nAChR were also examined by various solid-state NMR methods [32-34], including PISEMA [33]. However, no solid-state NMR study on neuronal nAChR has been reported previously. In the present study, we embedded the second transmembrane domains (TM2) of α4β2 nAChR in lipid bicelles, which served as membrane mimetic media and magnetically aligned the protein. The structural and dynamic properties of the TM2 α4β2 nAChR in the absence and presence of anesthetics halothane or isoflurane were investigated using solid state NMR, especially PISEMA experiments. Anesthetics were found to affect both helical tilting and rotational motions that have been identified computationally as critical elements for ion channel functions. This study suggested that anesthetics could alter these motions to modulate channel functions.

2. Materials and methods

2.1. Materials and sample preparation

The second transmembrane (TM2) domains of the human nAChR were obtained by solid phase synthesis [35,36]. The α_4 and β_2 TM2 domains have the sequences of EKIT**L**CISV**LLS**LTVF**LLL**ITE and EKMTLCISVLLALTVFLLLISK, respectively. In order to simplify the studies, only seven leucine residues in α_4 TM2 domain, as indicated in bold letters, were ^{15}N labeled.

Lipids were purchased from Avanti Polar Lipids (Alabaster, AL). A conventional protocol of bicelle preparation [37] was followed. 1,2-dimyristoyl-sn-glycero-3-phosphocoline (DMPC) and 1,2-dihexyl-sn-glycero-3-phosphocholine (DHPC) were mixed in a desired molar ratio ($q = 3.2$). Lipid concentration was 28% of sample volume (typically 220 μL). To extend sample stability for samples containing the nAChR TM2 domains, 1,2-O-ditetradecyl-sn-glycero-3-phosphocoline (14-O-PC)) and 1,2-O-dihexyl-sn-glycero-3-phosphocholine (6-O-PC) replaced DMPC and DHPC, respectively. A small amount of deuterated $DMPC_{d54}$ (~1 mg) was added to each sample for ^{2}H NMR. The α4 or β2 TM2 was dissolved in 100 μL trifluoroethanol and added to the 6-O-PC-chloroform solution. The organic solvents were removed under a stream of nitrogen gas, followed by further evaporation under high vacuum overnight. The aqueous solutions were prepared by adding 110 μL of deuterium-depleted water to dried 14-O-PC and 6-O-PC/peptide. The 14-O-PC suspension was vortexed extensively followed by three freeze/thaw cycles (liquid nitrogen/42 °C). The 14-O-PC suspension at 42 °C was then added to the 6-O-PC/peptide, followed by vortexing and three freeze/thaw cycles. Slow-speed centrifugation was sometimes necessary to remove air bubbles in the sample. A transparent solution was obtained that was viscous at 38 °C and fluid at 4 °C. Parallel-oriented peptide-containing bicelles were prepared by adding 100 mM $YbCl_3$ $6H_2O$ to the peptide-bicelle solution to reach a final lanthanide concentration of 3 mM. The sample was transferred to a 5-mm OD glass tube (New Era Enterprises, Newfield, NJ) using a pre-cooled pipet tip at 4 °C. The glass tube was sealed with a tight fitting rubber cap and further sealed with hard bees wax. The α4-TM2 concentration was 7.4 mM in the α4 samples and 3 mM in the α4β2 samples. The molar ratio of β2 to α4 was 1.5 in the α4β2 samples to ensure a formation of $(\alpha4)_2(\beta2)_3$. The peptide to lipid ratio is ~1:60. Anesthetics halothane (2-bromo-2-chloro-1,1,1-trifluoro-ethane) and isoflurane (2-chloro-2-(difluoromethoxy)-1,1,1-trifluoro-ethane) were added directly to the NMR tube (pre-cooled in an ice bath) and mixed thoroughly with the samples. The anesthetic concentrations were determined using ^{19}F NMR with 5 mM trifluoroacetic acid (TFA) as a reference.

2.2. NMR spectroscopy

All solid state NMR experiments were performed at 40 °C on a Bruker Avance 600 MHz NMR spectrometer equipped with a ^{1}H/^{31}P/^{15}N(^{2}H) Bruker flat-coil probe. ^{19}F NMR experiments were performed on a Bruker Avance 600 spectrometer with a Bruker TXO probe. The 1-D ^{15}N cross-polarization experiments were conducted using a ^{1}H 90° pulse of 5.1 μs, a 49 kHz ^{1}H-decoupling field, 1 ms contact time, 3 s recycle delay, and 10,000 scans. The same cross-polarization parameters were used in the 2-D ^{15}N-^{1}H PISEMA [38]. Other parameters included ±35 kHz frequency jumps for the Lee-Goldberg condition, 400–1000 scans, and 6–8 s recycle delay. The ^{1}H carrier frequency was set at ~4.5 ppm on parallel oriented bicelle samples. The ^{15}N chemical shift frequencies were referenced to solid ammonium sulfate at 26.8 ppm (relative to liquid ammonia at 0 ppm). The ^{2}H NMR experiments were performed using a solid echo sequence $((\pi/2) - \tau - (\pi/2) - \tau)$. The 90° pulse length was 2 μs and τ values were ~40 μs (perpendicular bicelle) and ~20 μs (parallel bicelle). The recycle delay of 0.5 s and the scans of 256 to 10,000 were used.

2.3. NMR data processing

All NMR spectra were processed using NMRPipe [39] and analyzed using Sparky [40]. The data from PISEMA experiments were fitted to the PISA (Polarity Index Slant Angle) [41,42] wheels using the program developed by Veglia's group [26]. The tilt angle (θ) of the helix axis with respect to the bicelle normal, rotation angle (ρ) of the helix around its axis, the angle between the N-H bond and helix axis (δ), and the dipolar coupling constant (K_{DD}) were determined via fittings. The principal values of the ^{15}N chemical shift tensors [24] for non-glycine residues, $\sigma11 = 64$ ppm, $\sigma22 = 77$ ppm, and $\sigma33 = 217$ ppm, were adopted for the fittings. These values were multiplied uniformly by a factor of 0.95 to accommodate reduced ^{15}N chemical shift anisotropy of proteins in bicelles, as reflected in the reduction of spectral span of the same proteins in bicelles in comparison to those in mechanically aligned lipids.

The TM2 chemical shift assignments were accomplished by combining several sources of information, including the previous assignments of δ–TM2 nAChR [33], the solution NMR structure of β2-TM2 nAChR [36], and the best fitting of PISA wheel. L19 is distinctly separated from the rest of leucine residues in a top view of the NMR structure (pdb code: 2K59) [36]. L19 also has weaker NMR signal than other leucines, presumably because it is located at the lipid-water interface and has less protection from solvent exchange. The distinct location and intensity of L19 convinced us to assign L19 to the most downfield peak in the α4-TM2 PISEMA spectra. Once L19 is defined, the rest of peaks were assigned automatically by PISA wheel fitting. The final assignment of our α4-TM2 PISEMA spectra matches very well with a 2-D projection of the leucine distribution along helical axis from N- to C-terminus in the solution NMR structure [36]. The assignment also agrees well with that for δ–TM2 nAChR [33].

The orientational order parameter, S_i^{CD}, of the ith CD bond vector can relate to the residual quadrupolar splitting, $\Delta\nu^i_Q$, in a ^{2}H NMR spectrum using the equation [43]

$$\Delta\nu_Q^i = \frac{3}{2}A_Q\frac{3\cos^2\theta - 1}{2}S_i^{CD} \quad (1)$$

where $A_Q = e^2Qq/h = 167$ kHz is the static deuterium quadrupolar coupling constant for aliphatic CD bonds, θ is the angle between the bilayer normal and the magnetic field.

2.4. The Na^+ flux assay and confocal fluorescence microscopy

The Na^+ flux assay, as measured by the enhancement of Sodium Green™ dye (Invitrogen, Carlsbad, CA) fluorescence due to Na^+ entry into vesicles through open nAChR channels, is an effective way to assess nAChR activity macroscopically. We prepared 30 mM large lamellar vesicles with 250 μM α4β2. The vesicles contain phosphatidylcholine (PC) and phosphatidylglycerol (PG) in a 4:1 molar ratio

experiments [30,31]. The structures of the transmembrane domains of the *Torpedo* nAChR were also examined by various solid-state NMR methods [32-34], including PISEMA [33]. However, no solid-state NMR study on neuronal nAChR has been reported previously. In the present study, we embedded the second transmembrane domains (TM2) of α4β2 nAChR in lipid bicelles, which served as membrane mimetic media and magnetically aligned the protein. The structural and dynamic properties of the TM2 α4β2 nAChR in the absence and presence of anesthetics halothane or isoflurane were investigated using solid state NMR, especially PISEMA experiments. Anesthetics were found to affect both helical tilting and rotational motions that have been identified computationally as critical elements for ion channel functions. This study suggested that anesthetics could alter these motions to modulate channel functions.

2. Materials and methods

2.1. Materials and sample preparation

The second transmembrane (TM2) domains of the human nAChR were obtained by solid phase synthesis [35,36]. The α_4 and β_2 TM2 domains have the sequences of EKIT**L**CISV**LL**S**L**TVF**LLL**ITE and EKMTLCISVLLALTVFLLLISK, respectively. In order to simplify the studies, only seven leucine residues in α_4 TM2 domain, as indicated in bold letters, were ^{15}N labeled.

Lipids were purchased from Avanti Polar Lipids (Alabaster, AL). A conventional protocol of bicelle preparation [37] was followed. 1,2-dimyristoyl-sn-glycero-3-phosphocoline (DMPC) and 1,2-dihexyl-sn-glycero-3-phosphocholine (DHPC) were mixed in a desired molar ratio ($q = 3.2$). Lipid concentration was 28% of sample volume (typically 220 μL). To extend sample stability for samples containing the nAChR TM2 domains, 1,2-O-ditetradecyl-sn-glycero-3-phosphocoline (14-O-PC)) and 1,2-O-dihexyl-sn-glycero-3-phosphocholine (6-O-PC) replaced DMPC and DHPC, respectively. A small amount of deuterated $DMPC_{d54}$ (~1 mg) was added to each sample for ^{2}H NMR. The α4 or β2 TM2 was dissolved in 100 μL trifluoroethanol and added to the 6-O-PC-chloroform solution. The organic solvents were removed under a stream of nitrogen gas, followed by further evaporation under high vacuum overnight. The aqueous solutions were prepared by adding 110 μL of deuterium-depleted water to dried 14-O-PC and 6-O-PC/peptide. The 14-O-PC suspension was vortexed extensively followed by three freeze/thaw cycles (liquid nitrogen/42 °C). The 14-O-PC suspension at 42 °C was then added to the 6-O-PC/peptide, followed by vortexing and three freeze/thaw cycles. Slow-speed centrifugation was sometimes necessary to remove air bubbles in the sample. A transparent solution was obtained that was viscous at 38 °C and fluid at 4 °C. Parallel-oriented peptide-containing bicelles were prepared by adding 100 mM $YbCl_3$ $6H_2O$ to the peptide-bicelle solution to reach a final lanthanide concentration of 3 mM. The sample was transferred to a 5-mm OD glass tube (New Era Enterprises, Newfield, NJ) using a pre-cooled pipet tip at 4 °C. The glass tube was sealed with a tight fitting rubber cap and further sealed with hard bees wax. The α4-TM2 concentration was 7.4 mM in the α4 samples and 3 mM in the α4β2 samples. The molar ratio of β2 to α4 was 1.5 in the α4β2 samples to ensure a formation of $(\alpha4)_2(\beta2)_3$. The peptide to lipid ratio is ~1:60. Anesthetics halothane (2-bromo-2-chloro-1,1,1-trifluoro-ethane) and isoflurane (2-chloro-2-(difluoromethoxy)-1,1,1-trifluoro-ethane) were added directly to the NMR tube (pre-cooled in an ice bath) and mixed thoroughly with the samples. The anesthetic concentrations were determined using ^{19}F NMR with 5 mM trifluoroacetic acid (TFA) as a reference.

2.2. NMR spectroscopy

All solid state NMR experiments were performed at 40 °C on a Bruker Avance 600 MHz NMR spectrometer equipped with a ^{1}H/^{31}P/^{15}N(^{2}H) Bruker flat-coil probe. ^{19}F NMR experiments were performed on a Bruker Avance 600 spectrometer with a Bruker TXO probe. The 1-D ^{15}N cross-polarization experiments were conducted using a ^{1}H 90° pulse of 5.1 μs, a 49 kHz ^{1}H-decoupling field, 1 ms contact time, 3 s recycle delay, and 10,000 scans. The same cross-polarization parameters were used in the 2-D ^{15}N-^{1}H PISEMA [38]. Other parameters included ±35 kHz frequency jumps for the Lee-Goldberg condition, 400–1000 scans, and 6–8 s recycle delay. The ^{1}H carrier frequency was set at ~4.5 ppm on parallel oriented bicelle samples. The ^{15}N chemical shift frequencies were referenced to solid ammonium sulfate at 26.8 ppm (relative to liquid ammonia at 0 ppm). The ^{2}H NMR experiments were performed using a solid echo sequence $((\pi/2) - \tau - (\pi/2) - \tau)$. The 90° pulse length was 2 μs and τ values were ~40 μs (perpendicular bicelle) and ~20 μs (parallel bicelle). The recycle delay of 0.5 s and the scans of 256 to 10,000 were used.

2.3. NMR data processing

All NMR spectra were processed using NMRPipe [39] and analyzed using Sparky [40]. The data from PISEMA experiments were fitted to the PISA (Polarity Index Slant Angle) [41,42] wheels using the program developed by Veglia's group [26]. The tilt angle (θ) of the helix axis with respect to the bicelle normal, rotation angle (ρ) of the helix around its axis, the angle between the N-H bond and helix axis (δ), and the dipolar coupling constant (K_{DD}) were determined via fittings. The principal values of the ^{15}N chemical shift tensors [24] for non-glycine residues, $\sigma11 = 64$ ppm, $\sigma22 = 77$ ppm, and $\sigma33 = 217$ ppm, were adopted for the fittings. These values were multiplied uniformly by a factor of 0.95 to accommodate reduced ^{15}N chemical shift anisotropy of proteins in bicelles, as reflected in the reduction of spectral span of the same proteins in bicelles in comparison to those in mechanically aligned lipids.

The TM2 chemical shift assignments were accomplished by combining several sources of information, including the previous assignments of δ–TM2 nAChR [33], the solution NMR structure of β2-TM2 nAChR [36], and the best fitting of PISA wheel. L19 is distinctly separated from the rest of leucine residues in a top view of the NMR structure (pdb code: 2K59) [36]. L19 also has weaker NMR signal than other leucines, presumably because it is located at the lipid-water interface and has less protection from solvent exchange. The distinct location and intensity of L19 convinced us to assign L19 to the most downfield peak in the α4-TM2 PISEMA spectra. Once L19 is defined, the rest of peaks were assigned automatically by PISA wheel fitting. The final assignment of our α4-TM2 PISEMA spectra matches very well with a 2-D projection of the leucine distribution along helical axis from N- to C-terminus in the solution NMR structure [36]. The assignment also agrees well with that for δ–TM2 nAChR [33].

The orientational order parameter, S_i^{CD}, of the ith CD bond vector can relate to the residual quadrupolar splitting, $\Delta\nu_Q^i$, in a ^{2}H NMR spectrum using the equation [43]

$$\Delta\nu_Q^i = \frac{3}{2} A_Q \frac{3\cos^2\theta - 1}{2} S_i^{CD} \quad (1)$$

where $A_Q = e^2Qq/h = 167$ kHz is the static deuterium quadrupolar coupling constant for aliphatic CD bonds, θ is the angle between the bilayer normal and the magnetic field.

2.4. The Na^+ flux assay and confocal fluorescence microscopy

The Na^+ flux assay, as measured by the enhancement of Sodium Green™ dye (Invitrogen, Carlsbad, CA) fluorescence due to Na^+ entry into vesicles through open nAChR channels, is an effective way to assess nAChR activity macroscopically. We prepared 30 mM large lamellar vesicles with 250 μM α4β2. The vesicles contain phosphatidylcholine (PC) and phosphatidylglycerol (PG) in a 4:1 molar ratio

[44]. PC and PG were mixed in chloroform. α4 and β2 were mixed in a molar ratio of 2:3 and dissolved in TFE. The dissolved lipids and α4β2 were mixed and dried to a thin film. Residual organic solvent was removed by vacuum overnight. The lipid–protein mixture was hydrated with a buffer solution at pH 7.5 containing 20 mM Tris, 50 mM $CaCl_2$, and 6uM membrane impermeable Sodium Green™. The vesicles were obtained by incubating the lipid–protein solution at 42 °C overnight and subsequent multiple cycles of freeze and thaw. An extensive dialysis was performed to remove Sodium Green™ dye outside the vesicles.

The Na^+ flux assay was performed using an Olympus Fluoview300 Confocal Laser Scanning head with an Olympus IX70 inverted microscope (Olympus, Melville, NY). Sodium Green™ was excited by the 488-nm argon laser line and the emission was detected using sharp cutoff 510IF long-pass and BA530RIF short-pass filters. For each measurement, 50 μL vesicles containing α4β2 were added into a tray coated with poly-lysine that facilitated vesicle adhesion due to the interactions between negatively charged PG and positively charged poly-lysine. The image acquisition began before the addition of an isotonic 100 mM NaCl solution to the media outside the vesicles and continued for 200 s after the exposure to Na^+. The program MetaMorph was used for analyzing the image data.

3. Results and discussion

3.1. Anesthetic effects on bicelles

Solid-state ^2H NMR spectra of bicelles with deuterated $DMPC_{d54}$, as shown in Fig. 1, provided insight of lipid alignment and dynamics. The high-resolution ^2H NMR spectra with distinguished quadrupolar splittings in Fig. 1A and 1B attested that the bicelles, without incorporating proteins, were well oriented. The quadrupolar splitting of individual ^2H peaks corresponding to carbon positions close to the tail of the aliphatic chains showed little difference in Fig. 1A and 1B, suggesting that anesthetic halothane molecules had no access to the hydrophobic tail region. However, halothane diffused to the carbon positions close to the glycerol group, as evidenced by significantly broadened ^2H signals of the region in Fig. 1B. The order parameters of individual C-^2H bonds of $DMPC_{d54}$, S_{CD}, were calculated using Eq. (1) in the presence and absence of 6 mM halothane. S_{CD} normally contains information on (a) collective motions of lipids, including bicelle wobbling, (b) trans-gauche isomerizations around C-C bonds of lipids, and (c) the anisotropic reorientation of a whole lipid molecule. Collective motions of lipids were small in our systems, in which a 72% hydration level was remained and bicelles were well magnetically oriented. A recent comprehensive NMR analysis also suggested a good bicelle alignment at such a hydration level [45]. The contribution of anisotropic lipid reorientation to S_{CD} was expected to be uniform for all C–^2H bonds linked to a rigid structure. Therefore, a small increase in S_{CD} values in the presence of halothane in Fig. 2 predominately resulted from orientation of the C–^2H bonds with respect to the principal axis of motion of individual lipid molecule. However, since only the readable quadrupolar splitting was used for S_{CD} calculations, the disordered component reflected in the broader peaks might be underestimated in Fig. 2.

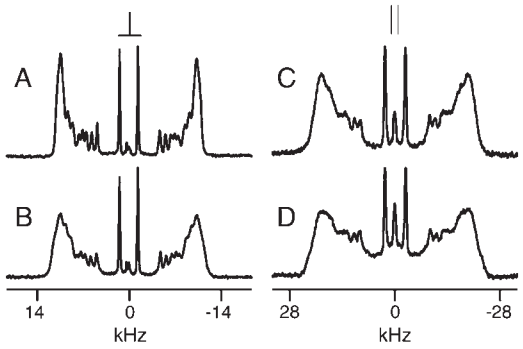

Fig. 1. ^2H NMR spectra of perdeuterated $DPMC_{d54}$ phospholipids embedded in (A) a pure DMPC/DHPC ($q = 3.2$) bicelle system; (B) after adding 6 mM halothane to the system in (A); (C) the 4OPC/6OPC bicelle system incorporated with $(\alpha4)_2(\beta2)_3$ nAChR TM2 domains; (D) after adding 6 mM halothane to the system in (C). The bicelle normal was perpendicular to the magnetic field in (A) and (B), parallel to the magnetic field in (C) and (D) due to the addition of 3 mM lanthanide. The spectra were acquired with the solid echo pulse sequence at 40 °C. The spectrum center was arbitrarily set to 0 Hz.

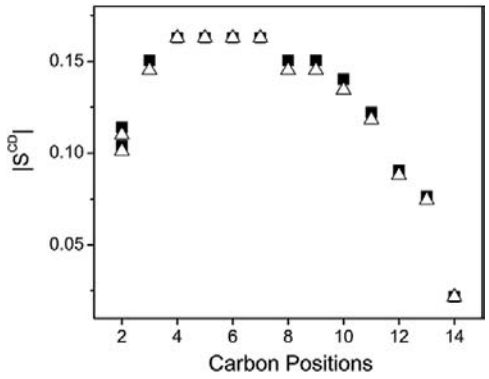

Fig. 2. C-^2H order parameter S_{CD} as a function of $DPMC_{d54}$ carbon positions in the absence (△) and presence (■) of 6 mM anesthetic halothane.

Fig. 1C and D shows the solid-state ^2H NMR spectra of the bicelles incorporated with the $(\alpha4)_2(\beta2)_3$ TM2 in the absence and presence of 6 mM anesthetic isoflurane, respectively. The bicelles were flipped 90° by $YbCl_3$ so that their quadropolar splittings were double of that in Fig. 1A and 1B. The presence of the $(\alpha4)_2(\beta2)_3$ TM2 made the ^2H peaks much broader, presumably because the lipid bilayer was severely disturbed by the insertion of the TM2 domains. A small amount of lipids were in isotropic phase after incorporating TM2 domains into the bicelles and the amount increased upon addition of 6 mM isoflurane, as reflected in the peak at zero frequency. The degree of anesthetics-induced ^2H peak broadening in Fig. 1D seemed to be more severe than that in Fig. 1B, especially to the carbon positions at the middle of DMPC aliphatic chains. Formation of the $(\alpha4)_2(\beta2)_3$ channels might facilitate anesthetic diffusion into the deep bilayer where anesthetics normally have less access. Direct interactions between anesthetics and transmembrane proteins were observed previously [35,46-48]. Anesthetics could modulate protein dynamics directly and allosterically [46]. Such changes in protein motions could affect lipids surrounding proteins and contribute to the observed lipid peak broadening in Fig. 1D.

3.2. TM2 domains in channel and non-channel forms

The α4 and β2 subunits of nAChR need to be in 2:3 stoichiometry to form pentameric channels [49]. Our Na^+ flux experiments confirmed that ion channels could be formed by combining the α4 and β2 TM2 domains in a 2:3 molar ratio, but not by the α4 TM2 domain alone. As shown in Fig. 3, large vesicles made of phosphatidylcholine (PC) and phosphatidylglycerol (PG) with $(\alpha4)_2(\beta2)_3$ TM2 could be easily identified. A time-dependent increase of sodium green fluorescence intensity upon injection of 10 μL 100 mM NaCl signaled channel formation. Control vesicles without channels showed no increase in fluorescence intensity, nor did the channel-containing vesicles when isotonic $CaCl_2$ was added instead of the NaCl solution. The same experiment was also performed on the PC-PG vesicles containing the α4 TM2 domain alone and found no indication of

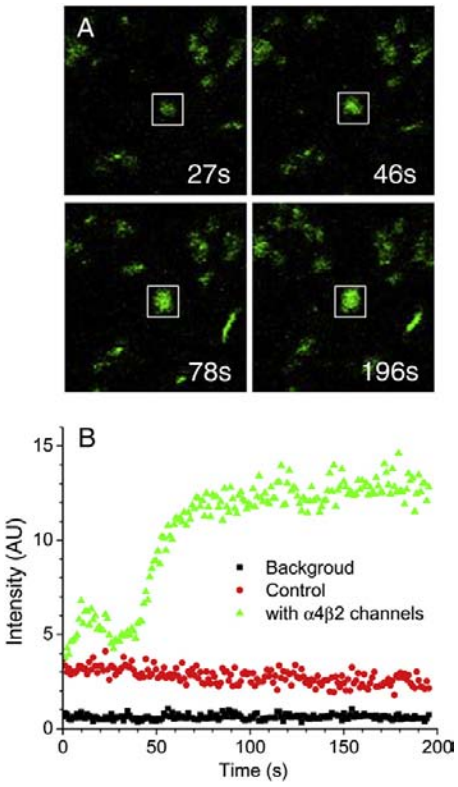

Fig. 3. (A) Confocal fluorescence images of large unilamellar vesicles (LUV) made of phosphatidylcholine and phosphatidylglycerol containing α4β2 nAChR channels after exposure to ~100 mM NaCl solution at different time points. Membrane-impermeable Sodium Green fluorescent dyes were enclosed and trapped inside the LUVs to indicate intra-vesicle Na^+ concentration. The fluorescence intensity of the vesicles with α4β2 channels increased significantly within a short period of time after exposure to extra-vesicle NaCl, indicating an influx of Na^+ through the channels. (B) The intensity changes in the circled vesicles over time after the exposure to extra-vesicle Na^+. The background refers to the region without vesicles. The control refers to vesicles without channels, whose fluorescence intensity remained constant before and after exposure to extra-vesicle Na^+.

channel formation, suggesting different topology and dynamics of the α4 and $(\alpha4)_2(\beta2)_3$ TM2 assemblies.

3.2.1. PISEMA: Effect of β2 TM2 on α4 TM2

The solid state ^1H-^{15}N dipolar /^{15}N chemical shift correlation PISEMA spectra of the ^{15}N-Leu labeled α4 TM2 in Fig. 4 demonstrated distinct differences in the absence and presence of the unlabeled β2 TM2. Wheel-like patterns in the PISEMA spectra of parallel 14-O-PC/6-O-PC bicelles confirmed the transmembrane helical structure of the TM2 domains [36]. Six out of seven total leucine residues of the α4 TM2 showed amide ^{15}N resonances between ~180 and 200 ppm. Their resonance patterns are similar to those composed by the TM2 of the δ nAChR [33]. Leu 5 at the N-terminus of the TM2 did not show up in this region of PISEMA spectra, confirming our early solution NMR finding that Leu 5 was not part of the TM2 helix [36]. Leu 19 resides close to the C terminus of the TM2. Its relatively weak intensity in the PISEMA spectra is probably due to a conformational exchange and less efficient cross-polarization in the dynamic C-terminal region. The most downfield ^{15}N chemical shift in the PISEMA spectra is ~12 ppm smaller than the conventional value of σ33 (217 ppm), suggesting a more dynamical environment in bicelles.

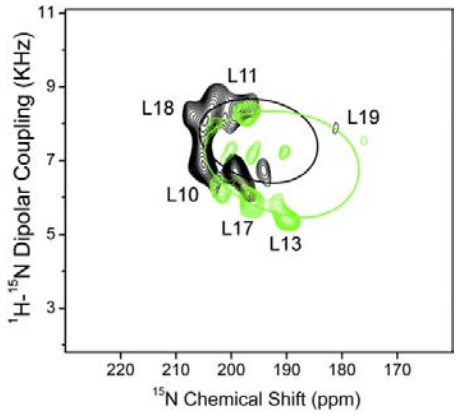

Fig. 4. PISEMA spectra of the ^{15}N-Leu labeled α4 TM2 in the absence (black) and presence (green) of unlabeled β2 TM2. Best fit simulations to the PISEMA data reveal the helical tilt angles of $12\pm1°$ and $16\pm1°$ of the α4 TM2 and the $(\alpha4)_2(\beta2)_3$ TM2, respectively. The notable difference between two PISEMA spectra suggests that the α4 TM2 must have experienced the existence of the β2 TM2 in the $(\alpha4)_2(\beta2)_3$ TM2 sample.

Although the α4 TM2 had a single set of ^{15}N-Leu resonances in the PISEMA spectrum in Fig. 4, the presence of unlabeled β2 TM2 brought up several minor resonances for the $(\alpha4)_2(\beta2)_3$ TM2. Leu10, Leu17, and Leu13 showed almost the same ^{15}N chemical shifts in both major and minor resonances, but their dipolar couplings were about 1 kHz greater in the minor resonances. Although it was almost impossible to accurately define topology of the minor conformation due to too few numbers of resonances, the chemical shift and dipolar coupling data suggested that the helix tilt angle relative to the bicelle normal must be smaller in the minor conformation than in the major population [41,42]. The minor peaks might also result from a sub-population α4 TM2 in a slightly different motional environment.

A more noticeable difference between the α4 and $(\alpha4)_2(\beta2)_3$ spectra in Fig. 4 is the shift of the amide resonances along both ^{15}N chemical shift and ^1H-^{15}N dipolar coupling axis. Leu11 and Leu18 of the α4 TM2 experienced relatively small shifts before and after mixing with the β2 TM2, but Leu10, Leu13, Leu17 and Leu19 had more profound changes. It is plausible that Leu11 and Leu18 have experienced little interaction with residues in other helices. The best fitting of all downfield resonances to ideal PISA wheels revealed the helical tilt angles of $12\pm1°$ and $16\pm1°$ of the α4 TM2 and the $(\alpha4)_2(\beta2)_3$ TM2, respectively. The rotation angle, ρ, was 65° for both α4 and $(\alpha4)_2(\beta2)_3$. The tilt angle of 12° for the α4 TM2 in bicelles agrees with the result of the δ nAChR [33], where the δ TM2 helix was also tilted 12° relative to the normal of mechanically oriented DMPC bilayers. Neither α4 nor δ subunit could form nAChR channels without partitioning of other subunit types [49]. The tilt angle of $16\pm1°$ of the $(\alpha4)_2(\beta2)_3$ TM2 is comparable to the tilt angle of $15\pm2°$ found for the $GABA_A$ receptor TM2 domain, an anion channel-forming peptide, by a recent solid-state NMR study [18].

It is worth mentioning that all the resonances in our PISEMA spectra resulted solely from the ^{15}N-Leu residues of the α4 TM2. The unlabeled β2 TM2 did not generate ^{15}N NMR signals. If the α4 TM2 was isolated from the β2 TM2, the $(\alpha4)_2(\beta2)_3$ TM2 would give the same PISEMA spectrum as the α4 TM2. The notable difference between the two spectra in Fig. 4 prove that the α4 TM2 must have interacted with the β2 TM2 in the $(\alpha4)_2(\beta2)_3$ TM2 sample. A thorough NMR characterization of oligomerization states of ^2H selective labeled transmembrane peptides in oriented lipid bilayers was demonstrated previously [50]. The same method can also be applied to the α4 and β2 TM2 if proper labeled samples become available. Nevertheless, the data in Fig. 4 indicate that interaction

between α4 and β2 subunits that might be the driving force for assembling a functional channel. The larger helix tilt angle found in the $(\alpha4)_2(\beta2)_3$ TM2 supported the previous prediction that channel opening might involve tilting of pore lining helices [10,12,51,52].

3.3. Anesthetic effect on the TM2 domains

Fig. 5 displays an overlay of the PISEMA spectra of the α4 TM2 in the absence and presence of 6 mM halothane. Halothane lowered ^{1}H-^{15}N dipolar coupling and ^{15}N chemical shift of six leucine residues noticeably. The data fitting into PISA wheels provided a helical tilt angle of 14° in the presence of halothane. The dipolar coupling constant, K_{DD}, decreased from 8700 to 8100 KHz, but the rotational angle ($\rho = 65°$) and the angle between N-H bone and helix axis ($\delta = 13°$) remained the same in the absence and presence of 6 mM halothane.

In comparison to the α4 TM2, the $(\alpha4)_2(\beta2)_3$ TM2 seemed less susceptible to anesthetics. Fig. 6 shows the PISEMA spectra of the $(\alpha4)_2(\beta2)_3$ TM2 before and after adding 12 mM anesthetic isoflurane. The helix tilt angle of the $(\alpha4)_2(\beta2)_3$ TM2 with respect to the bicelle normal changed less than 1° ($\theta = 16.5°$). The K_{DD} value changed from 8400 to 7900 KHz. The other two parameters, $\rho = 65°$ and $\delta = 13°$, remain unchanged. To the majority of the $(\alpha4)_2(\beta2)_3$ TM2 in the sample, anesthetic isoflurane had a subtle but real impact on their helical orientation in bicelles. The anesthetic-induced changes in the major resonance pattern also implicate the possibility of a wobbling motion of the helix axis with respect to the bicelle normal [53]. Those aforementioned minor resonances of Leu10, Leu13, and Leu17 shown in Fig. 4 disappeared after adding 6 mM isoflurane to the sample (see the on-line supporting information). However, another subset of minor resonances appeared upon further increasing the isoflurane concentration to 12 mM, as shown in Fig. 6. The new minor peaks, labeled as L19′, L11′, L13′ L17′, and L19′ in Fig. 6, appeared as if they resulted from corresponding major resonances rotating ~50° counterclockwise around the helical axis. Distinct major and minor resonances signify that the helix rotational motion was on a time scale slower than 10^{-4} s [54]. Both tilting and rotational motions of the TM2 helices are critical elements for channel functions [10]. Our data reveal that anesthetic molecules are able to alter motions of the TM2 helices that could account, at least partially, for anesthetic inhibition effects on the α4β2 nAChR [7].

It is not surprising to observe different responses of the α4 TM2 and the $(\alpha4)_2(\beta2)_3$ to anesthetics, considering that one might exist as monomer but the other could form channels. Without the presence of

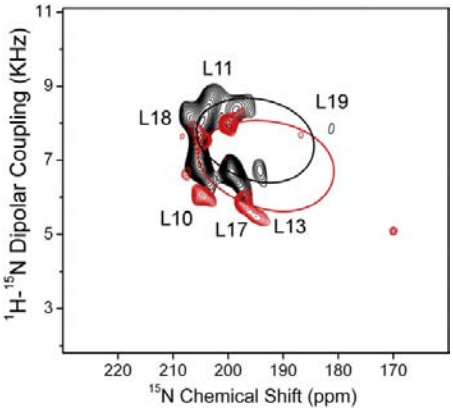

Fig. 5. An overlay of PISEMA spectra of the α4 TM2 in the absence (black) and presence (red) of 6 mM halothane. PISA wheel fitting of the α4 TM2 in the presence of 6 mM halothane reveals an increase in tilt angle from 12° ± 1° to 14° ± 1°.

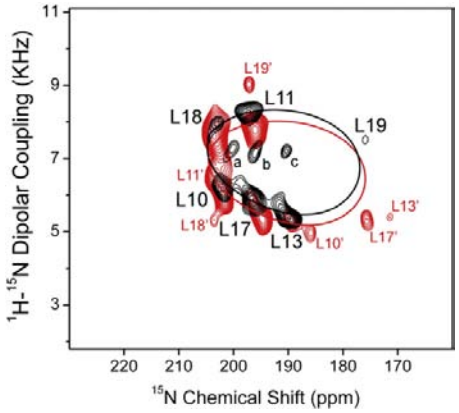

Fig. 6. An overlay of PISEMA spectra of the $(\alpha4)_2(\beta2)_3$ TM2 in the absence (black) and presence (red) of 12 mM anesthetic isoflurane. Notice the appearance of subset resonance peaks (a, b, c in black and L19′, L11′, L18′, L19′, L13′, L17′ in red). The minor resonance peaks in red seem to result from rotating corresponding major resonances ~50° counterclockwise around the helical axis.

the β2 TM2, the α4 TM2 interacted loosely with other α4 TM2 helices so that individual helix orientation was affected by anesthetics more severely. In a pentameric $(\alpha4)_2(\beta2)_3$ TM2, the helix tilting in respect to the bicelle normal became less sensitive to the addition of anesthetics, presumably due to stronger interaction between the α4 TM2 and its adjacent β2 TM2. One may wonder if small changes in helix orientation induced by anesthetics, either through tilting or rotational motion, are significant enough to alter channel functions. The X-ray structures of pentameric ion channels from bacterial demonstrated that the pore-lining TM2 domains in closed- and open-channel conformations differ by merely 9° rotation around an axis that is parallel to the membrane normal [12-14], suggesting that a small change in the TM2 orientation could elicit a sizable change in channel functions. Although further structural and dynamical investigations on integral α4β2 nAChR are necessary to define a final answer, the present study highlights the possibility that anesthetics may modulate the channel function via altering the motion as well as orientation of the pore-ling domain.

4. Conclusions

Several key findings emerged from the current study. First, transmembrane proteins could facilitate anesthetic diffusion into deep membrane bilayers even though anesthetics normally prefer amphiphilic lipid-water interface region [55]. Consequently, anesthetics affected lipid alignment and conformation more severely in bicelles containing proteins. Secondly, the α4 TM2 could not form channels unless it had been mixed with the β2 TM2. The interactions between the α4 and β2 TM2 subunits do exist and such interactions may be essential to drive channel formation. Thirdly, general anesthetics could perturb orientations of the transmembrane helices in lipid bilayers and introduce changes in helical motions. The observed anesthetic effects on the tilt and rotational angles of pore lining TM2 helices reveal a potential pathway for anesthetic inhibition of channel functions. A more challenging question has arisen based on the current study: how do anesthetics make changes in transmembrane protein orientations and motions that are related to protein functions? This is certainly a question worth further investigation.

Acknowledgements

The authors thank Dr. Yuanyuan Jia for her contribution to sample preparations and initial experiment set up, Dr. Jochem Struppe of

Bruker for his suggestions in setting up the PISEMA experiment, Dr. Christopher V. Grant of UCSD for his suggestions in initial sample preparation and selection of parameters for experiments and data process, Prof. Gianluigi Veglia and Dr. Nate Traaseth of University of Minnesota and Prof. Timothy A. Cross and Dr. Conggang Li of Florida State University for sharing their PISA wheel simulation programs with us. This work was supported in part by grants from the National Institute of Health (R01GM56257 and R01GM66358 to P.T. and R37GM049202 to Y.X.).

Appendix A. Supplementary data

Supplementary data associated with this article can be found, in the online version, at doi:10.1016/j.bbamem.2009.08.009.

References

[1] S.A. Forman, K.W. Miller, G. Yellen, A discrete site for general anesthetics on a postsynaptic receptor, Mol. Pharmacol. 48 (1995) 574–581.
[2] R.A. Cardoso, S.J. Brozowski, L.E. Chavez-Noriega, M. Harpold, C.F. Valenzuela, R.A. Harris, Effects of ethanol on recombinant human neuronal nicotinic acetylcholine receptors expressed in Xenopus oocytes, J. Pharmacol. Exp. Ther. 289 (1999) 774–780.
[3] D.E. Raines, V.T. Zachariah, Isoflurane increases the apparent agonist affinity of the nicotinic acetylcholine receptor [see comments], Anesthesiology 90 (1999) 135–146.
[4] T. Mori, X. Zhao, Y. Zuo, G.L. Aistrup, K. Nishikawa, W. Marszalec, J.Z. Yeh, T. Narahashi, Modulation of neuronal nicotinic acetylcholine receptors by halothane in rat cortical neurons, Mol. Pharmacol. 59 (2001) 732–743.
[5] M. Yamashita, T. Mori, K. Nagata, J.Z. Yeh, T. Narahashi, Isoflurane modulation of neuronal nicotinic acetylcholine receptors expressed in human embryonic kidney cells, Anesthesiology 102 (2005) 76–84.
[6] E. Arevalo, D.C. Chiara, S.A. Forman, J.B. Cohen, K.W. Miller, Gating-enhanced accessibility of hydrophobic sites within the transmembrane region of the nicotinic acetylcholine receptor's {delta}-subunit. A time-resolved photolabeling study, J. Biol. Chem. 280 (2005) 13631–13640.
[7] P. Flood, J. Ramirez-Latorre, L. Role, Alpha 4 beta 2 neuronal nicotinic acetylcholine receptors in the central nervous system are inhibited by isoflurane and propofol, but alpha 7-type nicotinic acetylcholine receptors are unaffected, Anesthesiology 86 (1997) 859–865.
[8] N.P. Franks, W.R. Lieb, Do general anaesthetics act by competitive binding to specific receptors? Nature 310 (1984) 599–601.
[9] J.A. Campagna, K.W. Miller, S.A. Forman, Mechanisms of actions of inhaled anesthetics, N. Engl. J. Med. 348 (2003) 2110–2124.
[10] E.J. Haddadian, M.H. Cheng, R.D. Coalson, Y. Xu, P. Tang, In Silico Models for the Human alpha4beta2 Nicotinic Acetylcholine Receptor, J. Phys. Chem. B. 112 (2008) 13981–13990.
[11] N. Unwin, Refined structure of the nicotinic acetylcholine receptor at 4 Å resolution, J. Mol. Biol. 346 (2005) 967–989.
[12] R.J. Hilf, R. Dutzler, X-ray structure of a prokaryotic pentameric ligand-gated ion channel, Nature 452 (2008) 375–379.
[13] R.J. Hilf, R. Dutzler, Structure of a potentially open state of a proton-activated pentameric ligand-gated ion channel, Nature 457 (2009) 115–118.
[14] N. Bocquet, H. Nury, M. Baaden, C. Le Poupon, J.P. Changeux, M. Delarue, P.J. Corringer, X-ray structure of a pentameric ligand-gated ion channel in an apparently open conformation, Nature 457 (2009) 111–114.
[15] N.J. Traaseth, L. Shi, R. Verardi, D.G. Mullen, G. Barany, G. Veglia, Structure and topology of monomeric phospholamban in lipid membranes determined by a hybrid solution and solid-state NMR approach, Proc. Natl. Acad. Sci. U. S. A. 106 (2009) 10165–10170.
[16] V.S. Bajaj, M.L. Mak-Jurkauskas, M. Belenky, J. Herzfeld, R.G. Griffin, Functional and shunt states of bacteriorhodopsin resolved by 250 GHz dynamic nuclear polarization-enhanced solid-state NMR, Proc. Natl. Acad. Sci. U. S. A. 106 (2009) 9244–9249.
[17] E. Salnikov, C. Aisenbrey, V. Vidovic, B. Bechinger, Solid-state NMR approaches to measure topological equilibria and dynamics of membrane polypeptides, Biochim. Biophys. Acta (2009).
[18] S.K. Kandasamy, D.K. Lee, R.P. Nanga, J. Xu, J.S. Santos, R.G. Larson, A. Ramamoorthy, Solid-state NMR and molecular dynamics simulations reveal the oligomeric ion-channels of TM2-GABA(A) stabilized by intermolecular hydrogen bonding, Biochim. Biophys. Acta 1788 (2009) 686–695.
[19] A. McDermott, Structure and dynamics of membrane proteins by magic angle spinning solid-state NMR, Annu. Rev. Biophys. 38 (2009) 385–403.
[20] C. Li, M. Yi, J. Hu, H.X. Zhou, T.A. Cross, Solid-state NMR and MD simulations of the antiviral drug amantadine solubilized in DMPC bilayers, Biophys. J. 94 (2008) 1295–1302.
[21] S.J. Opella, A.C. Zeri, S.H. Park, Structure, dynamics, and assembly of filamentous bacteriophages by nuclear magnetic resonance spectroscopy, Annu. Rev. Phys. Chem. 59 (2008) 635–657.
[22] M. Hong, Structure, topology, and dynamics of membrane peptides and proteins from solid-state NMR spectroscopy, J. Phys. Chem. B. 111 (2007) 10340–10351.
[23] A. Watts, Solid-state NMR in drug design and discovery for membrane-embedded targets, Nat. Rev. Drug Discov. 4 (2005) 555–568.
[24] C.H. Wu, A. Ramamoorthy, L.M. Gierasch, S.J. Opella, Simultaneous Characterization of the Amide 1H Chemical Shift, 1H-15N Dipolar, and 15N Chemical Shift Interaction Tensors in a Peptide Bond by Three-Dimensional Solid-State NMR Spectroscopy, J. Am. Chem. Soc. 117 (1995) 6148–6149.
[25] R. Fu, M. Truong, R.J. Saager, M. Cotten, T.A. Cross, High-resolution heteronuclear correlation spectroscopy in solid state NMR of aligned samples, J. Magn. Reson. 188 (2007) 41–48.
[26] J.J. Buffy, N.J. Traaseth, A. Mascioni, P.L. Gor'kov, E.Y. Chekmenev, W.W. Brey, G. Veglia, Two-dimensional solid-state NMR reveals two topologies of sarcolipin in oriented lipid bilayers, Biochemistry 45 (2006) 10939–10946.
[27] C. Li, P. Gao, H. Qin, R. Chase, P.L. Gor'kov, W.W. Brey, T.A. Cross, Uniformly aligned full-length membrane proteins in liquid crystalline bilayers for structural characterization, J. Am. Chem. Soc. 129 (2007) 5304–5305.
[28] U.H. Durr, L. Waskell, A. Ramamoorthy, The cytochromes P450 and b5 and their reductases–promising targets for structural studies by advanced solid-state NMR spectroscopy, Biochim. Biophys. Acta 1768 (2007) 3235–3259.
[29] A.W. Ramamoorthy, Y. Lee, D.K., PISEMA solid-state NMR spectroscopy, Ann. Rep. NMR Spectrosc. 52 (2004) 1–52.
[30] P.T. Williamson, A. Verhoeven, K.W. Miller, B.H. Meier, A. Watts, The conformation of acetylcholine at its target site in the membrane-embedded nicotinic acetylcholine receptor, Proc. Natl. Acad. Sci. U. S. A. 104 (2007) 18031–18036.
[31] P.T. Williamson, B.H. Meier, A. Watts, Structural and functional studies of the nicotinic acetylcholine receptor by solid-state NMR, Eur. Biophys. J. 33 (2004) 247–254.
[32] M.R. de Planque, D.T. Rijkers, J.I. Fletcher, R.M. Liskamp, F. Separovic, The alphaM1 segment of the nicotinic acetylcholine receptor exhibits conformational flexibility in a membrane environment, Biochim. Biophys. Acta 1665 (2004) 40–47.
[33] S.J. Opella, F.M. Marassi, J.J. Gesell, A.P. Valente, Y. Kim, M. Oblatt-Montal, M. Montal, Structures of the M2 channel-lining segments from nicotinic acetylcholine and NMDA receptors by NMR spectroscopy, Nat. Struct. Biol. 6 (1999) 374–379.
[34] P.T. Williamson, G. Zandomeneghi, F.J. Barrantes, A. Watts, B.H. Meier, Structural and dynamic studies of the gamma-M4 trans-membrane domain of the nicotinic acetylcholine receptor, Mol. Membr. Biol. 22 (2005) 485–496.
[35] V. Bondarenko, V.E. Yushmanov, Y. Xu, P. Tang, NMR study of general anesthetic interaction with nAChR beta2 subunit, Biophys. J. 94 (2008) 1681–1688.
[36] V.E. Yushmanov, Y. Xu, P. Tang, NMR structure and dynamics of the second transmembrane domain of the neuronal acetylcholine receptor beta 2 subunit, Biochemistry 42 (2003) 13058–13065.
[37] A.A. De Angelis, S.C. Howell, A.A. Nevzorov, S.J. Opella, Structure determination of a membrane protein with two trans-membrane helices in aligned phospholipid bicelles by solid-state NMR spectroscopy, J. Am. Chem. Soc. 128 (2006) 12256–12267.
[38] C.H. Wu, A. Ramamoorthy, S.J. Opella, High-Resolution Heteronuclear Dipolar Solid-State NMR Spectroscopy, J. Magn. Reson., Ser. A 109 (1994) 270–272.
[39] F. Delaglio, S. Grzesiek, G.W. Vuister, G. Zhu, J. Pfeifer, A. Bax, NMRPipe: a multidimensional spectral processing system based on UNIX pipes, J. Biomol. NMR 6 (1995) 277–293.
[40] T.D. Goddard, and Kneller, D.G, University of California, San Francisco.
[41] J. Wang, J. Denny, C. Tian, S. Kim, Y. Mo, F. Kovacs, Z. Song, K. Nishimura, Z. Gan, R. Fu, J.R. Quine, T.A. Cross, Imaging membrane protein helical wheels, J. Magn. Reson. 144 (2000) 162–167.
[42] F.M. Marassi, S.J. Opella, A solid-state NMR index of helical membrane protein structure and topology, J. Magn. Reson. 144 (2000) 150–155.
[43] J.H. Davis, The description of membrane lipid conformation, order and dynamics by 2H-NMR, Biochim. Biophys. Acta 737 (1983) 117–171.
[44] P. Tang, J. Hu, S. Liachenko, Y. Xu, Distinctly different interactions of anesthetic and nonimmobilizer with transmembrane channel peptides, Biophys. J. 77 (1999) 739–746.
[45] K. Yamamoto, R. Soong, A. Ramamoorthy, Comprehensive analysis of lipid dynamics variation with lipid composition and hydration of bicelles using nuclear magnetic resonance (NMR) spectroscopy, Langmuir 25 (2009) 7010–7018.
[46] C.G. Canlas, T. Cui, L. Li, Y. Xu, P. Tang, Anesthetic modulation of protein dynamics: insights from a NMR study, J. Phys. Chem. B. 112 (2008) 14312–14318.
[47] Y. Xu, T. Seto, P. Tang, L. Firestone, NMR study of volatile anesthetic binding to nicotinic acetylcholine receptors, Biophys. J. 78 (2000) 746–751.
[48] Y. Xu, P. Tang, Amphiphilic sites for general anesthetic action? Evidence from 129Xe-[1H] intermolecular nuclear Overhauser effects, Biochim. Biophys. Acta 1323 (1997) 154–162.
[49] D.S. McGehee, Molecular diversity of neuronal nicotinic acetylcholine receptors, Ann. N. Y. Acad Sci. 868 (1999) 565–577.
[50] C. Aisenbrey, B. Bechinger, Investigations of polypeptide rotational diffusion in aligned membranes by 2H and 15 N solid-state NMR spectroscopy, J. Am. Chem. Soc. 126 (2004) 16676–16683.
[51] P. Tang, P.K. Mandal, Y. Xu, NMR structures of the second transmembrane domain of the human glycine receptor alpha(1) subunit: model of pore architecture and channel gating, Biophys. J. 83 (2002) 252–262.
[52] A. Szarecka, Y. Xu, P. Tang, Dynamics of heteropentameric nicotinic acetylcholine receptor: implications of the gating mechanism, Proteins 68 (2007) 948–960.
[53] R.C. Page, S. Kim, T.A. Cross, Transmembrane helix uniformity examined by spectral mapping of torsion angles, Structure 16 (2008) 787–797.
[54] A. Abragam, Principles of Nuclear Magnetism, 315, Oxford University Press, New York, 1961.
[55] P. Tang, B. Yan, Y. Xu, Different distribution of fluorinated anesthetics and nonanesthetics in model membrane: a 19F NMR study, Biophys. J. 72 (1997) 1676–1682.

BIBLIOGRAPHY

1 Wallin, E. & von Heijne, G. Genome-wide analysis of integral membrane proteins from eubacterial, archaean, and eukaryotic organisms. *Protein Sci* **7**, 1029-1038, doi:10.1002/pro.5560070420 (1998).

2 Yildirim, M. A., Goh, K. I., Cusick, M. E., Barabasi, A. L. & Vidal, M. Drug-target network. *Nat Biotechnol* **25**, 1119-1126, doi:nbt1338 [pii]10.1038/nbt1338 (2007).

3 Celie, P. H. *et al.* Nicotine and carbamylcholine binding to nicotinic acetylcholine receptors as studied in AChBP crystal structures. *Neuron* **41**, 907-914, doi:S0896627304001151 [pii] (2004).

4 Brejc, K. *et al.* Crystal structure of an ACh-binding protein reveals the ligand-binding domain of nicotinic receptors. *Nature* **411**, 269-276, doi:10.1038/3507701135077011 [pii] (2001).

5 Dellisanti, C. D., Yao, Y., Stroud, J. C., Wang, Z. Z. & Chen, L. Crystal structure of the extracellular domain of nAChR alpha1 bound to alpha-bungarotoxin at 1.94 A resolution. *Nat Neurosci* **10**, 953-962, doi:nn1942 [pii]10.1038/nn1942 (2007).

6 Hansen, S. B. *et al.* Structures of Aplysia AChBP complexes with nicotinic agonists and antagonists reveal distinctive binding interfaces and conformations. *EMBO J* **24**, 3635-3646, doi:7600828 [pii]10.1038/sj.emboj.7600828 (2005).

7 Miyazawa, A., Fujiyoshi, Y. & Unwin, N. Structure and gating mechanism of the acetylcholine receptor pore. *Nature* **423**, 949-955, doi:10.1038/nature01748nature01748 [pii] (2003).

8 Unwin, N. Refined structure of the nicotinic acetylcholine receptor at 4A resolution. *J Mol Biol* **346**, 967-989, doi:S0022-2836(04)01601-8 [pii]10.1016/j.jmb.2004.12.031 (2005).

9 Hilf, R. J. & Dutzler, R. Structure of a potentially open state of a proton-activated pentameric ligand-gated ion channel. *Nature* **457**, 115-118, doi:nature07461 [pii]10.1038/nature07461 (2009).

10 Hilf, R. J. & Dutzler, R. X-ray structure of a prokaryotic pentameric ligand-gated ion channel. *Nature* **452**, 375-379, doi:nature06717 [pii]10.1038/nature06717 (2008).

11 Bocquet, N. *et al.* X-ray structure of a pentameric ligand-gated ion channel in an apparently open conformation. *Nature* **457**, 111-114, doi:nature07462 [pii]10.1038/nature07462 (2009).

12 Le Novere, N. & Changeux, J. P. Molecular evolution of the nicotinic acetylcholine receptor: an example of multigene family in excitable cells. *J Mol Evol* **40**, 155-172 (1995).

13 Changeux, J. P., Kasai, M. & Lee, C. Y. Use of a snake venom toxin to characterize the cholinergic receptor protein. *Proc Natl Acad Sci U S A* **67**, 1241-1247 (1970).

14 Williams, B. M. *et al.* The long internal loop of the alpha 3 subunit targets nAChRs to subdomains within individual synapses on neurons in vivo. *Nat Neurosci* **1**, 557-562, doi:10.1038/2792 (1998).

15 Jeanclos, E. M. *et al.* The chaperone protein 14-3-3eta interacts with the nicotinic acetylcholine receptor alpha 4 subunit. Evidence for a dynamic role in subunit stabilization. *J Biol Chem* **276**, 28281-28290, doi:10.1074/jbc.M011549200M011549200 [pii] (2001).

16 Huebsch, K. A. & Maimone, M. M. Rapsyn-mediated clustering of acetylcholine receptor subunits requires the major cytoplasmic loop of the receptor subunits. *J Neurobiol* **54**, 486-501, doi:10.1002/neu.10177 (2003).

17 Kelley, S. P., Dunlop, J. I., Kirkness, E. F., Lambert, J. J. & Peters, J. A. A cytoplasmic region determines single-channel conductance in 5-HT3 receptors. *Nature* **424**, 321-324, doi:10.1038/nature01788nature01788 [pii] (2003).

18 Hales, T. G. *et al.* Common determinants of single channel conductance within the large cytoplasmic loop of 5-hydroxytryptamine type 3 and alpha4beta2 nicotinic acetylcholine receptors. *J Biol Chem* **281**, 8062-8071, doi:M513222200 [pii]10.1074/jbc.M513222200 (2006).

19 Gee, V. J., Kracun, S., Cooper, S. T., Gibb, A. J. & Millar, N. S. Identification of domains influencing assembly and ion channel properties in alpha 7 nicotinic receptor and 5-HT3 receptor subunit chimaeras. *Br J Pharmacol* **152**, 501-512, doi:0707429 [pii]10.1038/sj.bjp.0707429 (2007).

20 Kracun, S., Harkness, P. C., Gibb, A. J. & Millar, N. S. Influence of the M3-M4 intracellular domain upon nicotinic acetylcholine receptor assembly, targeting and function. *Br J Pharmacol* **153**, 1474-1484, doi:0707676 [pii]10.1038/sj.bjp.0707676 (2008).

21 Campagna, J. A., Miller, K. W. & Forman, S. A. Mechanisms of actions of inhaled anesthetics. *N Engl J Med* **348**, 2110-2124, doi:10.1056/NEJMra021261348/21/2110 [pii] (2003).

22 Eckenhoff, R. G., and J. S. Johansson. Molecular interactions between inhaled anesthetics and proteins. *Pharmacol. Rev.* **49**, 25 (1997).

23 Szarecka, A., Xu, Y. & Tang, P. Dynamics of firefly luciferase inhibition by general anesthetics: Gaussian and anisotropic network analyses. *Biophys J* **93**, 1895-1905, doi:S0006-3495(07)71446-7 [pii]10.1529/biophysj.106.102780 (2007).

24 Tang, P. & Xu, Y. Large-scale molecular dynamics simulations of general anesthetic effects on the ion channel in the fully hydrated membrane: the implication of molecular mechanisms of general anesthesia. *Proc Natl Acad Sci U S A* **99**, 16035-16040, doi:10.1073/pnas.252522299252522299 [pii] (2002).

25 Xu, Y. & Tang, P. Amphiphilic sites for general anesthetic action? Evidence from 129Xe-[1H] intermolecular nuclear Overhauser effects. *Biochim Biophys Acta* **1323**, 154-162, doi:S0005-2736(96)00184-8 [pii] (1997).

26 Xu, Y., Tang, P. & Liachenko, S. Unifying characteristics of sites of anesthetic action revealed by combined use of anesthetics and non-anesthetics. *Toxicol Lett* **100-101**, 347-352 (1998).

27 Yonkunas, M. J., Xu, Y. & Tang, P. Anesthetic interaction with ketosteroid isomerase: insights from molecular dynamics simulations. *Biophys J* **89**, 2350-2356, doi:S0006-3495(05)72877-0 [pii]10.1529/biophysj.105.063396 (2005).

28 Franks, N. P., Jenkins, A., Conti, E., Lieb, W. R. & Brick, P. Structural basis for the inhibition of firefly luciferase by a general anesthetic. *Biophys J* **75**, 2205-2211, doi:S0006-3495(98)77664-7 [pii]10.1016/S0006-3495(98)77664-7 (1998).

29 Franks, N. P. & Lieb, W. R. Mapping of general anaesthetic target sites provides a molecular basis for cutoff effects. *Nature* **316**, 349-351 (1985).

30 Franks, N. P. & Lieb, W. R. Do general anaesthetics act by competitive binding to specific receptors? *Nature* **310**, 599-601 (1984).

31 Canlas, C. G., Cui, T., Li, L., Xu, Y. & Tang, P. Anesthetic modulation of protein dynamics: insight from an NMR study. *J Phys Chem B* **112**, 14312-14318, doi:10.1021/jp805952w (2008).

32 Cui, T. *et al.* Four-alpha-helix bundle with designed anesthetic binding pockets. Part II: halothane effects on structure and dynamics. *Biophys J* **94**, 4464-4472, doi:S0006-3495(08)70101-2 [pii]10.1529/biophysj.107.117853 (2008).

33 Cui, T., Canlas, C. G., Xu, Y. & Tang, P. Anesthetic effects on the structure and dynamics of the second transmembrane domains of nAChR alpha4beta2. *Biochim Biophys Acta*, doi:S0005-2736(09)00292-2 [pii]10.1016/j.bbamem.2009.08.009 (2009).

34 Ma, D. *et al.* Four-alpha-helix bundle with designed anesthetic binding pockets. Part I: structural and dynamical analyses. *Biophys J* **94**, 4454-4463, doi:S0006-3495(08)70100-0 [pii]10.1529/biophysj.107.117838 (2008).

35 Flood, P., Ramirez-Latorre, J. & Role, L. Alpha 4 beta 2 neuronal nicotinic acetylcholine receptors in the central nervous system are inhibited by isoflurane and propofol, but alpha 7-type nicotinic acetylcholine receptors are unaffected. *Anesthesiology* **86**, 859-865 (1997).

36 Ramirez-Latorre, J. *et al.* Functional contributions of alpha5 subunit to neuronal acetylcholine receptor channels. *Nature* **380**, 347-351, doi:10.1038/380347a0 (1996).

37 Zhang, L., Oz, M., Stewart, R. R., Peoples, R. W. & Weight, F. F. Volatile general anaesthetic actions on recombinant nACh alpha 7, 5-HT3 and chimeric nACh alpha 7-5-HT3 receptors expressed in Xenopus oocytes. *Br J Pharmacol* **120**, 353-355, doi:10.1038/sj.bjp.0700934 (1997).

38 Eckenhoff, R. G. An inhalational anesthetic binding domain in the nicotinic acetylcholine receptor. *P Natl Acad Sci USA* **93**, 2807-2810 (1996).

39 Eckenhoff, R. G. & Johansson, J. S. Molecular interactions between inhaled anesthetics and proteins. *Pharmacol Rev* **49**, 343-367 (1997).

40 Bondarenko, V., Yushmanov, V. E., Xu, Y. & Tang, P. NMR study of general anesthetic interaction with nAChR beta2 subunit. *Biophys J* **94**, 1681-1688, doi:S0006-3495(08)70606-4 [pii]10.1529/biophysj.107.116772 (2008).

41 Tang, P., Hu, J., Liachenko, S. & Xu, Y. Distinctly different interactions of anesthetic and nonimmobilizer with transmembrane channel peptides. *Biophys J* **77**, 739-746, doi:S0006-3495(99)76928-6 [pii]10.1016/S0006-3495(99)76928-6 (1999).

42 Tang, P., Simplaceanu, V. & Xu, Y. Structural consequences of anesthetic and nonimmobilizer interaction with gramicidin A channels. *Biophys J* **76**, 2346-2350, doi:S0006-3495(99)77391-1 [pii]10.1016/S0006-3495(99)77391-1 (1999).

43 Tang, P., Yan, B. & Xu, Y. Different distribution of fluorinated anesthetics and nonanesthetics in model membrane: a 19F NMR study. *Biophys J* **72**, 1676-1682, doi:S0006-3495(97)78813-1 [pii]10.1016/S0006-3495(97)78813-1 (1997).

44 Xu, Y., Seto, T., Tang, P. & Firestone, L. NMR study of volatile anesthetic binding to nicotinic acetylcholine receptors. *Biophys J* **78**, 746-751 (2000).

45 Xu, Y., Tang, P., Firestone, L. & Zhang, T. T. 19F nuclear magnetic resonance investigation of stereoselective binding of isoflurane to bovine serum albumin. *Biophys J* **70**, 532-538 (1996).

46 Xu, Y., Yushmanov, V. E. & Tang, P. NMR studies of drug interaction with membranes and membrane-associated proteins. *Biosci Rep* **22**, 175-196 (2002).

47 Roosild, T. P. *et al.* NMR structure of Mistic, a membrane-integrating protein for membrane protein expression. *Science* **307**, 1317-1321, doi:307/5713/1317 [pii]10.1126/science.1106392 (2005).

48 Opella, S. J. *et al.* Structures of the M2 channel-lining segments from nicotinic acetylcholine and NMDA receptors by NMR spectroscopy. *Nat Struct Biol* **6**, 374-379, doi:10.1038/7610 (1999).

49 Haddadian, E. J., Cheng, M. H., Coalson, R. D., Xu, Y. & Tang, P. In silico models for the human alpha4beta2 nicotinic acetylcholine receptor. *J Phys Chem B* **112**, 13981-13990, doi:10.1021/jp804868s (2008).

50 Shen, Y., Delaglio, F., Cornilescu, G. & Bax, A. TALOS plus : a hybrid method for predicting protein backbone torsion angles from NMR chemical shifts. *Journal of Biomolecular Nmr* **44**, 213-223, doi:Doi 10.1007/S10858-009-9333-Z (2009).

51 Mandel, A. M., Akke, M. & Palmer, A. G., 3rd. Backbone dynamics of Escherichia coli ribonuclease HI: correlations with structure and function in an active enzyme. *J Mol Biol* **246**, 144-163, doi:S0022283684700738 [pii] (1995).

52 Denny, J. K., Wang, J. F., Cross, T. A. & Quine, J. R. PISEMA powder patterns and PISA wheels. *Journal of Magnetic Resonance* **152**, 217-226, doi:Doi 10.1006/Jmre.2001.2405 (2001).

53 Wu, C. H., Ramamoorthy, A., Gierasch, L. M. & Opella, S. J. Simultaneous Characterization of the Amide H-1 Chemical Shift,H-1-N-15 Dipolar, and N-15 Chemical-Shift Interaction Tensors in a Peptide-Bond by 3-Dimensional Solid-State Nmr-Spectroscopy. *Journal of the American Chemical Society* **117**, 6148-6149 (1995).

54 Bruggmann, D., Lips, K. S., Pfeil, U., Haberberger, R. V. & Kummer, W. Multiple nicotinic acetylcholine receptor alpha-subunits are expressed in the arterial system of the rat. *Histochem Cell Biol* **118**, 441-447, doi:10.1007/s00418-002-0475-2 (2002).

55 Arias, H. R. Topology of ligand binding sites on the nicotinic acetylcholine receptor. *Brain Res Brain Res Rev* **25**, 133-191, doi:S0165017397000209 [pii] (1997).

56 Bronson, J., Lee, O. S. & Saven, J. G. Molecular Dynamics Simulation of WSK-3, a Computationally Designed, Water-Soluble Variant of the Integral Membrane Protein KcsA. *Biophys J* **90**, 1156-1163, doi:S0006-3495(06)72307-4 [pii]10.1529/biophysj.105.068965 (2006).

57 Ma, D. *et al.* NMR studies of a channel protein without membranes: structure and dynamics of water-solubilized KcsA. *Proc Natl Acad Sci U S A* **105**, 16537-16542, doi:0805501105 [pii]10.1073/pnas.0805501105 (2008).

58 Slovic, A. M., Kono, H., Lear, J. D., Saven, J. G. & DeGrado, W. F. Computational design of water-soluble analogues of the potassium channel KcsA. *Proc Natl Acad Sci U S A* **101**, 1828-1833, doi:10.1073/pnas.0306417101010306417101 [pii] (2004).

59 Fraczkiewicz, R., Braun, W. Exact and efficient analytical calculation of the accessible surface areas and their gradients for macromolecules. *J Comput Chem* **19**, 15 (1998).

60 Kono, H. & Saven, J. G. Statistical theory for protein combinatorial libraries. Packing interactions, backbone flexibility, and the sequence variability of a main-chain structure. *J Mol Biol* **306**, 607-628, doi:10.1006/jmbi.2000.4422S0022-2836(00)94422-X [pii] (2001).

61 Calhoun, J. R. *et al.* Computational design and characterization of a monomeric helical dinuclear metalloprotein. *J Mol Biol* **334**, 1101-1115, doi:S0022283603012579 [pii] (2003).

62 Cochran, F. V. *et al.* Computational de novo design and characterization of a four-helix bundle protein that selectively binds a nonbiological cofactor. *J Am Chem Soc* **127**, 1346-1347, doi:10.1021/ja044129a (2005).

63 Nanda, V. *et al.* De novo design of a redox-active minimal rubredoxin mimic. *J Am Chem Soc* **127**, 5804-5805, doi:10.1021/ja050553f (2005).

64 Bender, G. M. *et al.* De novo design of a single-chain diphenylporphyrin metalloprotein. *J Am Chem Soc* **129**, 10732-10740, doi:10.1021/ja071199j (2007).

65 Dunbrack, R. L., Jr. & Cohen, F. E. Bayesian statistical analysis of protein side-chain rotamer preferences. *Protein Sci* **6**, 1661-1681, doi:10.1002/pro.5560060807 (1997).

66 Weiner, S. J., Kollman, P. A., Case, D. A., Singh, U. C., Ghio, C., Alagona, G., Profeta, S., and Weiner, P. A New Force-Field For Molecular Mechanical Simulation Of Nucleic-Acids And Proteins. *J. Am. Chem. Soc.* **106**, 20 (1984).

67 Fiser, A., Do, R. K. & Sali, A. Modeling of loops in protein structures. *Protein Sci* **9**, 1753-1773, doi:10.1110/ps.9.9.1753 (2000).

68 Phillips, J. C. *et al.* Scalable molecular dynamics with NAMD. *J Comput Chem* **26**, 1781-1802, doi:10.1002/jcc.20289 (2005).

69 MacKerell, A. D., Bashford, D., Bellott, M., Dunbrack, R. L., Evanseck, J. D., Field, M. J., Fischer, S., Gao, J., Guo, H., Ha, S., Joseph-McCarthy, D., Kuchnir, L., Kuczera, K., Lau, F. T. K., Mattos, C., Michnick, S., Ngo, T., Nguyen, D. T., Prodhom, B., Reiher, W. E., Roux, B., Schlenkrich, M., Smith, J. C., Stote, R., Straub, J., Watanabe, M., Wiorkiewicz-Kuczera, J., Yin, D., and Karplus, M. All-atom empirical potential for molecular modeling and dynamics studies of proteins. *J. Phys. Chem. B* **102**, 31 (1998).

70 Loria, J. P., M. Rance, and A. G. Palmer. A Relaxation-Compensated Carr-Purcell-Meiboom-Gill Sequence for Characterizing Chemical Exchange by NMR Spectroscopy. *J. Am. Chem. Soc.* **121**, 1 (1999).

71 Tollinger, M., Skrynnikov, N. R., Mulder, F. A., Forman-Kay, J. D. & Kay, L. E. Slow dynamics in folded and unfolded states of an SH3 domain. *J Am Chem Soc* **123**, 11341-11352, doi:ja011300z [pii] (2001).

72 Delaglio, F. *et al.* NMRPipe: a multidimensional spectral processing system based on UNIX pipes. *J Biomol NMR* **6**, 277-293 (1995).

73 Goddard, T. D. & Kneller, D. G. Sparky 3 (University of California, San Francisco). (2002).

74 Guntert, P., Mumenthaler, C. & Wuthrich, K. Torsion angle dynamics for NMR structure calculation with the new program DYANA. *J Mol Biol* **273**, 283-298 (1997).

75 Cornilescu, G., Delaglio, F. & Bax, A. Protein backbone angle restraints from searching a database for chemical shift and sequence homology. *J Biomol NMR* **13**, 289-302 (1999).

76 Baxter, N. J. & Williamson, M. P. Temperature dependence of 1H chemical shifts in proteins. *J Biomol NMR* **9**, 359-369 (1997).

77 Humphrey, W., Dalke, A. & Schulten, K. VMD: visual molecular dynamics. *J Mol Graph* **14**, 33-38, 27-38, doi:0263785596000185 [pii] (1996).

78 Koradi, R., Billeter, M. & Wuthrich, K. MOLMOL: a program for display and analysis of macromolecular structures. *J Mol Graph* **14**, 51-55, 29-32, doi:0263785596000094 [pii] (1996).

79 Clore, G. M. *et al.* Deviations from the simple two-parameter model-free approach to the interpretation of nitrogen-15 nuclear magnetic relaxation of proteins. *Journal of the American Chemical Society* **112**, 4989-4991, doi:10.1021/ja00168a070 (1990).

80 Fushman, D., Cahill, S. & Cowburn, D. The main-chain dynamics of the dynamin pleckstrin homology (PH) domain in solution: analysis of 15N relaxation with monomer/dimer equilibration. *Journal of Molecular Biology* **266**, 173-194 (1997).

81 Tang, P., Mandal, P. K. & Xu, Y. NMR structures of the second transmembrane domain of the human glycine receptor alpha(1) subunit: model of pore architecture and channel gating. *Biophys J* **83**, 252-262, doi:S0006-3495(02)75166-7 [pii]10.1016/S0006-3495(02)75166-7 (2002).

82 Yushmanov, V. E., Xu, Y. & Tang, P. NMR structure and dynamics of the second transmembrane domain of the neuronal acetylcholine receptor beta 2 subunit. *Biochemistry* **42**, 13058-13065, doi:10.1021/bi0350396 (2003).

83 Yushmanov, V. E., Mandal, P. K., Liu, Z., Tang, P. & Xu, Y. NMR structure and backbone dynamics of the extended second transmembrane domain of the human neuronal glycine receptor alpha1 subunit. *Biochemistry* **42**, 3989-3995, doi:10.1021/bi026767g (2003).

84 Bondarenko, V., Xu, Y. & Tang, P. Structure of the first transmembrane domain of the neuronal acetylcholine receptor beta2 subunit. *Biophys J* **92**, 1616-1622, doi:S0006-3495(07)70969-4 [pii]10.1529/biophysj.106.095364 (2007).

85 Ma, D., Liu, Z., Li, L., Tang, P. & Xu, Y. Structure and dynamics of the second and third transmembrane domains of human glycine receptor. *Biochemistry* **44**, 8790-8800, doi:10.1021/bi050256n (2005).

86 Smart, O. S., Neduvelil, J. G., Wang, X., Wallace, B. A. & Sansom, M. S. P. HOLE: A program for the analysis of the pore dimensions of ion channel structural models. *J Mol Graph Model* **14**, 354-& (1996).

87 Loria, J. P., Rance, M. & Palmer, A. G. A Relaxation-Compensated Carr,àíPurcell,àíMeiboom,àíGill Sequence for Characterizing Chemical Exchange by NMR Spectroscopy. *Journal of the American Chemical Society* **121**, 2331-2332, doi:10.1021/ja983961a (1999).

88 Tollinger, M., Skrynnikov, N. R., Mulder, F. A. A., Forman-Kay, J. D. & Kay, L. E. Slow Dynamics in Folded and Unfolded States of an SH3 Domain. *Journal of the American Chemical Society* **123**, 11341-11352, doi:10.1021/ja011300z (2001).

89 Brandl, C. J. & Deber, C. M. Hypothesis about the function of membrane-buried proline residues in transport proteins. *Proc Natl Acad Sci U S A* **83**, 5 (1986).

90 Kim, J. & McNamee, M. G. Topological Disposition of Cys 222 in the Œ±-Subunit of Nicotinic Acetylcholine Receptor Analyzed by Fluorescence-Quenching and Electron Paramagnetic Resonance Measurements‚Ä†. *Biochemistry* **37**, 4680-4686, doi:10.1021/bi972666k (1998).

91 Le Novere, N., Corringer, P. J. & Changeux, J. P. Improved secondary structure predictions for a nicotinic receptor subunit: incorporation of solvent accessibility and experimental data into a two-dimensional representation. *Biophys J* **76**, 2329-2345, doi:S0006-3495(99)77390-X [pii]10.1016/S0006-3495(99)77390-X (1999).

92 Reddy, G. L., Iwamoto, T., Tomich, J. M. & Montal, M. Synthetic peptides and four-helix bundle proteins as model systems for the pore-forming structure of channel proteins. II. Transmembrane segment M2 of the brain glycine receptor is a plausible candidate for the pore-lining structure. *J Biol Chem* **268**, 14608-14615 (1993).

93 Opella, S. J., J. Gesell, A. R. Valente, F. M. Marassi, M. Oblatt-Montal, W. Sun, A. F. Montiel, and M. Montal. Structural studies of the pore-lining segments of neurotransmitter-gated channels. *Biochem. Mol. Biol* **10**, 21 (1997).

94 Marsh, D. Peptide models for membrane channels. *Biochem J* **315 (Pt 2)**, 345-361 (1996).

95 Loria, J. P., Rance, M. & Palmer, A. G., 3rd. A relaxation-compensated Carr-Purcell-Meiboom-Gill sequence for characterizing chemical exchange by NMR spectroscopy. *J Am Chem Soc* **121**, 1 (1999).

96 Cui, T., Canlas, C. G., Xu, Y. & Tang, P. Anesthetic effects on the structure and dynamics of the second transmembrane domains of nAChR alpha4beta2. *Biochim Biophys Acta* **1798**, 161-166, doi:S0005-2736(09)00292-2 [pii]10.1016/j.bbamem.2009.08.009 (2010).

97 Unwin, N. Acetylcholine receptor channel imaged in the open state. *Nature* **373**, 37-43, doi:10.1038/373037a0 (1995).

98 Johansson, J. S., Gibney, B. R., Rabanal, F., Reddy, K. S. & Dutton, P. L. A designed cavity in the hydrophobic core of a four-alpha-helix bundle improves volatile anesthetic binding affinity. *Biochemistry* **37**, 1421-1429 (1998).

99 Johansson, J. S., Scharf, D., Davies, L. A., Reddy, K. S. & Eckenhoff, R. G. A designed four-alpha-helix bundle that binds the volatile general anesthetic halothane with high affinity. *Biophys J* **78**, 982-993 (2000).

100 Pidikiti, R., Shamim, M., Mallela, K. M., Reddy, K. S. & Johansson, J. S. Expression and characterization of a four-alpha-helix bundle protein that binds the volatile general anesthetic halothane. *Biomacromolecules* **6**, 1516-1523 (2005).

101 Fielding, L. NMR methods for the determination of protein-ligand dissociation constants. *Current topics in medicinal chemistry* **3**, 39-53 (2003).

102 Morton, C. J. *et al.* Solution structure and peptide binding of the SH3 domain from human Fyn. *Structure* **4**, 705-714 (1996).

103 Lipari, G. & Szabo, A. Model-free approach to the interpretation of nuclear magnetic resonance relaxation in macromolecules. 1. Theory and range of validity. *J Am Chem Soc* **104**, 4546-4559 (1982).

104 Lipari, G. & Szabo, A. Model-Free Approach to the Interpretation of Nuclear Magnetic Resonance Relaxation in Macromolecules. 2. Analysis of Experimental Results. *J Am Chem Soc* **104**, 4559-4570 (1982).

105 Wishart, D. S. *et al.* 1H, 13C and 15N chemical shift referencing in biomolecular NMR. *J Biomol NMR* **6**, 135-140 (1995).

106 Mulder, F. A., Skrynnikov, N. R., Hon, B., Dahlquist, F. W. & Kay, L. E. Measurement of slow (micros-ms) time scale dynamics in protein side chains by (15)N relaxation dispersion NMR spectroscopy: application to Asn and Gln residues in a cavity mutant of T4 lysozyme. *J Am Chem Soc* **123**, 967-975, doi:ja003447g [pii] (2001).

107 Luz, Z., and S. Meiboom. Nuclear magnetic resonance study of the protolysis of trimethylammonium ion in aqueous solution—order of the reaction with respect to solvent. *J. Chem. Phys* **39**, 5 (1963).

108 Perazzolo, C., Verde, M., Homans, S. W. & Bodenhausen, G. Evidence of chemical exchange in recombinant Major Urinary Protein and quenching thereof upon pheromone binding. *J Biomol NMR* **38**, 3-9, doi:10.1007/s10858-006-9110-1 (2007).

109 Loria, J. P., M. Rance, and A. G. Palmer. Relaxation-Compensated Carr-Purcell-Meiboom-Gill Sequence for Characterizing Chemical Exchange by NMR Spectroscopy. *J. Am. Chem. Soc.* **121**, 2 (1999).

110 Meyer, B. & Peters, T. NMR spectroscopy techniques for screening and identifying ligand binding to protein receptors. *Angewandte Chemie (International ed* **42**, 864-890 (2003).

111 Davies, L. A., Zhong, Q., Klein, M. L. & Scharf, D. Molecular dynamics simulation of four-alpha-helix bundles that bind the anesthetic halothane. *FEBS Lett* **478**, 61-66 (2000).

112 Tang, P., I. Zubryzcki, and Y. Xu. Ab initio calculation of structures and properties of halogenated general anesthetics: halothane and sevoflurane. *J. Comput. Chem.* **22**, 9 (2001).

113 Kneller, J. M., Lu, M. & Bracken, C. An effective method for the discrimination of motional anisotropy and chemical exchange. *J Am Chem Soc* **124**, 1852-1853, doi:ja017461k [pii] (2002).

114 Ishima, R. & Torchia, D. A. Extending the range of amide proton relaxation dispersion experiments in proteins using a constant-time relaxation-compensated CPMG approach. *J Biomol NMR* **25**, 243-248, doi:5113797 [pii] (2003).

115 Morris, G. M. *et al.* Automated docking using a Lamarckian genetic algorithm and an empirical binding free energy function. *Journal of Computational Chemistry* **19**, 1639-1662 (1998).

116 Laurie, A. T. & Jackson, R. M. Q-SiteFinder: an energy-based method for the prediction of protein-ligand binding sites. *Bioinformatics* **21**, 1908-1916, doi:bti315 [pii]10.1093/bioinformatics/bti315 (2005).

117 Lopez, M. M. & Kosk-Kosicka, D. Entropy-driven interactions of anesthetics with membrane proteins. *Biochemistry* **36**, 8864-8872, doi:10.1021/bi970028wbi970028w [pii] (1997).

118 Eckenhoff, M. F., Chan, K. & Eckenhoff, R. G. Multiple specific binding targets for inhaled anesthetics in the mammalian brain. *J Pharmacol Exp Ther* **300**, 172-179 (2002).

119 Liu, Z., Xu, Y. & Tang, P. Molecular dynamics simulations of C2F6 effects on gramicidin A: implications of the mechanisms of general anesthesia. *Biophys J* **88**, 3784-3791, doi:S0006-3495(05)73433-0 [pii]10.1529/biophysj.104.055566 (2005).

120 Liu, Z., Xu, Y. & Tang, P. Steered molecular dynamics simulations of Na+ permeation across the gramicidin A channel. *J Phys Chem B* **110**, 12789-12795, doi:10.1021/jp060688n (2006).

121 Szarecka, A., Xu, Y. & Tang, P. Dynamics of heteropentameric nicotinic acetylcholine receptor: implications of the gating mechanism. *Proteins* **68**, 948-960, doi:10.1002/prot.21462 (2007).

122 Krizova, H., Zidek, L., Stone, M. J., Novotny, M. V. & Sklenar, V. Temperature-dependent spectral density analysis applied to monitoring backbone dynamics of major urinary protein-I complexed with the pheromone 2- sec-butyl-4,5-dihydrothiazole. *J Biomol NMR* **28**, 369-384, doi:10.1023/B:JNMR.0000015404.61574.655256334 [pii] (2004).

123 Kyte, J. & Doolittle, R. F. A simple method for displaying the hydropathic character of a protein. *J Mol Biol* **157**, 105-132, doi:0022-2836(82)90515-0 [pii] (1982).

124 Mihic, S. J. *et al.* Sites of alcohol and volatile anaesthetic action on GABA(A) and glycine receptors. *Nature* **389**, 385-389, doi:10.1038/38738 (1997).

125 Liu, R., Loll, P. J. & Eckenhoff, R. G. Structural basis for high-affinity volatile anesthetic binding in a natural 4-helix bundle protein. *FASEB J* **19**, 567-576, doi:19/6/567 [pii]10.1096/fj.04-3171com (2005).

126 Marley, J., Lu, M. & Bracken, C. A method for efficient isotopic labeling of recombinant proteins. *J Biomol NMR* **20**, 71-75 (2001).

127 Mayer, M. & Meyer, B. Characterization of ligand binding by saturation transfer difference NMR spectroscopy. *Angew Chem Int Edit* **38**, 1784-1788 (1999).

128 Hwang, T. L. & Shaka, A. J. Water Suppression That Works - Excitation Sculpting Using Arbitrary Wave-Forms and Pulsed-Field Gradients. *J Magn Reson Ser A* **112**, 275-279 (1995).

129 Streiff, J. H. *et al.* Saturation transfer difference nuclear magnetic resonance spectroscopy as a method for screening proteins for anesthetic binding. *Mol Pharmacol* **66**, 929-935 (2004).

130 Farrow, N. A. *et al.* Backbone dynamics of a free and phosphopeptide-complexed Src homology 2 domain studied by 15N NMR relaxation. *Biochemistry* **33**, 5984-6003 (1994).

131 Zimmerman, D. E. *et al.* Automated analysis of protein NMR assignments using methods from artificial intelligence. *Journal of Molecular Biology* **269**, 592-610 (1997).

132 Schwieters, C. D., Kuszewski, J. J., Tjandra, N. & Clore, G. M. The Xplor-NIH NMR molecular structure determination package. *J Magn Reson* **160**, 65-73, doi:S1090780702000149 [pii] (2003).

133 Clore, G. M., Gronenborn, A. M. & Bax, A. A robust method for determining the magnitude of the fully asymmetric alignment tensor of oriented macromolecules in the absence of structural information. *J Magn Reson* **133**, 216-221, doi:S1090-7807(98)91419-7 [pii]10.1006/jmre.1998.1419 (1998).

134 Dosset, P., Hus, J. C., Marion, D. & Blackledge, M. A novel interactive tool for rigid-body modeling of multi-domain macromolecules using residual dipolar couplings. *J Biomol NMR* **20**, 223-231 (2001).

135 Richards, J. P. C. a. R. E. A general two-site solution for the chemical exchange produced dependence of T2 upon the carr-Purcell pulse separation. *Journal of Magnetic Resonance (1969)* **6**, 17 (1972).

136 Kash, T. L., Jenkins, A., Kelley, J. C., Trudell, J. R. & Harrison, N. L. Coupling of agonist binding to channel gating in the GABA(A) receptor. *Nature* **421**, 272-275, doi:10.1038/nature01280nature01280 [pii] (2003).

137 Kruse, S. W., Zhao, R., Smith, D. P. & Jones, D. N. Structure of a specific alcohol-binding site defined by the odorant binding protein LUSH from Drosophila melanogaster. *Nat Struct Biol* **10**, 694-700, doi:10.1038/nsb960nsb960 [pii] (2003).

138 Colloc'h, N. *et al.* Protein crystallography under xenon and nitrous oxide pressure: comparison with in vivo pharmacology studies and implications for the mechanism of inhaled anesthetic action. *Biophys J* **92**, 217-224, doi:S0006-3495(07)70819-6 [pii]10.1529/biophysj.106.093807 (2007).

139 Mittag, T., Schaffhausen, B. & Gunther, U. L. Direct observation of protein-ligand interaction kinetics. *Biochemistry* **42**, 11128-11136, doi:10.1021/bi0347499 (2003).

140 Arevalo, E., Chiara, D. C., Forman, S. A., Cohen, J. B. & Miller, K. W. Gating-enhanced accessibility of hydrophobic sites within the transmembrane region of the nicotinic acetylcholine receptor's {delta}-subunit. A time-resolved photolabeling study. *J Biol Chem* **280**, 13631-13640, doi:M413911200 [pii]10.1074/jbc.M413911200 (2005).

141 Cardoso, R. A. *et al.* Effects of ethanol on recombinant human neuronal nicotinic acetylcholine receptors expressed in Xenopus oocytes. *J Pharmacol Exp Ther* **289**, 774-780 (1999).

142 Forman, S. A., Miller, K. W. & Yellen, G. A discrete site for general anesthetics on a postsynaptic receptor. *Mol Pharmacol* **48**, 574-581 (1995).

143 Mori, T. *et al.* Modulation of neuronal nicotinic acetylcholine receptors by halothane in rat cortical neurons. *Mol Pharmacol* **59**, 732-743 (2001).

144 Raines, D. E. & Zachariah, V. T. Isoflurane increases the apparent agonist affinity of the nicotinic acetylcholine receptor. *Anesthesiology* **90**, 135-146 (1999).

145 Raines, D. E. & Zachariah, V. T. Isoflurane increases the apparent agonist affinity of the nicotinic acetylcholine receptor by reducing the microscopic agonist dissociation constant. *Anesthesiology* **92**, 775-785 (2000).

146 Yamashita, M., Mori, T., Nagata, K., Yeh, J. Z. & Narahashi, T. Isoflurane modulation of neuronal nicotinic acetylcholine receptors expressed in human embryonic kidney cells. *Anesthesiology* **102**, 76-84, doi:00000542-200501000-00015 [pii] (2005).

147 Flores, C. M., Rogers, S. W., Pabreza, L. A., Wolfe, B. B. & Kellar, K. J. A subtype of nicotinic cholinergic receptor in rat brain is composed of alpha 4 and beta 2 subunits and is up-regulated by chronic nicotine treatment. *Mol Pharmacol* **41**, 31-37 (1992).

148 Traaseth, N. J. *et al.* Structure and topology of monomeric phospholamban in lipid membranes determined by a hybrid solution and solid-state NMR approach. *Proc Natl Acad Sci U S A* **106**, 10165-10170, doi:0904290106 [pii]10.1073/pnas.0904290106 (2009).

149 Bajaj, V. S., Mak-Jurkauskas, M. L., Belenky, M., Herzfeld, J. & Griffin, R. G. Functional and shunt states of bacteriorhodopsin resolved by 250 GHz dynamic nuclear polarization-enhanced solid-state NMR. *Proc Natl Acad Sci U S A* **106**, 9244-9249, doi:0900908106 [pii]10.1073/pnas.0900908106 (2009).

150 Salnikov, E., Aisenbrey, C., Vidovic, V. & Bechinger, B. Solid-state NMR approaches to measure topological equilibria and dynamics of membrane

polypeptides. *Biochim Biophys Acta* **1798**, 258-265, doi:S0005-2736(09)00220-X [pii]10.1016/j.bbamem.2009.06.021 (2010).

151 Kandasamy, S. K. *et al.* Solid-state NMR and molecular dynamics simulations reveal the oligomeric ion-channels of TM2-GABA(A) stabilized by intermolecular hydrogen bonding. *Biochim Biophys Acta* **1788**, 686-695, doi:S0005-2736(08)00358-1 [pii]10.1016/j.bbamem.2008.11.009 (2009).

152 McDermott, A. Structure and dynamics of membrane proteins by magic angle spinning solid-state NMR. *Annu Rev Biophys* **38**, 385-403, doi:10.1146/annurev.biophys.050708.133719 (2009).

153 Li, C., Yi, M., Hu, J., Zhou, H. X. & Cross, T. A. Solid-state NMR and MD simulations of the antiviral drug amantadine solubilized in DMPC bilayers. *Biophys J* **94**, 1295-1302, doi:S0006-3495(08)70646-5 [pii]10.1529/biophysj.107.112482 (2008).

154 Opella, S. J., Zeri, A. C. & Park, S. H. Structure, dynamics, and assembly of filamentous bacteriophages by nuclear magnetic resonance spectroscopy. *Annu Rev Phys Chem* **59**, 635-657, doi:10.1146/annurev.physchem.58.032806.104640 (2008).

155 Hong, M. Structure, topology, and dynamics of membrane peptides and proteins from solid-state NMR spectroscopy. *J Phys Chem B* **111**, 10340-10351, doi:10.1021/jp073652j (2007).

156 Watts, A. Solid-state NMR in drug design and discovery for membrane-embedded targets. *Nat Rev Drug Discov* **4**, 555-568, doi:nrd1773 [pii]10.1038/nrd1773 (2005).

157 Fu, R., Truong, M., Saager, R. J., Cotten, M. & Cross, T. A. High-resolution heteronuclear correlation spectroscopy in solid state NMR of aligned samples. *J Magn Reson* **188**, 41-48, doi:S1090-7807(07)00197-8 [pii]10.1016/j.jmr.2007.06.004 (2007).

158 Buffy, J. J. *et al.* Two-dimensional solid-state NMR reveals two topologies of sarcolipin in oriented lipid bilayers. *Biochemistry* **45**, 10939-10946, doi:10.1021/bi060728d (2006).

159 Li, C. *et al.* Uniformly aligned full-length membrane proteins in liquid crystalline bilayers for structural characterization. *J Am Chem Soc* **129**, 5304-5305, doi:10.1021/ja068402f (2007).

160 Durr, U. H., Waskell, L. & Ramamoorthy, A. The cytochromes P450 and b5 and their reductases--promising targets for structural studies by advanced solid-state NMR spectroscopy. *Biochim Biophys Acta* **1768**,

3235-3259, doi:S0005-2736(07)00294-5 [pii]10.1016/j.bbamem.2007.08.007 (2007).

161 Williamson, P. T., Verhoeven, A., Miller, K. W., Meier, B. H. & Watts, A. The conformation of acetylcholine at its target site in the membrane-embedded nicotinic acetylcholine receptor. *Proc Natl Acad Sci U S A* **104**, 18031-18036, doi:0704785104 [pii]10.1073/pnas.0704785104 (2007).

162 Williamson, P. T., Meier, B. H. & Watts, A. Structural and functional studies of the nicotinic acetylcholine receptor by solid-state NMR. *Eur Biophys J* **33**, 247-254, doi:10.1007/s00249-003-0380-1 (2004).

163 de Planque, M. R., Rijkers, D. T., Fletcher, J. I., Liskamp, R. M. & Separovic, F. The alphaM1 segment of the nicotinic acetylcholine receptor exhibits conformational flexibility in a membrane environment. *Biochim Biophys Acta* **1665**, 40-47, doi:S0005-2736(04)00155-5 [pii]10.1016/j.bbamem.2004.06.021 (2004).

164 Williamson, P. T., Zandomeneghi, G., Barrantes, F. J., Watts, A. & Meier, B. H. Structural and dynamic studies of the gamma-M4 trans-membrane domain of the nicotinic acetylcholine receptor. *Mol Membr Biol* **22**, 485-496, doi:W285662N81032837 [pii]10.1080/09687860500370653 (2005).

165 De Angelis, A. A., Howell, S. C., Nevzorov, A. A. & Opella, S. J. Structure determination of a membrane protein with two trans-membrane helices in aligned phospholipid bicelles by solid-state NMR spectroscopy. *J Am Chem Soc* **128**, 12256-12267, doi:10.1021/ja063640w (2006).

166 Wu, C. H., Ramamoorthy, A. & Opella, S. J. High-Resolution Heteronuclear Dipolar Solid-State Nmr-Spectroscopy. *J Magn Reson Ser A* **109**, 270-272 (1994).

167 Delaglio, F. *et al.* Nmrpipe - a Multidimensional Spectral Processing System Based on Unix Pipes. *Journal of Biomolecular Nmr* **6**, 277-293 (1995).

168 Wang, J. *et al.* Imaging membrane protein helical wheels. *J Magn Reson* **144**, 162-167, doi:10.1006/jmre.2000.2037S1090-7807(00)92037-8 [pii] (2000).

169 Marassi, F. M. & Opella, S. J. A solid-state NMR index of helical membrane protein structure and topology. *J Magn Reson* **144**, 150-155, doi:10.1006/jmre.2000.2035S1090-7807(00)92035-4 [pii] (2000).

170 Davis, J. H. The description of membrane lipid conformation, order and dynamics by 2H-NMR. *Biochim Biophys Acta* **737**, 117-171, doi:0304-4157(83)90015-1 [pii] (1983).

171 Yamamoto, K., Soong, R. & Ramamoorthy, A. Comprehensive Analysis of Lipid Dynamics Variation with Lipid Composition and Hydration of Bicelles Using Nuclear Magnetic Resonance (NMR) Spectroscopy. *Langmuir* **25**, 7010-7018, doi:Doi 10.1021/La900200s (2009).

172 McGehee, D. S. Molecular diversity of neuronal nicotinic acetylcholine receptors. *Ann N Y Acad Sci* **868**, 565-577 (1999).

173 Aisenbrey, C. & Bechinger, B. Investigations of polypeptide rotational diffusion in aligned membranes by 2H and 15N solid-state NMR spectroscopy. *J Am Chem Soc* **126**, 16676-16683, doi:10.1021/ja0468675 (2004).

174 Page, R. C., Kim, S. & Cross, T. A. Transmembrane helix uniformity examined by spectral mapping of torsion angles. *Structure* **16**, 787-797, doi:S0969-2126(08)00132-9 [pii]10.1016/j.str.2008.02.018 (2008).

175 Abragam, A. Principles of Nuclear Magnetism. 315 (1961).

176 Pfeiffer, F., Graham, D. & Betz, H. Purification by affinity chromatography of the glycine receptor of rat spinal cord. *J Biol Chem* **257**, 9389-9393 (1982).

177 Hinton, J. F., Newkirk, D. K., Fletcher, T. G. & Shungu, D. C. Application of the Magnetization-Inversion-Transfer Technique to the Transport of Li-7(+), Na-23(+), and K-39(+) Ions through the Gramicidin Channel and the M2-Delta Transmembrane Domain of the Nicotinic Acetylcholine-Receptor. *J Magn Reson Ser B* **105**, 11-16 (1994).

178 Tang, P., Hu, J., Liachenko, S. & Xu, Y. Distinctly different interactions of anesthetic and nonimmobilizer with transmembrane channel peptides. *Biophysical Journal* **77**, 739-746 (1999).

179 Correa, A. M. & Agnew, W. S. Fusion of native or reconstituted membranes to liposomes, optimized for single channel recording. *Biophys J* **54**, 569-575, doi:S0006-3495(88)82991-6 [pii]10.1016/S0006-3495(88)82991-6 (1988).

180 Diven, C. F. *et al.* Evaluation of [Co(gly)3]- as a 35Cl- NMR shift reagent for cellular studies. *Inorg Chem* **42**, 2774-2782, doi:10.1021/ic0258680 (2003).

181 Pribilla, I., Takagi, T., Langosch, D., Bormann, J. & Betz, H. The atypical M2 segment of the beta subunit confers picrotoxinin resistance to inhibitory glycine receptor channels. *EMBO J* **11**, 4305-4311 (1992).